

MODELING OF CHARGE INJECTION AND TRANSPORT IN
ORGANIC SEMICONDUCTORS WITH APPLICATIONS TO
CONDUCTING ATOMIC FORCE MICROSCOPY

By

Kanokkorn Pimcharoen

A DISSERTATION

Submitted to
Michigan State University
in partial fulfillment of the requirements
for the degree of

Physics — Doctor of Philosophy

2018

ABSTRACT

MODELING OF CHARGE INJECTION AND TRANSPORT IN ORGANIC SEMICONDUCTORS WITH APPLICATIONS TO CONDUCTING ATOMIC FORCE MICROSCOPY

By

Kanokkorn Pimcharoen

Charge injection and transport in organic semiconductors are key factors controlling the device performance, and have been intensively investigated by conductive atomic force microscope (c-AFM) experiments in the space-charge-limited current (SCLC) regime. The simplified SCLC theory, despite being widely used to describe the unipolar SCLC, has limitations in explaining the current-voltage responses of c-AFM measurements due to two major reasons. First, the conventional planar model does not include the effect of current spreading commonly found beneath the conducting tip. Secondly, the theory only considers drift transport, and assumes that charge diffusion can be neglected, causing discrepancies in its predictions of transport behaviors that will be discussed thoroughly here. The focus of this thesis is on developing numerical models for hole-only devices with the full description of drift and diffusion transport mechanisms, which is called the drift-diffusion (DD-) SCLC model. The applications of the models in the analysis of c-AFM experimental data are presented.

We generalize the theory which takes both drift and diffusion currents into account, leading to more realistic DD-SCLC models for several applications. We then develop numerical approaches that efficiently simulate the hole-only SCLCs for one-, two-, and three- dimensional systems. In the case of fully 3-D calculations, the DD-SCLC model is able to treat inhomogeneous systems including spatially varying trap distributions, nanoscale morphologies, and the tip-plane (c-AFM) geometry. In the theoretical studies, the device simulations

elucidate a number of crucial factors that affect the charge transport in the SCLC regime, including charge diffusion, traps, as well as, nanoscale morphology. We introduce the methodology of characterizing the current-voltage responses from c-AFM measurements, which has been used in elucidating the experiments on semiconductor poly(3-hexylthiophene) (P3HT) thin films that develop fibrous morphologies after thermal annealing.

*Vita brevis,
ars longa,
occasio praeceps,
experimentum periculosum,
iudicium difficile.*

— Hippocrates; c.460-c.370 BC

ACKNOWLEDGMENTS

My PhD journey was nothing but one eventful ride that I was so fortunate to experience. For that I would like to express my gratitude to all the people who taught me how science worked in both simple and elegant ways.

First and foremost, I would like to express my deepest gratitude to my advisor, Professor Phillip M. Duxbury, for guiding me through my graduate program with his insight, support and great patience. Your broad spectrum from an awesome physicist, an excellent sportsman as well as an article (a/an/the) modulator, will lesson me for life. Also, I would like to extend my gratitude to the rest of my committee members, Professor Andrew J. Christlieb, Professor Richard R. Lunt, Professor Vladimir G. Zelevinsky and Professor Pengpeng Zhang. It was valuable to learn from you all.

It will always be my honor to have been a part of Professor Duxbury's group. I would like to express my gratitude to the former and the current members. To Jiwu, Dan, Luke, Saurabh, Jenni, Corey, Non, Bin, Xukun, Tim and Brandon, thank you for all productive discussions and amazing friendships. I cannot say enough thanks to Dan for simulating plenty of model morphologies I can play with, and to Tim for proofreading my final draft. The thanks are also due to Jibing and Sean from Professor Zhang's group for their contributions in the experiments of semiconducting poly(thiophene).

Last but not least, I could not have ended my PhD years without my friends and family. Thanks all my friends for being there for me through my ups and downs. My dissertation would not have been possible without the very first proofread from Jiwu. I do not think I would make it out in one piece. It has been the best time of my life because you were there to keep me sane, to remind me to live to the fullest, to toughen up, to have faith, to laugh,

to cry, and much more. I saved the largest thanks for last. To our big family in China and Thailand, your invincible loves and ultimate supports meant the world to me.

I acknowledge the financial support during my first five years at MSU from the Thai government scholarship.

TABLE OF CONTENTS

LIST OF TABLES	ix
LIST OF FIGURES	xi
KEY TO SYMBOLS	xx
Chapter 1 Introduction	1
1.1 Motivation	1
1.2 Overview	4
Chapter 2 Theory of Charge Carrier Injection - Background	6
2.1 Charge Injection in Organic Semiconductors	6
2.2 Fundamental Equations to Describe SCLC in Hole Injection System	8
2.3 The Simplified Theory of SCLC: Planar (Plane-Parallel) Geometry	10
2.3.1 Trap-Free SCLC	12
2.3.2 SCLC with The Exponential Distribution of Trap States	14
2.4 The Simplified Model of SCLC: Tip-Plane (c-AFM) Geometry	18
Chapter 3 The Drift-Diffusion SCLC Transport Models - New Method	22
3.1 Modeling the Hole Injection System	22
3.1.1 Governing Equations	23
3.1.2 Electrode Boundary Conditions	26
3.1.3 Scaling Factors	27
3.2 Numerical Method	28
3.2.1 Numerical Derivatives	29
3.2.2 Numerical Integrations	32
3.2.3 Scharfetter-Gummel Discretization	34
3.2.4 Numerical Calculation Scheme	37
3.3 1-D DD-SCLC Model: Homogeneous Planar Geometry	40
3.3.1 Discretization	41
3.3.2 Potential Solver	42
3.3.3 Hole Density Solver	43
3.3.4 Verification	44
3.4 2-D DD-SCLC Model: Semi-Homogeneous Tip-Plane Geometry	50
3.4.1 Discretization	52
3.4.2 Potential Solver	55
3.4.3 Hole Density Solver	59
3.4.4 Verification	63
3.5 The Fully 3-D DD-SCLC Model in a Cartesian Coordinate System	72
3.5.1 Discretization	75

3.5.2	Potential Solver	77
3.5.3	Hole Density Solver	80
3.5.4	Verification	84
3.6	Conclusions	89
Chapter 4	The Drift-Diffusion SCLC Transport Models - New Results . .	91
4.1	Diffusion Effects	91
4.1.1	Planar Geometry	96
4.1.2	Tip-Plane Geometry	99
4.2	Trap Effects	103
4.2.1	Planar Geometry	104
4.2.2	Tip-Plane Geometry	110
4.3	Morphological Effects: Semi-Crystalline P3HT Thin Films	116
4.3.1	An Isolated Fiber: ‘Face-On’ Fiber and ‘Edge-On’ Fiber	119
4.3.2	An ‘Edge-On’ Fiber Network	132
4.4	Conclusions	136
Chapter 5	The Drift-Diffusion SCLC Transport Models - Application to an Experimental System	140
5.1	Experiments and Results	141
5.2	Theoretical Simulations and Analyses	144
5.2.1	Trap and Mobility Anisotropic Effects	147
5.2.2	Traps and Morphological Effects	156
5.3	Conclusions	160
Chapter 6	Conclusions	162
APPENDIX	168
BIBLIOGRAPHY	175

LIST OF TABLES

Table 2.1: Unipolar space-charge-limited current (SCLC) for hole injection of a planar device.	21
Table 4.1: Summary of parameters used in the device simulations	92
Table 5.1: Summary of parameters used in the device simulations to analyze c-AFM data	147
Table 5.2: The effective mobilities in the vertical direction found from fitting a representative examples of c-AFM current-voltage responses measured from an annealed P3HT sample for a range of anisotropic ratios.	155
Table 5.3: An analysis of point-to-point variation in transport properties across the film is presented for c-AFM data taken at 48 locations on the surface of an annealed sample. The average, standard deviation, minimum and maximum of the effective mobility in the vertical direction found from fitting the experimental data for a range of anisotropic ratio.	155
Table 5.4: The effective mobilities in the vertical direction found from fitting a representative example of c-AFM current-voltage responses measured from a non-annealed P3HT sample	155
Table A.1: Summary of parameters m and k_J estimated by fitting theoretical current-voltage characteristics of planar devices in the SCLC regime (see section 4.2.1 for details of device simulations) to the semi-empirical expression (4.3) for a range of trap parameters f_t and r_t . Note that R-square of regression is high ($R^2 > 0.9999$).	170
Table A.2: Summary of parameters m and k_J estimated by fitting theoretical current-voltage characteristics in the tip-plane geometry in the SCLC regime (see section 4.2.2 for details of device simulations) to the semi-empirical expression (4.4) for a range of trap parameters f_t and r_t and a range of mobility anisotropy μ_ρ/μ_z . Note that $R^2 > 0.9999$ for all regressions. Table continued on the next page.	171
Table A.2: (cont'd)	172

Table A.3: Summary of parameters m and k_J estimated by fitting theoretical current-voltage characteristics in the tip-plane geometry in the SCLC regime (see section 5.2.1 for details of device simulations) to the semi-empirical expression (4.4) for a range of trap parameters f_t and r_t and a range of mobility anisotropy μ_ρ/μ_z . Note that $R^2 > 0.9999$ for all regressions. Table continued on the next page.	173
Table A.3: (cont'd)	174

LIST OF FIGURES

Figure 3.1:	The schematic representation of hole-only devices The path of hole injection and hole transport are indicated	23
Figure 3.2:	Numerical method: (a) illustration of spatial discretization in a one-dimensional Cartesian coordinate system,(b) numerical derivative df/dx at the mid point x_i , (c) numerical integration $\int_{x_i}^{x_{i+1}} f(x)dx$ around the mid point $x_{i+1/2}$	29
Figure 3.3:	A flow diagram used to calculate the current-voltage characteristic of hole-only devices. The algorithm is based on the self-consistent scheme. We first establish the device setup with its morphology and parameter values, and then generate initial trial values for electric potential ψ^o and free hole carrier p_f^o . Subsequently, Poisson's equation is solved numerically to find the estimated values of potential ψ^n . Utilizing the new trial values of potential ψ , the estimated values of free hole carrier density p_f^n are evaluated from the continuity equation and the drift-diffusion equation, leading to the new trial values p_f . This entire process is repeated until convergence is reached, when the relative correction of free hole carrier density is less than the value of the tolerance δ	39
Figure 3.4:	Schematic illustration of a planar hole-only device made of a thin-film of organic semiconductor. The arrows illustrate the hole current path responding to hole injection at the top electrode. When the material is homogeneous, the vertical conductance is uniform. A 1-D DD-SCLC model is often sufficient to describe the hole carrier transport in such a device.	40
Figure 3.5:	Illustration of the spatial discretization in 1-dimensional Cartesian coordinate system. The device thickness L is discretized into the grid of $N + 2$ mesh points. Each mesh point is equally separated by $\Delta x = L/(N + 1)$	41
Figure 3.6:	Mesh size Verification – Convergence of the simulated hole current density with respect to the number of mesh points, when the applied voltage $V_a = 0.1, 1, 10V$. Hole current density is calculated from the 1-D DD-SCLC model of the trap-free ($f_t = 0$) hole-only devices of $80nm$ thickness ($N_v = 1.25 \times 10^{-21}cm^{-3}$, $\mu_p = 10^{-4}cm^2V^{-1}s^{-1}$). Discretizing the system into 41 mesh points with the constant $2nm$ mesh interval provides a well converged solution, and results in a maximum 7% error compared to the result from 801 mesh points ($0.1nm$ mesh interval).	47

Figure 3.7: N_v Verification – Convergence of the simulated hole current density with respect to the effective density of states in HOMO (N_v), when the applied voltage $V_a = 0.1, 1, 10V$. Hole current density is calculated from the 1-D DD-SCLC model of the trap-free ($f_t = 0$) hole-only devices of $80nm$ thickness ($\mu_p = 10^{-4}cm^2V^{-1}s^{-1}$). The N_v value of $1.25 \times 10^{21}cm^{-3}$ will be used in all following calculations.	48
Figure 3.8: Mott-Gurney convergence – The theoretical current-voltage characteristic calculated from the 1-D DD-SCLC model of the trap-free ($f_t = 0$) hole-only device obeys the power law $J \propto V^m$, demonstrating the transition from the diffusion affected regime of the fitting exponent $m = 1.52$ to the Mott-Gurney regime of the fitting exponent $m = 2$ with increasing applied voltage.	49
Figure 3.9: Schematic illustration of a three-dimensional hole-only device of tip-plane geometry. The numerical calculation is performed using a cylindrical coordinate system with the cylindrical symmetry, reducing the calculation domain to the two-dimensional system as shown. Hole transport is then described by a 2-D DD-SCLC model.	51
Figure 3.10: Schematic illustration of the spatial discretization in a cylindrical coordinate system. With cylindrical symmetry, the two-dimensional device is divided into the sub-area of size $\Delta\rho \times \Delta z$ with mesh points located at each corner. Each sub-area carries the single values of dielectric constant, hole mobility, and trap parameters. While it is homogeneous within sub-area, each sub-area can have different parameter values, producing the inhomogeneity in the system.	53
Figure 3.11: Schematic illustration of Gaussian Surface of (a) axis cell for the centered mesh at z-axis ($i = 0$), and (b) regular cell for the centered mesh elsewhere	53
Figure 3.12: BiCGSTAB VS Inversion – The theoretical current-voltage characteristic of the trap-free ($f_t = 0$) hole-only device solved iteratively by using BiCGSTAB module is compared with that solved directly by inversion of a tridiagonal matrix. In both calculations, we use a 1-D DD-SCLC model with $L = 80nm$, $N_v = 1.25 \times 10^{21}cm^{-3}$, $\epsilon_r = 3$, $\mu_p = 10^{-4}cm^2V^{-1}s^{-1}$. . .	64
Figure 3.13: The comparison of the theoretical current-voltage characteristics of the trap-free ($f_t = 0$) hole-only device calculated from 1-D and 2-D DD-SCLC models. In both models, the transport layer (orange) is homogeneous with the constant parameters: $\epsilon_r = 3$, $\mu_p = 10^{-4}cm^2V^{-1}s^{-1}$, and $N_v = 1.25 \times 10^{21}cm^{-3}$	65

Figure 3.14: Finite-size effect–Convergence of the simulated hole current with respect to device dimensional ratio of radius to thickness, when the applied voltage $V_a = 0.1, 1, 10V$. By using a 2-D DD-SCLC model, the trap-free ($f_t = 0$) hole-only device is modeled in tip-plane geometry ($R_{tip} \sim 1nm$), assuming homogeneous transport layer ($\epsilon_r = 3$, $N_v = 1.25 \times 10^{21}cm^{-3}$) with isotropic hole mobility ($\mu_{p,\rho} = \mu_{p,z} = 10^{-4}cm^2V^{-1}s^{-1}$). Using the dimensional ratio $R/L = 3.75$ provides a well-converged solutions while the finite-size effect is negligible. All the following calculations of tip-plane devices with an isotropic mobility will be performed with this dimensional ratio.	68
Figure 3.15: Finite-size effect–Convergence of the simulated hole current with respect to device dimensional ratio of radius to thickness, when the applied voltage $V_a = 0.1, 1, 10V$. By using a 2-D DD-SCLC model, the trap-free ($f_t = 0$) hole-only device is modeled in tip-plane geometry ($R_{tip} \sim 1nm$), assuming homogeneous transport layer ($\epsilon_r = 3$, $N_v = 1.25 \times 10^{21}cm^{-3}$) with anisotropic hole mobility ($\mu_{p,\rho}/\mu_{p,z} = 25$, $\mu_{p,z} = 10^{-4}cm^2V^{-1}s^{-1}$). Using the dimensional ratio $R/L = 6.25$ provides a well-converged solutions while the finite-size effect is negligible. All the following calculations of tip-plane devices with anisotropic mobility will be performed with this dimensional ratio.	69
Figure 3.16: Current as a function of vacuum layer thickness simulated using the given device structure, compared to the current calculated from a 2-D DD-SCLC model with insulating boundary conditions described by eq.(3.59), when $V_a = 0.5, 1, 10V$. At high vacuum layer thickness, the consistency of the numerical current between the two device geometries is observed with approximately a maximum of 1% difference. For the transport layer (orange), we use $L = 80nm$, $\epsilon_r = 3$, $\mu_{p,\rho} = \mu_{p,z} = 10^{-4}cm^2V^{-1}s^{-1}$, and $N_v = 1.25 \times 10^{21}cm^{-3}$	71
Figure 3.17: Illustration of a three-dimensional hole-only device of tip-plane geometry. The numerical calculation is performed using a three-dimensional coordinate system, allowing full customization of trap distribution and nanoscale morphology in the transport layer.	73
Figure 3.18: Illustration of the spatial discretization in a three-dimensional Cartesian coordinate system; (a) the device is divided into cube cells ($h \times h \times h$) with mesh points located at each corner; (b) each mesh point is surrounded by six nearest neighbors, and is adjacent to eight cells; (c) each cell contains constant values of dielectric constant, hole mobility, and trap parameters. The inhomogeneity is generated by varying the values of these parameters from one cell to another.	76

Figure 3.19: Gaussian surface S_G as a cube of size $h \times h \times h$ surrounding mesh point (i, j, k)	76
Figure 3.20: The comparison of the theoretical current-voltage characteristics of trap-free ($f_t = 0$) hole-only devices calculated from 1-D and 3-D DD-SCLC models. In both models, the transport layer (orange) is homogeneous with the constant parameters: $\epsilon_r = 3$, $\mu_p = 10^{-4}cm^2V^{-1}s^{-1}$, and $N_v = 1.25 \times 10^{21}cm^{-3}$	85
Figure 3.21: The schematic representation of tip contacts in a 3-D DD-SCLC model, constructed on the $2nm \times 2nm$ square grid as (a) an approximately circular geometry of $6nm$ radius and (b) a square geometry of $10nm$ side-length. In a 2-D DD-SCLC model, the tip contact is assigned as the circular area of $6nm$ radius (red dashed circle). Due to the difference in the discretization, the tip models in the 3-D model are slightly smaller than in the 2-D model, such that $A_{3-D(a)}/A_{2-D} = 0.85$ and $A_{3-D(b)}/A_{2-D} = 0.88$, respectively.	86
Figure 3.22: The comparison of the theoretical current-voltage characteristics of the trap-free ($f_t = 0$) hole-only devices calculated from 2-D and 3-D DD-SCLC models, in which the tip electrode is approximated by a circular contact of $6nm$ radius, as illustrated in figure 3.21(a). In both models, the transport layer (orange) is homogeneous with the constant parameters: $\epsilon_r = 3$, $\mu_p = 10^{-4}cm^2V^{-1}s^{-1}$, and $N_v = 1.25 \times 10^{21}cm^{-3}$	87
Figure 3.23: The comparison of the theoretical current-voltage characteristics of the trap-free ($f_t = 0$) hole-only devices calculated from 2-D and 3-D DD-SCLC models, in which the tip electrode is approximated by a circular contact of $6nm$ radius and a square contact of $10nm$ side length, respectively. (See figure 3.21(b)) In both models, the transport layer (orange) is homogeneous with the constant parameters: $\epsilon_r = 3$, $\mu_p = 10^{-4}cm^2V^{-1}s^{-1}$, and $N_v = 1.25 \times 10^{21}cm^{-3}$	88
Figure 4.1: Based on the simplified SCLC model of a trap-free hole-only device in the planar geometry, the analytical profiles of electric potential (solid black line) and hole carrier density (dashed red line) are demonstrated using non-dimensional scales.	93

Figure 4.2:	Plot of the analytical ratio of diffusion current density to drift current density of a planar flow, trap-free, hole-only device, $J_{p,di}/J_{p,dr}$, versus the dimensionless coordinate, x/L . While the drift current density is the immediate analytic solution of the simplified SCLC model as known as Mott-Gurney equation (2.13), the diffusion current density is obtained from the further derivation of the analytic solutions of the model. The extremely large value of diffusion current near the injecting electrode ($x = 0$) suggests the diffusion assists hole injection at the injecting contact.	95
Figure 4.3:	The theoretical profile of electric potential and hole carrier density as a function of the distance from the injecting electrode for planar geometry, generated using the 1-D DD-SCLC model described in section 3.3, using parameters given in table 4.1. The profiles exhibit three distinct transport regimes, plotted for three different applied voltages $V_a = 0.1, 1, 10V$, from top to bottom.	98
Figure 4.4:	The theoretical profile of electric potential and hole carrier density at the center of a circular tip ($\rho = 0$) as a function of the distance from the injecting electrode for tip-plane geometry, generated by the 2-D DD-SCLC model described in section 3.4, using parameters given in table 4.1. The profiles exhibits three distinct transport regimes, plotted for three different applied voltages $V_a = 0.1, 1, 10V$	100
Figure 4.5:	Position of virtual anode (dashed line) and virtual cathode (solid line) as a function of applied voltage for planar (black) and tip-plane (red) geometries, as seen in figure 4.3 and figure 4.4 respectively. The inset shows the convergence of the virtual tip position.	102
Figure 4.6:	The trap influenced current-voltage characteristic of a hole-only device in planar geometry obeys the power law $J \propto V^m$, exhibiting three regimes: Ohm's law $m = 1$ (red), trap-limited SCLC $m > 2$ (green), and trap-filled SCLC $m = 2$ (blue).	106
Figure 4.7:	The theoretical current-voltage characteristics of planar hole-only devices in the SCLC regime obey the power law ($I \propto V^m$) when (a) $f_t = 0.005$ with varying r_t yielding the exponent in the range $m = 2.23 - 4.71$, and (b) $r_t = 0.30$ with varying f_t yielding the exponent in the range $m = 1.89 - 3.72$	108
Figure 4.8:	Dependence of the exponent m on the two trap parameters; trap density characterized by parameter f_t and trap temperature characterized by parameter r_t for hole-only devices in planar geometry based on (a) the simplified SCLC model as described by eq.(2.27), (b) 1-D DD-SCLC model as seen in figure 4.7 and described by eq.(4.3).	109

Figure 4.9: The trap influenced current-voltage characteristic of a hole-only device in the tip-plane geometry obeys the power law $J \propto V^m$, exhibiting three regimes: Ohm's law $m = 1$ (red), trap limited SCLC $m > 2$ (green), and trap filled SCLC $m = 2$ (blue). Hole mobility is assumed to be isotropic.	111
Figure 4.10: The theoretical current-voltage characteristics of tip-plane devices in the SCLC regime obey the power law ($I \propto V^m$) when (a) $f_t = 0.005$ with varying r_t yielding the exponent in the range $m = 2.89-5.52$, and (b) $r_t = 0.30$ with varying f_t yielding the exponent in the range $m = 2.00 - 4.19$. Hole mobility is assumed to be isotropic.	113
Figure 4.11: The theoretical current-voltage characteristics of tip-plane devices in the SCLC regime for a range of mobility anisotropic ratios, μ_ρ/μ_z , with fixed trap parameters $f_t = 0.005$, $r_t = 0.30$.	114
Figure 4.12: Dependence of the exponent m on the exponentially distributed trap DOSs characterized by parameters f_t and r_t for hole-only devices in tip-plane geometry in the SCLC regime, resulting from extensive calculations for theoretical current-voltage characteristics as demonstrated in figure 4.10 and described by the semi-empirical expression (4.4).	115
Figure 4.13: Schematic illustration of crystallized P3HT nanofibers in three possible orientation schemes, including (a) 'face-on', (b) 'edge-on' and (c) 'end-on' orientations, corresponding to the parallel and perpendicular alignments of self-organized P3HT lamellae to the substrate, respectively.	117
Figure 4.14: Schematic illustration of device structures with the tip-plane electrode configuration to study the morphological effect of an isolated fiber with (a) 'face-on' and (b) 'edge-on' orientations.	120
Figure 4.15: Based on the hole-only devices with an isolated P3HT fiber shown in figure 4.14, the theoretical current-voltage characteristics when the tip is in contact with the fiber are plotted with varying the fiber mobility along the polythiophene backbone direction (μ_B). The theoretical current-voltage characteristic of an amorphous device is plotted as the reference to demonstrate the current enhancement in the presence of a single nanofiber. The inset shows the same data plotted in the double logarithmic scale.	122

- Figure 4.16: The vertical (a-e) and lateral (f-j) current of the semiconducting P3HT devices when the biasing voltage $V_a = 1V$ is applied to the conducting tip (red dot) and the bottom electrode is grounded. Three different types of morphologies have been used in the device simulation: (a)&(f) an amorphous (no-fiber) domain; (b-c)&(g-h) an isolated ‘face-on’ fiber embedded in an amorphous domain; and (d-e)&(i-j) an isolated ‘edge-on’ fiber embedded in an amorphous domain. In the last two morphologies, the comparison of current flows when tip is and is not in contact with the fiber is demonstrated. 127
- Figure 4.17: Simulating the c-AFM measurements, the dependence of the vertical current as a function of tip position on the profile trace crossing the ‘face-on’ fiber along; (a) the polythiophene backbone direction and (b) the alkyl side chain direction, at the applied voltages $V_a = 0.1, 1, 10V$. The profile trace is indicated by the dashed line shown in the inset. 129
- Figure 4.18: Simulating c-AFM measurements, (a) the dependence of the vertical current as a function of tip position on the profile trace crossing the ‘edge-on’ fiber along the polythiophene backbone direction and (b) the dependence of the vertical current as a function of tip-electrode separation, at the applied voltage $V_a = 0.1, 1, 10V$ 131
- Figure 4.19: The $600nm \times 600nm$ cross-sections of three model morphologies consisting of ‘edge-on’ fibers aligned in-plane with (a) random spacing (fiber fraction = 0.40), (b) random spacing and random orientation (fiber fraction = 0.40) and (c) random spacing and random length (fiber fraction = 0.32). 133
- Figure 4.20: Theoretical current-voltage characteristics of hole-only devices in the tip-plane geometry with three model morphologies (see figure 4.19) simulated when the conducting tip is in contact with the fiber and when it is not, as labeled by ‘ON’ and ‘OFF’, respectively. The inset shows the same data plotted in the double logarithmic scale. Despite the differences in model morphologies, the total currents simulated from the devices with an ‘edge-on’ fiber network increase by approximately 50% compared to those simulated from the devices with a single With the presence of an ‘edge-on’ fiber network, the total currents, despite the differences in model morphologies and tip locations, increases by approximately 50% compared to those simulated from the devices with a single ‘edge-on’ fiber. 134

- Figure 5.1: Reported in ref. [1], (a) an image of the topography of the annealed sample for fixed-spot current-voltage (I - V) measurement; (b) I - V spectra with the tip located on/off the fibers at locations labeled in (a). The inset of (b) shows log-log plots of the I - V spectra ($\text{Log}|I|$ vs. $\text{Log}|V|$) from the negative bias regime. (c) Typical I - V curves in the negative sample bias for annealed samples (blue) and non-annealed samples (green), and the fitting to power laws $I \propto V^m$ (red). For annealed samples, the I - V spectra have three distinct segments: Ohms law ($m = 1$), space-charge limited transport with shallow traps ($m = 2 - 2.25$), and a higher slope regime ($m > 5$) with increase of the applied bias. In non-annealed samples, trap effects are pronounced in the SCLC regime as the exponent is significantly higher ($m = 4 - 5$). 142
- Figure 5.2: The schematic representation of the device structure (a) and the corresponding energy alignment (b) of the hole-only device. This device behaves similarly to a semiconductor diode. When the device is positive biased, no charge carrier transport presents. Conversely, under the negative bias, holes are injected from Pt probe into the system, traveling through the layer of P3HT and PEDOT:PSS, and collected at the ITO contact; while electrons injected from ITO cannot transport into the system due to the layer of PEDOT:PSS. Therefore, this is the hole only injection system. 145
- Figure 5.3: Based on the setup of c-AFM measurements [1], the theoretical current-voltage characteristics in the SCLC regime are well-described by the semi-empirical expression (4.4) when (a) trap parameters is fixed ($f_t = 0.001$ $r_t = 0.30$) with varying mobility anisotropic ratios μ_ρ/μ_z ; (b) mobility is isotropic and $f_t = 0.005$ with the varying r_t yielding the exponent in range $m = 2.31 - 5.19$; and (c) mobility is isotropic and $r_t = 0.35$ with varying f_t yielding the exponent in range $m = 1.96 - 3.61$ 149
- Figure 5.4: Dependence of the exponent m on the parameters f_t and r_t for hole-only devices in the SCLC regime, resulting from extensive calculations of theoretical current-voltage characteristics demonstrated in figure 5.3 [1]. 150
- Figure 5.5: The representative current-voltage (I - V) response from the annealed sample (solid circle) is fitted to the theoretical I - V relation (solid red line) in the low trap regime with two pairs of trap parameters that result in the same slope: (a) $f_t = 0.0005$ and $r_t = 0.35$, (b) $f_t = 0.001$ and $r_t = 0.40$. Shown in the inset are the same plot in linear scale. (c) A histogram of the normalized vertical hole mobility extracted from 48 I - V datasets on the annealed P3HT film, with the comparison of an isotropic model and an anisotropic model with $\mu_r/\mu_z = 25$. The mobility is normalized to the maximum value of each case. 152

- Figure 5.6: The representative current-voltage response from the non-annealed sample (solid circle) is fitted to the theoretical current-voltage relation (solid red line) in the low trap regime with two pairs of trap parameters that result in the same slope: (a) $f_t = 0.0075$ and $r_t = 0.25$, (b) $f_t = 0.01$ and $r_t = 0.25$. Shown in the inset are the same plot in linear scale. 154
- Figure 5.7: The $600nm \times 600nm$ cross-sections of the representative morphology at the vertical position z in the device thickness direction demonstrating the crystallized P3HT fibers of $20nm$ width (green wires) aligned with random spacing in the amorphous region (brown area). The fiber fraction of cross-section surface area is 0.33. The bottom electrode is placed at $z = 0nm$, and the locations of tip contact are marked on the $z = 80nm$ cross-section for the on-fiber and off-fiber c-AFM simulations. 158
- Figure 5.8: Adapted from [1], the on-fiber and off-fiber current-voltage responses of the annealed P3HT sample are well described by the theoretical current-voltage characteristics simulated from the representative 3-D morphology of an ‘edge-on’ fiber network shown in the inset on the bottom-right corner. (see figure 5.7 for cross-section morphology) To described the anisotropic transport in fibers (green), the in-plane mobility is 100 times larger than the vertical mobility and the background mobility of amorphous region (brown). The background mobility is fitted to be $7.78 \times 10^{-5} cm^2 V^{-1} s^{-1}$ with trap parameters $f_t = 1.00 \times 10^{-3}$ and $r_t = 0.30$. In the inset on the top-left corner, the vertical current flow when the c-AFM tip is located on the fiber is visualized. 159

KEY TO SYMBOLS

k_b	Boltzmann's constant
q	The fundamental charge
T	Temperature
V_t	Thermal potential, defined as $V_t = k_b T / q \approx 0.026V$ at room temperature.
V, V_a	Externally applied voltage
ψ	Electric potential
\mathcal{E}	Electric field
ϵ_r	Dielectric constant
ϵ_o	The vacuum permittivity
p_o	Total intrinsic hole carrier density, consisting of free and trap hole densities, <i>i.e.</i> , $p_o = p_{o,f} + p_{o,t}$.
p	Total injected hole carrier density, consisting of free and trap hole densities, <i>i.e.</i> , $p = p_f + p_t$
Q_p	Total holes
μ_p	Hole mobility
μ_o	The effective hole mobility in the vertical direction
D_p	Hole diffusion coefficient
I, I_p	Total hole current, consisting of drift and diffusion currents, <i>i.e.</i> , $I_p = I_{p,dr} + I_{p,di}$
J, J_p	Total hole current density, consisting of drift and diffusion current densities, <i>i.e.</i> , $J_p = J_{p,dr} + J_{p,di}$
\mathcal{B}	The Bernoulli function, defined as $\mathcal{B}(x) = \frac{x}{e^x - 1}$.
N_v	The effective density of states in the HOMO
N_t	Total trap density
T_t, E_t	Trap temperature and trap energy ($E_t = k_b T_t$)
f_t, r_t	Normalized trap parameters, defined as $f_t = N_t / N_v$ and $r_t = T / T_t$, respectively.
\mathcal{S}	The spatial distribution of traps

S_G	Gaussian surface
L, L_z	Device thickness
L_x, L_y	Device side lengths in the x - and y - directions in Gaussian coordinate systems
L_{tip}	Square tip side length
R	Device radius in the cylindrical coordinate systems
R_{tip}	Circular tip radius
\mathcal{D}_{tip}	Generalized tip domain
x_c	Characteristic coordinate
k_J, k_I, m	The fitting parameters of the power relation $J = \mu_o k_J V^m$ and $I = \mu_o k_I V^m$.

Chapter 1

Introduction

1.1 Motivation

With the drastic growth of global energy consumption as well as worldwide environmental concern, renewable energy has drawn an extensive interest in the past decades. Solar energy is widely recognized as one of the most essential energy sources for the future sustainable economy. Photovoltaic energy conversion has been developing to harvest solar energy and to efficiently generate electricity. As well as well-known technologies, such as the conventional inorganic and the emerging perovskite photovoltaic devices, organic photovoltaic (OPV) devices are promising, owing to several attractive features [2, 3, 4, 5, 6, 7, 8]. The fabrication processes of OPV devices involve low-temperature and low-cost deposition techniques that easily translate to large-scale production. Since their manufacturing speed is very high and their thermal budget is very low, the OPV devices possess advantages over their inorganic counterparts in the aspect of ecological footprint and energy payback time, meaning that organic materials are more environment-friendly and they need shorter operation time to recover the energy spent in their fabrications, respectively. Furthermore, OPV devices are light weight, flexible and semi-transparent, offering versatile applications. Over the course of time, the power conversion efficiency of OPVs has vastly improved.

Since the basic structure of the OPVs was established as early as the mid-1950s consisted

of a single layer of organic semiconductor with electrodes attached to its top and bottom surfaces [9], we observed the improvement of the device performance with respect to the large variation of the organic materials and the electrodes [10, 11, 12, 13, 14, 15, 16]. After that, double layered OPV devices were introduced in 1986 [17], and the bulk heterojunction (BHJ) design came about in 1995 [18]. It was found that the new structures can boost the performance of OPV devices greatly. Many other works have been done in this direction to achieve ever better optimization in OPV structures and morphologies, yielding over 10% power conversion efficiency recently [19, 20]. However, the underlying mechanisms regarding how the device operates is not yet well understood due to the large variation in the device materials and complex interactions among them. A clear understanding of this matter will not only push forward the study of OPV materials, but will also shed light on the investigation of other related devices, such as organic light emitting diodes (OLEDs) [21, 22, 23] and organic field effect transistors (OFETs) [24, 25].

Charge carrier transport is crucial in organic semiconductors, and has been investigated broadly via various methods such as time-of-flight (TOF) methods, field-effect transistor (FET) configurations, pulse-radiolysis time-resolved microwave conductivity (PR-TRMC), as well as the measurement of current-voltage characteristics in the *space-charge limited current* (SCLC) regime [26]. Among them, the method involving the SCLC is particularly interesting because of its simplicity and flexibility. The experiment is based on the measurement of SCLC in a diode configuration, the so called planar (plane-parallel) geometry, in which an organic layer is fabricated on the substrate in contact with top and bottom electrodes [26, 27, 28]. With the appropriate analytical and/or numerical model, these current-voltage data in the SCLC regime can be analyzed to determine the effective carrier mobility, as well as some other physical parameters, such as energy barriers, trap density, and trap

energy states.

Theoretically, the *drift-diffusion* (DD) model describing bulk transport of charge carriers in the SCLC regime is governed by three basic equations, including Poisson’s equation, the continuity equation at steady state, and the drift-diffusion equations of the charge carriers. The early theoretical work is vastly simplified by ignoring the contribution of charge diffusion and only considering the drift driven transport, such that the theoretical model can be solved analytically. The analytical expressions describing the dependences of trap-free SCLC and trap-limited SCLC on applied voltage in a planar geometry are rather simple, and have been widely used to determine charge carrier mobilities in experiments [26,27,28]. The simplified SCLC theory for the planar-flow current will be reviewed in section 2.3.

Conductive atomic force microscope (c-AFM) has been used extensively to study organic semiconductor devices in the past decade [29,30,31,32,33,34]. One of the efforts is to use the local current-voltage data measured by c-AFM to determine the local charge carrier mobility at specific locations of the film. Many studies indicated the importance of c-AFM tip geometry, and the existing analytical solutions for the conventional planar geometry, that is the Mott-Gurney equation, can no longer be applied [29,35]. Reid *et al.* [32] introduced a semi-empirical formula that made a correction due to the tip geometry, which will be reviewed in section 2.4.

However, the topic of SCLC in an organic semiconductor is more complicated than that described by the semi-empirical formula of [32] and its predecessor, the Mott-Gurney equation. This is due to the fact that in the results of the simplified SCLC model, the effect of charge diffusion is excluded from the theory. In many situations ignoring the diffusion current can lead to the misinterpretation of the experiment results. With this consideration in mind, the full description of the DD-SCLC model is not only crucial to characterize SCLC

in experiments, but also to understand the effect of charge diffusion on the simplified SCLC model.

1.2 Overview

The central focus of this dissertation is to develop the computational methods of DD-SCLC model to describe charge carrier transport in hole injection systems. We will extend the simplified model to consider the mechanism of charge diffusion and the inhomogeneity of devices including the c-AFM tip geometry, nanoscale morphologies, and spatially-varying trap distributions. This can be seen as a building block to gain more insight into the SCLC transport and to better characterize the experiments. To do so, this dissertation is constructed as follows.

Chapter 2 explains the theory of charge carrier injection in an organic semiconductor, emphasizing the SCLC model for hole-only devices. To gain insight into the current stage of the SCLC model, this chapter will give an overview of the theoretical works on the simplified SCLC model that have been done in the past, including the simplified model of trap-free SCLC and trap-limited SCLC in a planar geometry, as well as the semi-empirical model of trap-free SCLC in a tip-plane geometry.

In **chapter 3**, we present our development in the DD-SCLC model for hole-only devices. The model will be described in detail, along with the numerical methods used to achieve numerical solutions of the models in one-, two- and three- dimensional systems. All one-, two- and three- dimensional models are verified to be consistent with each other, and validated against the simplified SCLC theory in the drift-dominated SCLC regime.

In **chapter 4**, we proceed to the simulation of hole-only devices in the SCLC regime

using the numerical tools we successfully developed. Theoretical study on various topics of SCLC will be presented, including the diffusion effect in planar and tip-plane geometries, the trap effect in planar and tip-plane geometries, as well as morphological effects, particularly in the tip-plane geometry. The fibrous morphology of semi-crystalline poly(3-hexylthiophene) (P3HT) thin films will be used as a model system to demonstrate the mechanism enabling c-AFM to visualize the surface morphology in experiments [1, 31, 36, 37, 38]. The model morphologies used in the studies are generated by Dr. Daniel Olds.

In **chapter 5**, two- and three- dimensional DD-SCLC models will be used to elucidate the c-AFM experiments carried out by Professor Zhang's group at Michigan State University [1]. The experiment aims to investigate the effect of thermal annealing on the morphology of P3HT thin films. The statistical variation in local electrical conductivity of P3HT films was characterized by measuring the c-AFM current-voltage responses across the film surface. These current-voltage data are analyzed using the two- and three- dimensional DD-SCLC models, in which the effect of current spreading beneath the c-AFM tip, the effect of traps, the mobility anisotropy and the nanoscale morphology are incorporated.

Chapter 6 presents the conclusions of this dissertation and an outlook on future research directions.

Chapter 2

Theory of Charge Carrier Injection - Background

2.1 Charge Injection in Organic Semiconductors

Organic semiconductors are typically wide band gap semiconductors, where the charge carrier concentration in thermal equilibrium at room temperature is very low, and so is its electrical conductivity. The shortage of charge carriers can be overcome by incorporating an extrinsic source of free charges, including doping, dissociation of photogenerated electron-hole pairs (excitons), and charge injection at the electrodes. The topic of charge injection has drawn a great deal of attention, due to its ability to probe the intrinsic properties of the material, such as charge carrier mobility, defects, and traps.

Charge injection experiments are often done in the dark environment to eliminate the exciton effect. Dark charge injection is widely used to investigate electronic properties of organic semiconductors [27, 29, 31, 35, 39, 40, 41, 42]. The experiments involve the measurement of current-voltage response in a diode device configuration (planar or plane-parallel geometry), in which an organic layer is fabricated on the substrate in contact with top and bottom electrodes. When voltage is applied, the amount of electric current flowing through the organic semiconductor device primarily depends on two basic processes: (i) the charge

injection at the electrode/organic-semiconductor interfaces, and (ii) the charge transport in the bulk organic semiconductor. Two mechanisms thus control the electric current in the two distinct regimes: *injection-limited current (ILC)*, and *space-charge-limited current (SCLC)*, respectively.

In the ILC regime, the dark injection current is controlled by the efficiency of charge injection at the electrodes. An injection barrier often occurs when a metal electrode comes into contact with an organic semiconductor, preventing charges from being injected into the organic material, hence suppressing the current. In order to resolve this limitation, one can select proper electrodes so that the injection barrier at the electrode/organic-semiconductor contact is negligible. The ideal injecting contact is essentially an unlimited charge reservoir. This contact, known as *ohmic contact*, can eliminate the effect of ILC.

On the other hand, in the SCLC regime, the dark injection current is governed by charge carrier transport. In general, organic semiconductors are highly disordered, especially in the amorphous state, and hence the charge carrier mobility is much smaller than that of conventional inorganic semiconductors. When charges are injected into the material, they do not spread out efficiently. Instead, they form a cloud of space charge around the contact. The presence of space charge distorts the local electric field strength, and particularly reduces the electric field at the injecting electrode. When the electric field strength generated by the induced space charges is in equilibrium with the electric field strength from the applied voltage, the device reaches steady state with constant electric current, *i.e.*, the so-called SCLC.

In addition to space charge, the current in the SCLC regime can also be affected by other bulk properties of the organic semiconductor, including spatially-varying charge mobility, nanoscale morphologies, as well as trap states. A complete model including all the relevant

bulk properties can provide more insights into the underlying charge transport mechanism in organic semiconductors. In the rest of this chapter, we will review the simplified theoretical model considering only the space charge effect. An extended theoretical model will be the focus of the later chapter.

2.2 Fundamental Equations to Describe SCLC in Hole Injection System

To eliminate the interaction of electrons and holes, charge injection experiments are mostly unipolar, where one carrier type is dominant. Whether it is the injection of electrons or holes depends on the energy level alignment of the devices, the energy level mismatch between the device material and the metal electrode in particular. The ground-state electronic structure of organic semiconductors is described by the sequence of molecular orbitals filled by electrons up to the *highest occupied molecular orbital* (HOMO), and from the *lowest unoccupied molecular orbital* (LUMO) onward are empty. In analogy to the traditional band structure of inorganic semiconductors, the HOMO and LUMO energies take the role of valance and conduction band edges, respectively. When an electron is injected to the system, it will occupy that empty orbital at the lowest energy level, *i.e.*, the so called LUMO. Similarly, the injection of a hole is equivalent to an electron being removed from the HOMO and extracted at the electrode. Since the topic of hole injection system is the central focus of this dissertation, the following derivations and notations will be emphasized on hole transport, and note that the reverse will be equally true for electron injection devices. A thorough discussion of an electron injection device has been provided by Lampert and Mark [43].

The behavior of hole SCLC at steady state is governed by Poisson’s equation, the conti-

nality equation in steady state, and the drift-diffusion equation:

$$(\epsilon/q)(\vec{\nabla} \cdot \vec{\mathcal{E}}) = p - p_o, \quad (2.1)$$

$$\vec{\nabla} \cdot \vec{J}_p = 0, \quad (2.2)$$

$$\vec{J}_p = \vec{J}_{p,dr} + \vec{J}_{p,di} = q\mu_p p_f \vec{\mathcal{E}} - qD_p \vec{\nabla} p_f, \quad (2.3)$$

where ϵ is the dielectric constant, q is the fundamental charge, μ_p is the effective hole mobility, and D_p is the hole diffusion coefficient.

Poisson's equation (2.1) describes the instantaneous electric field produced by space charges in the system as shown on the right hand side of the equation. $p_o = p_{fo} + p_{to}$ is the total hole density in thermal equilibrium, consisting of the free hole density p_{fo} and trapped hole density p_{to} . After voltage is applied, a number of holes are injected into the system, thus increasing the total hole density p . Similarly, $p(\vec{r}) = p_f(\vec{r}) + p_t(\vec{r})$, where p_f and p_t are the actual, spatially varying free and trapped hole density in the steady-state injection. As discussed in section 2.1, the pristine (undoped) organic semiconductor has a relatively low free carrier concentration at thermal equilibrium, and most of the charges that carry the current must be injected. Therefore, we can safely omit the thermal equilibrium hole density p_0 from Poisson's equation, such that $p - p_o \simeq p$.

In addition, the transport of charges can be described by the hole current density J_p . There are two types of hole current, drift current $J_{p,dr}$ and diffusion current $J_{p,di}$, driven by electric field $\vec{\mathcal{E}}$ and the gradient of free hole density, respectively. Both of them are considered in the drift-diffusion equation (2.3), while the total current density is conserved according to the continuity equation (2.2).

By simultaneously solving the set of three governing equations (2.1)-(2.3) together with appropriate boundary conditions, the theoretical current-voltage characteristics of hole-only devices can be determined, as well as the theoretical profiles of the electric field and hole carrier density which can not be measured directly from experiments. We will first introduce the closed form solution to the simplified equations, and dedicate the next chapter to extensive computational studies of the problem in its complete unsimplified form. As we shall see, the comparison between the two methods demonstrates the importance of the full computation.

2.3 The Simplified Theory of SCLC: Planar (Plane-Parallel) Geometry

The simplified SCLC theory of unipolar injection is based on two fundamental assumptions [43]: (i) the injecting contact is ohmic, and (ii) the diffusion current is negligible.

In the first assumption, the ohmic contact is defined as a low-resistance contact, behaving as an infinite source of charges available for injection. As we discussed in section 2.1, the electric current of the dark charge injection is controlled by either the injection barrier at the electrode, or space charges in bulk organic semiconductors. By applying the approximation (i), the simplified theory is independent of the contact properties at the electrode/organic-semiconductor interface, and only the bulk transport properties are considered.

Next, the assumption (ii) is directly related to the charge transport. When the electric field is sufficiently strong, the drift current dominates, and we can safely omit the contribution of charge diffusion. It is also important to note that the two assumptions do not hold near contacts where the diffusion current is significant. Therefore, while the theory provides

a good approximation to the charge transport in bulk, namely the current-voltage characteristics of organic semiconductor devices, one shall bear in mind that the result contains approximations that are invalid near the electrodes.

In this section, the current-voltage characteristics of the hole-only devices in planar geometries are investigated, where the fully three-dimensional *partial differential equations* (PDEs) can be reduced to one-dimensional *ordinary differential equations* (ODEs). We will consider an organic semiconductor thin film of thickness L , in which holes are injected into the device at the anode $x = 0$, and extracted from the device at the cathode $x = L$. In order to do so, the device is grounded at the anode $\psi(0) = 0$, and negative bias is applied at the cathode $\psi(L) = -V$. Based on the assumptions above, the set of governing equations can be written as

$$(\epsilon/q)(d\mathcal{E}/dx) = p_f + p_t, \quad (2.4)$$

$$dJ_p/dx = 0 \quad \text{or} \quad J_p = \text{constant}, \quad (2.5)$$

$$J_p = q\mu_p p_f \mathcal{E}, \quad (2.6)$$

where $\vec{\mathcal{E}} = \mathcal{E}\hat{x}$ and $\vec{J}_p = J_p\hat{x}$. Note an additional boundary condition arises from assumption (i). In order to have finite current yet infinite charge density at the injecting electrode, the electric field must vanish there, so that

$$\mathcal{E} = 0 \quad \text{at the injecting electrode.} \quad (2.7)$$

This is the mathematical representation of an ohmic contact for the simplified SCLC theory.

Next, the problem of SCLC in the planar device geometry will be solved using the simplest

model where the device is assumed to be free of traps. More realistic solution will be given later which takes into account device traps that assume exponentially distributed density of trap states.

2.3.1 Trap-Free SCLC

The simplest model of unipolar SCLC does not consider traps, such that $p_t = 0$. Substituting the free hole density p_f from Poisson's equation (2.4) into equation (2.6), we can derive the drift current as:

$$J_p = \epsilon\mu_p\mathcal{E}(d\mathcal{E}/dx) = (\epsilon\mu_p/2)(d\mathcal{E}^2/dx) \Rightarrow d\mathcal{E}^2/dx = 2J_p/\epsilon\mu_p. \quad (2.8)$$

The general solution has the form

$$\mathcal{E}^2(x) = ax + b. \quad (2.9)$$

Applying the ohmic boundary condition at the injecting electrode (in eq.(2.7)), we get

$$\mathcal{E}(x) = \sqrt{ax}^{1/2}. \quad (2.10)$$

To calculate the electric potential across the device, this equation may be integrated as follows.

$$\psi(x) = -\int \mathcal{E}(x)dx = -(2/3)\sqrt{a}x^{3/2} + c \quad (2.11)$$

It is important to note that this electric potential is based on the *flat band* condition, where there are no energy level shifts near the interface at which metal and organic semiconductor

come into contact. However, the validity of this flat band picture needs to be thoroughly examined, especially when the injecting electrode is ohmic. In analogy to an inorganic semiconductor picture, when forming an ohmic contact at *short-circuit* condition ($V = 0$), charge transfer from the ohmic electrode into the organic semiconductor occurs, resulting in the formation of a space-charge layer near the contact at equilibrium. The contact potential then influences the *bending* of the valance band edge, *i.e.*, the so called HOMO band edge in the case of organic semiconductors. The simplified theory clearly neglects the *band bending* condition. Nevertheless it remains consistent with the initial assumption to exclude contact behavior. Applying the boundary conditions $\psi(x = 0) = 0$ and $\psi(x = L) = -V$, the integral constants can be determined as

$$a = (9/8)(V^2/L^3) \quad \text{and} \quad c = 0. \quad (2.12)$$

Substituting the constant a into the solution (2.10) and the combined differential equation (2.8), we have the hole current

$$J_p = \frac{9}{8} \epsilon \mu_p \frac{V^2}{L^3}, \quad (2.13)$$

which is known as *Mott-Gurney equation*, or the *Child Law for unipolar SCLC* [43]. The trap-free SCLC can be observed as a slope 2 regime in a $\text{Log} J_p - \text{Log} V$ plot. This characteristic is clearly observed in various unipolar injection experiments, and can be used to evaluate the effective charge carrier mobility of organic semiconductors [27, 39, 40, 41, 42].

Often the anode and cathode are made of different materials with different work functions, leading to a *built-in* field across the device. Consider a hole-only device with asymmetric contacts, such that the anode is ohmic while the cathode is non-ohmic with barrier potential equivalent to built-in potential V_{bi} . In the high voltage regime $V > V_{bi}$, as suggested by

Lampert and Mark [43], equation (2.13) shall be modified to handle this case by replacing V with $V - V_{bi}$.

The equations for the electric field, the electric potential, as well as the hole density can be derived as follows,

$$\frac{\mathcal{E}(x)}{\mathcal{E}_\Omega} = \frac{3}{2} \left(\frac{x}{L} \right)^{1/2}, \quad \frac{\psi(x)}{-V} = \left(\frac{x}{L} \right)^{3/2}, \quad \frac{p_f(x)}{\bar{p}_f} = \frac{1}{2} \left(\frac{x}{L} \right)^{-1/2}, \quad (2.14)$$

where \mathcal{E}_Ω is the spatial average of the electric field which is in the form of the ohmic field,

$$\mathcal{E}_\Omega = (1/L) \int_0^L \mathcal{E}(x) dx = V/L, \quad (2.15)$$

and \bar{p}_f is the spatial average of the hole carrier density,

$$\bar{p}_f = (1/L) \int_0^L p_f(x) dx = (3/2)(\epsilon V/qL^2), \quad (2.16)$$

2.3.2 SCLC with The Exponential Distribution of Trap States

Trap states are commonly observed in pristine organic semiconductors with poor crystallinity, and charge transport is often hindered by the presence of such traps. Because of the structural disorder in organic semiconductors, traps do not have a single well-defined energy state. Rather a Gaussian distribution is employed to describe a single set of traps, whereas an exponential distribution is often used for multiple sets of traps [43]. Recently, Campbell *et al.* proposed an alternative trap model for electrons and holes as the tail states of the approximately Gaussian distributed LUMO and HOMO density of states respectively [44]. These tail states are pseudo-exponential: the further the tail is away from the center of the distri-

bution toward the energy gap, the deeper the trap it represents. An exponential distribution is then a reasonable approximation for the distribution of traps in organic semiconductors.

The field-independent exponentially distributed traps are characterized by the total trap density N_t and the trap energy E_t , which represents their energetic depth for thermally activated detrapping, $E_t = k_b T_t$ where k_b is Boltzmann's constant. The distribution of the trap states, *i.e.*, the density of hole trapping states per unit energy, is defined as

$$\mathcal{G}_t(E) = (N_t/k_b T_t) e^{(-E/k_b T_t)}. \quad (2.17)$$

The density of trapped holes is

$$p_t(x) = \int_{E_f(x)}^{\infty} \mathcal{G}_t(E) dE = N_t \exp(-E_f(x)/k_b T_t), \quad (2.18)$$

where $E_f(x)$ is the quasi Fermi level of holes at distance x from the anode. As long as the temperature is sufficiently low ($T \ll E_f(x)/k_b$), all the energy states below $E_f(x)$ are occupied, while those above $E_f(x)$ are empty. Assuming $E_f(x) \gg k_b T$, the free hole density is approximately

$$p_f(x) = N_v \exp(-E_f(x)/k_b T), \quad (2.19)$$

and the trapped hole density can be written in terms of the free hole density as

$$p_t(x) = N_t N_v^{-1/l} p_f(x)^{1/l}, \quad (2.20)$$

where N_v is the effective DOSs in the HOMO, and $l = T_t/T \gg 1$.

In the particular case when trapped holes are dominant ($p_t \gg p_f$), the local electric

field in bulk organic semiconductors are controlled by the density and the energy distribution of the trapping states. Then Poisson's equation (2.4) can be rewritten as

$$(\epsilon/q)(d\mathcal{E}/dx) = p_t(x). \quad (2.21)$$

Combining the modified Poisson's equation (2.21) with the drift current model in equation (2.6), we have

$$\begin{aligned} (\epsilon/q)(d\mathcal{E}/dx) = N_t N_v^{-1/l} (J_p / \mu_p q \mathcal{E})^{1/l} &\Rightarrow d\mathcal{E}/dx = K[\mathcal{E}(x)]^{-1/l} \\ &\Rightarrow d\mathcal{E}^{(l+1)/l} / dx = \frac{l+1}{l} K, \end{aligned} \quad (2.22)$$

where the constant $K = (N_t/\epsilon)q^{(l-1)/l}(J_p/N_v\mu_p)^{1/l}$. The general solution is in the form

$$\mathcal{E}^{(l+1)/l}(x) = ax + b. \quad (2.23)$$

Applying the ohmic boundary condition (in eq. (2.7)), we find the electric field

$$\mathcal{E}(x) = a^{l/(l+1)} x^{l/(l+1)}, \quad (2.24)$$

and the electric potential

$$\psi(x) = - \int \mathcal{E}(x) dx = -a^{l/(l+1)} \left(\frac{l+1}{2l+1} \right) x^{(2l+1)/(l+1)} + c. \quad (2.25)$$

Again, this electric potential is valid when the band bending effect near contacts is negligible.

Applying the boundary condition from the device setup: $\psi(x=0) = 0$ and $\psi(x=L) = -V$.

The integral constants can be determined as

$$a = \left(\frac{2l+1}{l+1} \right)^{(l+1)/l} \frac{V^{(l+1)/l}}{L^{(2l+1)/l}} \quad \text{and} \quad c = 0. \quad (2.26)$$

Substituting it into the solution in equation (2.24) and the combined differential equation (2.22), we have the hole current in the presence of a field-independent exponentially distributed traps,

$$J_{p,TL} = q^{1-l} \mu_p N_v \left(\frac{\epsilon}{N_t} \frac{l}{l+1} \right)^l \left(\frac{2l+1}{l+1} \right)^{l+1} \frac{V^{l+1}}{L^{2l+1}}. \quad (2.27)$$

Unlike the Mott-Gurney equation, the trap-limited SCLC gives a steeper slope of $(l+1)$ in the $\text{Log}J_p - \text{Log}V$ plot, and hence the characteristic trap temperature/energy can be determined by slope fitting [28,45]. Often this characteristic slope can be observed in organic semiconductors with low crystallinity, where traps dominate. The increasing of the applied voltage eventually allows most trap sites to be filled. The transition from trap-limited SCLC to trap-free SCLC occurs at voltage

$$V_{TFL} = \left[\frac{9}{8} N_v^{-1} \left(N_t \frac{l+1}{l} \right)^l \left(\frac{l+1}{2l+1} \right)^{(l+1)} \right]^{1/(l-1)} \frac{q}{\epsilon} L^2. \quad (2.28)$$

The corresponding equations for the electric field, the electric potential, and the hole density can be derived as follow,

$$\frac{\mathcal{E}(x)}{\mathcal{E}_\Omega} = \frac{2l+1}{l+1} \left(\frac{x}{L} \right)^{l/(l+1)}, \quad \frac{\psi(x)}{-V} = \left(\frac{x}{L} \right)^{(2l+1)/(l+1)}, \quad \frac{p_f(x)}{\bar{p}_f} = \frac{1}{l+1} \left(\frac{x}{L} \right)^{-l/(l+1)}, \quad (2.29)$$

where \mathcal{E}_Ω is an ohmic field defined in (2.15), and \bar{p}_f is the spatial average of the hole carrier

density,

$$\bar{p}_f = (1/L) \int_0^L p_f(x) dx = N_v(l+1) \left(\frac{\epsilon}{qN_t} \frac{l}{l+1} \frac{2l+1}{l+1} \right)^l \frac{V^l}{L^{2l}}, \quad (2.30)$$

The simplified theories of both trap-free SCLC and trap-limited SCLC in the presence of field-independent exponentially distributed traps are summarized in table 2.1.

2.4 The Simplified Model of SCLC: Tip-Plane (c-AFM)

Geometry

The *conductive atomic force microscope* (c-AFM) is a type of atomic force microscope equipped with a conductive cantilever tip. In addition to the ability to acquire topological properties, c-AFM is capable of obtaining the local electrical transport properties of the sample. During its operation, the conductive tip scans over the surface of the sample to construct an image of its morphology. In the mean time, a voltage is applied between its tip and the sample, and the induced current is measured to produce a high-resolution current map. Due to its unique ability of simultaneous investigation of nanoscale morphology and electronic properties, c-AFM has been used extensively to study organic semiconductors in the past decade [29, 30, 31, 32, 33, 34, 40, 41, 42, 46]. One of these efforts is to probe the local charge transport by measuring the local current-voltage characteristic of organic semiconductors in the SCLC regime, and quantitatively determining the local charge mobility [29, 31, 40, 41, 42, 46]. For studies of the local current-voltage response, the tip is positioned at a specific location on the surface. The working range of the applied voltage is typically between $\pm 10V$, and the current can be of the order of picoamperes when being used to study charge transport in organic semiconductors.

When getting beyond the conventional planar device geometry, the theory of SCLC meets a new challenge. In the early c-AFM work, the effective hole mobility in poly(3-hexylthiophene) (P3HT) was found to be $1.4 \times 10^{-2} \text{cm}^2 \text{V}^{-1} \text{s}^{-1}$ [31], which is much higher than what was previously observed in a planar diode configuration [27, 47, 48]. This discrepancy brought attention to the importance of the tip geometry, especially current spreading [29, 35], to which the existing analytical solutions for the conventional device geometry can no longer be applied. Reid *et al.* [32] introduced a semi-empirical formula that includes a tip geometry correction on the traditional Mott-Gurney law equation (2.13), which is written as

$$J_{p,c-AFM} = \alpha \epsilon \mu_p \frac{V^2}{L^3} \delta \left(\frac{L}{d} \right)^{1.6 \pm 0.1} \quad (2.31)$$

where α and δ are two empirical dimensionless parameters, d is the diameter of the tip/substrate contact area, and L is the film thickness.

The authors [32] observed that the electric current density measured by c-AFM was much higher than that in the conventional diode configuration. The scaling exponent was found to be 1.6 ± 0.1 , which reflects the current enhancement due to the altered tip/electrode geometry. The dimensionless prefactor α assumes a value of ~ 8.2 , as determined from the numerical calculation of the standard drift-diffusion model. Although the model includes charge diffusion, its effect is insignificant since the prefactor is achieved at quite high applied voltage ($V_a = 10\text{V}$). Another scaling parameter introduced in equation (2.31) is δ . This parameter scales the numerical solution to fit the experimental results of c-AFM measurements, and its empirical value depends on the ratio of the tip diameter and the sample thickness. For $0.01 \leq d/L \leq 2$, this scaling parameter δ was found to have a value

of 7.8 ± 1 . Later, the effective mobilities yielded by using the semi-empirical equation (2.31) on the c-AFM current-voltage data measured on the films of P3HT, poly[2-methoxy-5-(3',7'-dimethyloctyloxy)-1,4-phenylene vinylene] (MDMO-PPV), and poly-(9,9-dioctylfluorene-co-bis-N,N-(4-butylphenyl)-bis-N,N-phenyl-1,4-phenylenediamine (PFB) were shown to be consistent with the one reported from analyses of diode device measurements. With growing popularity of c-AFM technique in the research community, the formula (2.31), is utilized in many recent studies, evaluating values of charge carrier mobility in organic semiconductors [33, 34, 49].

Though the semi-empirical equation (2.31) successfully corrects the Mott-Gurney law by taking into account the tip geometry, the formula still follows the square law ($J_p \propto V^2$) which can only be observed in low trap devices. In the next chapter, we will extend the work by Reid *et al.* to cover various bulk properties, including trap states, spatially varying mobility, and morphological effects, under relatively low applied voltages such that diffusion cannot be neglected.

Table 2.1: Unipolar space-charge-limited current (SCLC) for hole injection of a planar device.

	No traps	Field-independent exponential distributed traps $\mathcal{G}_t(E) = (N_t/k_b T_t) \exp(-E/k_b T_t)$, $l = T_t/T$
Hole current density	$J_p = \frac{9}{8} \epsilon \mu_p \frac{V^2}{L^3}$	$J_p = q^{1-l} \mu_p N_v \left(\frac{\epsilon}{N_t} \frac{l}{l+1} \right)^l \left(\frac{2l+1}{l+1} \right)^{l+1} \frac{V^{l+1}}{L^{2l+1}}$
Electric field	$\mathcal{E}(x) = \frac{3}{2} \frac{V}{L} \left(\frac{x}{L} \right)^{1/2}$	$\mathcal{E}(x) = \frac{2l+1}{l+1} \frac{V}{L} \left(\frac{x}{L} \right)^{l/(l+1)}$
Electric potential	$\psi(x) = -V \left(\frac{x}{L} \right)^{3/2}$	$\psi(x) = -V \left(\frac{x}{L} \right)^{(2l+1)/(l+1)}$
Hole carrier density	$p_f(x) = \bar{p}_f \frac{1}{2} \left(\frac{L}{x} \right)^{1/2}$	$p_f(x) = \bar{p}_f \frac{1}{l+1} \left(\frac{x}{L} \right)^{-l/(l+1)}$
Spatial avg hole density	$\bar{p}_f = \frac{3}{2} \frac{\epsilon V}{q L^2}$	$\bar{p}_f = N_v (l+1) \left(\frac{\epsilon}{q N_t} \frac{l}{l+1} \frac{2l+1}{l+1} \right)^l \frac{V^l}{L^{2l}}$

Chapter 3

The Drift-Diffusion SCLC Transport Models - New Method

In this chapter, we begin by describing the drift-diffusion (DD) SCLC model for hole-only devices. Our theoretical model improves the simplified SCLC model, as previously described in chapter 2, in two aspects: (i) the model will incorporate both drift and diffusion transport mechanisms, and (ii) the model will enable the treatment of inhomogeneous systems including c-AFM tip geometry, nanoscale morphology, as well as spatially-varying trap distributions. As a result, this mathematical problem becomes very challenging, and impossible to solve analytically. We will explain the numerical techniques used to achieve numerical solutions of the DD-SCLC model. The numerical tools are written in Fortran 90 for one- two- and three- dimensional models. All models will be verified to be consistent with each other, and validated by reproducing the result of the simplified SCLC model in the drift-dominated regime.

3.1 Modeling the Hole Injection System

In figure 3.1, the typical operation of hole-only devices is schematically illustrated in a simple metal-insulator-metal (MIM) structure with ohmic contact at the electrodes. When

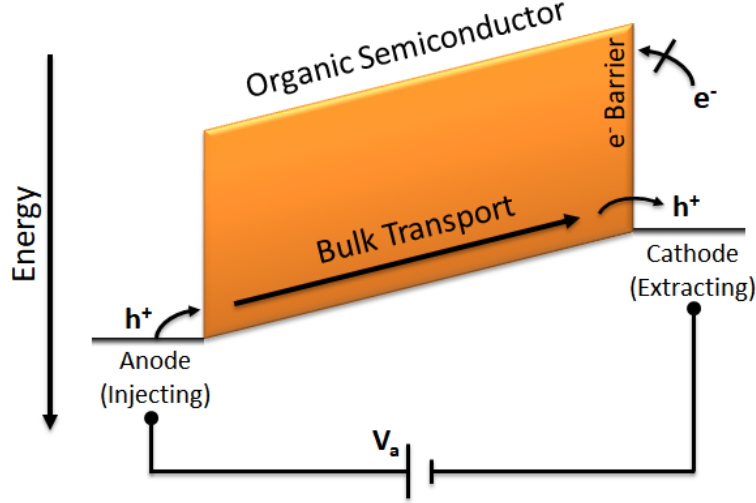


Figure 3.1: The schematic representation of hole-only devices. The path of hole injection and hole transport are indicated.

a positive bias V_a is applied, holes are injected from the anode, travel through the device, and are extracted at the cathode. This is the case of *unipolar* SCLC transport, where one carrier type is dominant. In this particular case, the charge carrier recombination can be ignored, and the hole transport is solely determined by the bulk properties of the organic semiconductors.

3.1.1 Governing Equations

As discussed previously in chapter 2, the bulk transport of holes in the SCLC regime can be described by three governing equations, including Poisson's equation (2.1), the continuity equation (2.2), and the drift-diffusion equation (2.3). The early theoretical work is vastly simplified by ignoring the contribution of charge diffusion and only considering the drift driven transport, such that the current-voltage characteristic of the hole-only device can be derived analytically. The theoretical model presented in this chapter, however, will include both types of charge transport, drift and diffusion. Furthermore, the material in-

homogeneity will also be studied by including the spatially-varying dielectric constant and the spatially-varying hole mobility. The numerical calculations will be developed for one- two- and three- dimensional models. The one-dimensional (1-D) model will use a Cartesian coordinate system, the two-dimensional (2-D) model will use a cylindrical coordinate system with cylindrical symmetry, and the three-dimensional (3-D) model will use a Cartesian coordinate system. Hence, all three governing equations are rewritten in more general form as follows

Poisson's equation :

Differential form,

$$\vec{\nabla} \cdot (\epsilon \vec{\mathcal{E}}) = q(p_f + p_t) \quad (3.1a)$$

Integral form,

$$\oint_{S=\partial V} \epsilon \vec{\mathcal{E}} \cdot d\vec{A} = q \left(\int_V p_f dV + \int_V p_t dV \right) = Q_p \quad (3.1b)$$

Continuity equation at steady state :

Differential form,

$$\vec{\nabla} \cdot \vec{J}_p = 0 \quad (3.2a)$$

Integral form,

$$\oint_{S=\partial V} \vec{J}_p \cdot d\vec{A} = 0 \quad (3.2b)$$

Drift-diffusion equation for holes :

$$\vec{J}_p = q\mu_p p_f \vec{\mathcal{E}} - qD_p \vec{\nabla} p_f \quad (3.3)$$

Poisson's equation (3.1) describes the relation between local electric field and local space

charge. Here, we present both differential and integral forms of the equation which will later be used in various discretization schemes. The equation is initially written in terms of the electric field. Later the numerical calculations will be performed to determine the electric potential $\psi(\vec{r})$, relating to the electric field through the relation $\vec{\mathcal{E}} = -\vec{\nabla}\psi$.

Due to the energetic disorder commonly found in organic semiconductors, it is important to include the trap states into the model. The total holes $Q_p(\vec{r})$ shall combine both trapped holes and free holes. Although these trapped holes do not contribute to the charge transport of the device, they do influence the local electric field; together with free holes. The trap DOSs is assumed to be exponentially distributed,

$$p_t(\vec{r}) = N_t(p_f/N_v)^{T/T_t}\mathcal{S}(\vec{r}) \quad (3.4)$$

where $\mathcal{S}(\vec{r})$ is the spatial distribution of traps. If trap density in the material is uniform, $\mathcal{S}(\vec{r})$ becomes unity. N_v is the effective DOSs in the HOMO, N_t is the total trap density and T_t is trap temperature.

While the trapped holes are localized, the free holes travel through the bulk material as is described by the well-known drift-diffusion model, as expressed in eq.(3.3). Unlike the simplified theory of SCLC, we conjecture that both drift and diffusion mechanisms are locally significant in the low voltage regime. While drift current is driven by the gradient of the electric potential (local electric field), diffusion current is driven by the gradient of the free hole density. The hole diffusion coefficient D_p reflects the local capability of charge diffusion, which obeys the *Einstein relation*

$$D_p(\vec{r}) = \mu_p(\vec{r})k_bT/q \quad (3.5)$$

where k_b is Boltzmann's constant and q is the fundamental charge. Note that, per eq.(3.5), the expression of the diffusion coefficient has been confirmed to be valid in the regime of low electric field [50,51]. It is also important to note that, due to the fact that the generation and recombination of charges do not occur away from the electrodes, the total hole current reaches the steady state and becomes conserved, as described by the Continuity equation(3.2).

3.1.2 Electrode Boundary Conditions

In order for the set of governing equations (3.1)-(3.3) to have a unique solution, boundary conditions are required. By increasing the number of degrees of freedom ranging from the one-, two and three- dimensional models, we can simulate more complex geometry and the suitable boundary conditions inevitably vary from model to model. Therefore, the complete set of boundary conditions for each model will later be explained in detail. However, the boundary condition at each electrode is similar to that of the simplified SCLC model defined in chapter 2.

Electrode boundary conditions :

$$\psi = V_a \quad \text{and} \quad p_f = N_v \quad \text{at the hole injecting electrode (anode)} \quad (3.6a)$$

$$\psi = 0 \quad \text{and} \quad p_f = N_v \quad \text{at the hole extracting electrode (cathode)} \quad (3.6b)$$

To inject holes into an organic semiconductor device, the positive bias V_a is applied at the injecting electrode. The injected holes then transport through the bulk material, and leave the device at the extracting electrode which is grounded. To be consistent with the derivation of the Mott-Gurney equation, both electrodes are assumed to be an *ohmic* contact, lining

up with the HOMO level of the organic semiconductor where the hole density is enormous ($N_v \sim 10^{21} \text{cm}^{-3}$). These boundary conditions at the electrode are similar to those used by Koster *et al.* [52].

3.1.3 Scaling Factors

In the previous section, we have introduced the governing equations and the boundary conditions at the electrodes. By performing numerical calculations (to be explained in section 3.2), we will obtain the numerical solutions for electric potential and free hole carrier density, which are different by many orders of magnitude. Therefore, these variables need to be scaled in order to increase the stability and improve the convergence of the calculations. The electric potential and the electric field are scaled by the thermal potential $V_t = k_b T/q$, while the hole carrier density is scaled by the effective DOSs in the HOMO (N_v). With these scaling factors, the three governing equations and the electrode boundary conditions can be rewritten as

Poisson's equation :

Differential form,

$$\vec{\nabla} \cdot (\epsilon \vec{\mathcal{E}}') = (qN_v/V_t)(p'_f + f_t \mathcal{S} \cdot p'^{r_t}_f) \quad (3.7a)$$

Integral form,

$$\oint_{S=\partial V} \epsilon \vec{\mathcal{E}}' \cdot d\vec{A} = \frac{qN_v}{V_t} \int_V (p'_f + f_t \mathcal{S} \cdot p'^{r_t}_f) dV \quad (3.7b)$$

where trap parameters $f_t = N_t/N_v$ and $r_t = T/T_t < 1$.

Continuity equation at steady state :

Differential form,

$$\vec{\nabla} \cdot \vec{J}_p = 0 \quad (3.8a)$$

Integral form,

$$\oint_{S=\partial V} \vec{J}_p \cdot d\vec{A} = 0 \quad (3.8b)$$

Drift-diffusion equation for holes :

$$\vec{J}_p = q\mu_p N_v V_t (p'_f \vec{\mathcal{E}}' - \vec{\nabla} p'_f) \quad (3.9)$$

Electrode boundary conditions :

$$\psi' = V_a/V_t \quad \text{and} \quad p'_f = 1 \quad \text{at the hole injecting electrode (anode)} \quad (3.10a)$$

$$\psi' = 0 \quad \text{and} \quad p'_f = 1 \quad \text{at the hole extracting electrode (cathode)} \quad (3.10b)$$

In the following sections, we will develop and apply numerical methods for one-, two- and three- dimensional DD-SCLC models, and prime(') will be dropped to simplify the notation.

3.2 Numerical Method

First, consider the one-dimensional case, the x coordinate is divided into N mesh points, separated by mesh size $\Delta x_i = x_{i+1} - x_i$ as shown in Figure 3.2(a). Then PDEs are discretized over the mesh points by using numerical derivative for their differential form, or numerical integration for their integral form. These discrete equations are presented as a set of linear equations with solutions as discrete functions. Unlike the analytical solutions, the values of the discrete functions are only defined at mesh points. Interpolation techniques are then applied to approximate the values of these functions away from mesh points. Here, finite difference methods (FDM) are used to approximate derivatives and integrations.

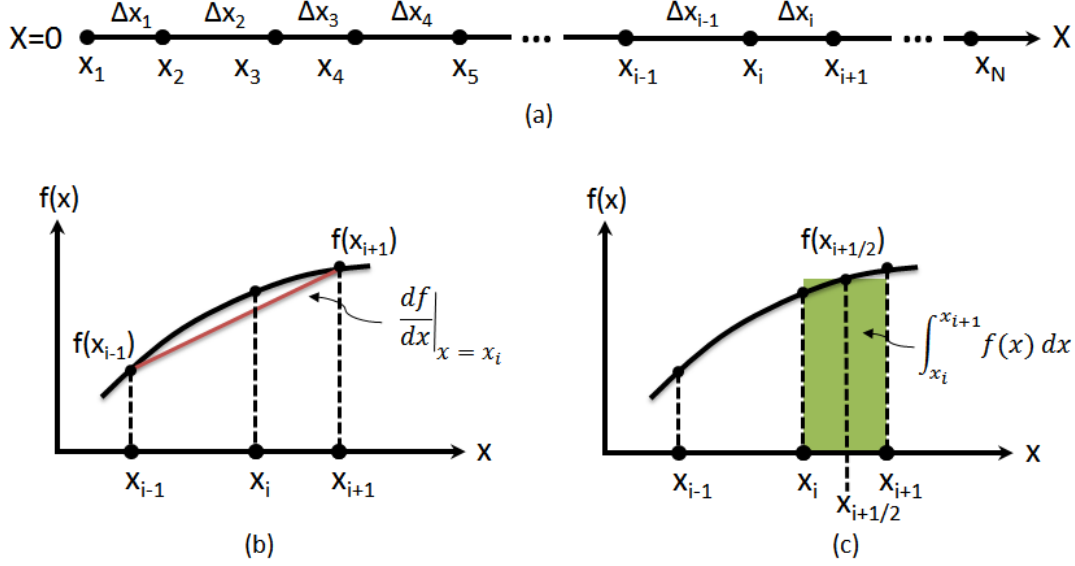


Figure 3.2: Numerical method: (a) illustration of spatial discretization in a one-dimensional Cartesian coordinate system, (b) numerical derivative df/dx at the mid point x_i , (c) numerical integration $\int_{x_i}^{x_{i+1}} f(x) dx$ around the mid point $x_{i+1/2}$

3.2.1 Numerical Derivatives

The numerical approximations to derivatives are based on Taylor's theorem. For the one-dimensional case, the truncated Taylor's series expansions of the function $f(x_{i\pm 1})$ around $x = x_i$ are

$$f(x_{i+1}) = f(x_i) + \Delta x_i \left. \frac{df}{dx} \right|_{x=x_i} + \frac{\Delta x_i^2}{2} \left. \frac{d^2 f}{dx^2} \right|_{x=x_i} + O(\Delta x_i^3) \quad (3.11a)$$

$$f(x_{i-1}) = f(x_i) - \Delta x_{i-1} \left. \frac{df}{dx} \right|_{x=x_i} + \frac{\Delta x_{i-1}^2}{2} \left. \frac{d^2 f}{dx^2} \right|_{x=x_i} + O(\Delta x_{i-1}^3) \quad (3.11b)$$

Subtracting these two equations gives

$$\left. \frac{df}{dx} \right|_{x=x_i} \approx \frac{f(x_{i+1}) - f(x_{i-1})}{\Delta x_i + \Delta x_{i-1}} \quad (3.12)$$

This expression is the finite difference approximation of the first-order derivative, as illustrated in figure 3.2(b). It is important to note that the numerical approximation converges to the analytical derivative as $(\Delta x_i + \Delta x_{i-1}) \rightarrow 0$. The equation (3.12) is rewritten in terms of the mid-point values as

$$\left. \frac{df}{dx} \right|_{x=x_i} \approx \frac{f(x_{i+1/2}) - f(x_{i-1/2})}{(\Delta x_i + \Delta x_{i-1})/2} \quad (3.13)$$

In a similar way, we can approximate the higher-order derivatives, for example, the second order derivative is given below

$$\begin{aligned} \left. \frac{d^2 f}{dx^2} \right|_{x=x_i} &\approx \frac{\left. \frac{df}{dx} \right|_{x=x_{i+1/2}} - \left. \frac{df}{dx} \right|_{x=x_{i-1/2}}}{(\Delta x_i + \Delta x_{i-1})/2} \\ &\approx \frac{\frac{f(x_{i+1}) - f(x_i)}{\Delta x_i} - \frac{f(x_i) - f(x_{i-1}))}{\Delta x_{i-1}}}{(\Delta x_i + \Delta x_{i-1})/2} \end{aligned} \quad (3.14)$$

When the domain is uniformly divided, such that $\Delta x_i = \Delta x_{i-1} = \Delta x$, the numerical approximation of first-order and second-order derivatives, as expressed in eq.(3.12) and eq.(3.14) respectively, are simplified to

$$\left. \frac{df}{dx} \right|_{x=x_i} \approx \frac{f(x_{i+1}) - f(x_{i-1}))}{2\Delta x} \quad (3.15)$$

$$\left. \frac{d^2 f}{dx^2} \right|_{x=x_i} \approx \frac{f(x_{i+1}) + f(x_{i-1})) - 2f(x_i)}{\Delta x^2} \quad (3.16)$$

To treat the inhomogeneity of organic materials, multi-dimensional calculations are re-

quired. In three-dimensional Cartesian coordinate systems, the computational domain is discretized using constant values of Δx , Δy and Δz in the x , y and z directions respectively. Each mesh point in the domain is indexed by (x_i, y_j, z_k) . In what follows, and unless otherwise stated, the mesh points are assumed to be equally separated on each dimension with constant distance $\Delta x = x_{i+1} - x_i$, $\Delta y = y_{j+1} - y_j$, and $\Delta z = z_{k+1} - z_k$. Consider the scalar function $F(x, y, z)$, which is discretized as $F(x_i, y_j, z_k)$.

$$\begin{aligned}
\vec{\nabla} F(x, y, z) \Big|_{(x_i, y_j, z_k)} &= \hat{x} \frac{\partial F}{\partial x} \Big|_{(x_i, y_j, z_k)} + \hat{y} \frac{\partial F}{\partial y} \Big|_{(x_i, y_j, z_k)} + \hat{z} \frac{\partial F}{\partial z} \Big|_{(x_i, y_j, z_k)} \\
&\approx \frac{F(x_{i+1}, y_j, z_k) - F(x_{i-1}, y_j, z_k)}{2\Delta x} \hat{x} \\
&\quad + \frac{F(x_i, y_{j+1}, z_k) - F(x_i, y_{j-1}, z_k)}{2\Delta y} \hat{y} \\
&\quad + \frac{F(x_i, y_j, z_{k+1}) - F(x_i, y_j, z_{k-1})}{2\Delta z} \hat{z}
\end{aligned} \tag{3.17}$$

$$\begin{aligned}
\nabla^2 F(x, y, z) \Big|_{(x_i, y_j, z_k)} &= \frac{\partial^2 F}{\partial x^2} \Big|_{(x_i, y_j, z_k)} + \frac{\partial^2 F}{\partial y^2} \Big|_{(x_i, y_j, z_k)} + \frac{\partial^2 F}{\partial z^2} \Big|_{(x_i, y_j, z_k)} \\
&\approx \frac{F(x_{i+1}, y_j, z_k) + F(x_{i-1}, y_j, z_k) - 2F(x_i, y_j, z_k)}{\Delta x^2} \\
&\quad + \frac{F(x_i, y_{j+1}, z_k) + F(x_i, y_{j-1}, z_k) - 2F(x_i, y_j, z_k)}{\Delta y^2} \\
&\quad + \frac{F(x_i, y_j, z_{k+1}) + F(x_i, y_j, z_{k-1}) - 2F(x_i, y_j, z_k)}{\Delta z^2}
\end{aligned} \tag{3.18}$$

For simplicity, we will write the discrete function with the index notation, such that $F(i, j, k) = F(x_i, y_j, z_k)$ and $(i, j, k) = (x_i, y_j, z_k)$. Equation (3.17) and equation (3.18) are rewritten as

$$\begin{aligned}
\vec{\nabla} F \Big|_{(i,j,k)} &= \hat{x} \frac{\partial F}{\partial x} \Big|_{(i,j,k)} + \hat{y} \frac{\partial F}{\partial y} \Big|_{(i,j,k)} + \hat{z} \frac{\partial F}{\partial z} \Big|_{(i,j,k)} \\
&\approx \frac{F(i+1, j, k) - F(i-1, j, k)}{2\Delta x} \hat{x} + \frac{F(i, j+1, k) - F(i, j-1, k)}{2\Delta y} \hat{y} \\
&\quad + \frac{F(i, j, k+1) - F(i, j, k-1)}{2\Delta z} \hat{z}
\end{aligned} \tag{3.19}$$

$$\begin{aligned}
\nabla^2 F(x, y, z) \Big|_{(i,j,k)} &= \frac{\partial^2 F}{\partial x^2} \Big|_{(i,j,k)} + \frac{\partial^2 F}{\partial y^2} \Big|_{(i,j,k)} + \frac{\partial^2 F}{\partial z^2} \Big|_{(i,j,k)} \\
&\approx \frac{F(i+1, j, k) + F(i-1, j, k) - 2F(i, j, k)}{\Delta x^2} \\
&\quad + \frac{F(i, j+1, k) + F(i, j-1, k) - 2F(i, j, k)}{\Delta y^2} \\
&\quad + \frac{F(i, j, k+1) + F(i, j, k-1) - 2F(i, j, k)}{\Delta z^2}
\end{aligned} \tag{3.20}$$

3.2.2 Numerical Integrations

We can also apply Taylor's theorem to obtain the numerical approximation to integration.

Consider a one-dimensional integral of function $f(x)$ from x_i to x_{i+1} . To evaluate the numerical integration, the function $f(x)$ is substituted by its truncated Taylor expansions

around the mid-point $x = x_{i+1/2}$.

$$\begin{aligned}
\int_{x_i}^{x_{i+1}} f(x') dx' &= \int_{x_i}^{x_{i+1}} \left[f(x_{i+1/2}) + (x' - x_{i+1/2}) \frac{df}{dx} \Big|_{x'=x_{i+1/2}} \right. \\
&\quad \left. + \frac{(x' - x_{i+1/2})^2}{2} \frac{d^2 f}{dx^2} \Big|_{x'=x_{i+1/2}} + O(\Delta x_i^3) \right] dx' \\
&\approx f(x_{i+1/2}) \Delta x_i
\end{aligned} \tag{3.21}$$

Equation (3.21) expresses the numerical integration, as illustrated in figure 3.2(c). Similarly, the numerical integral of the function $f(x)$ between the midpoint $x_{i-1/2}$ and $x_{i+1/2}$ is given

$$\begin{aligned}
\int_{x_{i-1/2}}^{x_{i+1/2}} f(x') dx' &= \int_{x_{i-1/2}}^{x_{i+1/2}} \left[f(x_i) + (x' - x_i) \frac{df}{dx} \Big|_{x'=x_i} \right. \\
&\quad \left. + \frac{(x' - x_i)^2}{2} \frac{d^2 f}{dx^2} \Big|_{x'=x_i} + O(\Delta x_i^3) \right] dx' \\
&\approx f(x_i) \frac{\Delta x_{i-1} + \Delta x_i}{2}
\end{aligned} \tag{3.22}$$

We prefer this form of integral since the approximation only involves the value of the function at the mesh point $f(x_i)$. Choosing the uniform mesh separation $\Delta x_{i-1} = \Delta x_i = \Delta x$, we have

$$\int_{x_{i-1/2}}^{x_{i+1/2}} f(x') dx' \approx f(x_i) \Delta x \tag{3.23}$$

Notice that it is written in a form analogous to equation (3.21).

Often we need to perform two- and three- dimensional integrals. Consider the uniform discretization in a three-dimensional domain, *i.e.*, suppose that mesh points are located at (x_i, y_j, z_k) , the distances between mesh points Δx , Δy , and Δz along each direction are

constant.

$$\int_{x_{i-1/2}}^{x_{i+1/2}} \int_{y_{j-1/2}}^{y_{j+1/2}} F(x', y') dx' dy' \approx F(x_i, y_j) \Delta x \Delta y \quad (3.24)$$

$$\int_{x_{i-1/2}}^{x_{i+1/2}} \int_{y_{j-1/2}}^{y_{j+1/2}} \int_{z_{k-1/2}}^{z_{k+1/2}} F(x', y', z') dx' dy' dz' \approx F(x_i, y_j, z_k) \Delta x \Delta y \Delta z \quad (3.25)$$

With the index notation, the numerical approximations to the one-, two- and three- dimensional integrals are rewritten as

$$\int_{x_{i-1/2}}^{x_{i+1/2}} f(x') dx' \approx f(i) \Delta x \quad (3.26)$$

$$\int_{x_{i-1/2}}^{x_{i+1/2}} \int_{y_{j-1/2}}^{y_{j+1/2}} F(x', y') dx' dy' \approx F(i, j) \Delta x \Delta y \quad (3.27)$$

$$\int_{x_{i-1/2}}^{x_{i+1/2}} \int_{y_{j-1/2}}^{y_{j+1/2}} \int_{z_{k-1/2}}^{z_{k+1/2}} F(x', y', z') dx' dy' dz' \approx F(i, j, k) \Delta x \Delta y \Delta z \quad (3.28)$$

3.2.3 Scharfetter-Gummel Discretization

Since the numerical solver of Poisson's equation (3.7) can be achieved by following the standard discretization discussed in section 3.2.1 and 3.2.2, one might expect to apply the same discretization scheme to the rest of the governing equations, which are the continuity equation (3.8) and the drift-diffusion equation (3.9). However, numerical instability limits the effectiveness of this approach.

Consider the one-dimensional case where the domain of interest is discretized into a set of mesh points indexed by $i = x_i$ with equal spacing Δx . The continuity equation (3.8) is discretized by using the numerical formula (3.13), thus we need to know the value of the hole current at the mid-point $J_p(i + 1/2)$ evaluated from the drift-diffusion equation (3.9).

Following the standard numerical discretization discussed in section 3.2.1 and 3.2.2, we have

$$J_{p,x}(i + 1/2) = q\mu_p N_v V_t \left[p_f(i + 1/2) \frac{\psi(i) - \psi(i + 1)}{\Delta x} - \frac{p_f(i + 1) - p_f(i)}{\Delta x} \right] \quad (3.29)$$

This is based on the assumption that the hole mobility is constant within the interval $[x_i, x_{i+1}]$. The value of hole density at the mid-point is approximated by the arithmetic average of the neighboring mesh points, such that $p_f(i + 1/2) \approx [p_f(i) + p_f(i + 1)] / 2$. Then, we have

$$J_{p,x}(i + 1/2) = q\mu_p N_v V_t \left[p_f(i) \left(\frac{\psi(i) - \psi(i + 1)}{2\Delta x} + \frac{1}{\Delta x} \right) + p_f(i + 1) \left(\frac{\psi(i) - \psi(i + 1)}{2\Delta x} - \frac{1}{\Delta x} \right) \right] \quad (3.30)$$

To guarantee a smooth flow of current between mesh points, the numerical calculation is restricted by *Reynolds number* [53]. Therefore, for the stability of the calculation, we need to have $\psi(i + 1) - \psi(i) \leq 2$ in the scaled units, which is equivalent to $\psi(i + 1) - \psi(i) \leq 2k_B T / q \approx 0.052V$ at room temperature ($300K$). Then the mesh interval needs to be sufficiently small for this condition to hold throughout the domain.

Scharfetter and Gummel have proposed the optimum solution to this problem [54]. With their approach, two fundamental assumptions need to be made:

- (i) hole current density $J_{p,x}$ is constant between mesh points,
- (ii) electric potential ψ is linear between mesh points, implying that electric field \mathcal{E}_x is also constant between mesh points.

We can rewrite the hole current density at the mid-point as

$$\begin{aligned} J_{p,x}(i+1/2) &= q\mu_p N_v V_t \left(\mathcal{E}_x(i+1/2) p_f(x) - \frac{dp_f}{dx} \right) \\ \Rightarrow \frac{dp_f}{dx} - \mathcal{E}_x(i+1/2) p_f(x) &= -\frac{J_{p,x}(i+1/2)}{q\mu_p N_v V_t} \end{aligned} \quad (3.31)$$

where $\mathcal{E}_x(i+1/2) = [\psi(i) - \psi(i+1)] / \Delta x = -\Delta\psi(i+1/2) / \Delta x$. Clearly, equation (3.31) is a first-order differential equation that has general solution in the form

$$p_f(x) = a + b e^{cx} \quad (3.32)$$

Substituting this expression into equation (3.31), we have

$$[\mathcal{E}_x(i+1/2) - c] e^{cx} = \frac{J_{p,x}}{q\mu_p N_v V_t} - \mathcal{E}_x(i+1/2) a \Rightarrow 0. \quad (3.33)$$

The left-hand side of the equation is x -explicitly-dependent, while the right-hand side is not.

This equation is only valid when the values on both sides are zero, so the constants a and c are then determined as

$$a = \frac{J_{p,x}}{q\mu_p N_v V_t \mathcal{E}_x(i+1/2)} \quad \text{and} \quad c = \mathcal{E}_x(i+1/2). \quad (3.34)$$

And, we now have

$$p_f(x) = \frac{J_{p,x}}{q\mu_p N_v V_t \mathcal{E}_x(i+1/2)} + b \cdot e^{\mathcal{E}_x(i+1/2)x} \quad (3.35)$$

Let's consider the value of hole density at mesh points i and $i + 1$.

$$p_f(i) = \frac{J_{p,x}}{q\mu_p N_v V_t \mathcal{E}_x(i + 1/2)} + b \cdot e^{\mathcal{E}_x(i+1/2) x_i} \quad (3.36a)$$

$$p_f(i + 1) = \frac{J_{p,x}}{q\mu_p N_v V_t \mathcal{E}_x(i + 1/2)} + b \cdot e^{\mathcal{E}_x(i+1/2) x_{i+1}} \quad (3.36b)$$

Combining the two equations, and eliminating the constant b , we obtain,

$$J_{p,x}(i + 1/2) = \frac{q\mu_p N_v V_t}{\Delta x} \left[\mathcal{B}(\Delta\psi(i + 1/2)) \cdot p_f(i) - \mathcal{B}(-\Delta\psi(i + 1/2)) \cdot p_f(i + 1) \right], \quad (3.37)$$

where the Bernoulli function

$$\mathcal{B}(x) = \frac{x}{e^x - 1} \quad \text{with} \quad \mathcal{B}(0) = 1. \quad (3.38)$$

Similarly, we can also derive

$$J_{p,x}(i - 1/2) = \frac{q\mu_p N_v V_t}{\Delta x} \left[\mathcal{B}(\Delta\psi(i - 1/2)) \cdot p_f(i - 1) - \mathcal{B}(-\Delta\psi(i - 1/2)) \cdot p_f(i) \right]. \quad (3.39)$$

The discretization given by eq.(3.37) and eq.(3.39) is known as *Scharfetter-Gummel discretization*; and is an important result in device physics [53, 55, 56, 57, 58, 59, 60].

3.2.4 Numerical Calculation Scheme

Adopting the strategy of Koster *et al.* [52], a self-consistent scheme will be used to solve the set of governing equations (3.7)-(3.9). A flow diagram of the numerical calculation scheme is shown in figure 3.3. To evaluate the current-voltage characteristic of the hole-only device,

we first define an initial guess of the solutions, which are the electric potential ψ^o and free hole carrier density p_f^o . We then employ the numerical technique to solve the discretized Poisson's equation, obtaining the new values of electric potential ψ^{new} . Next, the discretized continuity equation coupled with the discretized drift-diffusion equation is solved using the same numerical technique and the updated values of the electric potential, yielding the new values of free carrier density p_f^{new} . The correction of the resulting free hole carrier density determines if the simulation is converged, *i.e.*, when the relative correction of free hole carrier density is smaller than its tolerance δ . The tolerance used in this thesis is in the range of $10^{-12} - 10^{-15}$. The values of free hole carrier density are updated, and the process is repeated until convergence is reached.

To improve the rate of convergence, we will use a weighted average of the two most recent estimates to obtain the next estimate of the solution. In general, the updated numerical solution F is expressed as

$$F = w \cdot F^n + (1 - w) \cdot F^{n-1} \quad (3.40)$$

where n is the iteration number and w is the weighting parameter ($0 \leq w \leq 1$). When w is unity, we simply maintain the standard iterative scheme where the whole new value of solution is passed to the next iteration of the calculation.

To solve this mathematical problem numerically, we developed a computer program written in Fortran 90, which incorporates OpenMP to perform parallel computing. The calculations were carried out at the high performance computing center (HPCC) at Michigan State University.

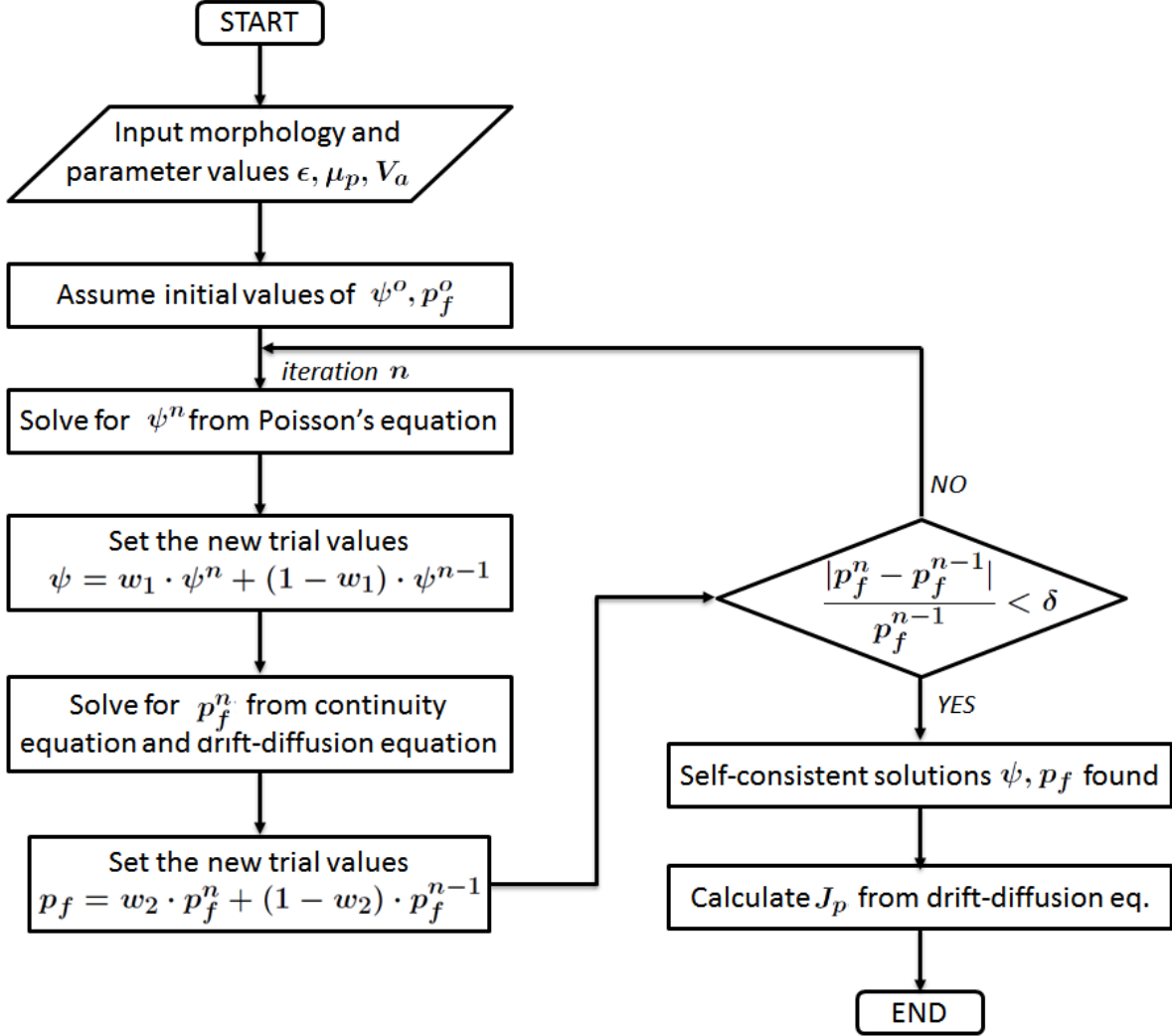


Figure 3.3: A flow diagram used to calculate the current-voltage characteristic of hole-only devices. The algorithm is based on the self-consistent scheme. We first establish the device setup with its morphology and parameter values, and then generate initial trial values for electric potential ψ^o and free hole carrier p_f^o . Subsequently, Poisson's equation is solved numerically to find the estimated values of potential ψ^n . Utilizing the new trial values of potential ψ , the estimated values of free hole carrier density p_f^n are evaluated from the continuity equation and the drift-diffusion equation, leading to the new trial values p_f . This entire process is repeated until convergence is reached, when the relative correction of free hole carrier density is less than the value of the tolerance δ .

3.3 1-D DD-SCLC Model: Homogeneous Planar Geometry

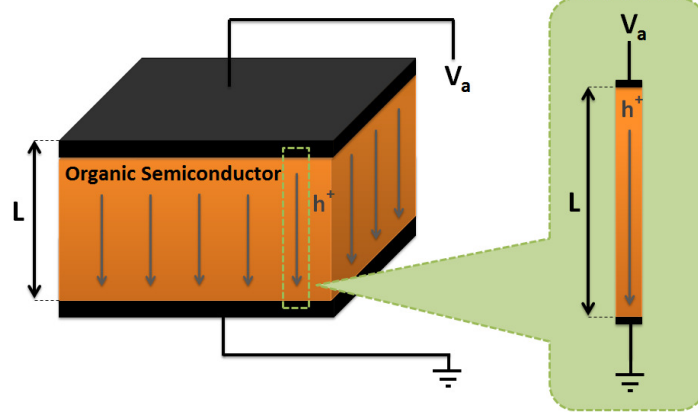


Figure 3.4: Schematic illustration of a planar hole-only device made of a thin-film of organic semiconductor. The arrows illustrate the hole current path responding to hole injection at the top electrode. When the material is homogeneous, the vertical conductance is uniform. A 1-D DD-SCLC model is often sufficient to describe the hole carrier transport in such a device.

To model charge transport in an organic semiconductor device, it is common to assume that the transport layer in a planar device is homogeneous, such that the dielectric constant is uniform, the hole carrier mobility is isotropic, and trap sites are evenly distributed throughout the device with constant trap density and trap energy. Therefore, only the vertical conductivity along the transport direction from one electrode to the other is considered, and the mathematical description is reduced to a one-dimensional problem. Shown in figure 3.4 is a schematic illustration of hole-only device that consists of an organic semiconductor thin film of thickness L fabricated in between conventional plane-parallel electrodes, and the scaled governing equations specifically for this 1-D DD-SCLC model, including Poisson's equation, the continuity equation at steady state, and the drift-diffusion equation for holes, are written as

$$d^2\psi/dx^2 = (qN_v/\epsilon V_t)(p_f + f_t \cdot p_f^{rt}) \quad (3.41)$$

$$dJ_p/dx = 0 \quad (3.42)$$

$$J_p = -q\mu_p N_v V_t (p_f \cdot d\psi/dx + dp_f/dx) \quad (3.43)$$

The boundary conditions at the electrodes ($x = 0, L$) are assigned as

$$\psi(x = 0) = V_a/V_t \quad \text{and} \quad p_f(x = 0) = 1 \quad (3.44a)$$

$$\psi(x = L) = 0 \quad \text{and} \quad p_f(x = L) = 1 \quad (3.44b)$$

It is worth emphasizing that this is the first step to extend the simplified SCLC theory to include the mechanism of charge diffusion.

3.3.1 Discretization

In figure 3.5, the one-dimensional device previously shown in figure 3.4 is uniformly discretized. The one-dimensional domain of length L is replaced by the total $N+2$ mesh points indexed by $i = 0, 1, 2, \dots, N+1$ with a constant mesh spacing $h = L/(N+1)$ or $x_i = i \cdot L/(N+1)$.

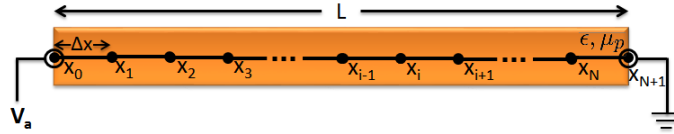


Figure 3.5: Illustration of the spatial discretization in 1-dimensional Cartesian coordinate system. The device thickness L is discretized into the grid of $N+2$ mesh points. Each mesh point is equally separated by $\Delta x = L/(N+1)$.

3.3.2 Potential Solver

On a uniform mesh, Poisson's equation (3.41) can be discretized by using the numerical approximation of the second-order derivative (3.20)

$$-\psi(i-1) + 2\psi(i) - \psi(i+1) = h^2(qN_v/\epsilon V_t) [p_f(i) + f_t \cdot p_f(i)^{rt}] \quad (3.45)$$

where $i = 1, 2, 3, \dots, N$. We have the boundary conditions for the electric potentials as

$$\psi(0) = V_a/V_t \quad \text{and} \quad \psi(N+1) = 0 \quad (3.46)$$

The mathematical treatment is straightforward. The N equations derived from equation (3.45) together with the two boundary conditions (3.46) result in a linear system of N equations with N unknown variables, which can be represented by

$$\begin{bmatrix} 2 & -1 & 0 & & \cdots & 0 \\ -1 & 2 & -1 & 0 & & \cdots & 0 \\ 0 & -1 & 2 & -1 & 0 & \cdots & 0 \\ \vdots & & & \ddots & \ddots & \ddots & \vdots \\ 0 & \cdots & & 0 & -1 & 2 & -1 & 0 \\ 0 & \cdots & & & 0 & -1 & 2 & -1 \\ 0 & \cdots & & & & 0 & -1 & 2 \end{bmatrix} \begin{bmatrix} \psi(1) \\ \psi(2) \\ \psi(3) \\ \vdots \\ \psi(N-2) \\ \psi(N-1) \\ \psi(N) \end{bmatrix} = \begin{bmatrix} b(1) + \psi(0) \\ b(2) \\ b(3) \\ \vdots \\ b(N-2) \\ b(N-1) \\ b(N) + \psi(N+1) \end{bmatrix} \quad (3.47)$$

where $b(i) = h^2(qN_v/\epsilon V_t) [p_f(i) + f_t \cdot p_f(i)^{rt}]$. Equation (3.47) can also be written in the vector form

$$\mathbb{A}\vec{\psi} = \vec{b} \quad (3.48)$$

where the vector $\vec{\psi}$ contains the unknown values of the electric potential, and the vector \vec{b} contains the constant $b(i)$ and the boundary conditions $\psi(0)$ and $\psi(N+1)$. The $N \times N$ matrix \mathbb{A} contains the coefficients of the variables, which are constant values and predominantly zero. Therefore, we employ *sparse matrix* storing techniques to reduce the memory usage while performing the numerical calculation.

There are two general schemes to solve the linear systems shown in equation (3.48) numerically: (i) direct elimination method and (ii) iterative method [61, 62]. In this case, the coefficient matrix \mathbb{A} is a *symmetric tridiagonal* matrix. The inversion of \mathbb{A} can thus be calculated by using the explicit inversion formula suggested by R. A. Usmani [63, 64]. The solution may be found by multiplying both sides of equation (3.48) by the matrix inverse \mathbb{A}^{-1} .

$$\vec{\psi} = \mathbb{A}^{-1} \vec{b} \quad (3.49)$$

3.3.3 Hole Density Solver

On a uniform mesh, the continuity equation (3.42) can be discretized by using the numerical approximation of the first-order derivative (3.19)

$$\left. \frac{dJ_p}{dx} \right|_i \approx \frac{J_p(i+1/2) - J_p(i-1/2)}{h} = 0. \quad (3.50)$$

Substituting the Scharfetter-Gummel discretization for the drift-diffusion equation (3.37)-(3.39), we have

$$\begin{aligned} -\mathcal{B}(\Delta\psi(i-1/2)) \cdot p_f(i-1) + \left[\mathcal{B}(-\Delta\psi(i-1/2)) + \mathcal{B}(\Delta\psi(i+1/2)) \right] \cdot p_f(i) \\ -\mathcal{B}(-\Delta\psi(i+1/2)) \cdot p_f(i+1) = 0 \end{aligned} \quad (3.51)$$

where $i = 1, 2, 3, \dots, N$ and \mathcal{B} is the Bernoulli function. The boundary conditions for the free hole density are

$$p_f(0) = 1 \quad \text{and} \quad p_f(N+1) = 1. \quad (3.52)$$

Following the similar mathematics, equation (3.51) may be written as

$$\mathbb{A} \vec{p}_f = \vec{b} \quad (3.53)$$

where the vector \vec{p}_f contains the unknown values of the free hole carrier density, the vector \vec{b} contains the boundary conditions ($\vec{b} = \{\mathcal{B}(\Delta\psi(i-1/2)) \cdot p_f(0), 0, \dots, 0, \mathcal{B}(-\Delta\psi(i+1/2)) \cdot p_f(N+1)\}$), and the matrix \mathbb{A} contains the coefficients of the variables, involving Bernoulli functions. Again, the coefficient matrix \mathbb{A} is a $N \times N$ matrix with predominantly zero elements, and is stored as a sparse matrix.

The matrix \mathbb{A} is again a *tridiagonal* matrix, which can be inversed using the formula proposed by Usmani [63, 64]. Subsequently, we find the solution as

$$\vec{p}_f = \mathbb{A}^{-1} \vec{b} \quad (3.54)$$

3.3.4 Verification

We have developed a program written in Fortran 90 to carry out the potential solver and hole density solver simultaneously by following the algorithm of the self-consistent scheme shown in figure 3.3. General guidelines for design and verification of the model include the following considerations :

- (i) minimize the error from numerical calculations

- (ii) verify the theoretical modeling

First of all, the result of numerical solutions are approximate. The two major sources of errors generally found in numerical calculations are *round-off error* and *discretization error*. Regardless of the methodology employed, the calculation usually has the round-off error, arising from the approximation of real numbers by the standard computer representation of the floating point numbers with finite digits. In our model, most parameters and variables are real. They are represented by double precision values in the program to minimize the corresponding round-off error. Discretization error, on the other hand, comes from the numerical approximations of the equations, which are usually proportional to a power of the mesh interval.

The effect of the discretization error can be seen from the numerical solution. To demonstrate this effect, we perform the numerical calculation to model hole carrier transport in the hole-only devices of $80nm$ thickness. Following the discretization scheme shown in figure 3.5, we gradually increase the mesh number, relating to the mesh interval through $h = L/(N+1)$, where N is the number of the unknown mesh points. The current density as simulated from our 1-D DD-SCLC model with varying numbers of mesh points is shown in figure 3.6. It approaches the saturated regime with respect to the increasing number of mesh points, whereas the discretization error is minimized. The calculation with a fine discretization requires a significant amount of computational time and resources, especially in the higher dimensional models. A good compromise between the computational effort and the computational accuracy was found to be at $2nm$ mesh interval, which results in approximately a maximum of 7% difference compared to the converged numerical solution of the system with $0.1nm$ mesh interval. Additionally, the $2nm$ mesh interval is an appropriate length scale for organic semiconductor devices consisting of nanoscale morphologies. Lowering the mesh interval

ever further only improves the numerical solutions quantitatively owing to the decrease of numerical errors, but does not vary the qualitative behaviors of devices. Therefore, the standard $2nm$ mesh interval will be used in the subsequent calculation.

Next, we would like to verify the capability of our model to capture the physical behavior of charge injection and transport in hole-only devices. According to the theory of SCLC, the injecting electrode does not limit the hole current in the devices and consequently is assumed to be ohmic, *i.e.*, an infinite source of charge carriers. Practically this implies a large charge carrier density at the injecting electrode. In our DD-SCLC model, the hole carrier density at the injecting contact is assumed to be equal to the effective DOSs in the HOMO (N_v), as expressed in eq.(3.6). The value of this parameter is determined from the regime where the current density is slowly varying over the value of N_v as shown in figure 3.7. A very large value of N_v , resulting in a steep gradient of charge density around the electrode, poses a challenge to the calculation convergence. Empirically, to have an ohmic injecting electrode yet ensure a well converged model, calculations will be performed with the value of N_v as $1.25 \times 10^{21} cm^{-3}$, which is more than sufficient for comparison with experiments.

To further verify the physical interpretation of our 1-D DD-SCLC model, we would like to demonstrate the effect of charge diffusion which is omitted from the simplified SCLC theory (discussed in chapter 2). Again, the calculation is performed in the absence of traps with a low hole mobility of $\mu_p = 10^{-4} cm^2 V^{-1} s^{-1}$. Figure 3.8 shows the simulated hole current density (J_p) as a function of applied voltage (V_a). By fitting to a power law $J \propto V^m$ (solid line), the current-voltage characteristic exhibit two distinct regimes. In the high voltage regime ($V_a > 10$) where drift current is dominant, the fit of the current-voltage relation yields the exponent $m = 2$, agreeing with the number predicted by the Mott-Gurney equation (2.13). On the other hand, in the low voltage regime ($V_a < 10$), the exponent is

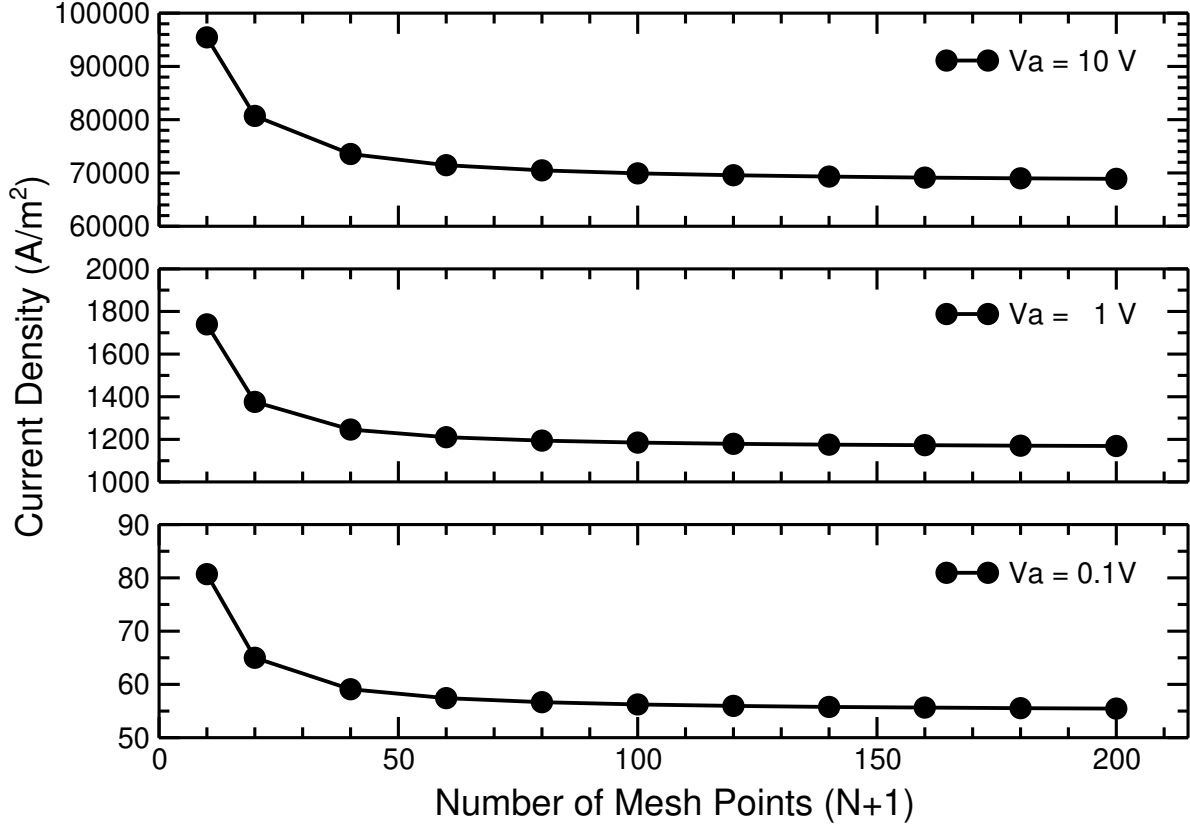


Figure 3.6: Mesh size Verification – Convergence of the simulated hole current density with respect to the number of mesh points, when the applied voltage $V_a = 0.1, 1, 10V$. Hole current density is calculated from the 1-D DD-SCLC model of the trap-free ($f_t = 0$) hole-only devices of $80nm$ thickness ($N_v = 1.25 \times 10^{-21} cm^{-3}$, $\mu_p = 10^{-4} cm^2 V^{-1} s^{-1}$). Discretizing the system into 41 mesh points with the constant $2nm$ mesh interval provides a well converged solution, and results in a maximum 7% error compared to the result from 801 mesh points ($0.1nm$ mesh interval).

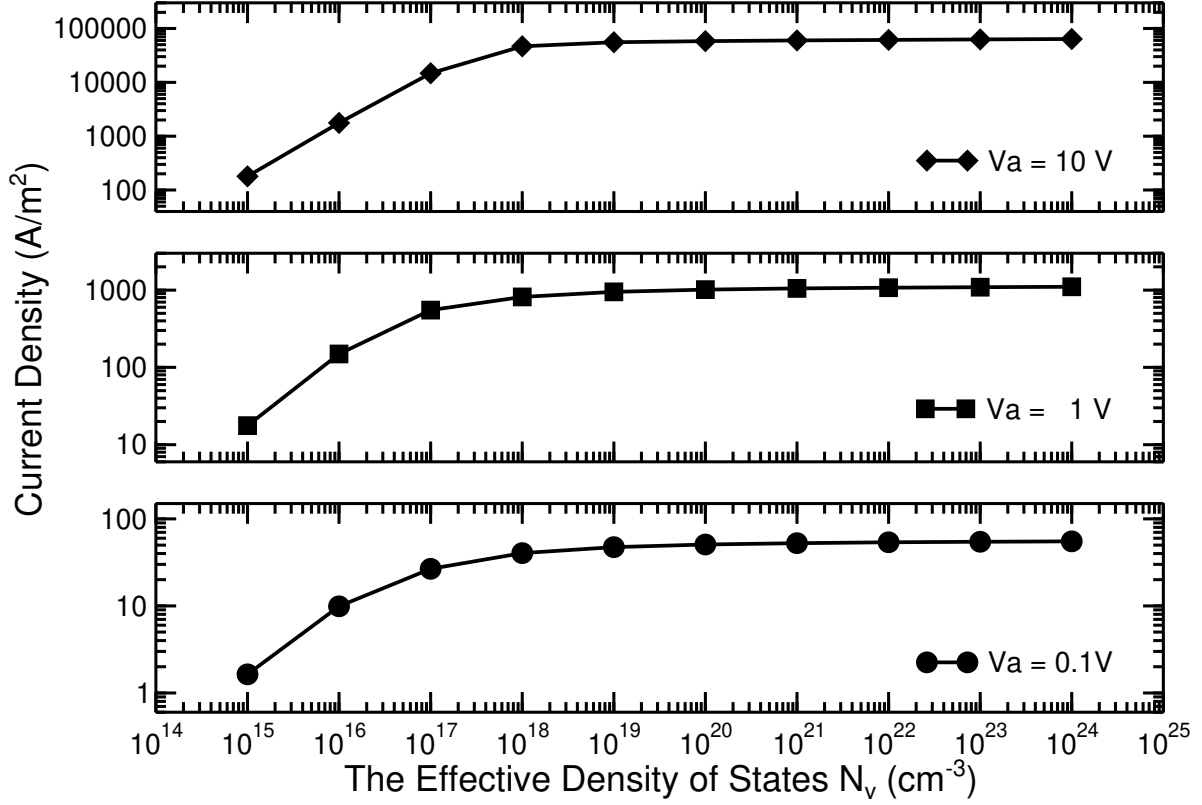


Figure 3.7: N_v Verification – Convergence of the simulated hole current density with respect to the effective density of states in HOMO (N_v), when the applied voltage $V_a = 0.1, 1, 10V$. Hole current density is calculated from the 1-D DD-SCLC model of the trap-free ($f_t = 0$) hole-only devices of $80nm$ thickness ($\mu_p = 10^{-4}cm^2V^{-1}s^{-1}$). The N_v value of $1.25 \times 10^{21}cm^{-3}$ will be used in all following calculations.

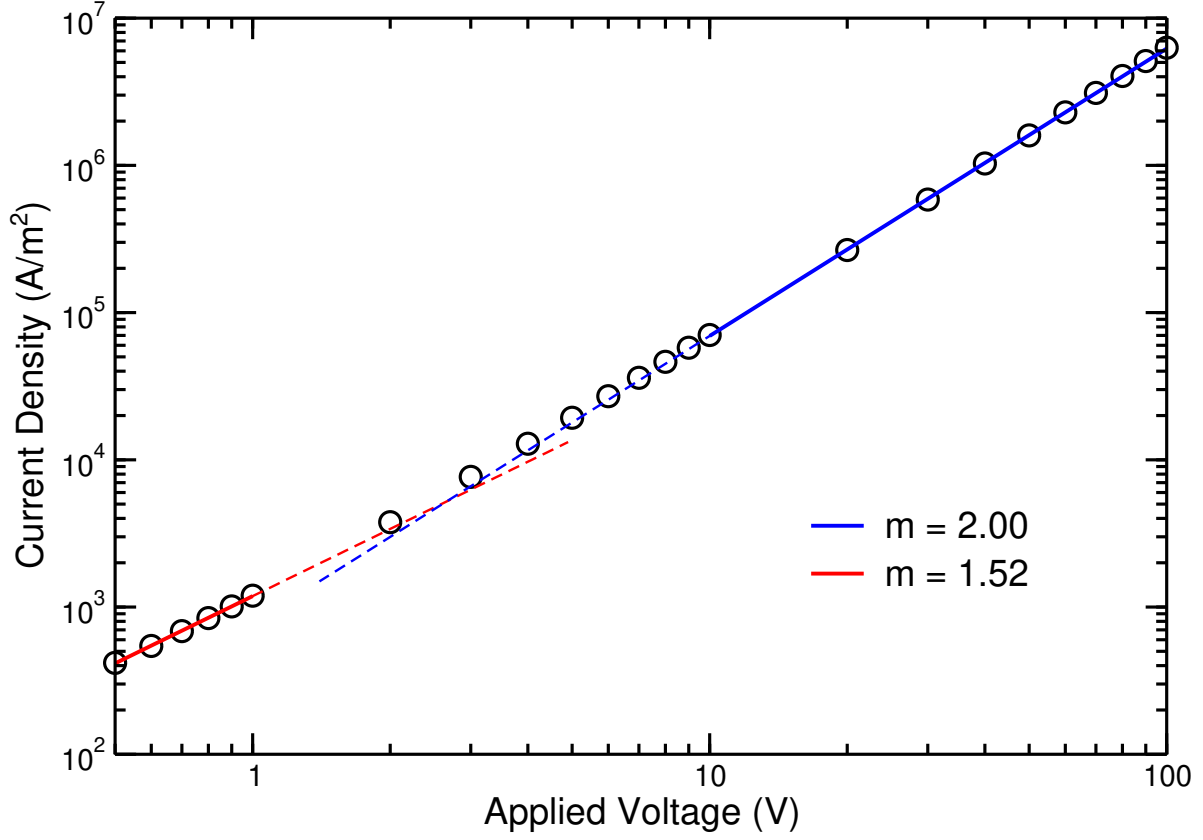


Figure 3.8: Mott-Gurney convergence – The theoretical current-voltage characteristic calculated from the 1-D DD-SCLC model of the trap-free ($f_t = 0$) hole-only device obeys the power law $J \propto V^m$, demonstrating the transition from the diffusion affected regime of the fitting exponent $m = 1.52$ to the Mott-Gurney regime of the fitting exponent $m = 2$ with increasing applied voltage.

lowered due to the contribution of charge diffusion. The current-voltage characteristic in the drift-dominated regime is clearly consistent to the prediction of the simplified SCLC model, validating the 1-D DD-SCLC model and its numerical approach.

3.4 2-D DD-SCLC Model: Semi-Homogeneous Tip-Plane Geometry

We have found that a 1-D DD-SCLC model is often sufficient to simulate the hole transport in the case of planar organic semiconductor devices. However, the organic semiconductor film is often composed of both amorphous and crystalline phases. Many studies have reported the exceptionally high conductance observed along the crystallized nanofibers of the organic semiconductor, resulting in an anisotropic mobility of hole carrier measured in thin films [34, 65, 66, 67]. Since the planar geometry demonstrates only the vertical conductance, one way to observe the effect of this lateral conductance is by replacing the top planar electrode by a tip electrode. The so-called tip-plane geometry is analogous to the electrode configuration of c-AFM measurements commonly used to study organic semiconductors.

In order to simulate the charge transport in a hole injection system of tip-plane geometry, the calculation is performed in the cylindrical coordinate system with cylindrical symmetry. The tip electrode is then approximated as the circular contact of radius (R_{tip}) as shown in figure 3.9. When this tip radius (R_{tip}) is equal to the device radius (R), the device setup reverts to the planar geometry. The governing equations for the 2-D DD-SCLC model in the

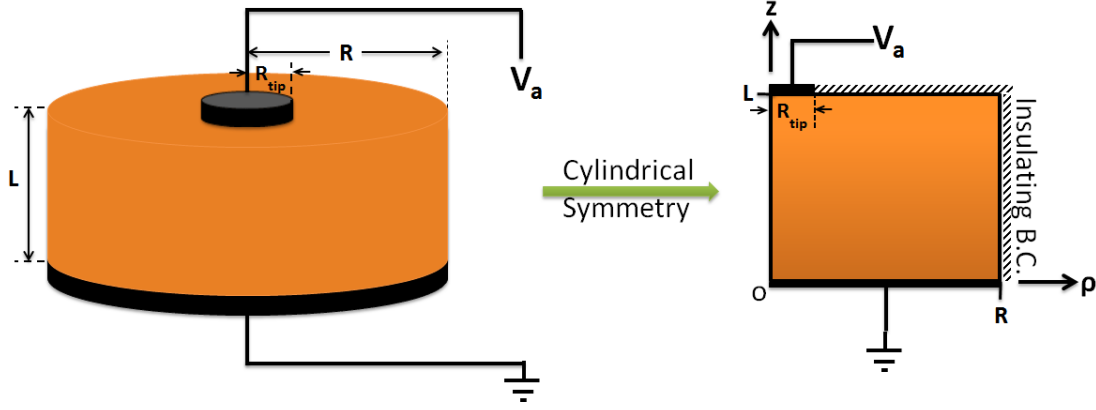


Figure 3.9: Schematic illustration of a three-dimensional hole-only device of tip-plane geometry. The numerical calculation is performed using a cylindrical coordinate system with the cylindrical symmetry, reducing the calculation domain to the two-dimensional system as shown. Hole transport is then described by a 2-D DD-SCLC model.

cylindrical coordinate system are written as

$$\oint_{S=\partial V} \epsilon(\rho, z) \vec{\mathcal{E}}(\rho, z) \cdot d\vec{A} = \frac{qN_v}{V_t} \int_V (p_f(\rho, z) + \mathcal{S}(\rho, z) f_t \cdot p_f(\rho, z)^{rt}) dV \quad (3.55)$$

$$\oint_{S=\partial V} \vec{J}_p(\rho, z) \cdot d\vec{A} = 0 \quad (3.56)$$

$$J_{p,\xi}(\rho, z) = q\mu_{p,\xi}(\rho, z)N_vV_t (p_f(\rho, z)\mathcal{E}_\xi(\rho, z) - \nabla_\xi p_f(\rho, z)) \quad (3.57)$$

where $\vec{J}_p(\rho, z) = \sum_\xi J_{p,\xi}(\rho, z)\hat{\xi}$ and $\xi = \{\rho, z\}$. Poisson's equation (3.55) and the continuity equation (3.56) are presented in the integral form using the divergence theorem. In contrast, the drift-diffusion equation (3.57) is shown in the differential form. The internal inhomogeneity of the material is included in the model by implementing the spatially varying parameters of dielectric constant $\epsilon(\rho, z) = \epsilon_r(\rho, z)\epsilon_o$, hole mobility $\vec{\mu}_p(\rho, z) = \sum_\xi \mu_{p,\xi}(\rho, z)\hat{\xi}$, and trap distribution $\mathcal{S}(\rho, z)$, where ϵ_o is the permittivity of vacuum.

In the two-dimensional configuration of figure 3.9, the organic semiconductor is grounded

on the bottom electrode, driven by the top electrode with the potential V_a , and bounded elsewhere by an insulator. Similar to the 1-D DD-SCLC model, the boundary conditions at the tip-planar electrodes are defined as

$$\psi(\rho, z) = V_a/V_t \quad \text{and} \quad p_f(\rho, z) = 1; \quad \text{where } \rho \in [0, R_{tip}], z = L \quad (3.58a)$$

$$\psi(\rho, z) = 0 \quad \text{and} \quad p_f(\rho, z) = 1; \quad \text{where } \rho \in [0, R], z = 0 \quad (3.58b)$$

Due to the absence of hole transport through the insulator, the normal component of hole current vanishes at the interface. The insulating boundary conditions for potential and hole density are assigned as

$$\hat{n} \cdot \nabla \psi = 0 \quad \text{and} \quad \hat{n} \cdot \nabla p_f = 0 \quad (3.59)$$

where \hat{n} is the unit vector normal to the insulating interface. Consider the physical meaning of the insulating boundary conditions. The zero-gradient of electric potential and current density can be interpreted as ‘no electric flux’ and ‘no current flux’ through the interface, which is the *Neumann boundary condition* for a fully insulating boundary.

3.4.1 Discretization

The cylindrical domain is discretized as shown in figure 3.10. The inhomogeneity of the material is also discretized. Each discrete volume, which later is reduced to a discrete area according to the cylindrical symmetry, has a uniform dielectric constant, hole mobility and trap parameters. Mesh points are then defined on the edge of each discrete volume/area. Therefore, the two-dimensional domain of radius R and thickness L shown in figure 3.9 is replaced by discrete areas of equal size $\Delta\rho \times \Delta z$ and a set of mesh points (ρ_i, z_k) ; $i =$

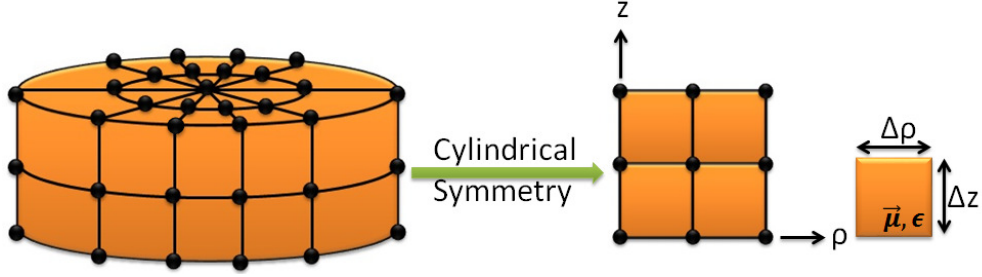


Figure 3.10: Schematic illustration of the spatial discretization in a cylindrical coordinate system. With cylindrical symmetry, the two-dimensional device is divided into the sub-area of size $\Delta\rho \times \Delta z$ with mesh points located at each corner. Each sub-area carries the single values of dielectric constant, hole mobility, and trap parameters. While it is homogeneous within sub-area, each sub-area can have different parameter values, producing the inhomogeneity in the system.

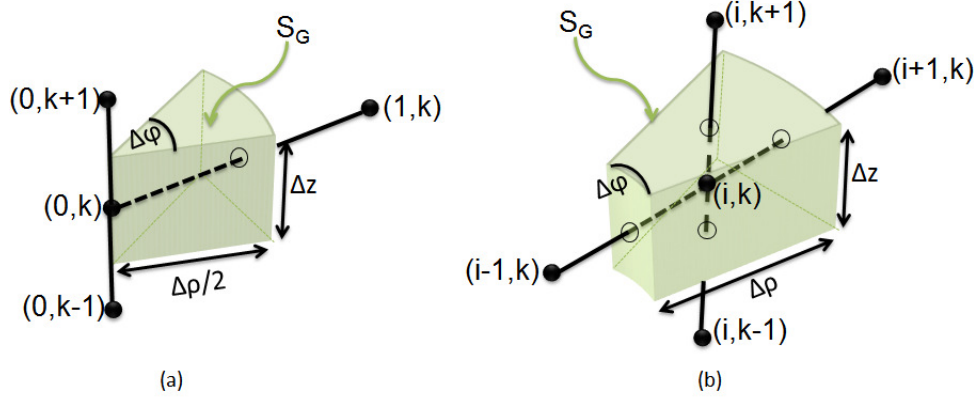


Figure 3.11: Schematic illustration of Gaussian Surface of (a) axis cell for the centered mesh at z -axis ($i = 0$), and (b) regular cell for the centered mesh elsewhere

$\{0, 1, 2, \dots, N\}$ and $k = \{0, 1, 2, \dots, M\}$, where $\rho_i = i \cdot R/N$ and $z_k = k \cdot L/M$.

In order to solve the governing equations in the integral form, we define a Gaussian surface (S_G) bounding a finite volume surrounding each mesh point over the small angle $\Delta\varphi$. Two kinds of Gaussian surfaces are chosen as demonstrated in figure 3.11. The axis cell is the wedge-like volume, corresponding to the mesh points at the z -axis ($i = 0$), which is adjacent to three nearest neighbors listed in figure 3.11(a). On the other hand, the regular cell is a parallelepipedic volume, corresponding to the mesh points elsewhere ($i = \{1, 2, 3, \dots, N\}$). A

regular mesh point is surrounded by four nearest neighbors listed in figure 3.11(b).

Because Poisson's equation and the continuity equation in the integral form evaluate the flux of electric field and hole current density at the Gaussian surface, three fundamental assumptions can be made:

- (i) hole current density J_p is constant between mesh points,
- (ii) electric potential ψ is linear between mesh points, implying that the electric field \mathcal{E} is also constant between mesh points.
- (iii) the normal component of the electric field at the Gaussian surface is continuous across the interface of two discrete volumes/areas.

The first two assumptions are meant to be consistent with those made in the Scharfetter-Gummel discretization (see section 3.2.3). The last assumption is based on the commonly-used interface boundary condition of the electric field, stating that the component of the electric field that is tangential to the interface of two materials is continuous. Recall that the internal inhomogeneity of the device is generated by varying the electrical and morphological properties of the discrete volumes/areas. In our numerical approach, the locations of mesh points are specifically chosen to be at the corners of the discrete units as shown in figure 3.10, and the correspondent Gaussian surfaces are always perpendicular to the interfaces between the units as seen in figure 3.19, reasoning the assumption (iii). With the combination of assumption (ii) and (iii), our numerical calculations selectively treat the internal heterogeneity of the devices locally through the average of the dielectric constant and mobility over the Gaussian surface, which will be clearly seen in the following sections.

3.4.2 Potential Solver

Poisson's equation (3.55) in the integral form is discretized by using the numerical approximation of the surface and volume integral, as expressed in eq.(3.27) and eq.(3.28) respectively, on the chosen Gaussian surface as shown in figure 3.11. The axis cell is specifically selected for the discretization of mesh points at the z-axis ($i = 0$), while the regular cell is for mesh points elsewhere ($i = \{1, 2, 3, \dots, N\}$). The discretized Poisson's equation based on two Gaussian surface are

At z-axis ($\rho = 0$ or $i = 0$)

$$\begin{aligned}
\left[\oint_{S_G} \epsilon \vec{\mathcal{E}} \cdot d\vec{A} \right]_{i,k} &= \iint_{S_G(i+\frac{1}{2})} \epsilon(\rho, z) \rho d\varphi dz \cdot \mathcal{E}_\rho(i + \frac{1}{2}, k) - \iint_{S_G(k-\frac{1}{2})} \epsilon(\rho, z) \rho d\rho d\varphi \cdot \mathcal{E}_z(i, k - \frac{1}{2}) \\
&\quad + \iint_{S_G(k+\frac{1}{2})} \epsilon(\rho, z) \rho d\rho d\varphi \cdot \mathcal{E}_z(i, k + \frac{1}{2}) \\
&= \left\{ 4\bar{\epsilon}_\rho(i + \frac{1}{2}, k) \cdot [\psi(i, k) - \psi(i + 1, k)] \right. \\
&\quad \left. - \left(\frac{\Delta\rho}{\Delta z} \right)^2 \bar{\epsilon}_z(i, k - \frac{1}{2}) \cdot [\psi(i, k - 1) - \psi(i, k)] \right. \\
&\quad \left. + \left(\frac{\Delta\rho}{\Delta z} \right)^2 \bar{\epsilon}_z(i, k + \frac{1}{2}) \cdot [\psi(i, k) - \psi(i, k + 1)] \right\} \cdot \frac{1}{8} \Delta\varphi \Delta z \\
&\equiv \frac{qN_v}{V_t\epsilon_o} \cdot \frac{1}{2} \left(\frac{\Delta\rho}{2} \right)^2 \Delta\varphi \Delta z \cdot \left[p_f(i, k) + f_t(i, k) \cdot p_f(i, k)^{r_t(i,k)} \right] \quad (3.60)
\end{aligned}$$

Otherwise ($\rho = i \cdot \Delta\rho$ where $i = \{1, 2, 3, \dots, N\}$)

$$\begin{aligned}
\left[\oint_{S_G} \epsilon \vec{\mathcal{E}} \cdot d\vec{A} \right]_{i,k} &= - \iint_{S_G(i-\frac{1}{2})} \epsilon(\rho, z) \rho d\varphi dz \cdot \mathcal{E}_\rho(i - \frac{1}{2}, k) + \iint_{S_G(i+\frac{1}{2})} \epsilon(\rho, z) \rho d\varphi dz \cdot \mathcal{E}_\rho(i + \frac{1}{2}, k) \\
&\quad - \iint_{S_G(k-\frac{1}{2})} \epsilon(\rho, z) \rho d\rho d\varphi \cdot \mathcal{E}_z(i, k - \frac{1}{2}) + \iint_{S_G(k+\frac{1}{2})} \epsilon(\rho, z) \rho d\rho d\varphi \cdot \mathcal{E}_z(i, k + \frac{1}{2}) \\
&= \left\{ - \left(1 - \frac{1}{2i}\right) \cdot \bar{\epsilon}_\rho(i - \frac{1}{2}, k) \cdot [\psi(i - 1, k) - \psi(i, k)] \right. \\
&\quad + \left(1 + \frac{1}{2i}\right) \cdot \bar{\epsilon}_\rho(i + \frac{1}{2}, k) \cdot [\psi(i, k) - \psi(i + 1, k)] \\
&\quad - \left(\frac{\Delta\rho}{\Delta z}\right)^2 \cdot \bar{\epsilon}_z(i, k - \frac{1}{2}) \cdot [\psi(i, k - 1) - \psi(i, k)] \\
&\quad \left. + \left(\frac{\Delta\rho}{\Delta z}\right)^2 \cdot \bar{\epsilon}_z(i, k + \frac{1}{2}) \cdot [\psi(i, k) - \psi(i, k + 1)] \right\} \cdot i \Delta z \Delta \phi \\
&\equiv \frac{qN_v}{V_t \epsilon_o} \cdot i (\Delta\rho)^2 \Delta z \Delta \phi \cdot \left[p_f(i, k) + f_t(i, k) \cdot p_f(i, k) r_t^{(i,k)} \right] \tag{3.61}
\end{aligned}$$

where the local averages of the dielectric constant over each section of Gaussian surface around the mesh point (i, k) are

$$\bar{\epsilon}_\rho(i \pm \frac{1}{2}, k) = \frac{1}{2} \cdot \left[\epsilon(i \pm \frac{1}{2}, k - \frac{1}{2}) + \epsilon(i \pm \frac{1}{2}, k + \frac{1}{2}) \right]; \text{ for } i = \{0, 1, 2, \dots, N\}, \tag{3.62a}$$

$$\bar{\epsilon}_z(i, k \pm \frac{1}{2}) = \begin{cases} \epsilon(i, k \pm \frac{1}{2}); & \text{for } i = 0, \\ \frac{\epsilon(i - \frac{1}{2}, k \pm \frac{1}{2}) \cdot \left(1 - \frac{1}{4i}\right) + \epsilon(i + \frac{1}{2}, k \pm \frac{1}{2}) \cdot \left(1 + \frac{1}{4i}\right)}{2}; & \end{cases} \tag{3.62b}$$

for $i = \{1, 2, 3, \dots, N\}$,

and $k = \{0, 1, 2, \dots, M\}$. When the domain is uniformly divided ($\Delta\rho = \Delta z = h$), the discretized equations (3.60)-(3.61) are simplified as

At z-axis ($\rho = 0$ or $i = 0$)

$$\begin{aligned}
& -4\bar{\epsilon}_\rho(i + \frac{1}{2}, k) \cdot \psi(i + 1, k) - \bar{\epsilon}_z(i, k - \frac{1}{2}) \cdot \psi(i, k - 1) - \bar{\epsilon}_z(i, k + \frac{1}{2}) \cdot \psi(i, k + 1) \\
& + \bar{\epsilon}(i, k) \cdot \psi(i, k) = \frac{qN_v h^2}{V_t \epsilon_o} \cdot \left[p_f(i, k) + f_t(i, k) \cdot p_f(i, k)^{r_t(i, k)} \right] \quad (3.63)
\end{aligned}$$

Otherwise ($\rho = i \cdot \Delta\rho$ where $i = \{1, 2, 3, \dots, N\}$)

$$\begin{aligned}
& -\left(1 - \frac{1}{2i}\right) \cdot \bar{\epsilon}_\rho(i - \frac{1}{2}, k) \cdot \psi(i - 1, k) - \left(1 + \frac{1}{2i}\right) \cdot \bar{\epsilon}_\rho(i + \frac{1}{2}, k) \cdot \psi(i + 1, k) \\
& - \bar{\epsilon}_z(i, k - \frac{1}{2}) \cdot \psi(i, k - 1) - \bar{\epsilon}_z(i, k + \frac{1}{2}) \cdot \psi(i, k + 1) + \bar{\epsilon}(i, k) \cdot \psi(i, k) \\
& = \frac{qN_v h^2 \cdot i}{V_t \epsilon_o} \cdot \left[p_f(i, k) + f_t(i, k) \cdot p_f(i, k)^{r_t(i, k)} \right] \quad (3.64)
\end{aligned}$$

where the local average of the dielectric constant at center point (i, k) are

$$\bar{\epsilon}(i, k) = \begin{cases} 4\bar{\epsilon}_\rho(i + \frac{1}{2}, k) + \bar{\epsilon}_z(i, k - \frac{1}{2}) + \bar{\epsilon}_z(i, k + \frac{1}{2}); & \text{for } i = 0, \\ \left(1 - \frac{1}{2i}\right) \bar{\epsilon}_\rho(i - \frac{1}{2}, k) + \left(1 + \frac{1}{2i}\right) \bar{\epsilon}_\rho(i + \frac{1}{2}, k) + \bar{\epsilon}_z(i, k - \frac{1}{2}) + \bar{\epsilon}_z(i, k + \frac{1}{2}); & \\ & \text{for } i = \{1, 2, 3, \dots, N\}, \end{cases} \quad (3.65)$$

and $k = \{0, 1, 2, \dots, M\}$.

We have established the discretized Poisson's equation (3.63) and (3.64), covering the whole domain ($\forall i \in [0, N], \forall k \in [0, M]$). In order to find the numerical solutions of the electric potential, all boundaries need to be assigned specific conditions, subject to the device geometry shown in figure 3.9. The boundary conditions for the electric potential at

the electrodes are

$$\psi(i, k) = \begin{cases} V_a/V_t & \text{for } i \in [0, R_{tip}/h], k = M \\ 0 & \text{for } i \in [0, R/h], k = 0 \end{cases} \quad (3.66)$$

Additionally, boundaries away from the electrodes are insulating, and the gradient of the potential normal to the interfaces are zero. In order to implement these condition, we define an additional set of mesh points along these interfaces, and we then apply the insulating boundary condition by setting,

$$\psi(i, k) = \begin{cases} \psi(i, k + 1) & \text{for } i \notin [0, R_{tip}/h], k = M \quad (\text{top boundary}) \\ \psi(i + 1, k) & \text{for } i = N, k = \{0, 1, 2, \dots, M\} \quad (\text{side boundary}) \end{cases} \quad (3.67)$$

These four boundary conditions (3.66)-(3.67) together with the discretized Poisson's equation (3.63) - (3.64) result in a system of linear equation, which can be represented in the matrix form (3.48); where vector $\vec{\mathbf{b}}$ contains the values of hole carrier density and boundary conditions, and Matrix \mathbb{A} reflects the morphological effect of the spatially-dependent dielectric constant. Unlike the 1-D DD-SCLC model, the matrix \mathbb{A} derived from tip-plane geometry is not a tridiagonal matrix, and the inversion formula suggested by Usmani can no longer be used. In our study, we used the *biconjugate gradient stabilized method (BiCGSTAB)* [68] to find solutions to this non-symmetric linear system iteratively.

3.4.3 Hole Density Solver

By pursuing the Schafetter-Gummel approach [54], hole current densities at the mesh mid-points in cylindrical coordinates are expressed as

$$\begin{aligned}
J_{p,\rho}(i \pm \tfrac{1}{2}, k) &= \mu_{p,\rho}(i \pm \tfrac{1}{2}, k) \cdot \frac{qV_t N_v}{\Delta \rho} \left\{ \mathcal{B}[\psi(i \pm 1, k) - \psi(i, k)] \cdot p_f(i, k) \right. \\
&\quad \left. \mp \mathcal{B}[\psi(i, k) - \psi(i \pm 1, k)] \cdot p_f(i \pm 1, k) \right\} \\
&\equiv \mu_{p,\rho}(i \pm \tfrac{1}{2}, k) \cdot \mathcal{J}_{p,\rho}(i \pm \tfrac{1}{2}, k) \tag{3.68a}
\end{aligned}$$

$$\begin{aligned}
J_{p,z}(i, k \pm \tfrac{1}{2}) &= \frac{q\mu_{p,z}(i, k \pm \tfrac{1}{2})V_t N_v}{\Delta z} \left\{ \mathcal{B}[\psi(i, k \pm 1) - \psi(i, k)] \cdot p_f(i, k) \right. \\
&\quad \left. \mp \mathcal{B}[\psi(i, k) - \psi(i, k \pm 1)] \cdot p_f(i \pm 1, k) \right\} \\
&\equiv \mu_{p,z}(i, k \pm \tfrac{1}{2}) \cdot \mathcal{J}_{p,z}(i, k \pm \tfrac{1}{2}) \tag{3.68b}
\end{aligned}$$

where \mathcal{B} is the Bernoulli function. The angular component of hole current density ($J_{p,\varphi}$) is zero, according to the cylindrical symmetry of the system.

Similar to the numerical method used for Poisson's equation, the flux of hole current density is calculated on the chosen Gaussian surfaces. We then obtain

At z-axis ($\rho = 0$ or $i = 0$)

$$\begin{aligned}
\left[\oint_{S_G} \vec{J}_p \cdot d\vec{A} \right]_{i,k} &= \iint_{S_G(i+\frac{1}{2})} \mu_{p,\rho} \rho d\varphi dz \cdot \mathcal{J}_{p,\rho}(i+\frac{1}{2}, k) - \iint_{S_G(k-\frac{1}{2})} \mu_{p,z} \rho d\rho d\varphi \cdot \mathcal{J}_{p,z}(i, k-\frac{1}{2}) \\
&\quad + \iint_{S_G(k+\frac{1}{2})} \mu_{p,z} \rho d\rho d\varphi \cdot \mathcal{J}_{p,z}(i, k+\frac{1}{2}) \\
&= \left\{ 4\bar{\mu}_{p,\rho}(i+\frac{1}{2}, k) \cdot \mathcal{J}_{p,\rho}(i+\frac{1}{2}, k) \right. \\
&\quad \left. - \left(\frac{\Delta\rho}{\Delta z} \right)^2 \bar{\mu}_{p,z}(i, k-\frac{1}{2}) \cdot \mathcal{J}_{p,z}(i, k-\frac{1}{2}) \right. \\
&\quad \left. + \left(\frac{\Delta\rho}{\Delta z} \right)^2 \bar{\mu}_{p,z}(i, k+\frac{1}{2}) \cdot \mathcal{J}_{p,z}(i, k+\frac{1}{2}) \right\} \cdot \frac{1}{8} \Delta\varphi \Delta z \\
&\equiv 0
\end{aligned} \tag{3.69}$$

Otherwise ($\rho = i \cdot \Delta\rho$ where $i = \{1, 2, 3, \dots, N\}$)

$$\begin{aligned}
\left[\oint_{S_G} \vec{J}_p \cdot d\vec{A} \right]_{i,k} &= - \iint_{S_G(i-\frac{1}{2})} \mu_{p,\rho} \rho d\varphi dz \cdot \mathcal{J}_{p,\rho}(i-\frac{1}{2}, k) + \iint_{S_G(i+\frac{1}{2})} \mu_{p,\rho} \rho d\varphi dz \cdot \mathcal{J}_{p,\rho}(i+\frac{1}{2}, k) \\
&\quad - \iint_{S_G(k-\frac{1}{2})} \mu_{p,z} \rho d\rho d\varphi \cdot \mathcal{J}_{p,z}(i, k-\frac{1}{2}) + \iint_{S_G(k+\frac{1}{2})} \mu_{p,z} \rho d\rho d\varphi \cdot \mathcal{J}_{p,z}(i, k+\frac{1}{2}) \\
&= \left\{ - \left(1 - \frac{1}{2i} \right) \cdot \bar{\mu}_{p,\rho}(i-\frac{1}{2}, k) \cdot \mathcal{J}_{p,\rho}(i-\frac{1}{2}, k) \right. \\
&\quad \left. + \left(1 + \frac{1}{2i} \right) \cdot \bar{\mu}_{p,\rho}(i+\frac{1}{2}, k) \cdot \mathcal{J}_{p,\rho}(i+\frac{1}{2}, k) \right. \\
&\quad \left. - \left(\frac{\Delta\rho}{\Delta z} \right)^2 \cdot \bar{\mu}_{p,z}(i, k-\frac{1}{2}) \cdot \mathcal{J}_{p,z}(i, k-\frac{1}{2}) \right. \\
&\quad \left. + \left(\frac{\Delta\rho}{\Delta z} \right)^2 \cdot \bar{\mu}_{p,z}(i, k+\frac{1}{2}) \cdot \mathcal{J}_{p,z}(i, k+\frac{1}{2}) \right\} \cdot i \Delta z \Delta\phi \\
&\equiv 0
\end{aligned} \tag{3.70}$$

where the local averages of the normal component of hole mobility over each section of Gaussian surface around the mesh point (i, k) are

$$\bar{\mu}_{p,\rho}(i \pm \frac{1}{2}, k) = \frac{1}{2} \cdot \left[\mu_{p,\rho}(i \pm \frac{1}{2}, k - \frac{1}{2}) + \mu_{p,\rho}(i \pm \frac{1}{2}, k + \frac{1}{2}) \right]; \quad (3.71a)$$

$$\text{for } i = \{0, 1, 2, \dots, N\},$$

$$\bar{\mu}_{p,z}(i, k \pm \frac{1}{2}) = \begin{cases} \mu_{p,z}(i, k \pm \frac{1}{2}); & \text{for } i = 0, \\ \frac{\mu_{p,z}(i - \frac{1}{2}, k \pm \frac{1}{2}) \cdot \left(1 - \frac{1}{4i}\right) + \mu_{p,z}(i + \frac{1}{2}, k \pm \frac{1}{2}) \cdot \left(1 + \frac{1}{4i}\right)}{2}; & \text{for } i = \{1, 2, 3, \dots, N\}, \end{cases} \quad (3.71b)$$

and $k = \{0, 1, 2, \dots, M\}$. By choosing the uniform grid where $\Delta\rho = \Delta z = h$, the discretized equations (3.69)-(3.70) are simplified as

At z-axis ($\rho = 0$ or $i = 0$)

$$\begin{aligned} & 4\bar{\mu}_\rho(i + \frac{1}{2}, k) \cdot \left[\mathcal{B}(\Delta_\rho \psi(i + 1, k)) \cdot p_f(i, k) - \mathcal{B}(-\Delta_\rho \psi(i + 1, k)) \cdot p_f(i + 1, k) \right] \\ & - \bar{\mu}_z(i, k - \frac{1}{2}) \cdot \left[\mathcal{B}(\Delta_z \psi(i, k)) \cdot p_f(i, k - 1) - \mathcal{B}(-\Delta_z \psi(i, k)) \cdot p_f(i, k) \right] \\ & + \bar{\mu}_z(i, k + \frac{1}{2}) \cdot \left[\mathcal{B}(\Delta_z \psi(i, k + 1)) \cdot p_f(i, k) - \mathcal{B}(-\Delta_z \psi(i, k + 1)) \cdot p_f(i, k + 1) \right] = 0 \quad (3.72) \end{aligned}$$

Otherwise ($\rho = i \cdot \Delta\rho$ where $i = 1, 2, 3, \dots$)

$$\begin{aligned}
& - \left(1 - \frac{1}{2i}\right) \cdot \bar{\mu}_{p,\rho}(i - \frac{1}{2}, k) \cdot \left[\mathcal{B}(\Delta_\rho \psi(i, k)) \cdot p_f(i - 1, k) - \mathcal{B}(-\Delta_\rho \psi(i, k)) \cdot p_f(i, k) \right] \\
& + \left(1 + \frac{1}{2i}\right) \cdot \bar{\mu}_{p,\rho}(i + \frac{1}{2}, k) \cdot \left[\mathcal{B}(\Delta_\rho \psi(i + 1, k)) \cdot p_f(i, k) - \mathcal{B}(-\Delta_\rho \psi(i + 1, k)) \cdot p_f(i + 1, k) \right] \\
& \quad - \bar{\mu}_{p,z}(i, k - \frac{1}{2}) \cdot \left[\mathcal{B}(\Delta_z \psi(i, k)) \cdot p_f(i, k - 1) - \mathcal{B}(-\Delta_z \psi(i, k)) \cdot p_f(i, k) \right] \\
& \quad + \bar{\mu}_{p,z}(i, k + \frac{1}{2}) \cdot \left[\mathcal{B}(\Delta_z \psi(i, k + 1)) \cdot p_f(i, k) - \mathcal{B}(-\Delta_z \psi(i, k + 1)) \cdot p_f(i, k + 1) \right] \\
& \hspace{25em} = 0 \quad (3.73)
\end{aligned}$$

where the spatial difference of electric potential is calculated as follow

$$\Delta_\rho \psi(i, k) = \psi(i, k) - \psi(i - 1, k) \quad (3.74a)$$

$$\Delta_z \psi(i, k) = \psi(i, k) - \psi(i, k - 1) \quad (3.74b)$$

Boundary conditions are required to solve the discretized continuity equation (3.72)-(3.73) numerically. At the electrodes, the boundary conditions are described as

$$p_f(i, k) = \begin{cases} 1 & \text{for } i \in [0, R_{tip}/h], k = M \\ 1 & \text{for } i \in [0, R/h], k = 0 \end{cases} \quad (3.75)$$

Following the same technique used when obtaining the insulating boundary conditions in the potential solver, we have

$$p_f(i, k) = \begin{cases} p_f(i, k + 1) & \text{for } i \notin [0, R_{tip}/h], k = M \quad (\text{top boundary}) \\ p_f(i + 1, k) & \text{for } i = N, k = \{0, 1, 2, \dots, M\} \quad (\text{side boundary}) \end{cases} \quad (3.76)$$

Once again, these four boundary conditions together with the discretized continuity equations (3.72)-(3.73) constitute a system of linear equations. In the corresponding matrix notation (3.53), the vector $\vec{\mathbf{b}}$ contains the boundary conditions, and the matrix \mathbb{A} encompasses the morphological effect through the spatially-dependent hole mobility. Unlike the 1-D DD-SCLC model, the matrix \mathbb{A} is asymmetric, and the numerical solutions of free hole carrier density $\vec{\mathbf{p}}_{\mathbf{f}}$ is achieved by the iterative method called BiCGSTAB [68].

3.4.4 Verification

Similar to the work done with the 1-D DD-SCLC model, we have developed a Fortran 90 program to find the unknown electric potentials and free hole densities of 2-D DD-SCLC models in cylindrical coordinate systems with cylindrical symmetry by following the algorithm shown in figure 3.3. Due to the asymmetric properties emerged from the tip-plane geometry, the direct method of inversion used in the 1-D DD-SCLC model is no longer applicable. Therefore, we have developed a Fortran 90 module to execute a routine of BiCGSTAB, which is an iterative method to solve the non-symmetric linear system. The programming code is written specifically to handle sparse matrices. To minimize the error associated with numerical calculation, all parameters and variables are represented by double precision values in the program.

First of all, we would like to verify the BiCGSTAB module by comparing the results with those acquired from the direct method. By retrofitting the module into the 1-D DD-SCLC model, we simulate charge transport of trap-free hole-only devices in planar geometry. The comparison of the current-voltage characteristics calculated from the two distinct methods, inversion of tridiagonal matrices and BiCGSTAB, is illustrated in figure 3.12. The error between the two methods is negligible.

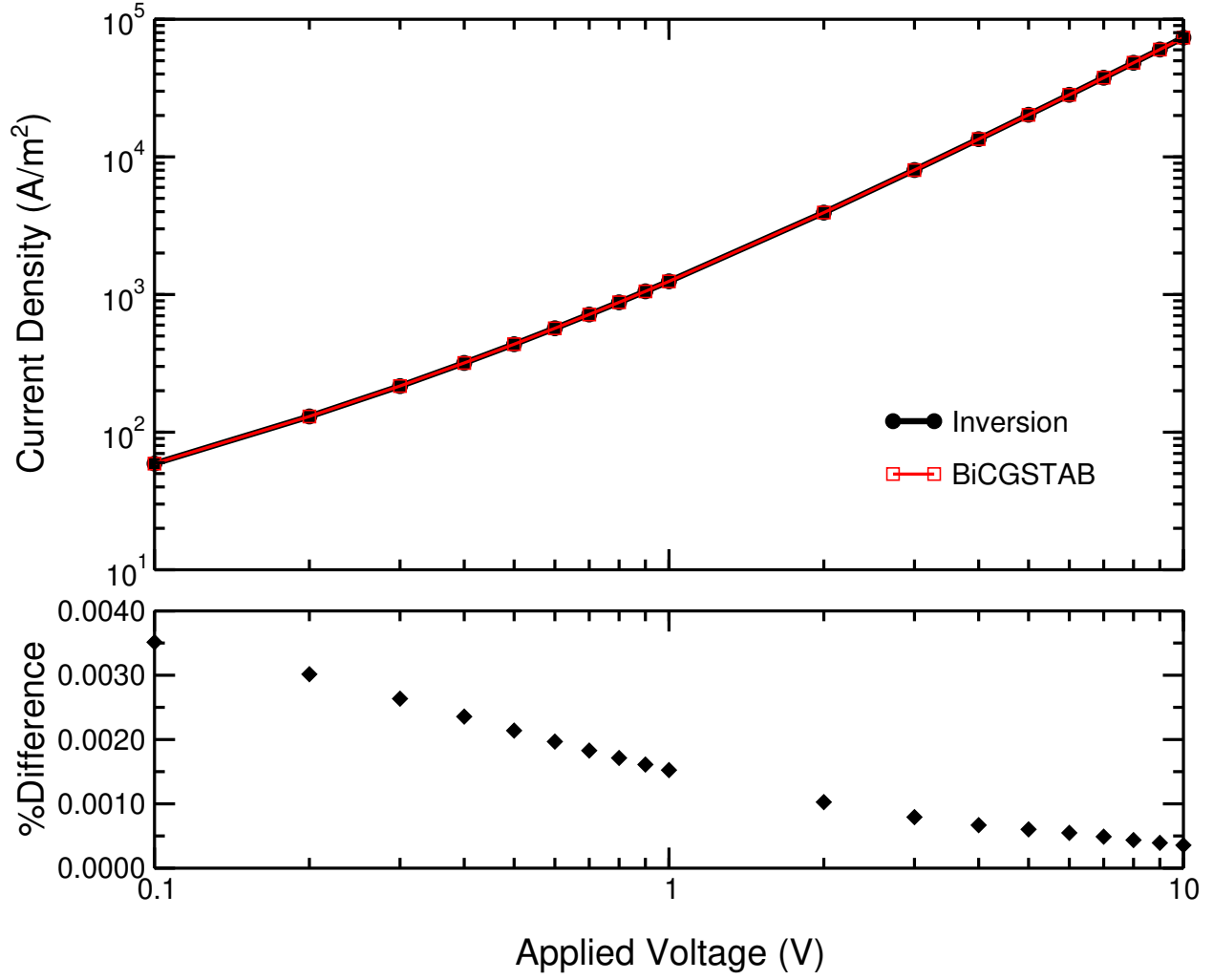


Figure 3.12: BiCGSTAB VS Inversion – The theoretical current-voltage characteristic of the trap-free ($f_t = 0$) hole-only device solved iteratively by using BiCGSTAB module is compared with that solved directly by inversion of a tridiagonal matrix. In both calculations, we use a 1-D DD-SCLC model with $L = 80nm$, $N_v = 1.25 \times 10^{21}cm^{-3}$, $\epsilon_r = 3$, $\mu_p = 10^{-4}cm^2V^{-1}s^{-1}$.

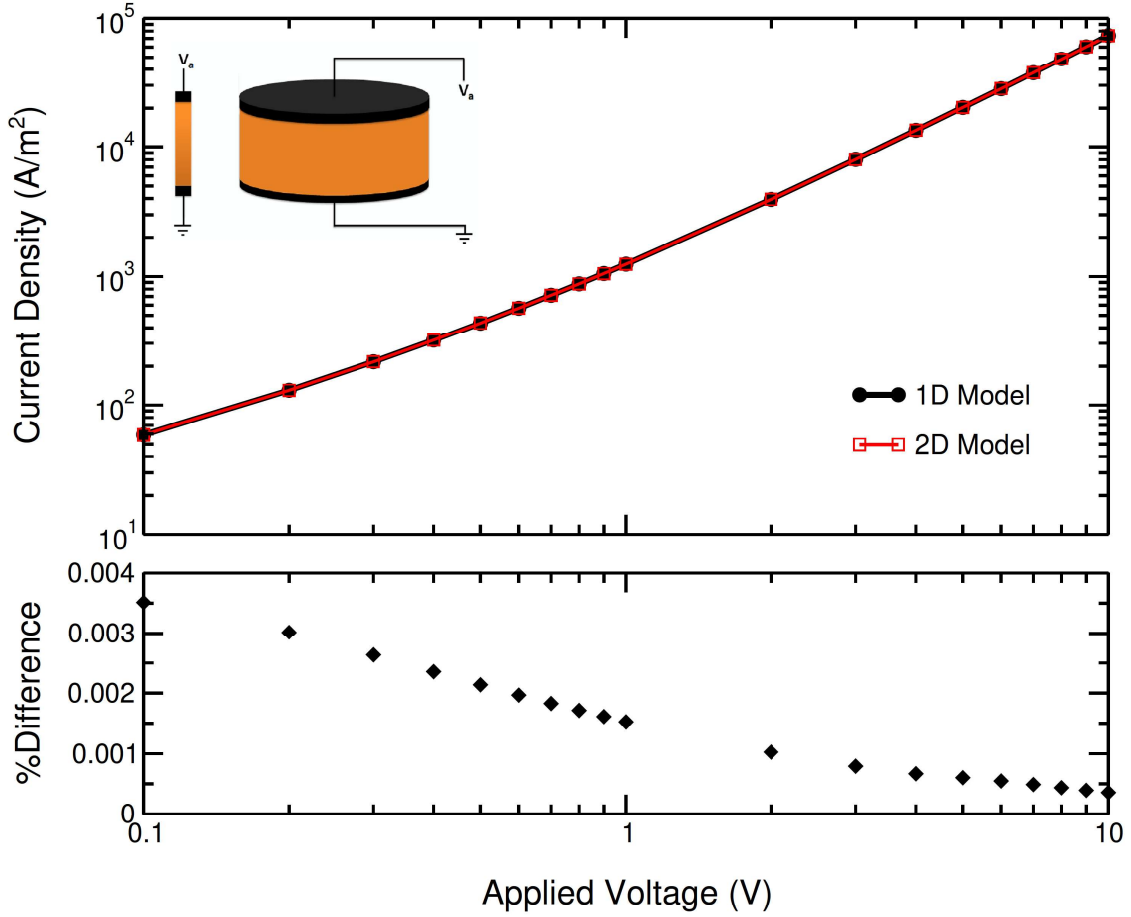


Figure 3.13: The comparison of the theoretical current-voltage characteristics of the trap-free ($f_t = 0$) hole-only device calculated from 1-D and 2-D DD-SCLC models. In both models, the transport layer (orange) is homogeneous with the constant parameters: $\epsilon_r = 3$, $\mu_p = 10^{-4} \text{cm}^2 \text{V}^{-1} \text{s}^{-1}$, and $N_v = 1.25 \times 10^{21} \text{cm}^{-3}$.

Next, we would like to verify the 2-D DD-SCLC model by reproducing the result of homogeneous planar device. Consider the trap-free hole-only device of thickness $80nm$ and radius $300nm$. To capture the planar case, the tip radius is extended to the size of the device radius. In figure 3.13, the current-voltage characteristic simulated from the 2-D DD-SCLC model is compared with that simulated from the 1-D DD-SCLC model. Although the 2-D DD-SCLC model has the possibility of the additional lateral transport compared to the 1-D DD-SCLC model where only vertical transport occurs, their current-voltage characteristics exhibit an inconsequential error less than 0.0035% . Therefore, only vertical conductance matters in charge transport of these planar devices, and the 2-D DD-SCLC model is verified for this case.

Replacing one of the planar electrodes with a tip-shaped electrode, one can expect a different amount of charge injection due to their distinct contact areas. Moreover, unlike in the conventional planar device, the charge transport in a tip-plane device is subject to the influence of the lateral current spreading induced by the tip geometry. As the 2-D DD-SCLC model can only simulate the transport behavior in finite systems surrounded by insulating boundaries, we need to ensure that the computational domain is sufficiently large to make the boundary effect negligible. To demonstrate this effect, we perform the numerical calculations to model the hole-only device, where holes are injected from a tip electrode of $1nm$ radius into a device of 80 nm thickness. The other electrode is planar of the same size as the device radius, which will be varied in the study. It is important to note that the approximate $1nm$ tip radius is the smallest tip allowed in the discretized domain of $2nm$ spacing, where it can be assigned to a single mesh point. The broadest lateral spreading corresponds to the smallest tip size.

Unlike the case of planar geometry, the hole-only device in tip-plane geometry no longer

maintain the uniform vertical current. Therefore, it is only informative to present the overall hole transport in term of a total current, which is the surface integral of current density over the device boundary. Due to the cylindrical symmetry of the 2-D DD-SCLC model, the total current in the lateral direction is zero. Therefore, the total hole current injected at the tip is simply the surface integral of the vertical current over the cross-sectional surface of the device, which is

$$I_p = 2\pi \int_0^R J_{p,z}(\rho, z) \rho d\rho. \quad (3.77)$$

This is the physical quantity that can be measured from the experiments with the tip-plane electrode configuration, *e.g.*, the c-AFM measurements. It is also useful to emphasize that the total current is independent of the vertical position of the device cross-section, *i.e.*, the total current is constant through the device. This manner is governed by the continuity equation at the steady state. In the discretized domain ($\rho \in [0, R]$ and $\rho = i \cdot \Delta\rho$; $i = \{0, 1, 2, \dots, N\}$), total current is calculated from

$$I_p = \frac{\pi}{4} \Delta\rho^2 J_{p,z}(0, k + \frac{1}{2}) + 2\pi \Delta\rho^2 \sum_{i=1}^N i J_{p,z}(i, k + \frac{1}{2}) \quad (3.78)$$

where $J_{p,z}(i, k + \frac{1}{2})$ is the discretized current density associated to Schafetter-Gummel discretization, as written in eq.(3.68b).

Figure 3.14 plots the hole current as a function of the radius to thickness ratio (R/L) of the device, where the simulation is carried out using a 2-D DD-SCLC model with tip-plane geometry. The transport layer is assumed to be homogeneous with isotropic hole mobility. For a fixed device thickness, the current approaches the saturated regime when device radius is sufficiently large so that the finite-size effect can be safely ignored. A good balance point

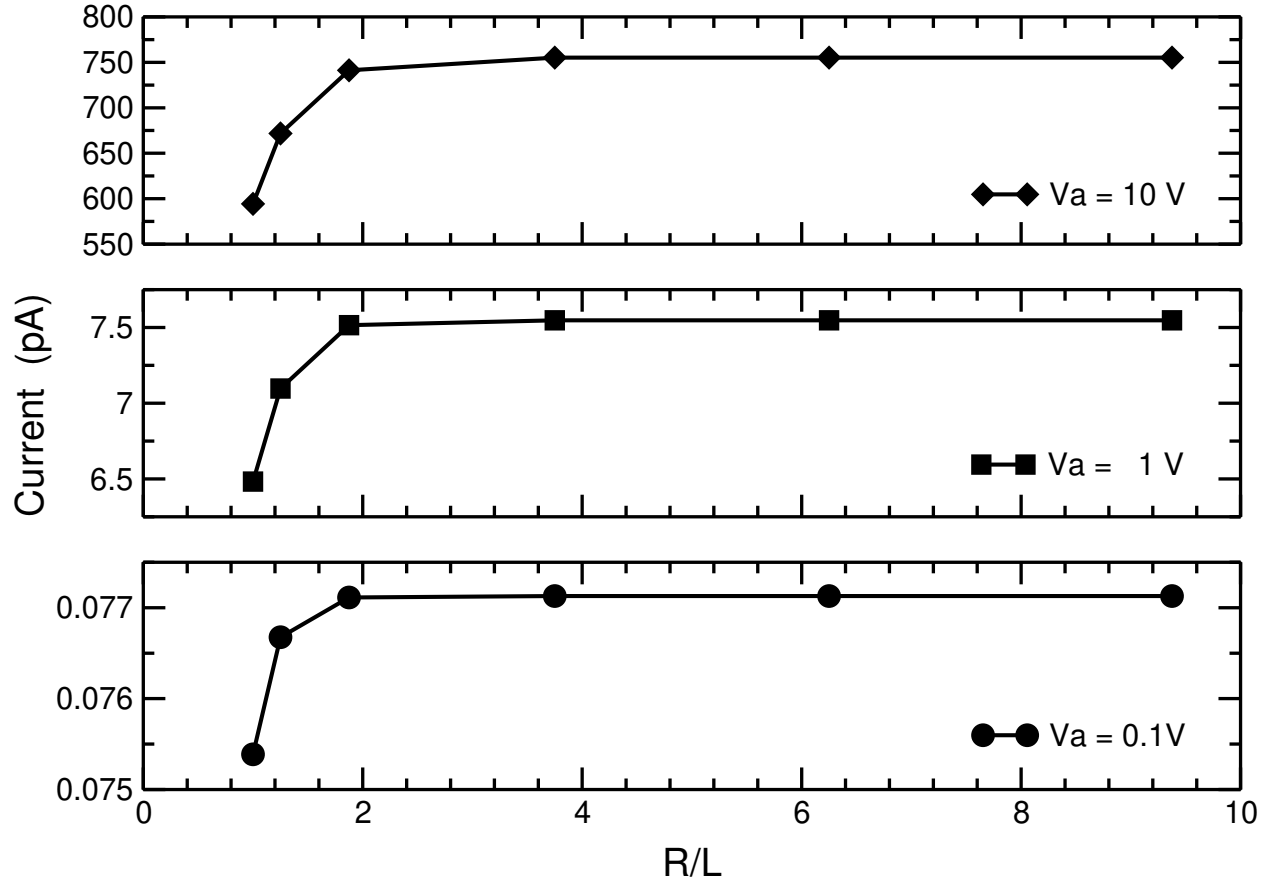


Figure 3.14: Finite-size effect–Convergence of the simulated hole current with respect to device dimensional ratio of radius to thickness, when the applied voltage $V_a = 0.1, 1, 10\text{ V}$. By using a 2-D DD-SCLC model, the trap-free ($f_t = 0$) hole-only device is modeled in tip-plane geometry ($R_{tip} \sim 1\text{ nm}$), assuming homogeneous transport layer ($\epsilon_r = 3$, $N_v = 1.25 \times 10^{21}\text{ cm}^{-3}$) with isotropic hole mobility ($\mu_{p,\rho} = \mu_{p,z} = 10^{-4}\text{ cm}^2\text{ V}^{-1}\text{ s}^{-1}$). Using the dimensional ratio $R/L = 3.75$ provides a well-converged solutions while the finite-size effect is negligible. All the following calculations of tip-plane devices with an isotropic mobility will be performed with this dimensional ratio.

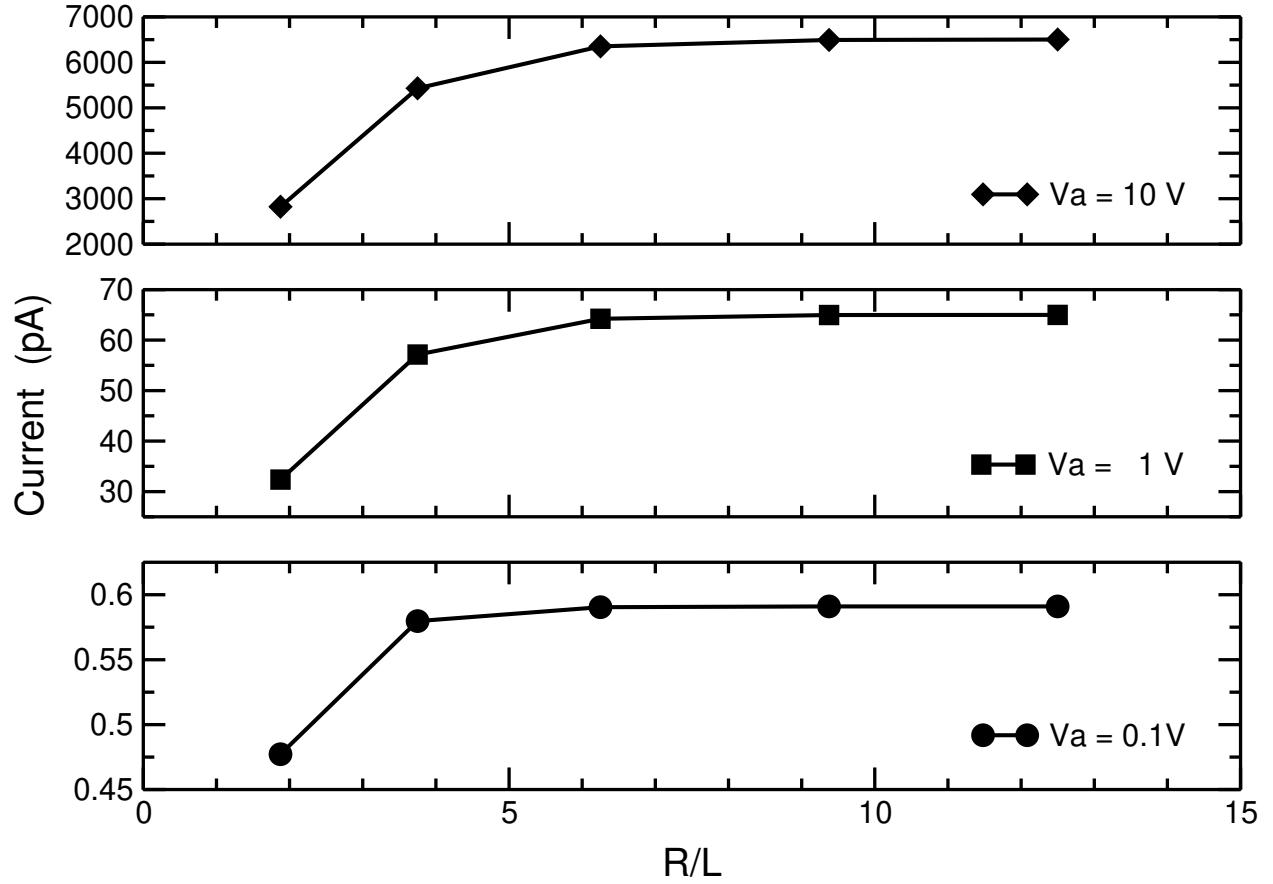


Figure 3.15: Finite-size effect–Convergence of the simulated hole current with respect to device dimensional ratio of radius to thickness, when the applied voltage $V_a = 0.1, 1, 10\text{V}$. By using a 2-D DD-SCLC model, the trap-free ($f_t = 0$) hole-only device is modeled in tip-plane geometry ($R_{tip} \sim 1\text{nm}$), assuming homogeneous transport layer ($\epsilon_r = 3$, $N_v = 1.25 \times 10^{21}\text{cm}^{-3}$) with anisotropic hole mobility ($\mu_{p,\rho}/\mu_{p,z} = 25$, $\mu_{p,z} = 10^{-4}\text{cm}^2\text{V}^{-1}\text{s}^{-1}$). Using the dimensional ratio $R/L = 6.25$ provides a well-converged solutions while the finite-size effect is negligible. All the following calculations of tip-plane devices with anisotropic mobility will be performed with this dimensional ratio.

with the feasible numerical domain and negligible finite-size effect is achieved at the device dimensional ratio of 3.75, which incurs less than a 1% difference compared to the converged numerical solution of a system with dimensional ratio of 10.

In addition to the isotropic system, we have also considered the case of hole-only device with anisotropic mobility. When the lateral mobility is larger than the vertical one, we expect an increasing amount of current spreads out beneath the tip, which consequently enhances the finite-size effect. The evidence is shown in figure 3.15. Current predicted from the simulation with anisotropic mobility ($\mu_\rho/\mu_z = 25$) converges at higher dimensional ratio compared to that of a homogeneous device with isotropic mobility. Empirically, to safely omit the finite-size effect at reasonable computational overhead, the simulation of tip-plane device with large anisotropic mobility ($\mu_\rho/\mu_z = 25$) shall be conducted at the dimensional ratio of 6.25, which results in approximately a maximum 2% difference compared to the converged numerical solutions from devices with ratio $R/L = 12.50$.

The phenomena of current spreading was emphasized in the recent work by Ginger and his coworkers [32], in which they modified the well-known Mott-Gurney equation to include this tip-induced effect, and established a semi-empirical formula to describe current-voltage characteristics in the SCLC regime measured from c-AFM. Because it is important to understand the c-AFM experimental results, we extend their theoretical model to include the morphological effect, *i.e.*, exponentially distributed trap and anisotropic mobility. We also alter the insulating boundary condition to increase the stability and improve the convergence of the calculation, especially in the region near the tip electrode. Here, we would like to verify that the insulating boundary of device is well described by our choice of the insulating boundary conditions used in the model, as expressed in eq.(3.59). To explicitly insulate the device, the top boundary that is not the injecting electrode is replaced by a vacuum layer

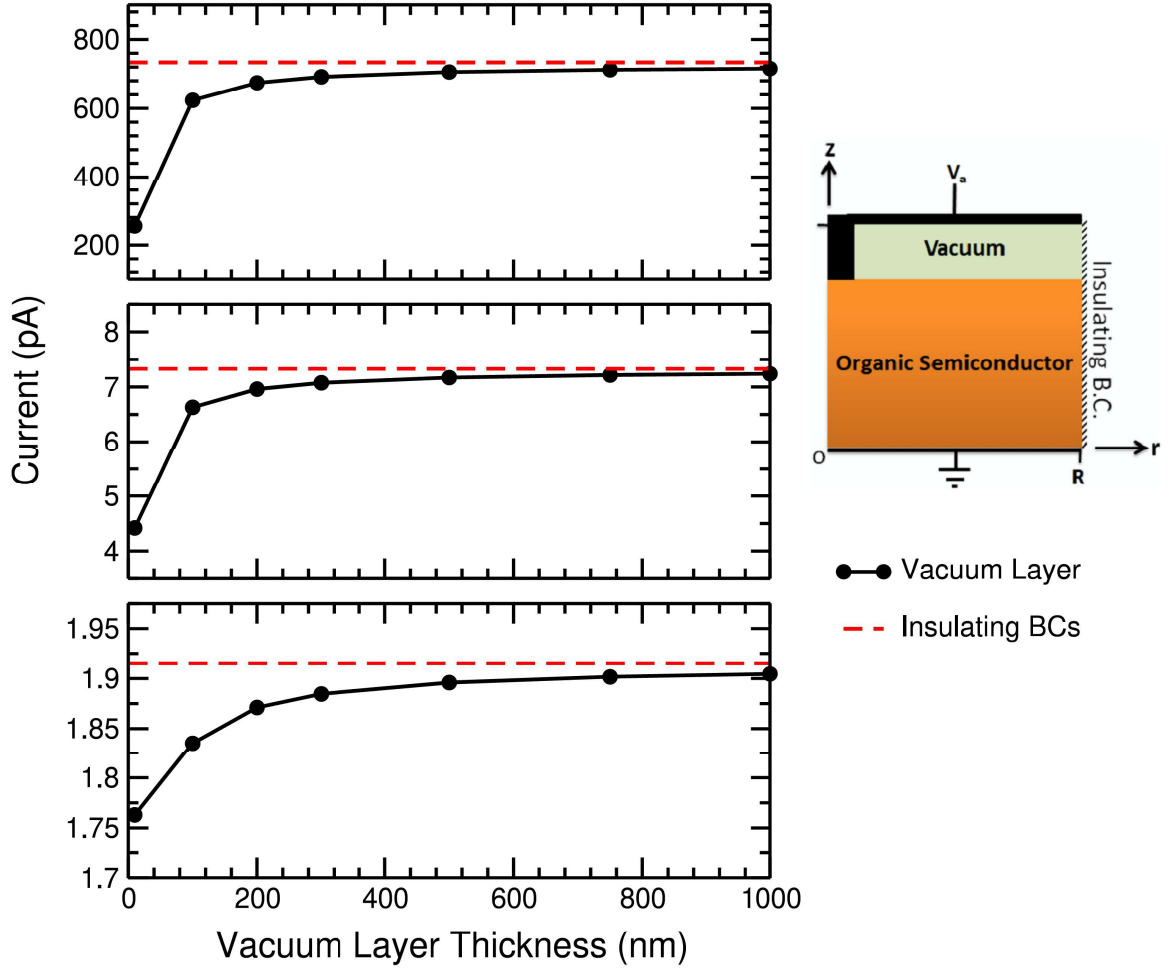


Figure 3.16: Current as a function of vacuum layer thickness simulated using the given device structure, compared to the current calculated from a 2-D DD-SCLC model with insulating boundary conditions described by eq.(3.59), when $V_a = 0.5, 1, 10V$. At high vacuum layer thickness, the consistency of the numerical current between the two device geometries is observed with approximately a maximum of 1% difference. For the transport layer (orange), we use $L = 80nm$, $\epsilon_r = 3$, $\mu_{p,\rho} = \mu_{p,z} = 10^{-4}cm^2V^{-1}s^{-1}$, and $N_v = 1.25 \times 10^{21}cm^{-3}$.

of vacuum permittivity ($\epsilon_r = 1$) and zero hole mobility ($\mu_p = 0$). The injecting electrode is transformed from a circular contact of $1nm$ radius to a cylindrical rod of the same radius. The conducting rod is then lengthened through the thickness of the vacuum layer, and connected to the topmost planar electrode. We have confirmed that the device radius is large enough that we can safely keep the insulating boundary condition on the side of the devices. The schematic representation of the new device structure is shown in figure 3.16.

Similarly, we carried out the numerical calculation to model the homogeneous hole-only device of $80nm$ thickness and $300nm$ radius with varying thickness of the insulating vacuum layer. Figure 3.16 plots the current versus the vacuum layer thickness when the applied voltage $V_a = 0.5, 1, 10V$. The currents simulated from the 2-D DD-SCLC model with the insulating boundary condition, as expressed in eq.(3.59), are plotted (dashed red line) for the comparison. It is shown that, with the increasing thickness of the vacuum layer, the simulated currents approach the saturated regime, demonstrating a good consistency ($< 1\%$ difference at the $100nm$ vacuum layer thickness) with the current calculated using only the insulating boundary conditions. Note that the maximum difference between the two device geometries occurs at the high applied voltage, which is $V_a = 10V$ in our calculations. The explanation to this observation is related to the field distortion caused by the planar electrode at the topmost interface that becomes more severe with increasing applied voltage.

3.5 The Fully 3-D DD-SCLC Model in a Cartesian Coordinate System

In the previous sections, we have introduced a 1-D DD-SCLC model to describe the vertical charge transport in a homogeneous planar device, and a 2-D DD-SCLC model that allows us

to observe the additional lateral transport in a tip-plane device with cylindrical symmetry. It is already well-known that electric conductance of an disordered organic semiconductor is considerably affected by its nanoscale morphology. Superior charge transport has been found in semi-crystalline materials due to the presence of a nanofibrillar network. To investigate the effect of such complex morphology, a fully three-dimensional model is obviously a good choice. The model also permits the implementation of tip geometry and spatially-varying traps.

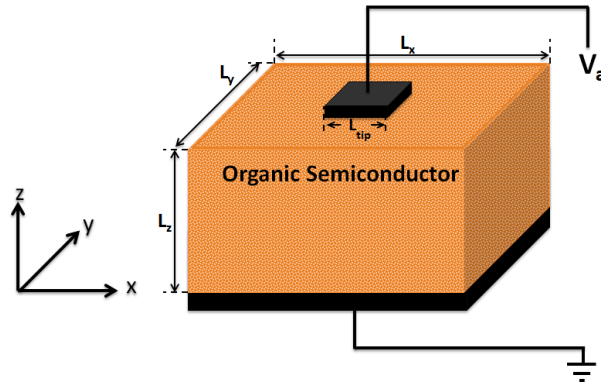


Figure 3.17: Illustration of a three-dimensional hole-only device of tip-plane geometry. The numerical calculation is performed using a three-dimensional coordinate system, allowing full customization of trap distribution and nanoscale morphology in the transport layer.

Figure 3.17 illustrates the three-dimensional device structure modeled as a $L_x \times L_y \times L_z$ cuboid of tip-plane geometry. For simplicity, we approximate the tip electrode as a square contact of L_{tip} side length. By enlarging the tip to cover the area $L_x \times L_y$, the device structure turns into a planar geometry. Similar to the 1-D and 2-D DD-SCLC models, charge transport in the hole injection system can be described by three governing equations, including Poisson's equation, the continuity equation at steady state and the drift-diffusion

equation. We have

$$\oint_{S=\partial V} \epsilon(\vec{r}) \vec{\mathcal{E}}(\vec{r}) \cdot d\vec{A} = \frac{qN_v}{V_t} \int_V (p_f(\vec{r}) + \mathcal{S}(\vec{r}) f_t \cdot p_f(\vec{r})^t) dV \quad (3.79)$$

$$\oint_{S=\partial V} \vec{J}_p(\vec{r}) \cdot d\vec{A} = 0 \quad (3.80)$$

$$J_{p,\xi}(\vec{r}) = q\mu_{p,\xi}(\vec{r})N_vV_t (p_f(\vec{r})\mathcal{E}_\xi(\vec{r}) - \partial p_f/\partial \xi) \quad (3.81)$$

where $\vec{J}_p(\vec{r}) = \sum_{\xi} J_{p,\xi}(\vec{r}) \cdot \hat{\xi}$ and $\xi = \{x, y, z\}$. The internal inhomogeneity, *i.e.*, nanoscale morphology and traps, is included in the model via the spatially varying parameters of dielectric constant $\epsilon(\vec{r}) = \epsilon_r(\vec{r})\epsilon_o$, hole mobility $\vec{\mu}_p(\vec{r}) = \sum_{\xi} \mu_{p,\xi}(\vec{r}) \cdot \hat{\xi}$, and trap distribution $\mathcal{S}(\vec{r})$. Poisson's equation and the continuity equation are presented in the integral form, which is convenient to treat the inhomogeneity under the discretization.

Similar to the 2-D DD-SCLC model, the device is grounded on the bottom electrode ($z = 0$), and driven at the top electrode ($z = L_z$) with the applied potential V_a . The top boundary is insulating. Therefore, the boundary condition at the top and bottom boundaries are defined as

$$\psi(x, y, L_z) = V_a/V_t \quad \text{and} \quad p_f(x, y, L_z) = 1, \quad \text{where } \{x, y\} \in \mathcal{D}_{tip} \quad (3.82a)$$

$$\left. \frac{\partial \psi}{\partial z} \right|_{(x,y,L_z)} = 0 \quad \text{and} \quad \left. \frac{\partial p_f}{\partial z} \right|_{(x,y,L_z)} = 0, \quad \text{where } \{x, y\} \notin \mathcal{D}_{tip} \quad (3.82b)$$

$$\psi(x, y, 0) = 0 \quad \text{and} \quad p_f(x, y, 0) = 1, \quad \text{where } x \in [0, L_x], y \in [0, L_y] \quad (3.82c)$$

where \mathcal{D}_{tip} is the two-dimensional domain of the tip contact area, *e.g.*, in the case of square tip shown in figure 3.17, we have $\mathcal{D}_{tip} \in [L_{tip}, L_{tip}]$. It should be noted that the 3-D DD-

SCLC model does not limit to this particular tip geometry, but can be generalized for any shape of tip contact that can be discretized by the numerical approach explained in the following section. Furthermore, for the more complex condition that the conducting tip is penetrated into the material, which commonly occurs in the c-AFM measurements, the tip is thus modeled by defining \mathcal{D}_{tip} as the three-dimensional domain of the tip geometry penetrated into the material domain. This is absolutely executable in the numerical tool we developed for the 3-D DD-SCLC model. However, to keep the derivation simple, we will assume that the penetration depth is negligible and the tip is approximated by the surface contact area at the top boundary.

In contrast to the 2-D DD-SCLC model, we apply periodic boundary conditions on the four sides of the device to mitigate finite-size effects. However, when considering tip-plane geometry, the device dimensions need to be large enough to allow complete current spreading. Based on the analysis of the 2-D DD-SCLC model (shown in figure 3.14-3.15), the proper dimensions for the device with isotropic mobility and extreme anisotropic mobility ($\mu_{p,x} = \mu_{p,y} = 25 \mu_{p,z}$) are $L_x = L_y = 3.75 L_z$ and $L_x = L_y = 6.25 L_z$ respectively.

3.5.1 Discretization

Choosing a uniform mesh separation equally in all directions ($\Delta x = \Delta y = \Delta z = h$), the three-dimensional device domain is replaced by a number of cube-shaped cells of volume h^3 and a set of mesh points (x_i, y_j, z_k) located on the edge of the cell; $i = \{0, 1, 2, \dots, N_x\}$, $j = \{0, 1, 2, \dots, N_y\}$, and $k = \{0, 1, 2, \dots, N_z\}$, where $x_i = i \cdot h$, $y_j = j \cdot h$, $z_k = k \cdot h$, and $h = L_x/N_x = L_y/N_y = L_z/N_z$, as shown in figure 3.18(a). A single mesh point is surrounded by eight adjacent cells and six nearest neighbors listed in figure 3.18(b), and each cell is assumed to carry invariable values of dielectric constant, hole mobility, and trap

parameters. The internal inhomogeneity of the material is then represented by the variation of cell properties from one cell to the other.

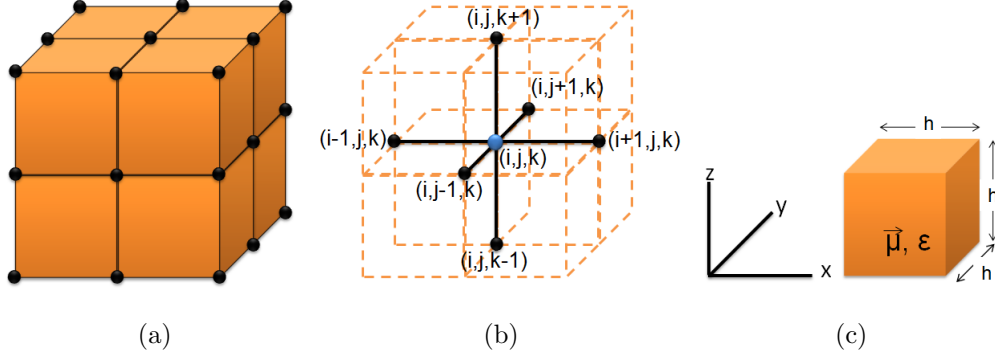


Figure 3.18: Illustration of the spatial discretization in a three-dimensional Cartesian coordinate system; (a) the device is divided into cube cells ($h \times h \times h$) with mesh points located at each corner; (b) each mesh point is surrounded by six nearest neighbors, and is adjacent to eight cells; (c) each cell contains constant values of dielectric constant, hole mobility, and trap parameters. The inhomogeneity is generated by varying the values of these parameters from one cell to another.

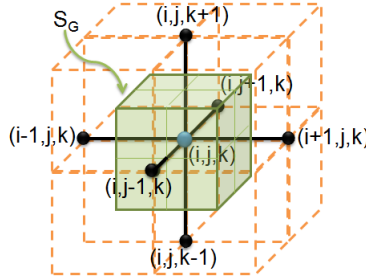


Figure 3.19: Gaussian surface S_G as a cube of size $h \times h \times h$ surrounding mesh point (i, j, k)

Considering Poisson's equation and the continuity equation in the integral form, we introduce a cube-shaped Gaussian surface (S_G) bounding the finite volume $h \times h \times h$, as shown in figure 3.19. Similar to the 2-D DD-SCLC model, the numerical surface and volume integration of the physical variables around each mesh point will be performed with respect to its Gaussian surface based on three assumptions: (i) hole current density is constant between

mesh points, (ii) electric field is also constant between mesh points, (iii) the tangential component of electric field is continuous at the interface of neighboring cells. It is worth emphasizing that by applying the assumption (ii) and (iii), the normal component of electric field at the Gaussian surface is constant and continuous due to the fact that the Gaussian surface is chosen to be perpendicular to the interface of neighboring cells.

3.5.2 Potential Solver

By applying the numerical approximation of surface integral (3.27) and volume integral (3.28) on the chosen Gaussian surface, Poisson's equation (3.79) in the three-dimensional Cartesian coordinate system can be discretized as

$$\begin{aligned}
\left[\oint_{S_G} \epsilon \vec{\mathcal{E}} \cdot d\vec{A} \right]_{i,j,k} &= - \iint_{S_G(i-\frac{1}{2})} \epsilon(\vec{r}) dydz \cdot \mathcal{E}_x(i-\frac{1}{2}, j, k) + \iint_{S_G(i+\frac{1}{2})} \epsilon(\vec{r}) dydz \cdot \mathcal{E}_x(i+\frac{1}{2}, j, k) \\
&\quad - \iint_{S_G(j-\frac{1}{2})} \epsilon(\vec{r}) dxdz \cdot \mathcal{E}_y(i, j-\frac{1}{2}, k) + \iint_{S_G(j+\frac{1}{2})} \epsilon(\vec{r}) dxdz \cdot \mathcal{E}_y(i, j+\frac{1}{2}, k) \\
&\quad - \iint_{S_G(k-\frac{1}{2})} \epsilon(\vec{r}) dxdy \cdot \mathcal{E}_z(i, j, k-\frac{1}{2}) + \iint_{S_G(k+\frac{1}{2})} \epsilon(\vec{r}) dxdy \cdot \mathcal{E}_z(i, j, k+\frac{1}{2}) \\
&= - \bar{\epsilon}_x(i-\frac{1}{2}, j, k) h^2 \mathcal{E}_x(i-\frac{1}{2}, j, k) + \bar{\epsilon}_x(i+\frac{1}{2}, j, k) h^2 \mathcal{E}_x(i+\frac{1}{2}, j, k) \\
&\quad - \bar{\epsilon}_y(i, j-\frac{1}{2}, k) h^2 \mathcal{E}_y(i, j-\frac{1}{2}, k) + \bar{\epsilon}_y(i, j+\frac{1}{2}, k) h^2 \mathcal{E}_y(i, j+\frac{1}{2}, k) \\
&\quad - \bar{\epsilon}_z(i, j, k-\frac{1}{2}) h^2 \mathcal{E}_z(i, j, k-\frac{1}{2}) + \bar{\epsilon}_z(i, j, k+\frac{1}{2}) h^2 \mathcal{E}_z(i, j, k+\frac{1}{2}) \\
&\equiv \frac{qN_v h^3}{V_t} [p_f(i, j, k) + f_t \mathcal{S}(i, j, k) \cdot p_f(i, j, k)^{rt}] . \tag{3.83}
\end{aligned}$$

Follow the numerical approximations for the first order derivative, and the discretized electric fields are then given by

$$\mathcal{E}_x(i \pm \frac{1}{2}, j, k) = [\psi(i, j, k) \mp \psi(i \pm 1, j, k)] / h \quad (3.84a)$$

$$\mathcal{E}_y(i, j \pm \frac{1}{2}, k) = [\psi(i, j, k) \mp \psi(i, j \pm 1, k)] / h \quad (3.84b)$$

$$\mathcal{E}_z(i, j, k \pm \frac{1}{2}) = [\psi(i, j, k) \mp \psi(i, j, k \pm 1)] / h \quad (3.84c)$$

where the local averages of dielectric constant over each Gaussian surface (S_G) are

$$\begin{aligned} \bar{\epsilon}_x(i \pm \frac{1}{2}, j, k) = & \left[\epsilon(i \pm \frac{1}{2}, j - \frac{1}{2}, k - \frac{1}{2}) + \epsilon(i \pm \frac{1}{2}, j + \frac{1}{2}, k - \frac{1}{2}) \right. \\ & \left. + \epsilon(i \pm \frac{1}{2}, j - \frac{1}{2}, k + \frac{1}{2}) + \epsilon(i \pm \frac{1}{2}, j + \frac{1}{2}, k + \frac{1}{2}) \right] / 4 \end{aligned} \quad (3.85a)$$

$$\begin{aligned} \bar{\epsilon}_y(i, j \pm \frac{1}{2}, k) = & \left[\epsilon(i - \frac{1}{2}, j \pm \frac{1}{2}, k - \frac{1}{2}) + \epsilon(i + \frac{1}{2}, j \pm \frac{1}{2}, k - \frac{1}{2}) \right. \\ & \left. + \epsilon(i - \frac{1}{2}, j \pm \frac{1}{2}, k + \frac{1}{2}) + \epsilon(i + \frac{1}{2}, j \pm \frac{1}{2}, k + \frac{1}{2}) \right] / 4 \end{aligned} \quad (3.85b)$$

$$\begin{aligned} \bar{\epsilon}_z(i, j, k \pm \frac{1}{2}) = & \left[\epsilon(i - \frac{1}{2}, j - \frac{1}{2}, k \pm \frac{1}{2}) + \epsilon(i + \frac{1}{2}, j - \frac{1}{2}, k \pm \frac{1}{2}) \right. \\ & \left. + \epsilon(i - \frac{1}{2}, j + \frac{1}{2}, k \pm \frac{1}{2}) + \epsilon(i + \frac{1}{2}, j + \frac{1}{2}, k \pm \frac{1}{2}) \right] / 4 \end{aligned} \quad (3.85c)$$

The discretized Poisson's equation (3.83) is then rewritten in terms of electric potential as

$$\begin{aligned} -\bar{\epsilon}_x(i - \frac{1}{2}, j, k) \cdot \psi(i - 1, j, k) - \bar{\epsilon}_x(i + \frac{1}{2}, j, k) \cdot \psi(i + 1, j, k) \\ -\bar{\epsilon}_y(i, j - \frac{1}{2}, k) \cdot \psi(i, j - 1, k) - \bar{\epsilon}_y(i, j + \frac{1}{2}, k) \cdot \psi(i, j + 1, k) \\ -\bar{\epsilon}_z(i, j, k - \frac{1}{2}) \cdot \psi(i, j, k - 1) - \bar{\epsilon}_z(i, j, k + \frac{1}{2}) \cdot \psi(i, j, k + 1) \\ + 6\bar{\epsilon}(i, j, k) \cdot \psi(i, j, k) = \frac{qN_v h^2}{V_t} [p_f(i, j, k) + f_t \mathcal{S}(i, j, k) \cdot p_f(i, j, k)^{rt}] \end{aligned} \quad (3.86)$$

where $\bar{\epsilon}(i, j, k)$ is the locally averaged dielectric constant at mesh point (i, j, k) , which is equivalent to the arithmetic average of the values from eight neighboring cells surrounding the considering mesh point. Meanwhile, the $\bar{\epsilon}(i, j, k)$ can also be expressed in term of the locally averaged values described in equation (3.85) as follows,

$$\begin{aligned}\bar{\epsilon}(i, j, k) = & \left[\bar{\epsilon}_x(i - \frac{1}{2}, j, k) + \bar{\epsilon}_x(i + \frac{1}{2}, j, k) + \bar{\epsilon}_y(i, j - \frac{1}{2}, k) \right. \\ & \left. + \bar{\epsilon}_y(i, j + \frac{1}{2}, k) + \bar{\epsilon}_z(i, j, k - \frac{1}{2}) + \bar{\epsilon}_z(i, j, k + \frac{1}{2}) \right] / 6.\end{aligned}\quad (3.87)$$

In order to achieve the unique solution, the boundary conditions are required. Adopting the technique we used when deriving the discretized boundary conditions in the 2-D DD-SCLC, we have the complete set of electrode- and insulating- conditions for both top ($k = N_z$) and bottom ($k = 0$) boundary as follow.

$$\psi(i, j, N_z) = \begin{cases} V_a/V_t & \text{for } (i, j) \in \mathcal{D}_{tip} \\ \psi(i, j, N_z + 1) & \text{for } (i, j) \notin \mathcal{D}_{tip} \end{cases} \quad (3.88a)$$

$$\psi(i, j, 0) = 0 \quad \text{for } i = \{0, 1, 2, \dots, N_x\}, j = \{0, 1, 2, \dots, N_y\} \quad (3.88b)$$

Four side boundaries of the system satisfy the periodic boundary condition, such that

$$\psi(0, j, k) = \psi(N_x, j, k) \quad \text{for } j = \{0, 1, 2, \dots, N_y\}, k = \{0, 1, 2, \dots, N_z\} \quad (3.89a)$$

$$\psi(i, 0, k) = \psi(i, N_y, k) \quad \text{for } i = \{0, 1, 2, \dots, N_x\}, k = \{0, 1, 2, \dots, N_z\} \quad (3.89b)$$

By substituting these boundary conditions into the discretized Poisson's equation (3.86), we have the system of linear equations in matrix and vector notation (3.48); where vector

\vec{b} reflects the disordered properties of the material in terms of trapped hole density, while matrix \mathbb{A} carries the morphological effect of the spatially varying dielectric constant. To find the numerical solution of potential ($\vec{\psi}$), we carried out the iterative calculation using the BiCGSTAB module.

3.5.3 Hole Density Solver

By pursuing the Schafetter-Gummel approach [54], hole current densities at the mesh mid-points in the three-dimensional Cartesian coordinate system are expressed as

$$\begin{aligned}
J_{p,x}(i \pm \frac{1}{2}, j, k) &= \mu_{p,x}(i \pm \frac{1}{2}, j, k) \cdot \frac{qV_t N_v}{h} \left\{ \mathcal{B}[\psi(i \pm 1, j, k) - \psi(i, j, k)] \cdot p_f(i, j, k) \right. \\
&\quad \left. \mp \mathcal{B}[\psi(i, j, k) - \psi(i \pm 1, j, k)] \cdot p_f(i \pm 1, j, k) \right\} \\
&\equiv \mu_{p,x}(i \pm \frac{1}{2}, j, k) \cdot \mathcal{J}_{p,x}(i \pm \frac{1}{2}, j, k) \tag{3.90a}
\end{aligned}$$

$$\begin{aligned}
J_{p,y}(i, j \pm \frac{1}{2}, k) &= \mu_{p,y}(i, j \pm \frac{1}{2}, k) \cdot \frac{qV_t N_v}{h} \left\{ \mathcal{B}[\psi(i, j \pm 1, k) - \psi(i, j, k)] \cdot p_f(i, j, k) \right. \\
&\quad \left. \mp \mathcal{B}[\psi(i, j, k) - \psi(i, j \pm 1, k)] \cdot p_f(i, j \pm 1, k) \right\} \\
&\equiv \mu_{p,y}(i, j \pm \frac{1}{2}, k) \cdot \mathcal{J}_{p,y}(i, j \pm \frac{1}{2}, k) \tag{3.90b}
\end{aligned}$$

$$\begin{aligned}
J_{p,z}(i, k \pm \frac{1}{2}) &= \frac{q\mu_{p,z}(i, j, k \pm \frac{1}{2})V_t N_v}{h} \left\{ \mathcal{B}[\psi(i, j, k \pm 1) - \psi(i, j, k)] \cdot p_f(i, j, k) \right. \\
&\quad \left. \mp \mathcal{B}[\psi(i, j, k) - \psi(i, j, k \pm 1)] \cdot p_f(i, j, k \pm 1) \right\} \\
&\equiv \mu_{p,z}(i, j, k \pm \frac{1}{2}) \cdot \mathcal{J}_{p,z}(i, j, k \pm \frac{1}{2}) \tag{3.90c}
\end{aligned}$$

where \mathcal{B} is the Bernoulli function. Similar to the numerical method for Poisson's equation, the flux of hole current density is calculated on the chosen Gaussian surfaces. We obtain

$$\begin{aligned}
\left[\oint_{S_G} \vec{J}_p \cdot d\vec{A} \right]_{i,j,k} &= - \iint_{S_G(i-\frac{1}{2})} \mu_{p,x} dydz \cdot \mathcal{J}_{p,x}(i-\frac{1}{2}, j, k) + \iint_{S_G(i+\frac{1}{2})} \mu_{p,x} dydz \cdot \mathcal{J}_{p,x}(i+\frac{1}{2}, j, k) \\
&\quad - \iint_{S_G(j-\frac{1}{2})} \mu_{p,y} dx dz \cdot \mathcal{J}_{p,y}(i, j-\frac{1}{2}, k) + \iint_{S_G(j+\frac{1}{2})} \mu_{p,y} dx dz \cdot \mathcal{J}_{p,y}(i, j+\frac{1}{2}, k) \\
&\quad - \iint_{S_G(k-\frac{1}{2})} \mu_{p,z} dx dy \cdot \mathcal{J}_{p,z}(i, j, k-\frac{1}{2}) + \iint_{S_G(k+\frac{1}{2})} \mu_{p,z} dx dy \cdot \mathcal{J}_{p,z}(i, j, k+\frac{1}{2}) \\
&= \left[-\bar{\mu}_{p,x}(i-\frac{1}{2}, j, k) \cdot \mathcal{J}_{p,x}(i-1, j, k) + \bar{\mu}_{p,x}(i+\frac{1}{2}, j, k) \cdot \mathcal{J}_{p,x}(i+1, j, k) \right. \\
&\quad - \bar{\mu}_{p,y}(i, j-\frac{1}{2}, k) \cdot \mathcal{J}_{p,y}(i, j-1, k) + \bar{\mu}_{p,y}(i, j+\frac{1}{2}, k) \cdot \mathcal{J}_{p,y}(i, j+1, k) \\
&\quad \left. - \bar{\mu}_{p,z}(i, j, k-\frac{1}{2}) \cdot \mathcal{J}_{p,z}(i, j, k-1) + \bar{\mu}_{p,z}(i, j, k+\frac{1}{2}) \cdot \mathcal{J}_{p,z}(i, j, k+1) \right] h^2 \\
&\equiv 0
\end{aligned} \tag{3.91}$$

where the locally-averaged hole mobilities over the Gaussian surface are written as,

$$\begin{aligned}
\bar{\mu}_{p,x}(i \pm \frac{1}{2}, j, k) &= \left[\mu_{p,x}(i \pm \frac{1}{2}, j - \frac{1}{2}, k - \frac{1}{2}) + \mu_{p,x}(i \pm \frac{1}{2}, j + \frac{1}{2}, k - \frac{1}{2}) \right. \\
&\quad \left. + \mu_{p,x}(i \pm \frac{1}{2}, j - \frac{1}{2}, k + \frac{1}{2}) + \mu_{p,x}(i \pm \frac{1}{2}, j + \frac{1}{2}, k + \frac{1}{2}) \right] / 4
\end{aligned} \tag{3.92a}$$

$$\begin{aligned}
\bar{\mu}_{p,y}(i, j \pm \frac{1}{2}, k) &= \left[\mu_{p,y}(i - \frac{1}{2}, j \pm \frac{1}{2}, k - \frac{1}{2}) + \mu_{p,y}(i + \frac{1}{2}, j \pm \frac{1}{2}, k - \frac{1}{2}) \right. \\
&\quad \left. + \mu_{p,y}(i - \frac{1}{2}, j \pm \frac{1}{2}, k + \frac{1}{2}) + \mu_{p,y}(i + \frac{1}{2}, j \pm \frac{1}{2}, k + \frac{1}{2}) \right] / 4
\end{aligned} \tag{3.92b}$$

$$\begin{aligned}
\bar{\mu}_{p,z}(i, j, k \pm \frac{1}{2}) &= \left[\mu_{p,z}(i - \frac{1}{2}, j - \frac{1}{2}, k \pm \frac{1}{2}) + \mu_{p,z}(i + \frac{1}{2}, j - \frac{1}{2}, k \pm \frac{1}{2}) \right. \\
&\quad \left. + \mu_{p,z}(i - \frac{1}{2}, j + \frac{1}{2}, k \pm \frac{1}{2}) + \mu_{p,z}(i + \frac{1}{2}, j + \frac{1}{2}, k \pm \frac{1}{2}) \right] / 4.
\end{aligned} \tag{3.92c}$$

This is similar to the locally-averaged dielectric constants, as in eq.(3.85), but not as simplified due to the fact that hole mobility is vector.

Substituting the discretized current density (3.90), we have the discretized continuity equation for the 3-D DD-SCLC model.

$$\begin{aligned}
& -\bar{\mu}_{p,x}(i - \frac{1}{2}, j, k) \cdot \left[\mathcal{B}(\Delta_x \psi(i, j, k)) \cdot p_f(i - 1, j, k) - \mathcal{B}(-\Delta_x \psi(i, j, k)) \cdot p_f(i, j, k) \right] \\
& + \bar{\mu}_{p,x}(i + \frac{1}{2}, j, k) \cdot \left[\mathcal{B}(\Delta_x \psi(i + 1, j, k)) \cdot p_f(i, j, k) - \mathcal{B}(-\Delta_x \psi(i + 1, j, k)) \cdot p_f(i + 1, j, k) \right] \\
& -\bar{\mu}_{p,y}(i, j - \frac{1}{2}, k) \cdot \left[\mathcal{B}(\Delta_y \psi(i, j, k)) \cdot p_f(i, j - 1, k) - \mathcal{B}(-\Delta_y \psi(i, j, k)) \cdot p_f(i, j, k) \right] \\
& + \bar{\mu}_{p,y}(i, j + \frac{1}{2}, k) \cdot \left[\mathcal{B}(\Delta_y \psi(i, j + 1, k)) \cdot p_f(i, j, k) - \mathcal{B}(-\Delta_y \psi(i, j + 1, k)) \cdot p_f(i, j + 1, k) \right] \\
& -\bar{\mu}_{p,z}(i, j, k - \frac{1}{2}) \cdot \left[\mathcal{B}(\Delta_z \psi(i, j, k)) \cdot p_f(i, j, k - 1) - \mathcal{B}(-\Delta_z \psi(i, j, k)) \cdot p_f(i, j, k) \right] \\
& + \bar{\mu}_{p,z}(i, j, k + \frac{1}{2}) \cdot \left[\mathcal{B}(\Delta_z \psi(i, j, k + 1)) \cdot p_f(i, j, k) - \mathcal{B}(-\Delta_z \psi(i, j, k + 1)) \cdot p_f(i, j, k + 1) \right] \\
& = 0 \quad (3.93)
\end{aligned}$$

where the spatial difference of electric potential is calculated as follows

$$\Delta_x \psi(i, j, k) = \psi(i, j, k) - \psi(i - 1, j, k) \quad (3.94a)$$

$$\Delta_y \psi(i, j, k) = \psi(i, j, k) - \psi(i, j - 1, k) \quad (3.94b)$$

$$\Delta_z \psi(i, j, k) = \psi(i, j, k) - \psi(i, j, k - 1) \quad (3.94c)$$

Boundary conditions are needed to find the unique solutions of free hole densities. For the hole density solver of the 3-D DD-SCLC model, the complete set of electrode- and insulating-

conditions for the top ($k = N_z$) and bottom ($k = 0$) boundaries are discretized as follow

$$p_f(i, j, N_z) = \begin{cases} 1 & \text{for } (i, j) \in \mathcal{D}_{tip} \\ p_f(i, j, N_z + 1) & \text{for } (i, j) \notin \mathcal{D}_{tip} \end{cases} \quad (3.95a)$$

$$p_f(i, j, 0) = 1 \quad \text{for } i = \{0, 1, 2, \dots, N_x\}, j = \{0, 1, 2, \dots, N_y\} \quad (3.95b)$$

where \mathcal{D}_{tip} is the two-dimensional domain of the tip contact. Note that the top boundary not corresponding to the tip contact is treated with the insulating boundary conditions, following the numerical approach previously used in the 2-D DD-SCLC model. Lastly, Four boundaries on the sides, *i.e.*, $S(i = 0)$, $S(i = N_x)$, $S(j = 0)$ and $S(j = N_y)$, satisfy the periodic boundary conditions, such that

$$p_f(0, j, k) = p_f(N_x, j, k) \quad (3.96a)$$

$$p_f(i, 0, k) = p_f(i, N_y, k) \quad (3.96b)$$

Following similar mathematics to that used for the potential solver, the combination of the boundary conditions (3.95)-(3.96) and the continuity equation (3.93) results in an asymmetric system of linear equations, which can be rewritten in the simple matrix form (3.53). While vector $\vec{\mathbf{b}}$ contains the boundary conditions, matrix \mathbb{A} captures the morphological effect in terms of the spatially-varying hole mobility. The numerical solutions for $\vec{\mathbf{p}}_f$ are achieved by the iterative method BiCGSTAB [68].

3.5.4 Verification

We have developed a Fortran 90 program to simulate current-voltage characteristics of the fully three-dimensional model in a Cartesian coordinate system by following the algorithm shown in figure 3.3. Due to the similar mathematical structure, the BiCGSTAB module previously used in the 2-D DD-SCLC model is implemented to handle both the potential and hole density solvers. As a standard protocol, all parameters and variables are represented by double precision values in the program, in order to minimize the error arisen from the iterative method used in the numerical calculations. To verify the 3-D DD-SCLC model, we carried out the numerical calculations of two limited cases that have been studied before using the 1-D and 2-D DD-SCLC models.

First, we would like to verify the 3-D DD-SCLC model by reproducing the results of the homogeneous planar devices. Consider the trap-free hole-only device of $600nm \times 600nm$ cross-sectional area and $80nm$ thickness. To resemble the planar geometry of the 1-D DD-SCLC model, the tip contact area is extended to the size of device's cross-section. Figure 3.20 shows the comparison of current-voltage characteristics of a trap-free hole-only device simulated from 1-D and 3-D DD-SCLC models. It is clear that the numerical results from the two different models are identical.

Secondly, we would like to include the 2-D DD-SCLC model in this part of verification and consider the device simulations in the tip-plane geometry. As schematically shown in figure 3.21, we portrait two possible tip designs to be constructed on the $2nm \times 2nm$ square grid of the 3-D DD-SCLC model, including (a) a circular contact of $6nm$ radius and (b) a square contact of $10nm$ side length, which are chosen to be roughly consistent with a circular tip used in the 2-D DD-SCLC model, as depicted by the red circle of $6nm$ radius.

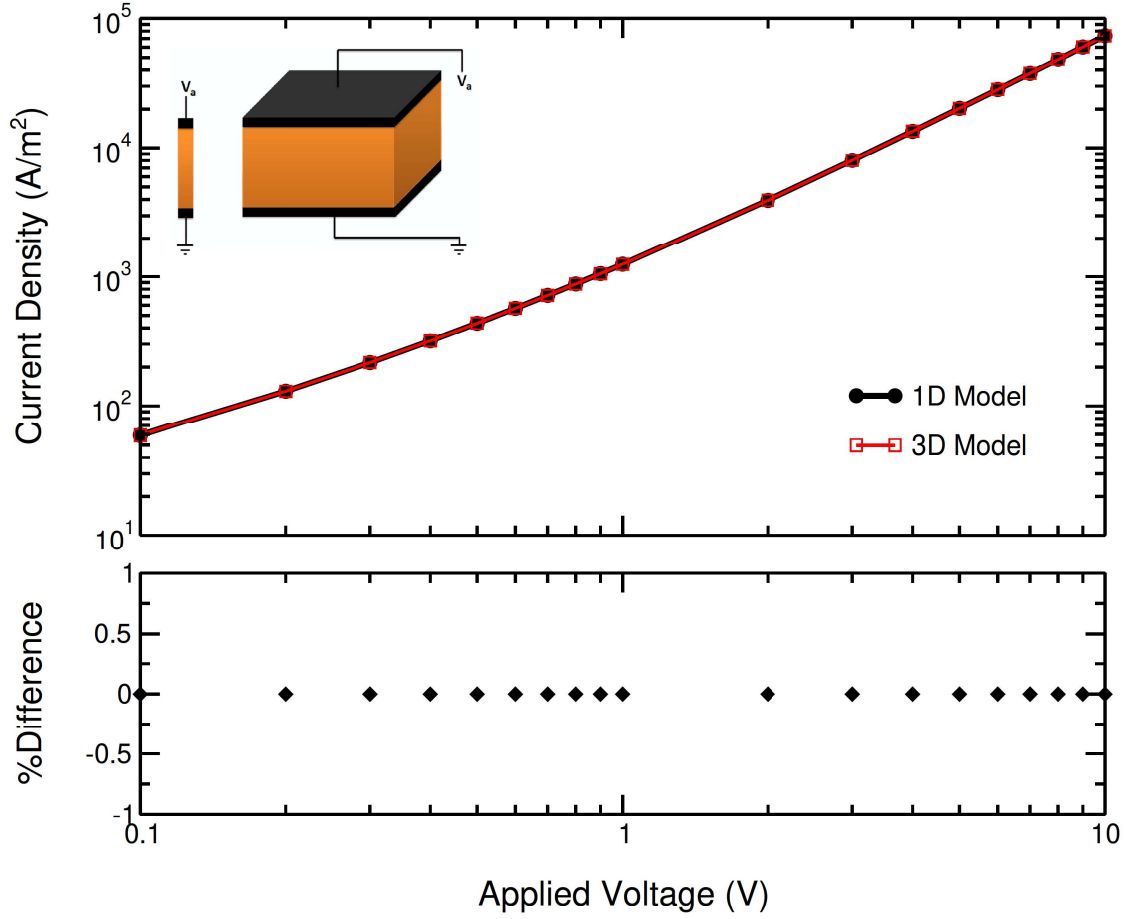


Figure 3.20: The comparison of the theoretical current-voltage characteristics of trap-free ($f_t = 0$) hole-only devices calculated from 1-D and 3-D DD-SCLC models. In both models, the transport layer (orange) is homogeneous with the constant parameters: $\epsilon_r = 3$, $\mu_p = 10^{-4} \text{cm}^2 \text{V}^{-1} \text{s}^{-1}$, and $N_v = 1.25 \times 10^{21} \text{cm}^{-3}$.

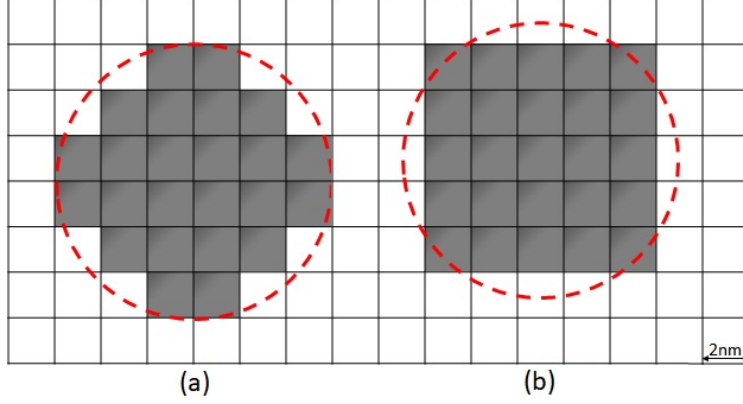


Figure 3.21: The schematic representation of tip contacts in a 3-D DD-SCLC model, constructed on the $2nm \times 2nm$ square grid as (a) an approximately circular geometry of $6nm$ radius and (b) a square geometry of $10nm$ side-length. In a 2-D DD-SCLC model, the tip contact is assigned as the circular area of $6nm$ radius (red dashed circle). Due to the difference in the discretization, the tip models in the 3-D model are slightly smaller than in the 2-D model, such that $A_{3-D(a)}/A_{2-D} = 0.85$ and $A_{3-D(b)}/A_{2-D} = 0.88$, respectively.

We then carried out the numerical calculations to simulate charge transport in the trap-free hole-only devices. In figure 3.22-3.23, the current-voltage characteristics simulated from the 3-D DD-SCLC model are compared with those simulated from the 2-D DD-SCLC model. In the models of the inset, the calculation domain is considered as a circular cylinder of $300nm$ radius and $80nm$ thickness for the 2-D DD-SCLC model, and as a rectangular prism of $300nm \times 300nm$ cross-sectional area and $80nm$ thickness for the 3-D DD-SCLC model.

As illustrated in figure 3.22-3.23, we observe a good agreement of the current-voltage characteristics of hole-only devices calculated from the two models. In the case of the round tip model, as shown in figure 3.22, the maximum of approximately 16% difference is expected, and can be explained by the slightly different contact area caused by the limitation of discretization in the cylindrical and Cartesian coordinate systems. However, we can narrow down these differences in the numerical solutions between the two models by using the square tip contact, as shown in figure 3.23.

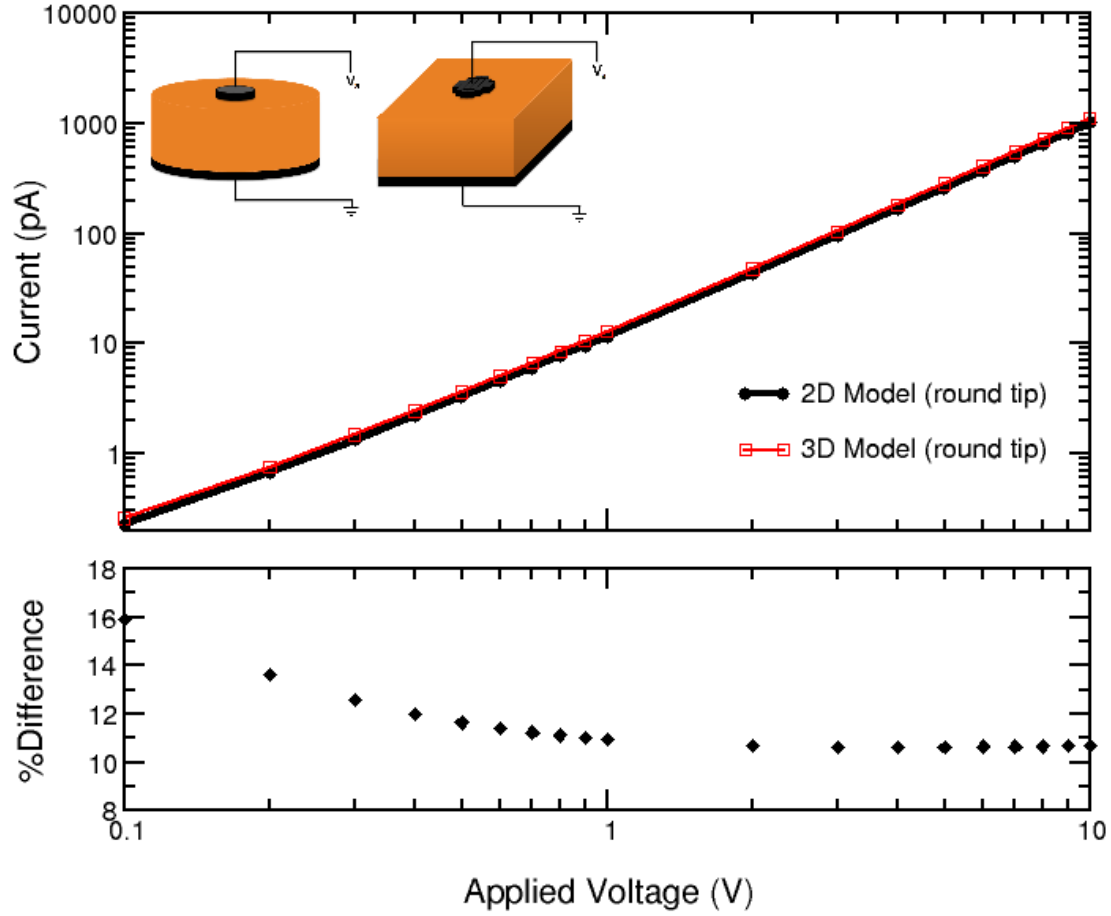


Figure 3.22: The comparison of the theoretical current-voltage characteristics of the trap-free ($f_t = 0$) hole-only devices calculated from 2-D and 3-D DD-SCLC models, in which the tip electrode is approximated by a circular contact of $6nm$ radius, as illustrated in figure 3.21(a). In both models, the transport layer (orange) is homogeneous with the constant parameters: $\epsilon_r = 3$, $\mu_p = 10^{-4}cm^2V^{-1}s^{-1}$, and $N_v = 1.25 \times 10^{21}cm^{-3}$.

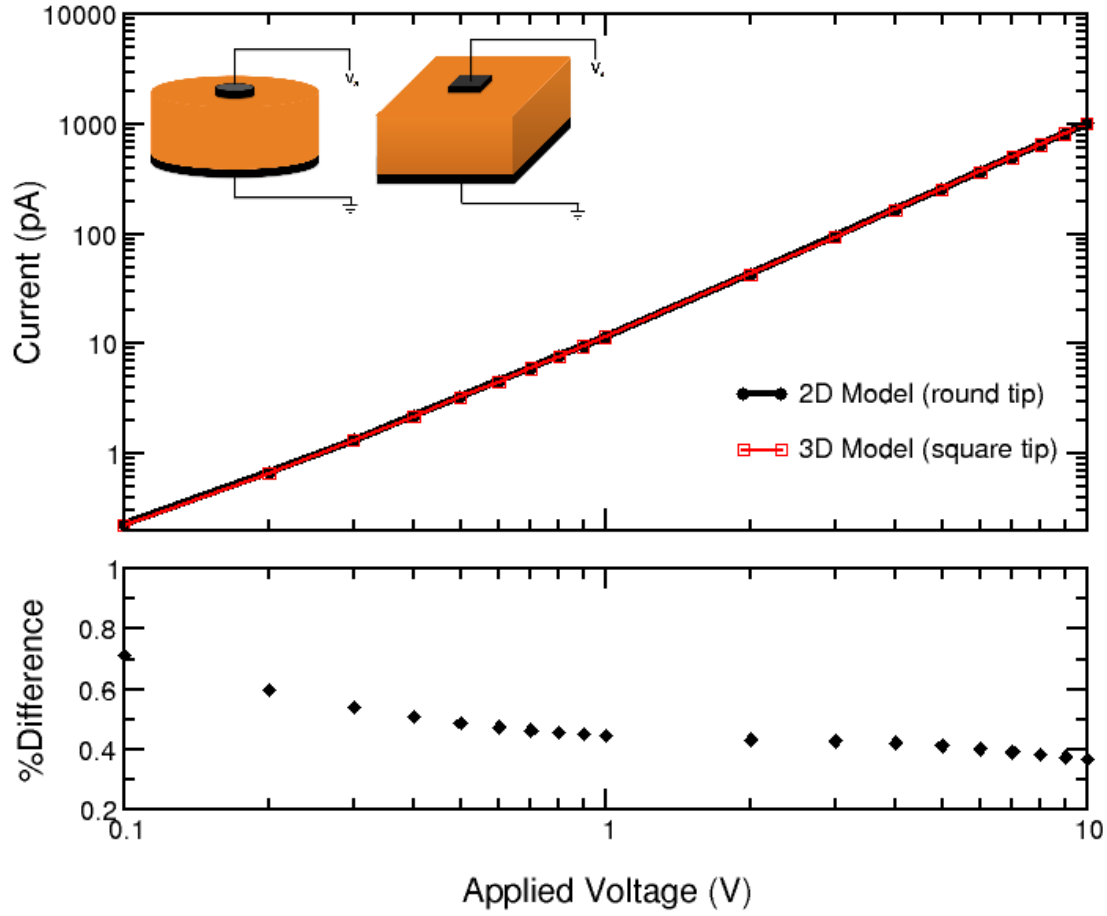


Figure 3.23: The comparison of the theoretical current-voltage characteristics of the trap-free ($f_t = 0$) hole-only devices calculated from 2-D and 3-D DD-SCLC models, in which the tip electrode is approximated by a circular contact of $6nm$ radius and a square contact of $10nm$ side length, respectively. (See figure 3.21(b)) In both models, the transport layer (orange) is homogeneous with the constant parameters: $\epsilon_r = 3$, $\mu_p = 10^{-4}cm^2V^{-1}s^{-1}$, and $N_v = 1.25 \times 10^{21}cm^{-3}$.

3.6 Conclusions

In this chapter the DD-SCLC model for hole injection systems was introduced. At the center of the model are three governing equations including Poisson's equation, the continuity equation at steady state, and the drift-diffusion equation for holes. Adopting the numerical technique presented by Koster *et al.* [52], all governing equations are solved simultaneously using a self-consistent scheme. We have developed the numerical tools written in Fortran 90 to carry out the numerical calculations for one-, two- and three- dimensional DD-SCLC models, which provide the insight to charge transport of hole-only devices with different geometries.

- The one-dimensional (1-D) DD-SCLC model is the simplest one among the three models, yet very essential. The numerical calculations are performed in a one-dimensional Cartesian coordinate system, and capable to simulate both drift and diffusion currents in homogeneous planar devices, in which traps are assumed to be uniformly distributed, with dielectric constant and hole mobility being constant. According to this description, the one-dimensional model improves the simplified SCLC model by just including the effect of charge diffusion. We have shown that a $\text{Log } J - \text{Log } V$ plot simulated from our model exhibits slope 2 in the drift-dominated regime ($V_a > 10V$). This is the signature of *Mott-Gurney* equation, validating our DD-SCLC model.
- The two-dimensional (2-D) DD-SCLC model is constructed in the cylindrical coordinate system with the cylindrical symmetry. The model is very efficient to study SCLC in tip-plane geometry with mobility anisotropy.
- The fully three-dimensional (3-D) DD-SCLC model is a big leap forward in the simu-

lation of SCLC. The numerical calculations are carried out using a three-dimensional Cartesian coordinate system, enabling the treatment of inhomogeneous systems, including the tip-plane electrode configuration, spatially-varying trap distributions, and nanoscale morphologies. However, the simulation is highly demanding in both computing time and memory.

Chapter 4

The Drift-Diffusion SCLC Transport

Models - New Results

In this chapter, we present theoretical studies of hole-only devices, including charge diffusion, traps, and nanoscale morphologies; in both planar and tip-plane (c-AFM) geometries. Examples of the applications of the *drift-diffusion* (DD) SCLC model will be carried out using the numerical tools we successfully developed for the one-, two- and three- dimensional DD-SCLC models described in the previous chapter. The parameters used in the device simulations are summarized in Table 4.1. Note that these values are the typical material and device parameters, which should be useful to capture the general physics of organic semiconductor devices. Our theoretical models do not limit to this particular system. In the next chapter, these methods and insights will be applied to an analysis of c-AFM experimental data provided by Dr. Pengpeng Zhang's group at Michigan State University.

4.1 Diffusion Effects

In chapter 2, we presented the simplified SCLC model for hole injection and transport problems in the conventional planar geometry. The exact analytical solution including the current-voltage characteristic, as known as the Mott-Gurney equation, and other physical

Table 4.1: Summary of parameters used in the device simulations

Parameter	Symbol	Numerical value
Dielectric constant	ε_r	3.0
The effective density of states in the HOMO ^a	N_v	$1.25 \times 10^{21} \text{ cm}^{-3}$
The effective hole mobility in the vertical direction	μ_o	$1.0 \times 10^{-4} \text{ cm}^2/Vs$
Temperature	T	300 K
Device thickness	L, L_z	80 nm
2-D DD-SCLC model :		
Circular tip contact radius ^b	R_{tip}	2 nm
Circular device radius ^c	R	300 nm for the isotropic transport 750 nm for the anisotropic transport
3-D DD-SCLC model :		
Square tip contact side length ^d	L_{tip}	5 nm
Square device cross-section side length ^e	L_x, L_y	600 nm for the isotropic transport 1500 nm for the anisotropic transport

^aThe number of N_v is determined from the regime where the current density is saturated over the value of N_v , as shown in figure 3.7.

^bFor the 2-D model, the computing domain is uniformly discretized with the 2nm mesh interval. Therefore, we choose the smallest tip size allowed by the discretization process to maximize the concentration of the electric field around the tip, and pronouncing the effect of lateral spreading.

^cThe circular device radius is determined from the regime where the current density is saturated over the value of R/L , as shown in figure 3.14-3.15 for the case of isotropic- and anisotropic- hole mobility respectively.

^dFor the 3-D model, the computing domain is uniformly discretized with the 5nm mesh interval. Same as b , we choose the smallest tip size allowed by the discretization process.

^eSame as c .

variables (such as electric potential, hole carrier density, *etc.*) are summarized in table 2.1. In figure 4.2, we plot the analytical profiles of the electric potential and hole carrier density in order to illustrate the characteristics of this hole-only SCLC transport model. For simplicity, the variables are plotted in their natural scales, such that the potential is scaled by the externally applied voltage V_a , the hole density is scaled by its spatial average \bar{p} (from table 2.1), and the internal device coordinate is scaled by the device thickness L .

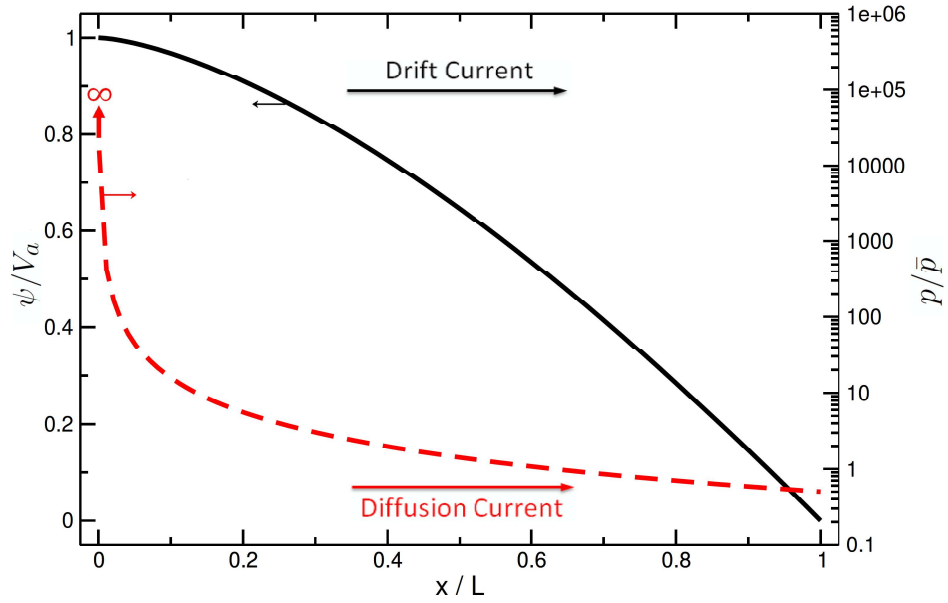


Figure 4.1: Based on the simplified SCLC model of a trap-free hole-only device in the planar geometry, the analytical profiles of electric potential (solid black line) and hole carrier density (dashed red line) are demonstrated using non-dimensional scales.

Although charge diffusion is omitted from the simplified SCLC model, the exact solution of hole charge carrier density exhibits a non-uniform distribution through the device thickness. When a gradient of charge carrier density exists, a process of diffusion occurs such that the charge carriers migrate from the regions of high density toward regions of low density. Assuming that the hole diffusion coefficient obeys the Einstein relation, the corresponding

hole diffusion current in the absence of traps is given by

$$J_{p,di} = \frac{3}{8} \epsilon \mu_p \frac{V_t V_a}{L^3} \left(\frac{x}{L} \right)^{-3/2} \quad (4.1)$$

Both drift and diffusion current densities are dependent on the externally applied voltage V_a , such that $J_{p,dr} \propto V_a^2$ and $J_{p,di} \propto V_a$, respectively. Since the drift current density increases quadratically with the applied voltage while the diffusion current density increases only linearly, the drift current density will dominate in the high voltage regime where the diffusion process is negligible.

Furthermore, per eq.(4.1), the diffusion current density is also non-uniform through the device thickness. It is infinite at the injecting electrode ($x = 0$), then dramatically declines, and gradually saturates toward the extracting electrode ($x = L$). This behavior explains one considerable discrepancy of the simplified SCLC model on the boundary condition at the injecting electrode. The model assumes the injecting contact to be ohmic, whence the local electric field $\mathcal{E} = 0$ and consequently the drift current vanishes. Therefore, the model clearly requires an additional form of charge transport to account for hole injection at the electrode. That is where the diffusion current comes into play, which is basically infinite at the ohmic contact of an infinite hole reservoir. In order to evaluate how significant the diffusion effect is compared to the drift effect in the model, figure 4.2 shows the plot of the current density ratio $J_{p,di}/J_{p,dr}$ versus the dimensionless coordinate along the direction of device thickness x/L . It is convenient to introduce the *characteristic coordinate* x_c as the location where the current density ratio is unity. The characteristic coordinate is given by

$$x_c = L \left(\frac{3V_a}{V_t} \right)^{-2/3} \quad (4.2)$$

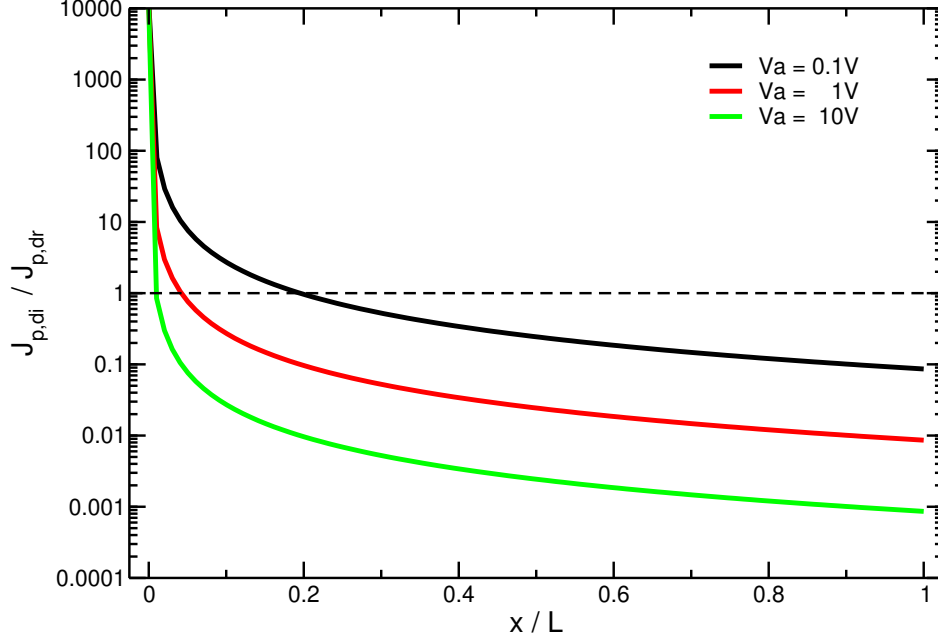


Figure 4.2: Plot of the analytical ratio of diffusion current density to drift current density of a planar flow, trap-free, hole-only device, $J_{p,di}/J_{p,dr}$, versus the dimensionless coordinate, x/L . While the drift current density is the immediate analytic solution of the simplified SCLC model as known as Mott-Gurney equation (2.13), the diffusion current density is obtained from the further derivation of the analytic solutions of the model. The extremely large value of diffusion current near the injecting electrode ($x = 0$) suggests the diffusion assists hole injection at the injecting contact.

In the region near x_c , diffusion and drift current densities are of the same order of magnitude. The diffusion current density then become dominant toward the injecting electrode ($x < x_c$). However, the dominance of charge diffusion diminishes with the increasing of the applied voltage. When the applied voltage is sufficiently high, the hole injection system is then well described by drift transport mechanism alone.

It is important to note that, by including the approximate diffusion current density expressed in equation (4.1) to the total current density, the continuity equation at steady state is indeed violated and total current is no longer conserved. This is expected since the diffusive transport is not initially considered in the simplified SCLC model. The drift current may dominate over the diffusion current if the externally applied voltage is sufficiently high,

but it is not thoroughly understood whether the diffusion current can be ignored or not in the intermediate range of applied voltage. Therefore, even where such analytical solutions are available, it is still useful to contemplate the full SCLC model that incorporates both drift and diffusion transport mechanisms, the so-called standard drift-diffusion model. Then the effect of diffusion process can be studied by solving the drift-diffusion equation coupled with Poisson's equation under the conservation law of current density described by continuity equation at steady state.

Now that we have developed a computer program that solves the three governing equations numerically in a self-consistent manner, it is instructive to first compare the theoretical profiles of electric potential and hole carrier density simulated from numerical calculation to that derived from the simplified SCLC model, previously demonstrated in figure 4.1. Using the parameters given in table 4.1, the simulations of hole-only devices with two distinct geometries; planar (plane-parallel) and tip-plane (c-AFM) geometries, will be investigated in detail in the following subsections. In order to focus solely on the influence of charge diffusion, the charge transport layer is assumed to be homogeneous and trap free, similar to that of the simplified SCLC model.

4.1.1 Planar Geometry

To begin with, let us examine the conventional case of planar hole-only device. The theoretical profiles of electric potential and hole carrier density as a function of the distance from the injecting electrode with the varying applied voltage ($V_a = 0.1, 1, 10V$) are shown in figure 4.3, which have all been generated by a 1-D DD-SCLC model of a hole-only device described in section 3.3. The numerical simulation includes both drift and diffusion transport mechanisms, resulting in the non-monotonic distributions of electric potential and

hole carrier density. Together, the theoretical profile can be categorized into three distinct regimes separated by two local transitions of charge-transport behaviors. The first transition is determined by the position of a potential maximum where electric field and drift current vanish. The second transition is located at the position of a hole density minimum where diffusion current becomes zero. Since the calculations are performed on the device at steady state, the total current which is the sum of drift and diffusion currents is conserved. By keeping this fact in mind, we will be able to understand the charge-transport mechanism in each regime qualitatively.

In the transport regime (I), space charges are built up near the injecting electrode ($x = 0$), resulting in a potential barrier. By overcoming the reverse drift current, the charge diffusion therefore is the dominant transport mechanism driving holes away from the injecting contact into the device. After passing the potential barrier and entering into regime (II), holes then travel forward driven by both drift and diffusion mechanisms. Finally, in regime (III), the diffusion current is reversed, counteracting the drift current, and leading to the reduction of the drift current toward the collecting electrode at $x = 80nm$. This is due to the ohmic nature of the extracting contact.

When quantitatively comparing the theoretical profile simulated from our 1-D DD-SCLC model (figure 4.3) to the analytical profile derived from the simplified SCLC model (figure 4.1), we observe subtle differences in the applied voltage dependence of the distribution. In the simplified SCLC model, the electric potential and hole carrier density have monotonic distribution along the device thickness, while the 1-D DD-SCLC model yields a more complicated result consisting of three distinct regimes. A similar observation has been described in the past by A.A. Grinberg and S. Luryi, particularly for the case of double junction (p-i-p) diode [69]. The idea can be extended to the case of hole-only devices by introducing

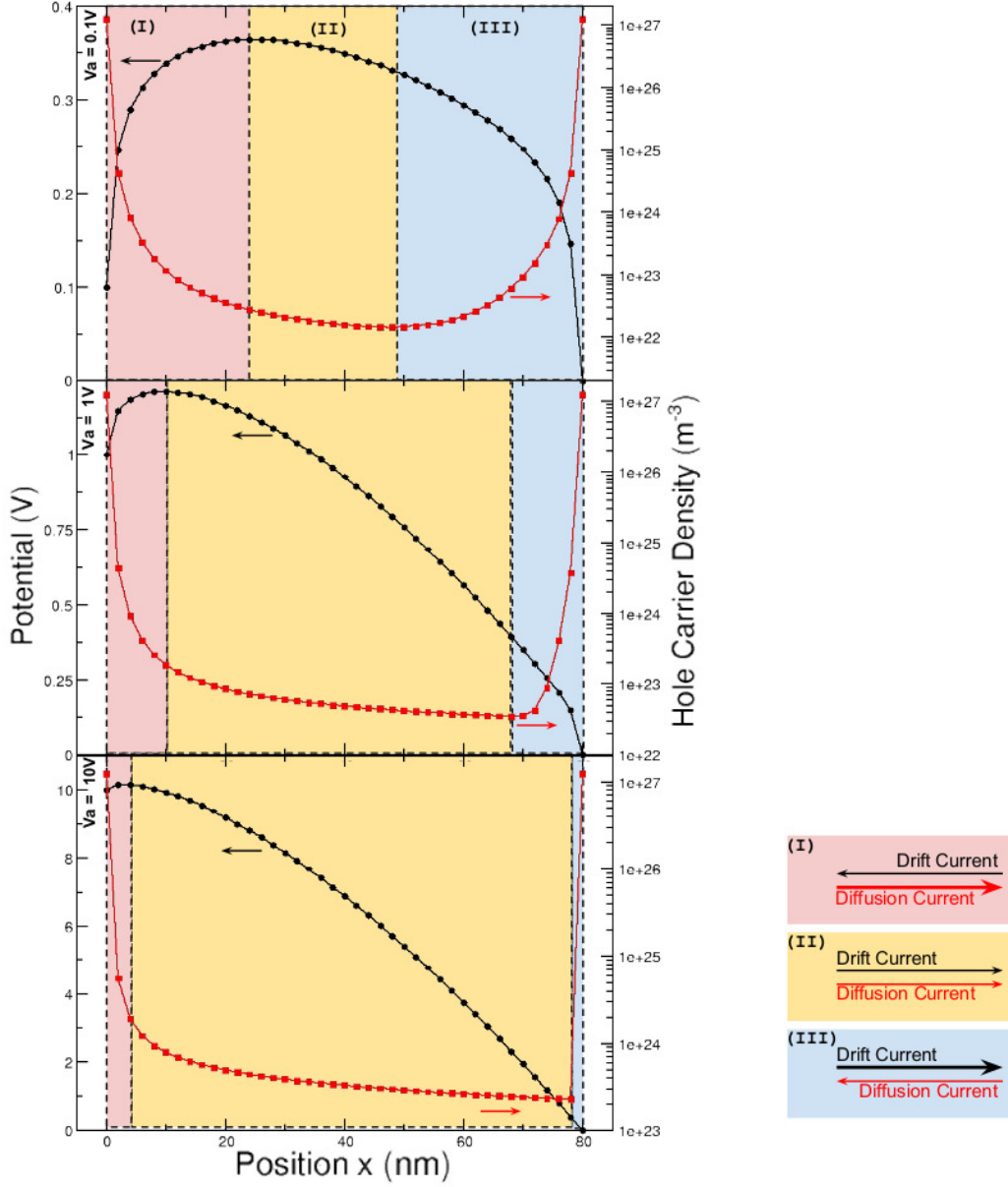


Figure 4.3: The theoretical profile of electric potential and hole carrier density as a function of the distance from the injecting electrode for planar geometry, generated using the 1-D DD-SCLC model described in section 3.3, using parameters given in table 4.1. The profiles exhibit three distinct transport regimes, plotted for three different applied voltages $V_a = 0.1, 1, 10V$, from top to bottom.

a *virtual* anode and a *virtual* cathode, located at the position of zero drift current (zero electric field) and zero diffusion current, respectively. The two virtual electrodes essentially mark the separation of the transport regimes (I), (II), and (III) on the simulated profile. With the increasing of the applied voltage, the virtual electrodes move toward the *actual* (fixed) electrodes. This phenomenon is governed by the charge diffusion, which is a missing transport mechanism in the simplified SCLC model.

4.1.2 Tip-Plane Geometry

Apart from the conventional planar geometry, the effect of charge diffusion is further studied by modifying the injecting electrode into a circular conducting tip, similar to that of c-AFM measurement. Assuming that the transport layer is homogeneous with an isotropic hole mobility, the device will have a cylindrical symmetry around the injecting electrode. This makes it easy to simulate the tip-plane electrode configuration using the 2-D DD-SCLC model, as presented in section 3.4. Charge transport comprises of two components; the lateral transport along the radial direction (ρ) and the vertical transport along the thickness direction (z). The influence of charge diffusion on transport behavior of tip-plane electrode configuration can be observed along the thickness direction in the same manner as that of plane-parallel electrode configuration. By choosing the vertical path at the center of the circular tip/electrode ($\rho = 0$), the lateral transport vanishes and only the vertical transport remains. As the result, figure 4.4 shows the theoretical profile of electric potential and hole carrier density as a function of z with the varying applied voltage $V_a = 0.1, 1, 10V$, where z is the coordinate along the vertical axis from tip center pointing to planar electrode. By applying the concept of virtual electrodes, similar to that of planar geometry, the theoretical profile of the tip-plane geometry exhibits three transport regimes:

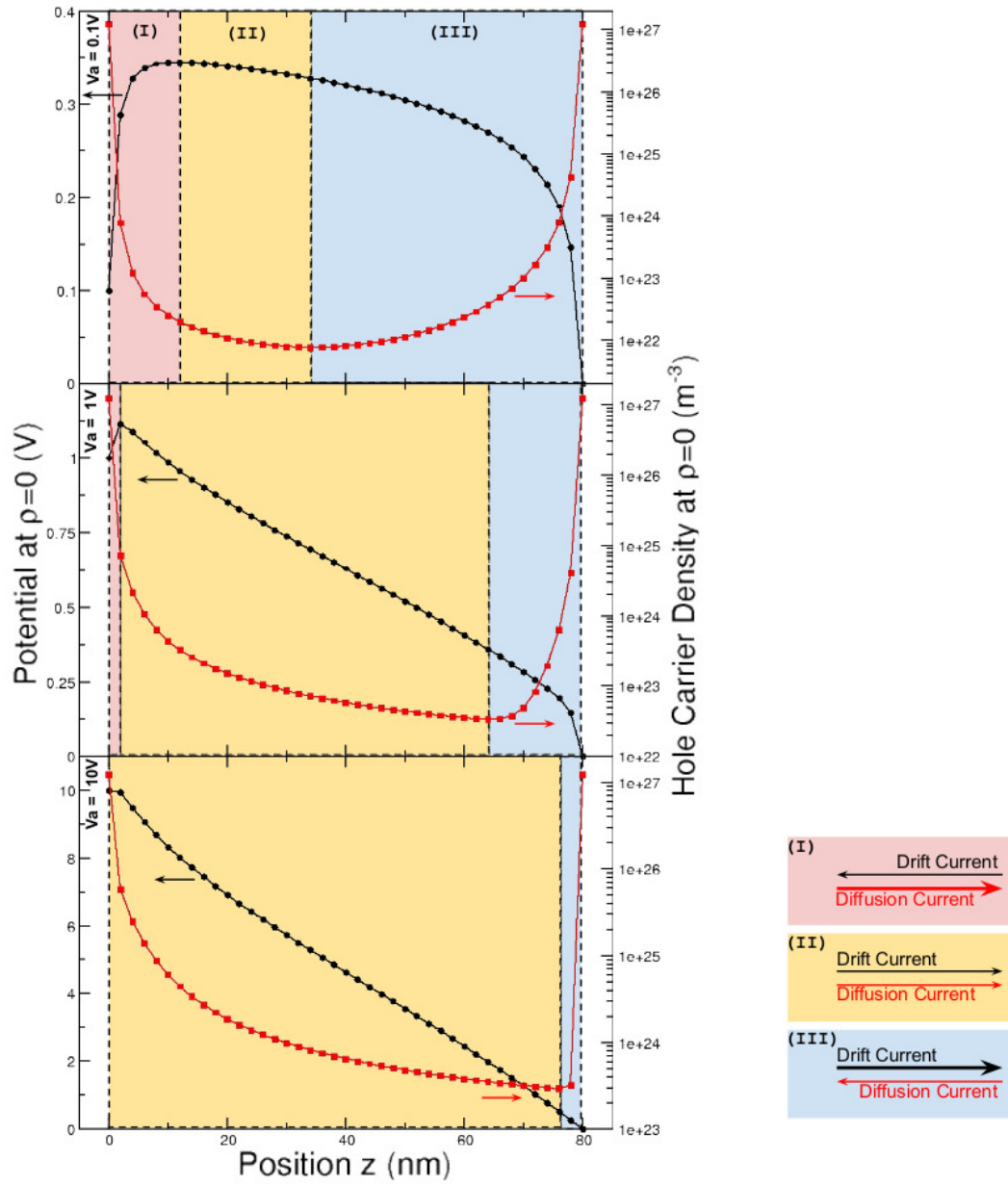


Figure 4.4: The theoretical profile of electric potential and hole carrier density at the center of a circular tip ($\rho = 0$) as a function of the distance from the injecting electrode for tip-plane geometry, generated by the 2-D DD-SCLC model described in section 3.4, using parameters given in table 4.1. The profiles exhibit three distinct transport regimes, plotted for three different applied voltages $V_a = 0.1, 1, 10$ V.

- regime (I) where the charge diffusion is the dominant form of charge transport, located between the actual anode ($z = 0$) and the virtual anode,
- regime(II) of the drift-diffusion assisted transport located between the virtual anode and the virtual cathode,
- regime (III) where drift becomes the dominant form of charge transport, located between the virtual cathode and the actual cathode ($z = L$).

Similarly to what has been observed in the study of planar geometry, the virtual electrodes of tip-plane geometry also move closer to the actual electrodes with the increasing of the externally applied voltage.

To illustrate the effect of the applied voltage on the movement of the virtual electrodes, we plot the displacement of virtual anode and virtual cathode as a function of applied voltage for both plane-parallel and tip-plane electrode configurations, as illustrated in figure 4.5. Due to the absence of intrinsic charge carriers and low carrier mobility in an organic semiconductor, without the external potential bias applied to the electrodes (the so-called *short-circuit* condition), there is no actual charge transport in the device. Although no current can be measured, theoretically we can demonstrate the non-uniform distribution of electric potential and charge carrier density. For the planar hole-only device, this is analogous to the case of a parallel plate capacitor filled with a dielectric, and the simulation yields a symmetric arrangement that both virtual electrodes are located at the same position half-way between the two actual electrodes. By applying the positive bias at the actual anode, holes are injected into the device, traveling through the transport layer via drift and diffusion mechanisms, and then extracted at the actual cathode. That is when the position of the virtual electrode starts shifting toward the actual one. In the situation of

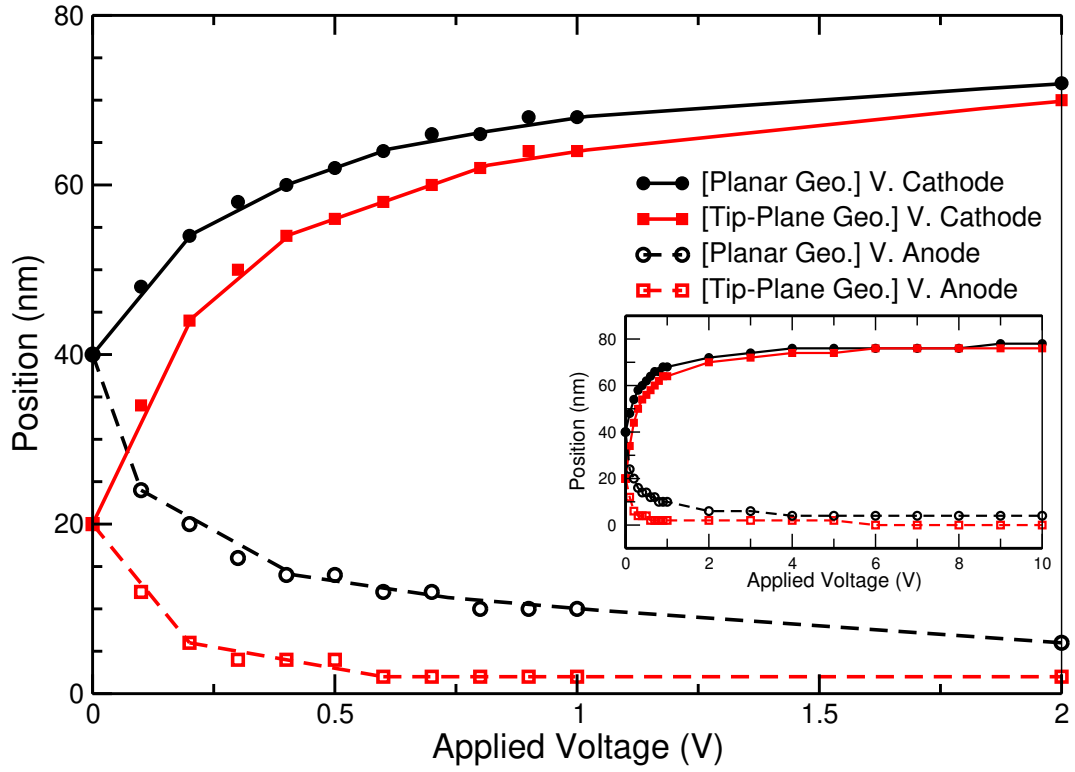


Figure 4.5: Position of virtual anode (dashed line) and virtual cathode (solid line) as a function of applied voltage for planar (black) and tip-plane (red) geometries, as seen in figure 4.3 and figure 4.4 respectively. The inset shows the convergence of the virtual tip position.

planar geometry, by increasing the applied voltage, the virtual electrodes move away from each other symmetrically. However, in the tip-plane electrode configuration, the symmetric behavior no longer holds. At the short-circuit condition, the virtual electrodes of the tip-plane geometry are located toward the injecting electrode, instead of the middle of the device thickness. This is due to an asymmetric pair of tip and plane electrodes and a lateral current spreading beneath the tip-like structure.

Although the concept of virtual electrodes is chosen for the explanation of charge transport involving the additional charge diffusion, it is not the new to the simplified SCLC model. But, per the chosen boundary conditions at the electrodes, the simplified SCLC model assumes that the virtual electrodes are fixed as the actual ones. The inset of figure 4.5 shows the convergence of the virtual electrodes' position with the externally applied voltage. When the virtual electrodes are co-located with the actual electrode, the influence of charge diffusion is negligible and the current-voltage characteristic of planar and tip-plane geometries are then well described by Mott-Gurney equation (2.13) and the semi-empirical formula (2.31) introduced by Ginger's group, respectively.

4.2 Trap Effects

Up to now, we have assumed that hole-only devices are free of traps. This situation typically does not exist since an organic semiconductor is commonly known for its energetic disorder. The topic of traps in organic semiconductors has been intensively studied by experiments on unipolar injection devices in planar geometry when either electrons or holes are injected into the devices. The corresponding current-voltage characteristics in the SCLC regime are then analyzed using the theory of trap-limited SCLC, as written in eq.(2.27). This is a variation

of the Mott-Gurney equation that has been developed to include trap effects. Therefore, the derivation leading to eq.(2.27) is based on two assumptions: (i) the electric field at the injecting electrode vanishes and (ii) the charge diffusion is negligible. These assumptions are only valid when the electric field across the device is sufficiently high. More importantly, traps often lead to the condition that diffusion current can no longer be neglected, which makes the drift-only transport model problematic. [45, 70, 71]

For a more accurate description of trap-limited SCLC, we developed the theoretical model described in chapter 3 that incorporates both drift and diffusion transport mechanisms. In the model, the energetically distributed traps are described by an exponential distribution within the band gap, characterized by trap density through the parameter $f_t = N_t/N_v$ and trap temperature through the parameter $r_t = T/T_t$, as expressed in eq.(3.4). With varying trap parameters (f_t, r_t) , the corresponding current-voltage characteristics will be analyzed in the SCLC regime. We carry out the numerical calculations in two different cases; planar and tip-electrode geometries, using parameters given in table 4.1. In this section, traps are assumed to be uniformly distributed throughout the device.

4.2.1 Planar Geometry

The effect of traps in the hole injection system can be studied by comparing the theoretical current-voltage characteristics simulated from the planar device with the presence of the exponentially distributed traps to that simulated from the trap-free planar device. As previously demonstrated in figure 3.8, the current-voltage characteristic of a trap-free hole injection device obeys the power law ($J \propto V^m$), showing the transition of charge transport behavior from the diffusion-influenced regime at low applied voltage ($m < 2$) to the drift-dominant regime at high applied voltage ($m = 2$). This characteristic slope of 2 is the key

aspect of trap-free SCLC in the drift-only transport model, as predicted by the well-known Mott-Gurney equation (2.13). Therefore, it shall be instructive to present and analyze the current-voltage characteristics of hole-only devices in the double logarithmic scale where the slope is the exponent m . We will mostly show the current-voltage characteristics in *log-log* representation from this point forward.

Figure 4.6 shows the theoretical current-voltage characteristic of a hole-only device with a low density of deep traps ($f_t = 0.005, r_t = 0.30$) generated by the 1-D DD-SCLC model (described in section 3.3). Unlike the trap-free current-voltage characteristic, one can distinguish three distinct regimes corresponding to Ohm's law ($m = 1$), trap limited SCLC ($m > 2$), and trap-filled SCLC ($m = 2$). In the absence of injection barriers, the number of holes injected into the device increases with an increase in the externally applied voltage. In the low voltage regime, the amount of injected holes is low, and become negligible compared to that of the intrinsic thermally activated holes. The electrical conduction in this regime is then due to the intrinsic charge carriers, and hence can be described by Ohm's law ($m = 1$). When increasing the applied voltage, the device accommodates an increasing number of hole carriers. The rapid growth of current with the small increment of applied voltage is caused by the flow of injected holes through the device. In an organic semiconductor device, this bulk transport is typically controlled by space charges. The intermediate voltage regime where the exponent $m > 2$ is uniquely related to the exponential distribution of traps within the band gap. When trap states are completely filled, the exponent then reduces to 2 as predicted by the Mott-Gurney equation for trap-free SCLC. Note that the theoretical current-voltage characteristic is plotted with the data of applied voltage up to 100V in order to observe all three key regimes. The working range of applied voltage for an organic semiconductor device is normally below 10V, which is large enough to observe the

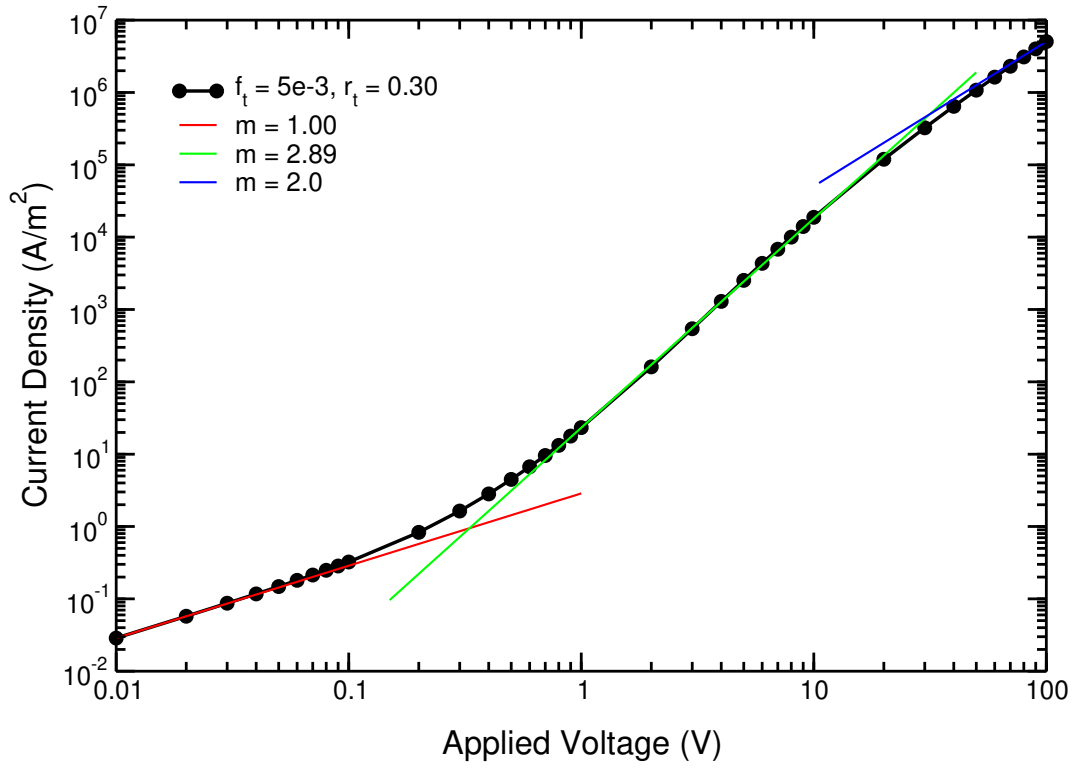


Figure 4.6: The trap influenced current-voltage characteristic of a hole-only device in planar geometry obeys the power law $J \propto V^m$, exhibiting three regimes: Ohm's law $m = 1$ (red), trap-limited SCLC $m > 2$ (green), and trap-filled SCLC $m = 2$ (blue).

trap filling regime.

In order to determine the dependence of current-voltage characteristics on traps, we performed a large number of device simulations over the wide range of trap parameters: $f_t = 0 - 0.05$ and $r_t = 0.20 - 0.40$. Examples of the theoretical current-voltage characteristics of hole-only devices in planar geometry are shown in figure 4.7 when (a) $f_t = 0.005$ with varying r_t , and (b) $r_t = 0.30$ with varying f_t . These data are plotted in the range of the intermediate applied voltage regime involving the trap filling process in SCL transport, and can be described by the semi-empirical expression

$$J(f_t, r_t) = \mu_o \cdot k_J(f_t, r_t) \cdot V^{m(f_t, r_t)} \quad (4.3)$$

with the fitting parameters k_J and m depending on trap parameters f_t and r_t . By using this expression to fit all simulated current-voltage characteristics, we obtain the database of fitting parameters k_J and m which lead to the understanding of how traps affect the current-voltage relations. This analysis is very challenging due to its nature of nonlinear regression and the large amount of data involved. Therefore, we have developed a program written in Python to carry out this extensive analysis. As a result, the fitting parameters are summarized in table A.1 of appendix A.

Although we cannot present the semi-empirical formula of the fitting parameters, we observe a monotonic dependence of the fitting exponent m on traps as illustrated by the contour plot in figure 4.8b. The exponent m varies from 1.89 to 5.00 corresponding to trap parameter variations over the ranges of $f_t = 0 - 0.05$ and $r_t = 0.20 - 0.40$. The contour plot demonstrates that there are many possible pairs of trap parameters $\{f_t, r_t\}$ along the contour line which can give the same slope of $\text{Log } J - \text{Log } V$ curve in the SCLC regime.

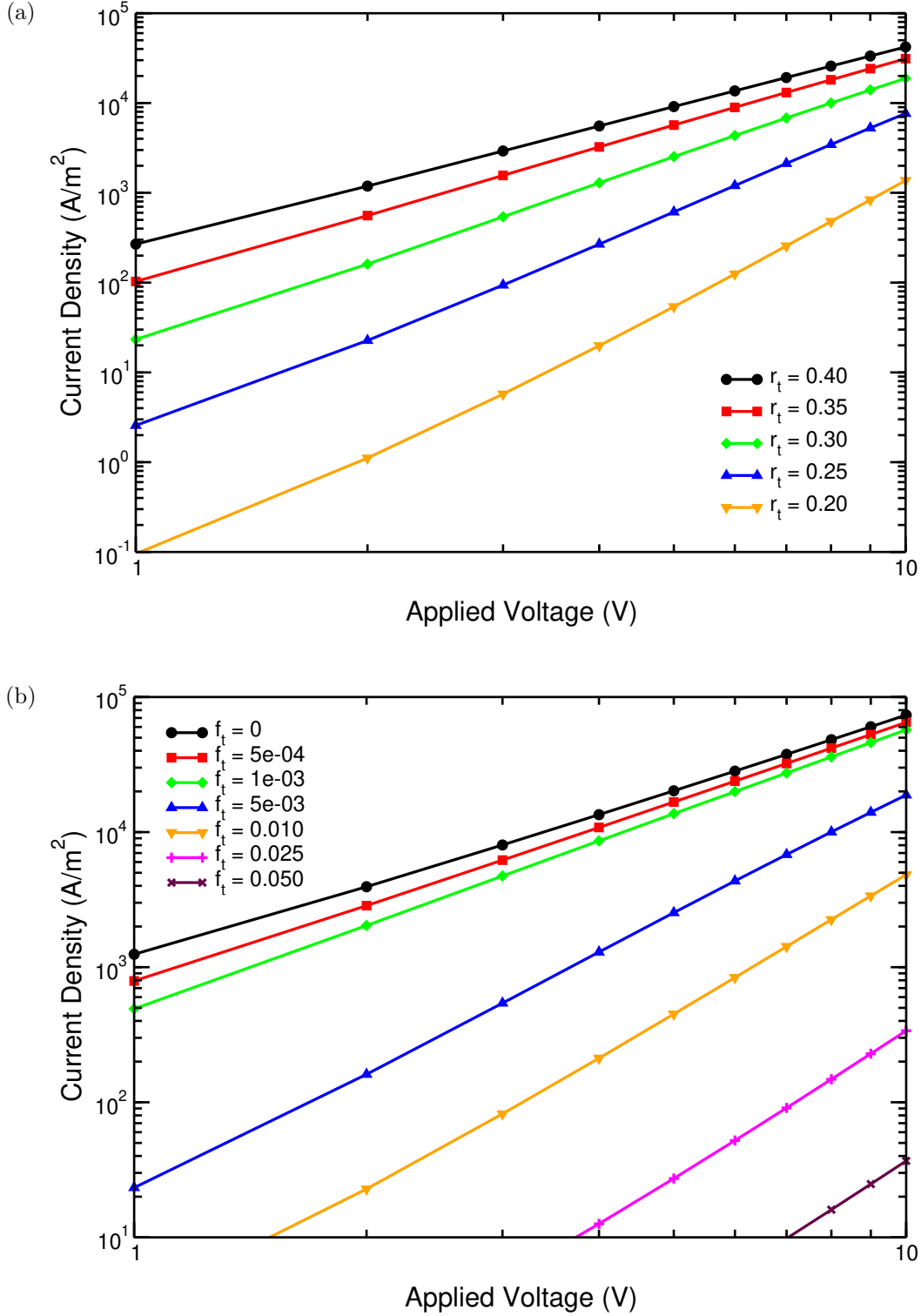


Figure 4.7: The theoretical current-voltage characteristics of planar hole-only devices in the SCLC regime obey the power law ($I \propto V^m$) when (a) $f_t = 0.005$ with varying r_t yielding the exponent in the range $m = 2.23 - 4.71$, and (b) $r_t = 0.30$ with varying f_t yielding the exponent in the range $m = 1.89 - 3.72$

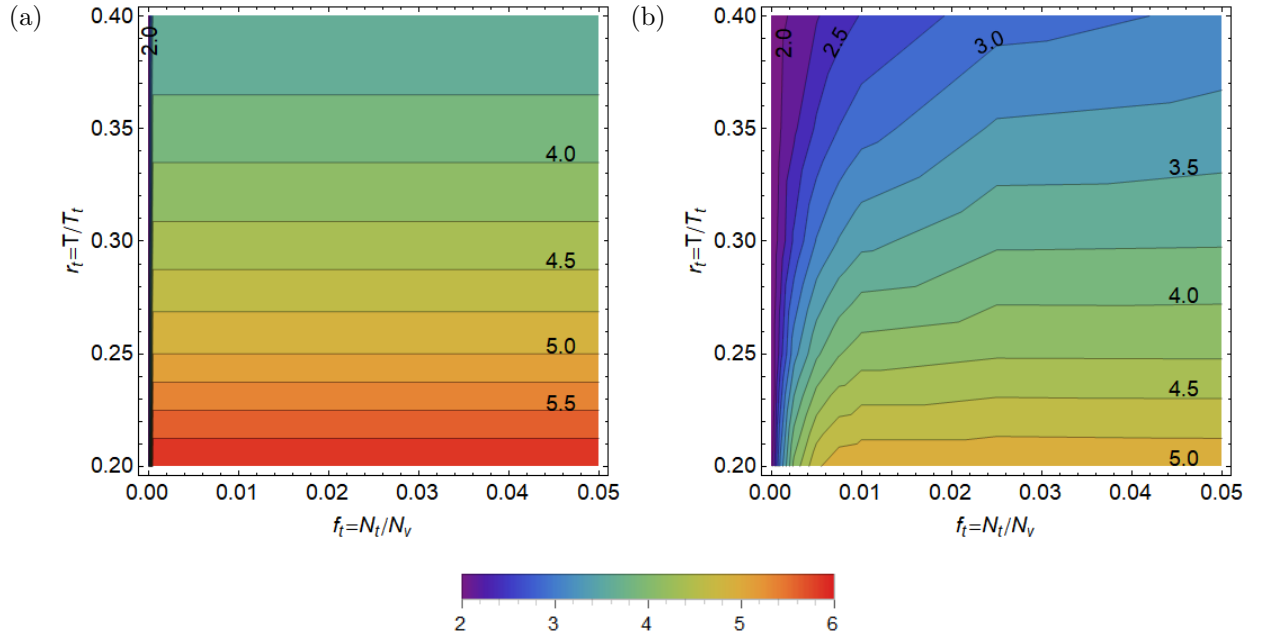


Figure 4.8: Dependence of the exponent m on the two trap parameters; trap density characterized by parameter f_t and trap temperature characterized by parameter r_t for hole-only devices in planar geometry based on (a) the simplified SCLC model as described by eq.(2.27), (b) 1-D DD-SCLC model as seen in figure 4.7 and described by eq.(4.3).

However, in the strong trap limit where the trap temperature is high and the trap density is large, the slope depends only on the trap temperature, while in the intermediate regime, the slope is influenced by both the trap temperature and the trap density. This dependence is quite different from what is predicted by the simplified SCLC model described by eq(4.7), in which the exponent m only depends on the parameter r_t related to trap temperature, as shown in figure 4.8a.

4.2.2 Tip-Plane Geometry

Taking into account the tip-plane electrode configuration, we simulate the charge injection and transport in hole-only device using the 2-D DD-SCLC model described in section 3.4. As the first step, the hole mobility is assumed to be isotropic. Figure 4.9 shows the theoretical current-voltage characteristic of a hole-only device in tip-plane geometry with a low density of deep traps ($f_t = 0.005, r_t = 0.30$), exhibiting three distinct regimes corresponding to

- Ohm's law in the low voltage regime,
- trap-limited SCLC in the intermediate voltage regime, and
- trap-filled SCLC in the high voltage regime.

This is similar to what has been observed in the theoretical current-voltage characteristic of the hole-only device in planar geometry (previously demonstrated in figure 4.6). The regime of interest is the trap-limited SCLC, which typically ranges from $1V$ to $10V$. More examples of the theoretical current-voltage characteristics in this intermediate regime are shown in figure 4.10 when (a) $f_t = 0.005$ with varying r_t and (b) $r_t = 0.30$ with varying f_t . This again suggests that the slope of the $\text{Log } I - \text{Log } V$ relations, *i.e.*, the exponent m , depends on trap parameters.

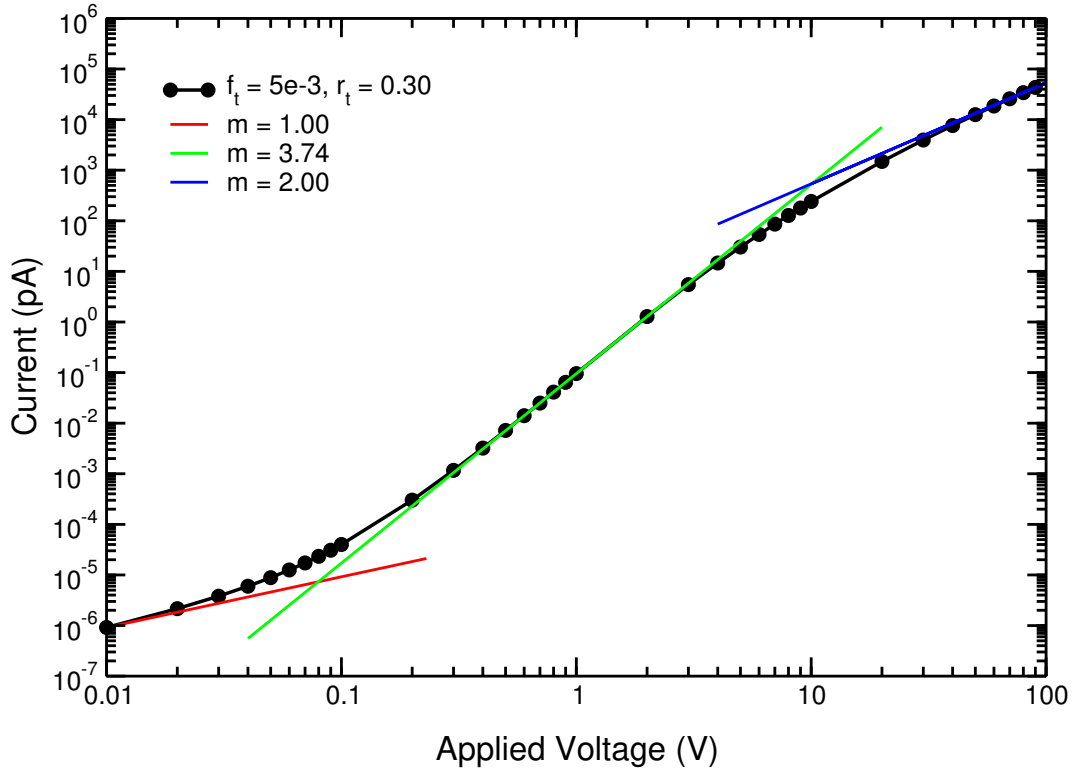


Figure 4.9: The trap influenced current-voltage characteristic of a hole-only device in the tip-plane geometry obeys the power law $J \propto V^m$, exhibiting three regimes: Ohm's law $m = 1$ (red), trap limited SCLC $m > 2$ (green), and trap filled SCLC $m = 2$ (blue). Hole mobility is assumed to be isotropic.

While the system has cylindrical symmetry, the hole mobility used in the calculation can be non-uniform. In this section, we will treat the mobility anisotropy in a simple manner, where we assume that the mobility is uniform in the lateral (ρ -) and vertical (z -) direction, and yet with different values of μ_ρ and μ_z , respectively. The situation often occurs in the experiments of semi-crystalline organic semiconductors (See chapter 5). The degree of mobility anisotropy is defined by the ratio μ_ρ/μ_z . As a preliminary study, we perform the numerical calculation with varying anisotropic mobility ratio up to 25, which has been observed in hole-transporting P3HT thin film composed of semi-crystalline whiskers [67]. Figure 4.11 shows the theoretical current-voltage characteristics in the low deep trap regime ($f_t = 0.005$, $r_t = 0.30$) with varying of the mobility anisotropic ratios (μ_ρ/μ_z). Interestingly, the exponent m in the power law does not show a dependence on the mobility anisotropy.

Following the analysis previously done on the trap study in the planar geometry, we carried out extensive calculations of the dependence of the theoretical current-voltage characteristics on the trap parameters and the mobility anisotropy. We found that the current-voltage relations can be described by the semi-empirical expression,

$$I(\mu_\rho/\mu_z, f_t, r_t) = \mu_o \cdot k_I(\mu_\rho/\mu_z, f_t, r_t) \cdot V^{m(f_t, r_t)} \quad (4.4)$$

where k_I is the fitting parameter and m is the power-law exponent. While the parameter k_I depends on both trap parameters and mobility anisotropy, the exponent m only depends on trap parameters. We have applied our Python program to fit the simulated current-voltage characteristics in the SCLC regime and have extracted the fitting values of k_I and m . The fitting results are summarized in table A.2 of appendix A. By analyzing the slope of $\text{Log } I - \text{Log } V$ curves, we observe the dependence of the exponent m on trap parameters

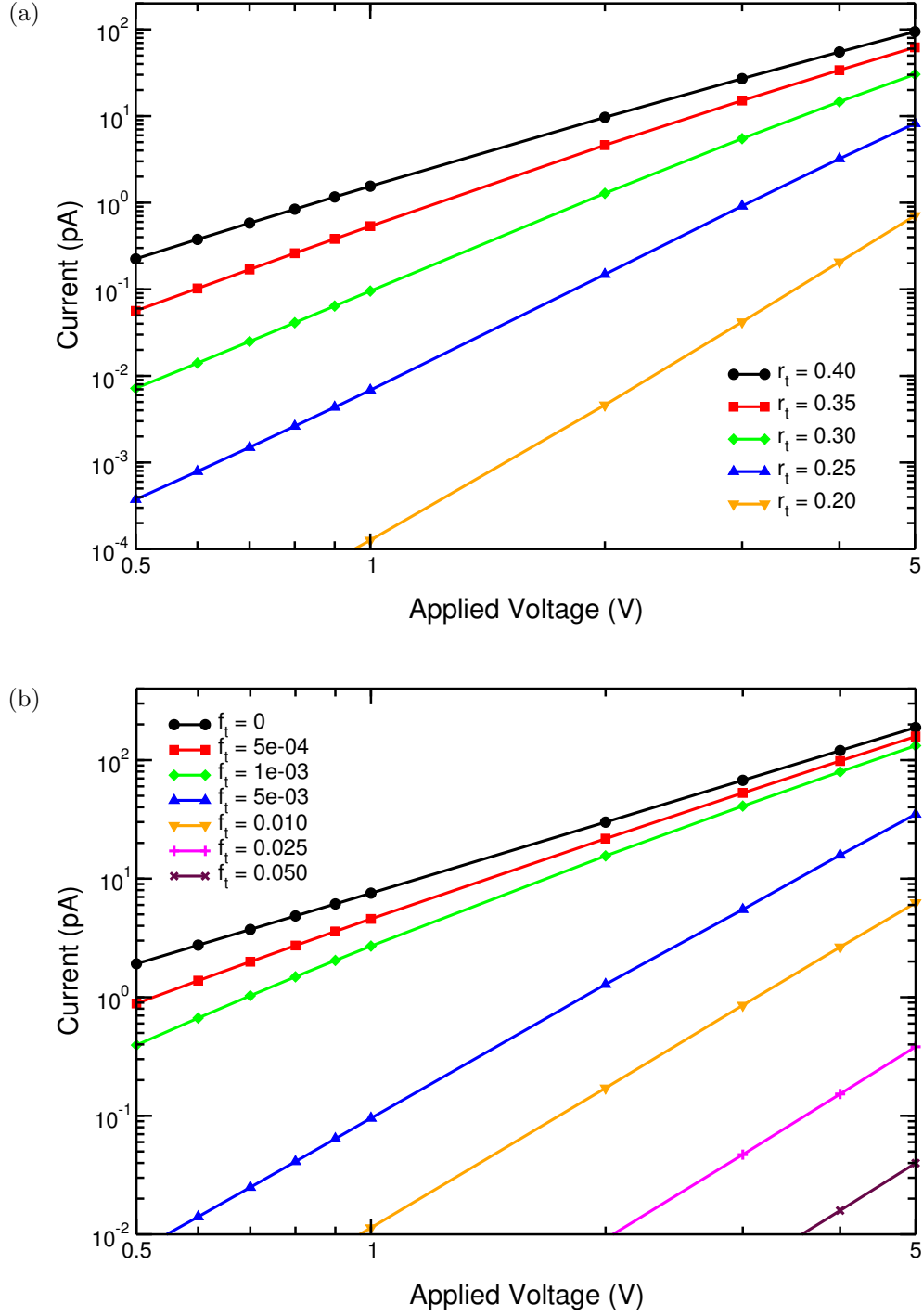


Figure 4.10: The theoretical current-voltage characteristics of tip-plane devices in the SCLC regime obey the power law ($I \propto V^m$) when (a) $f_t = 0.005$ with varying r_t yielding the exponent in the range $m = 2.89 - 5.52$, and (b) $r_t = 0.30$ with varying f_t yielding the exponent in the range $m = 2.00 - 4.19$. Hole mobility is assumed to be isotropic.

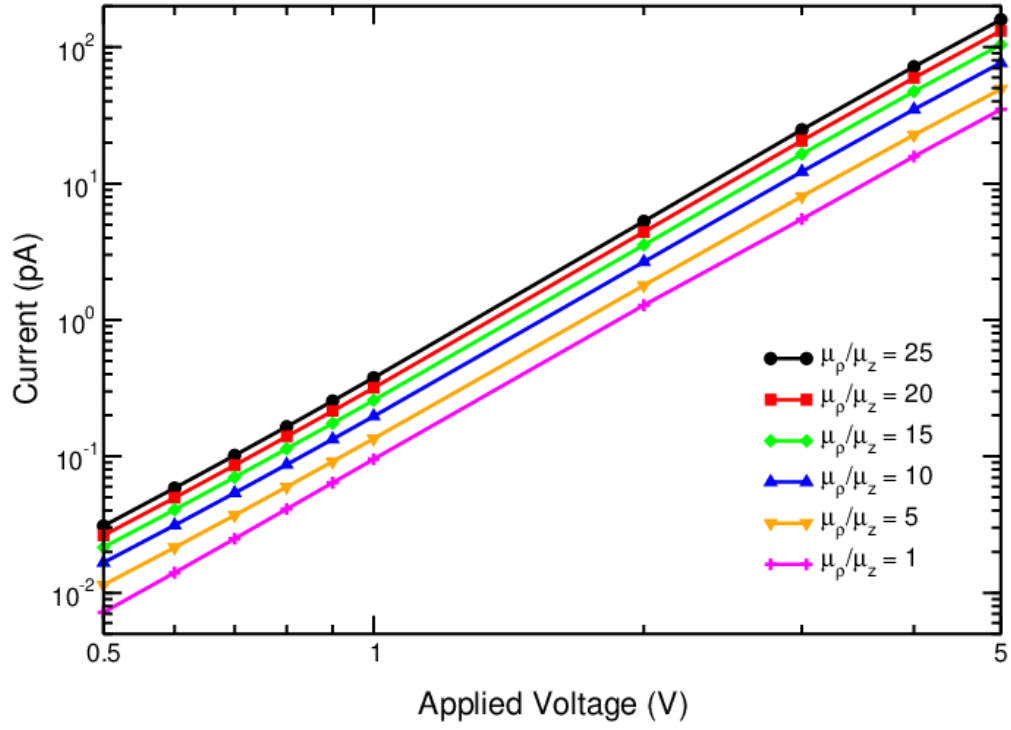


Figure 4.11: The theoretical current-voltage characteristics of tip-plane devices in the SCLC regime for a range of mobility anisotropic ratios, μ_ρ/μ_z , with fixed trap parameters $f_t = 0.005$, $r_t = 0.30$.

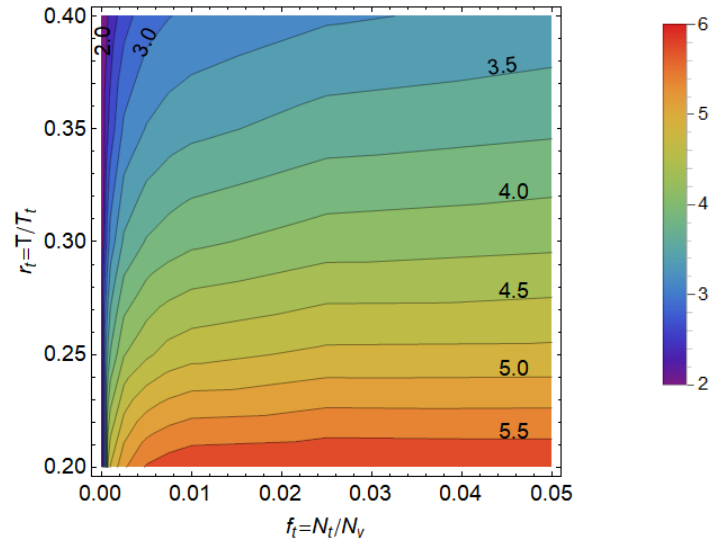


Figure 4.12: Dependence of the exponent m on the exponentially distributed trap DOSs characterized by parameters f_t and r_t for hole-only devices in tip-plane geometry in the SCLC regime, resulting from extensive calculations for theoretical current-voltage characteristics as demonstrated in figure 4.10 and described by the semi-empirical expression (4.4).

as illustrated by the contour plot in figure 4.12. The exponent m varies from 2.00 to 5.73 corresponding to trap parameter variations over the ranges of $f_t = 0 - 0.05$ and $r_t = 0.20 - 0.40$. The dependence of the exponent m on trap parameters resulting from device simulations in the tip-plane geometry is qualitatively similar to that of the planar geometry (shown in figure 4.8b).

4.3 Morphological Effects: Semi-Crystalline P3HT Thin Films

It has been shown that the overall performance of organic semiconductor devices have been improved significantly with the structural enhancement of their nanoscale morphologies [72, 73]. Semiconducting P3HT is among the most extensively studied polymers in the field, being the best-known representative that exhibits highly crystalline self-assembled nanostructures [1, 65, 66, 67, 74, 75, 76, 77]. Therefore, in this section, we carried out a theoretical study of the morphological effect in semi-crystalline P3HT films by analyzing the theoretical current-voltage characteristics simulated from tip-plane device geometry in analogy to c-AFM measurements.

Figure 4.13 shows a schematic illustration of crystallized P3HT nanofiber. In general, the self-organized P3HT exhibits a lamellar ordering via $\pi - \pi$ interactions that lengthen the nanofiber. Based on the alignment of P3HT lamellae with respect to the substrate, the nanofiber can be categorized into three orientation schemes: (i) ‘face-on’ orientation with the lamellae being parallel to the substrate, (ii) ‘edge-on’ orientation with the lamellae being perpendicular to the substrate, and (iii) ‘end-on’ orientation with both lamellae and polymer-backbone being perpendicular to the substrate, which are schematically shown in

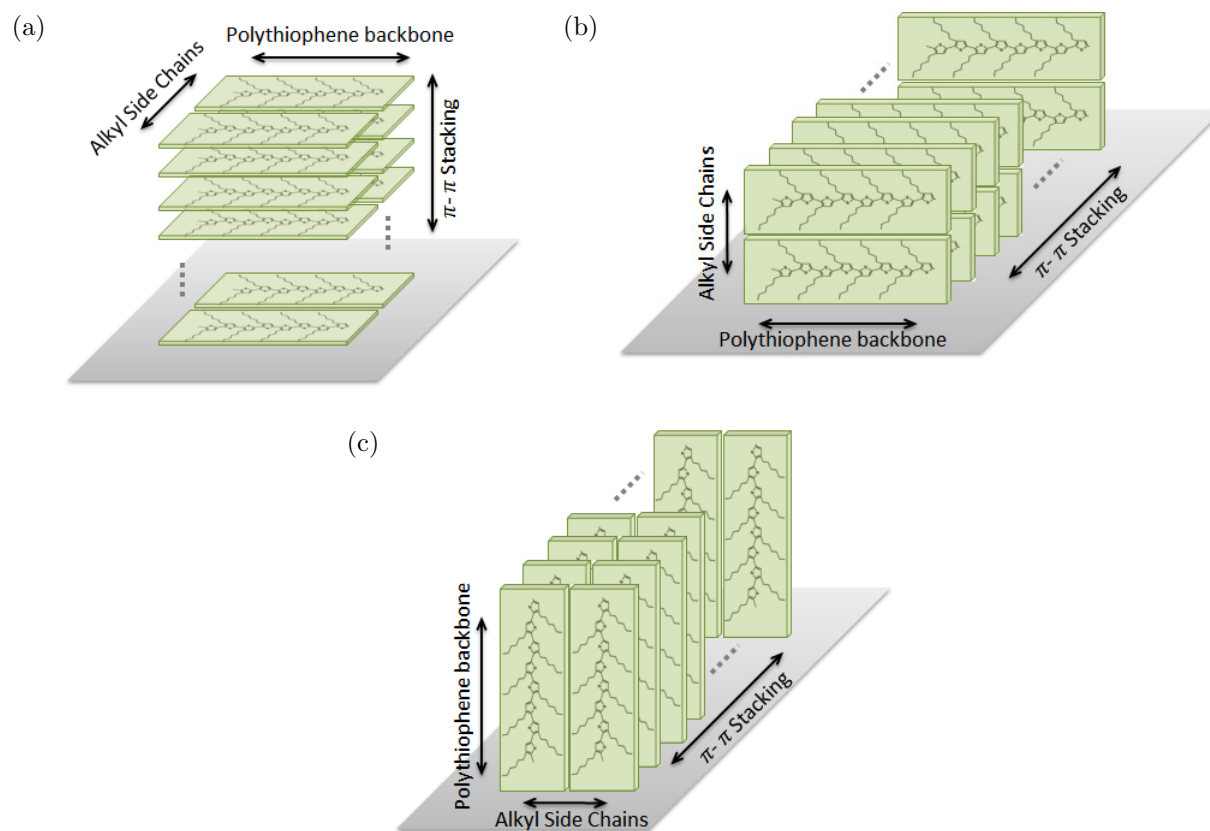


Figure 4.13: Schematic illustration of crystallized P3HT nanofibers in three possible orientation schemes, including (a) 'face-on', (b) 'edge-on' and (c) 'end-on' orientations, corresponding to the parallel and perpendicular alignments of self-organized P3HT lamellae to the substrate, respectively.

figure 4.13 (a),(b) and (c), respectively. While polymer crystallinity depends significantly on regioregularity [65,78,79], molecular weight [80,81,82,83] and fabrication process [84,85,86], P3HT typically forms micrometer long nanofibers along the $\pi - \pi$ stacking direction with a width of $20nm$ along the polythiophene backbone direction and a thickness of $5nm$ along the alkyl side chain direction [1,31,36,37,38,87]. Furthermore, it has been reported that producing the ‘end-on’ fibers is very challenging due to the difficulty of stacking up the long backbone direction [88,89]. Therefore, in this study, we will focus on the ‘edge-on’ and ‘face-on’ fibers, which is commonly found in the semi-crystalline P3HT thin films.

Experimentally, it has been shown that the crystallized P3HT nanofiber exhibits mobility anisotropy [65,67,90,91], such that the mobility along the $\pi - \pi$ stacking direction (fiber axis) is very high as compared to the mobility along the alkyl side chain direction, which is comparable to that of amorphous P3HT. Clearly, the high mobility channel through nanofibers is preferable for charge transport. While it is straightforward to make an assumption that the presence of nanofibers could lead to the enhancement of the overall device mobility, experiments [34,67] have shown that the ‘edge-on’ fibers do not significantly increase the mobility measured in the plane-parallel electrode configuration (planar geometry) and may slightly lower the mobility as compared to amorphous films. This observation can be explained by the characteristics of charge transport in the conventional planar geometry. In the experiments of this particular geometry, the current-voltage response is mainly subject to the vertical charge transport, and consequently the exceptionally high lateral mobility of ‘edge-on’ fibers may be left undetected. To obtain the comprehensive understanding of charge transport in both vertical and lateral directions, the current-voltage measurement in tip-plane geometry, similar to c-AFM, is preferred.

To study the morphological effect of crystallized P3HT fibers, we carried out the nu-

merical calculations using the fully 3-D DD-SCLC model, described in section 3.5, that is capable of incorporating the three-dimensional morphology of nanofibers as well as handling the device with tip-plane electrode configuration. The calculations were performed on the cubic grid, where the conducting tip is approximated by a $5nm \times 5nm$ square contact. In the following theoretical study discussed in this section, two assumptions have been made: (i) the device is free of traps; and (ii) while the anisotropic mobility is assigned to the fibers, the background mobility of amorphous regions is isotropic. The parameters used in the numerical calculations are summarized in table 4.1 unless stated otherwise.

4.3.1 An Isolated Fiber: ‘Face-On’ Fiber and ‘Edge-On’ Fiber

Although it is not common to selectively grow only one P3HT nanofiber in the film, the theoretical study of an isolated single fiber can give us the fundamental understanding of its morphological effect on the theoretical current-voltage characteristics. Also, we can investigate the contribution of an individual fiber without the interference from the near-by fibers, which cannot be observed directly from experiments.

To examine the morphological effect of an isolated crystalized P3HT nanofiber, we considered the case of a high mobility fiber embedded in an amorphous background. As schematically shown in figure 4.14, P3HT nanofibers are depicted by green wires with the cross-sectional areas of $20nm \times 5nm$. To maximize the effect, the fiber is lengthened across the entire device, which is about $80nm$ for ‘face-on’ fiber and $600nm$ for ‘edge-on’ fiber. This is generally consistent with the P3HT nanofibers visualized in experiments [1, 31, 36, 37, 38]. When compared to the amorphous domain, it has been shown that the ordered structures like nanofibers have at least improved the inter-molecular transport along the $\pi - \pi$ stacking direction [65, 67, 90, 91]. To proceed with the device simulations, the hole mobility in the

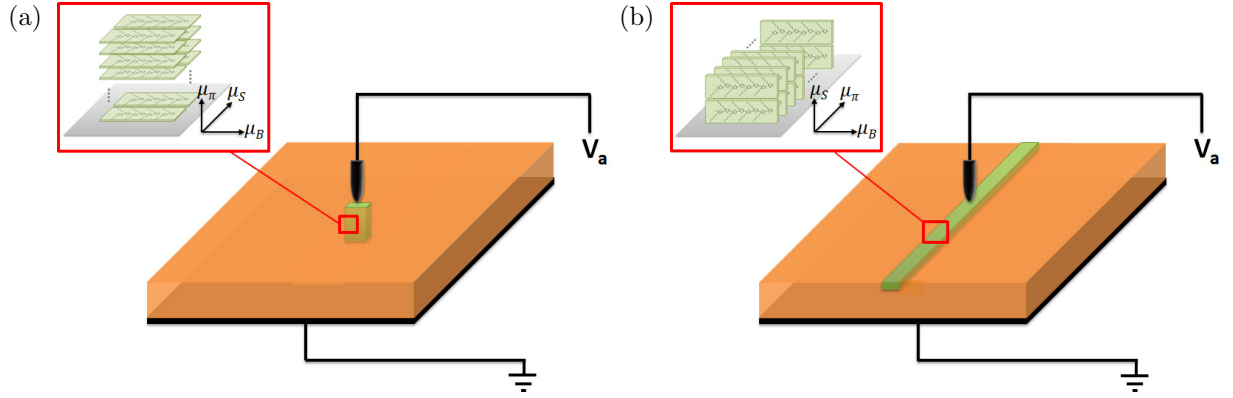


Figure 4.14: Schematic illustration of device structures with the tip-plane electrode configuration to study the morphological effect of an isolated fiber with (a) ‘face-on’ and (b) ‘edge-on’ orientations.

nanofiber needs to be parameterized.

Evidently, the mobility anisotropy of semi-crystalline P3HT films have been observed in experiments [65, 67, 90, 91]. Hole mobilities along the direction of $\pi - \pi$ stacking and alkyl side chains have been investigated by using field-effect transistor experiment [65] and c-AFM measurement [91]. These papers have reported that hole mobility along the $\pi - \pi$ stacking direction (μ_π) is significantly larger than that along the side chain direction (μ_S) by 2-3 orders of magnitudes. On the other hand, the hole mobility along polythiophene backbone direction (μ_B) cannot simply be determined by the same techniques. To the best of our knowledge, there is no report on the experimental measurement of the hole mobility along the backbone direction, and only one theoretical analysis by Lan and Haung [90] suggested that the hole mobility along the backbone direction (μ_B) is approximately 2 orders of magnitude larger than that along the $\pi - \pi$ stacking direction (μ_π). This implies that holes travel in nanofibers along the polymer backbone with mobility of 4 orders of magnitude higher than that along the polymer side chains. From the computational point of view, we have found

that this drastic transport anisotropy in P3HT nanofibers impacts the numerical stability of the calculations. To solve this issue, we need to evaluate how the high mobility anisotropy of nanofibers affects the overall hole transport in semi-crystalline P3HT devices.

The straightforward way to examine the overall hole transport in devices is by evaluating their current-voltage characteristic. For the present study, the conducting tip is located on nanofibers to maximize their impact on the macroscopic transport, as schematically illustrated in figure 4.14. We carried out extensive calculations of the dependence of theoretical current-voltage characteristics on the magnitude of hole mobility along the polythiophene backbone direction of a nanofiber (μ_B). While varying hole mobility along the backbone direction, hole mobility along the $\pi - \pi$ stacking direction and the alkyl side chain direction were fixed with the anisotropic mobility ratio $\mu_\pi/\mu_S = 100$. The background mobility of the amorphous region is chosen to be the same as that of the alkyl side chains, which is consistent with recent experiments [1, 34, 67].

Figure 4.15 shows the comparison of theoretical current-voltage characteristics simulated from hole-only devices consisting of an isolated P3HT nanofiber embedded in an amorphous domain, as schematically illustrated in figure 4.14, for the different values of mobility anisotropic ratio of the polymer backbone to the alkyl side chains (μ_B/μ_S). The theoretical current-voltage characteristic of an amorphous device (no fiber) is plotted as the baseline. The inset shows the same data plotted in double logarithmic scale, obeying the power law $I \propto V^m$ with the exponent of $m = 1.89$, which is close to the trap-free value, and consequently incorporating the high transport domain doesn't change the fitting value of the exponent.

From figure 4.15, two different fiber orientations reveal two distinct dependences of the theoretical current-voltage characteristic on the mobility anisotropic ratio μ_B/μ_S . In the

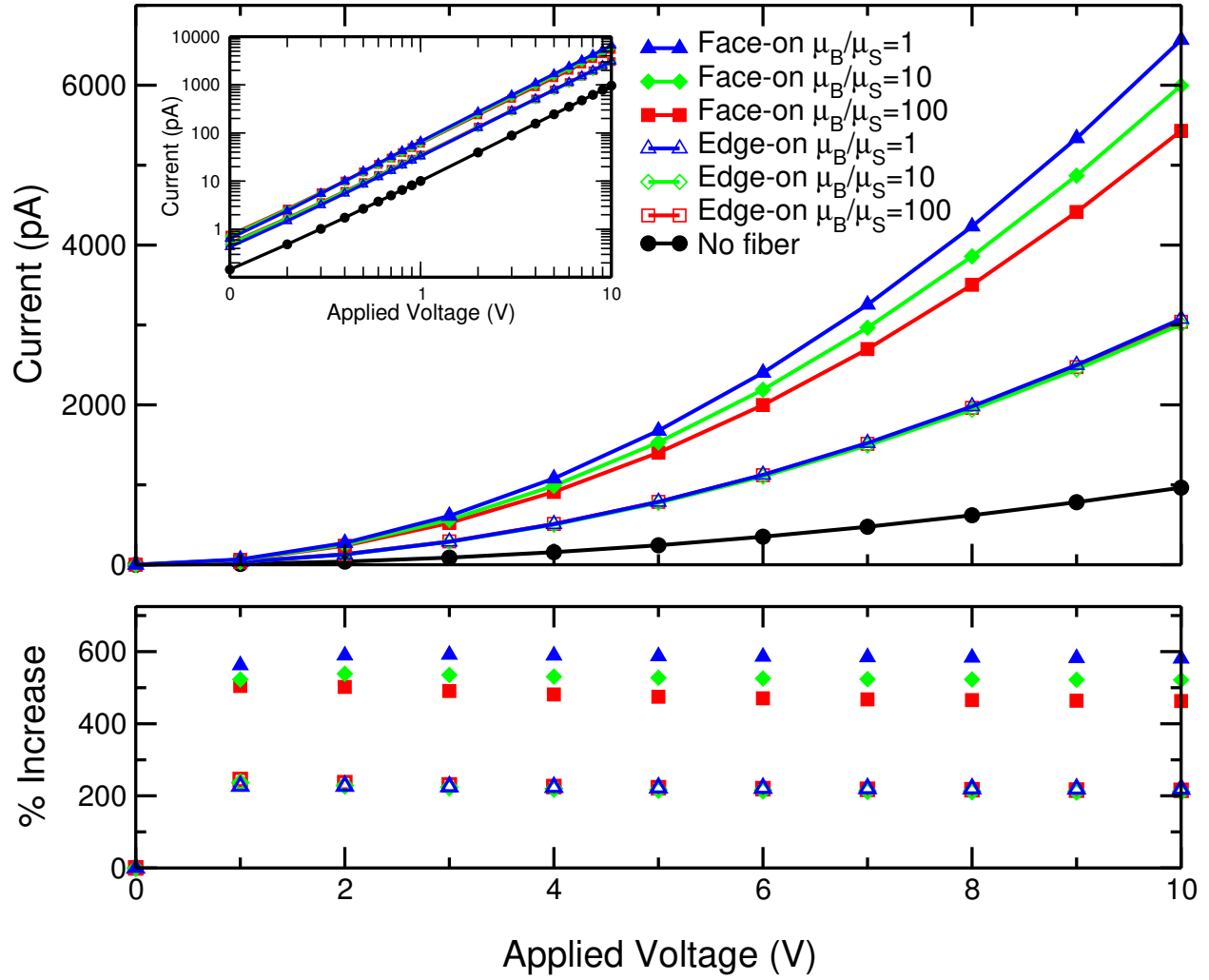


Figure 4.15: Based on the hole-only devices with an isolated P3HT fiber shown in figure 4.14, the theoretical current-voltage characteristics when the tip is in contact with the fiber are plotted with varying the fiber mobility along the polythiophene backbone direction (μ_B). The theoretical current-voltage characteristic of an amorphous device is plotted as the reference to demonstrate the current enhancement in the presence of a single nanofiber. The inset shows the same data plotted in the double logarithmic scale.

case of an isolated ‘edge-on’ fiber, the theoretical current-voltage characteristics remain unchanged with the variation of ratio μ_B/μ_S , indicating that hole transport in the ‘edge-on’ fiber is dominated by the high mobility along the $\pi - \pi$ stacking direction. On the other hand, the current of a device with an isolated ‘face-on’ fiber decreases with increasing hole mobility of the polymer backbone (μ_B). This setback in hole transport is associated to the enhancement of the lateral current spreading due to an increase of in-plane mobility along the backbone direction of the ‘face-on’ fiber. It should be noted that we verified that increasing the mobility anisotropic ratio μ_B/μ_S to 10^4 , as in the analysis by Lan and Haung [90], has a very small effect on the current-voltage characteristic ($< 1\%$ difference from the case of ratio $\mu_B/\mu_S = 100$). To reduce the difficulty in the numerical calculations without impacting the mobility anisotropy effect, the hole mobility along the $\pi - \pi$ stacking direction and the polythiophene backbone direction is set to be 100 times larger than that along the alkyl side chain direction. This is to be applied to all the numerical calculations on P3HT fibers from this point onward.

To further understand the morphological effect of an isolated nanofiber contained in the theoretical current-voltage characteristics shown in figure 4.15, we also plot the percentage increase of current when the tip is placed on an isolated nanofiber compared to when the tip is placed on an amorphous domain (no fiber), as a function of externally applied voltage. It is clear that the overall hole transport in the device is enhanced when tip is in contact with a high mobility nanofiber; approximately 200% and 500% increase of current are observed for an isolated ‘edge-on’ and ‘face-on’ fiber, respectively. This observation demonstrates a remarkable dependence of the overall hole transport on the orientation of a nanofiber in this particular setup. In the case of a ‘face-on’ orientation, the high mobility fiber is perpendicular to the substrate, and consequently improves the vertical hole transport from

the conducting tip to the bottom electrode, resulting in a tremendous increase of current. However, the explanation based on the improvement of vertical mobility cannot elucidate the current enhancement observed when tip is in contact with the 'edge-on' fiber, in which the high mobility direction is in-plane. Moreover, as previously seen in the case of a 'face-on' fiber that the increasing of lateral hole mobility results in the decreasing in current, one might wonder why we do not observe the same setback in the case of edge-on fiber when compares to the case of amorphous P3HT device (no-fiber case). With this complication, to consider just the theoretical current-voltage characteristics is not sufficient, and we need to explore the detailed information on current flow.

Figure 4.16 shows a selection of current maps, demonstrating three-dimensional current flow simulated from hole-only devices in the tip-plane geometry at the applied voltage $V_a = 1V$. Figure 4.16(a-e) presents the vertical current at different locations along the direction of device thickness, while figure 4.16(f-j) shows the lateral current at the top surface ($z = 80nm$) in contact with the conducting tip. Due to the large amount of current injecting vertically and laterally from the conducting tip, the tip contact area is visualized as a red dot in current maps of the top surface. In figure 4.16, three different morphologies associated to the semiconducting P3HT have been used in the device simulations, including (a,f) a purely amorphous domain (no fiber), (b-c, g-h) an isolated 'face-on' fiber embedded in an amorphous domain, and (d-e, i-j) an isolated 'edge-on' fiber embedded in an amorphous domain, which are schematically shown in figure 4.14. In the last two morphologies involving nanofibers, we compare the case when the conducting tip is located on fiber and the case when the tip is near but not in contact to the fiber. The current maps clearly show distinct correlation to their morphologies.

In figure 4.16(a,f), the amorphous device exhibits the behavior of an isotropic system,

showing the circularly symmetric distribution of the hole current. Figure 4.16 (a) shows the vertical current spreading into the larger cross-sectional area toward the bottom electrode. This 3-D cone of the vertical current is recognized as the signature of the tip-plane geometry caused by the lateral current spreading beneath the conducting tip, as obviously seen in figure 4.16(f).

In the case of an isolated ‘face-on’ fiber (figure 4.16(b-c, g-h)), we clearly observed the superposition of two features arising from the nature of tip-plane electrode configuration and the characteristics of high mobility fibers. First, it exhibits the circularly symmetric current spreading from the conducting tip shown as the background; second, the number of standout red dots in the vertical current maps indicate the intense vertical current at the specific location, revealing the exceptionally high-transport channel through the fiber. When the tip is located on the fiber, the fiber simply connect the upper tip to the bottom electrode. As shown in figure 4.16(b), the alignment of red dots could be seen as the ‘tip extension’ to the bottom electrode, which lead to the current enhancement previously observed in figure 4.15. Even when the tip is not in contact with the fiber (figure 4.16(c,h)), the lateral current spreading brings holes to the nearby fiber where holes are able to travel faster to the bottom electrode. In other words, the fiber assists hole transport by providing a ‘highway’ for current flow.

The last morphology to be discussed is the one with an isolated ‘edge-on’ fiber. In figure 4.16(d-e,i-j), the spherical symmetry of current spreading from the conducting tip is no longer maintained, and the current maps clearly characterize the surface morphology of the fiber that lies in-plane. Adopting the intuitive picture of the ‘tip extension’ described earlier, one can relate the enhancement of the vertical current when the tip is in contact with the fiber (as shown in figure 4.15) to the increase of the tip contact area, as clearly depicted by the red

wire in figure 4.16(d,i). Furthermore, in the condition that the fiber and the tip are no longer in contact (figure 4.16(e,j)), as long as the fiber is affected by the lateral current spreading from the tip, it is obvious that the fiber promotes current flow, behaving as a ‘highway’ for hole transport. It is less obvious, though, that this mechanism is sufficient to significantly raise the vertical current of the device.

In order to avoid confusion, it is worth noting that the current maps shown in figure 4.16 are not the same as the current map of c-AFM measurements, despite the similarity in the electrode configuration. While the simulated current map illustrates the 3-D current distribution, including both lateral and vertical currents, when the biased tip is positioned at the point of interest on the surface; the c-AFM current map is the 2-D plot of the vertical current measured at each location on the map by scanning the biased tip over the surface of the sample. Although the simulated current map of a single point probe is limited to the local morphological and electrical properties where the tip is located, these maps essentially provide the 3-D visualization of current flow which cannot be observed directly from experiments. Particularly, by comparing the current maps simulated from different morphologies as illustrated in figure 4.16, we reveal how the ‘face-on’ and ‘edge-on’ fibers, despite the difference in fiber orientation, enhance the current flow in the tip-plane geometry. This mechanism is qualitatively consistent with the contrast seen in the c-AFM current maps of fibrous films [1, 31, 36, 37, 38].

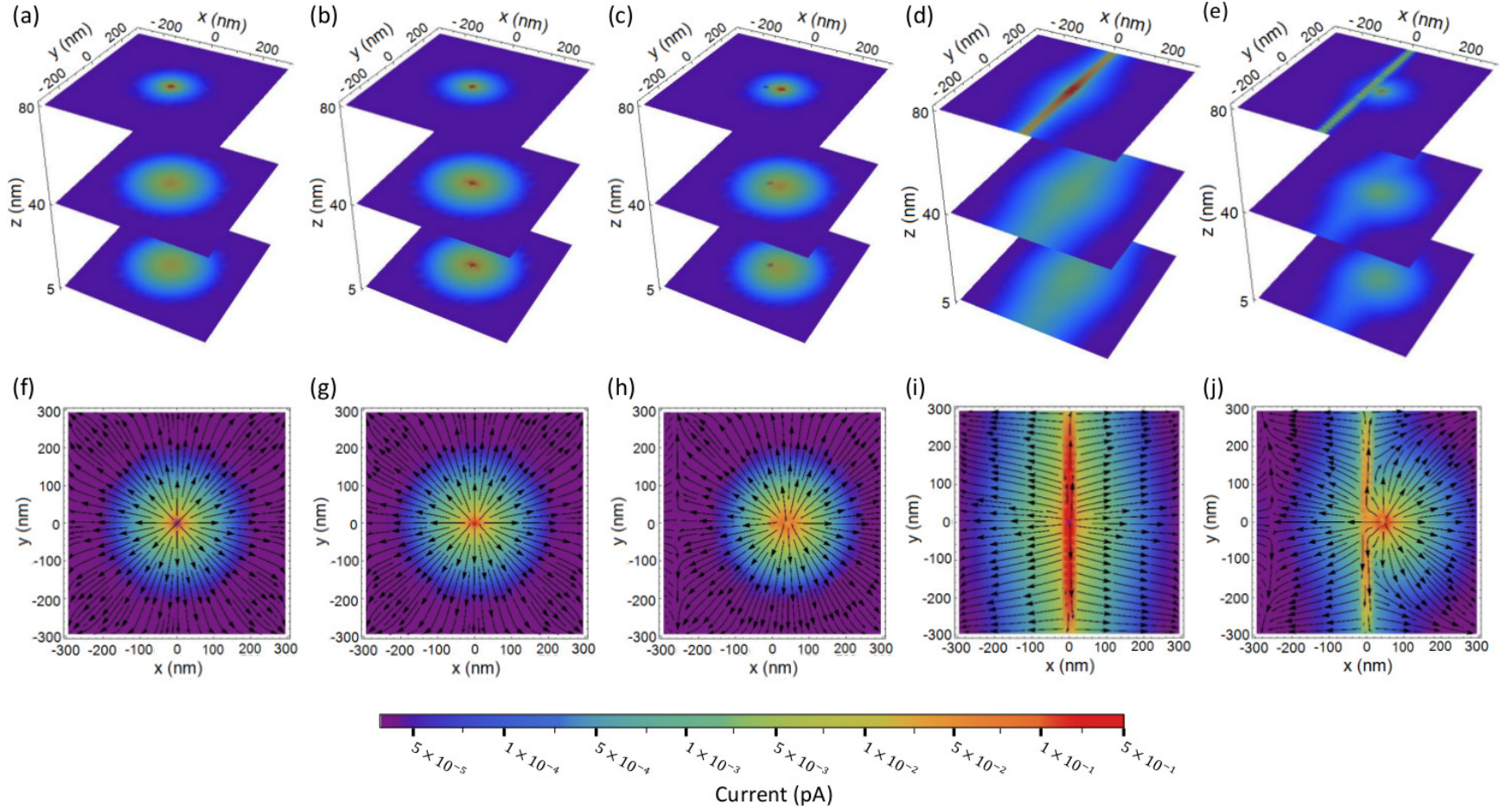
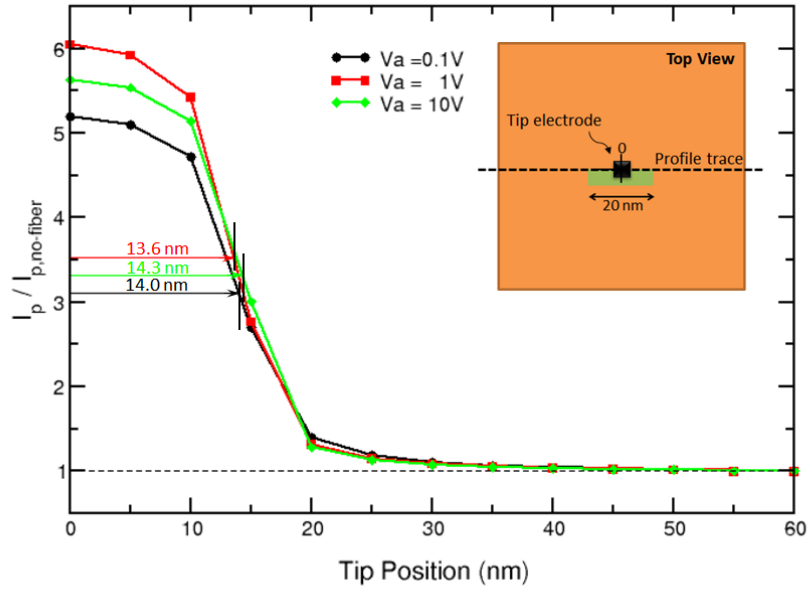


Figure 4.16: The vertical (a-e) and lateral (f-j) current of the semiconducting P3HT devices when the biasing voltage $V_a = 1V$ is applied to the conducting tip (red dot) and the bottom electrode is grounded. Three different types of morphologies have been used in the device simulation: (a)&(f) an amorphous (no-fiber) domain; (b-c)&(g-h) an isolated 'face-on' fiber embedded in an amorphous domain; and (d-e)&(i-j) an isolated 'edge-on' fiber embedded in an amorphous domain. In the last two morphologies, the comparison of current flows when tip is and is not in contact with the fiber is demonstrated.

Up to now, the current maps of a single-point probe have been helpful to qualitatively elucidate the mechanism for c-AFM contrast in fibrous films. However, to verify the ability of c-AFM current maps in visualizing each individual fiber, it is necessary to analyze the contrast of the map quantitatively. Resembling the c-AFM measurement, we carried out extensive calculations at different positions along the chosen profile trace. In this study, we consider the same morphologies used in simulating the current map, which consists of an isolated fiber embedded in an amorphous domain, as schematically shown in figure 4.14.

Figure 4.17 shows the dependence of the vertical current as a function of tip position on a trace crossing the ‘face-on’ fiber along; (a) the polythiophene backbone direction and (b) the alkyl side chain direction, at the applied voltages $V_a = 0.1, 1, 10V$. Shown in the inset is the surface morphology of the device in figure 4.14(a) with the profile trace indicated by the dashed line. Because of the symmetry of the morphology, we plotted the vertical current collected from one half of the profile trace, starting from the center of the fiber where tip position is set to zero. The vertical currents in figure 4.17 have been normalized to the vertical current of an amorphous (no fiber) device in order to make the comparison among the three values of the applied voltage. Despite the difference in fiber dimensions, two obvious similarities of the current distribution in the backbone direction and the side chain direction are: (i) the vertical current is at its maximum value when tip position is at 0nm (the center of fiber), (ii) the vertical current abruptly decreases when the tip is positioned outside the fiber edge (FE). The fiber edge (FE) is the key parameter that pinpoints the interface between the crystallized structure of the fiber and the amorphous domain, which is at the position $10nm$ and $2.5nm$ in the backbone direction and the side chain direction, respectively. To understand the information contained in these data, the distribution of the vertical current is parameterized in terms of the half-width at half maximum (HWHM) as marked and

(a)



(b)

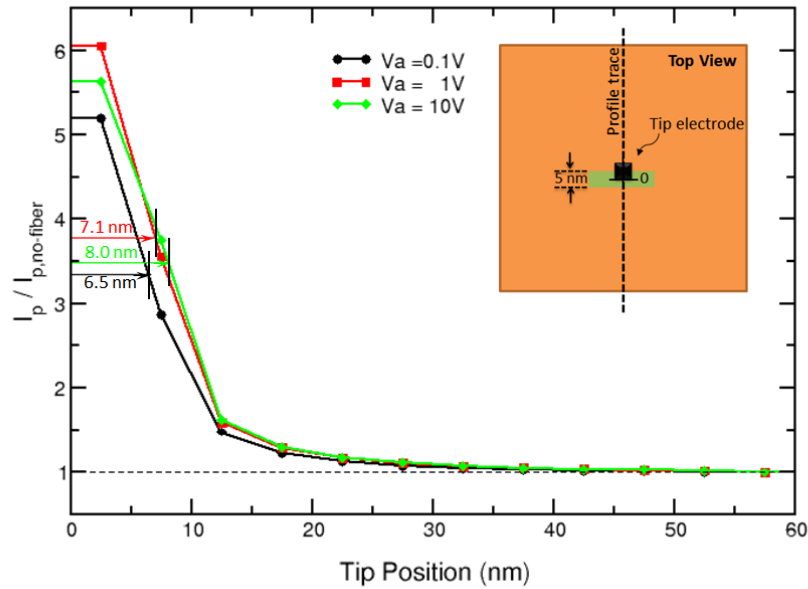


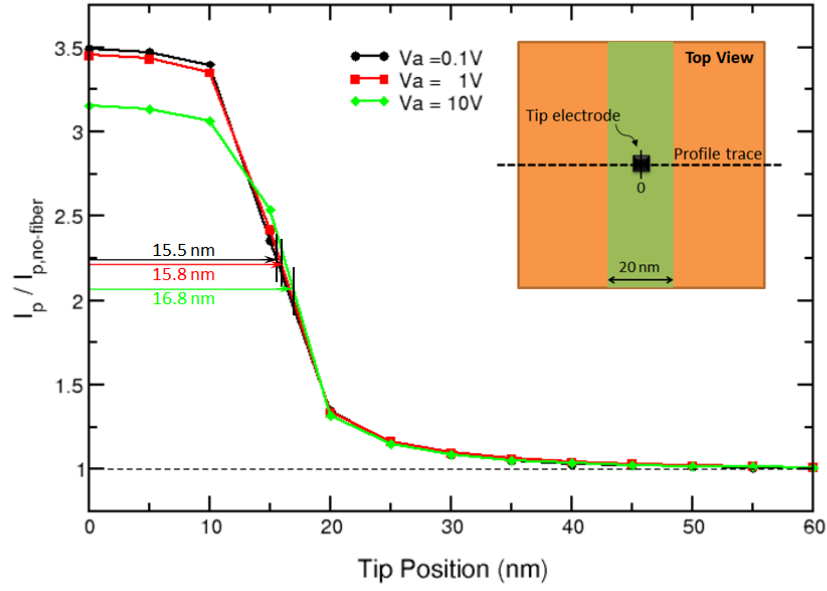
Figure 4.17: Simulating the c-AFM measurements, the dependence of the vertical current as a function of tip position on the profile trace crossing the ‘face-on’ fiber along; (a) the polythiophene backbone direction and (b) the alkyl side chain direction, at the applied voltages $V_a = 0.1, 1, 10\text{V}$. The profile trace is indicated by the dashed line shown in the inset.

labeled in the figure, yielding the averaged values $\overline{\text{HWHM}}$ of 14.0nm and 7.2nm in the backbone direction and the side chain direction, respectively. To generalize this parameter, we consider the value of $\overline{\text{HWHM}} - \text{FE}$, which simply indicates the tip position away from the fiber edge where the vertical current decreases to the half value of its maximum. As a result, $\overline{\text{HWHM}} - \text{FE}$ is estimated to be 4.0nm and 4.7nm for the c-AFM simulations along the profile trace of the backbone direction and the side chain direction, respectively. These values are comparable to the tip size, and confirm the high lateral resolution of c-AFM measurements on a ‘face-on’ fiber.

Figure 4.18(a) shows the dependence of the vertical current as a function of tip position on the trace crossing the ‘edge-on’ fiber along the polythiophene backbone direction at the applied voltages $V_a = 0.1, 1, 10\text{V}$. In the inset, the profile trace is indicated by the dashed line cross the surface morphology of the device schematically shown in figure 4.14(b). Similar to the case of ‘face-on’ fiber, the vertical current is maximized when the tip is positioned at the center of fiber (0nm), then falls off rapidly when the tip moves beyond the fiber edge (FE) at the position of 10nm . As marked and labeled in figure 4.18(a), the values of $\overline{\text{HWHM}}$ evaluated at the three different applied voltages are close, giving an average value of $\overline{\text{HWHM}}$ as 16.0nm . Consequently, $\overline{\text{HWHM}} - \text{FE}$ is estimated to be 6.0nm , which is comparable to the tip size. This confirms the high lateral resolution of c-AFM measurements on a ‘edge-on’ fiber.

Figure 4.18(b) illustrates an analysis of the vertical sensitivity of c-AFM measurement on an isolated ‘edge-on’ fiber at the applied voltage $V_a = 0.1, 1, 10\text{V}$. To investigate the vertical sensitivity of the measurement, we fixed the tip position and modified the morphology by embedding the ‘edge-on’ fiber away from the surface. In Figure 4.18(b), dependence of the vertical current as a function of the vertical separation between tip and fiber is illustrated

(a)



(b)

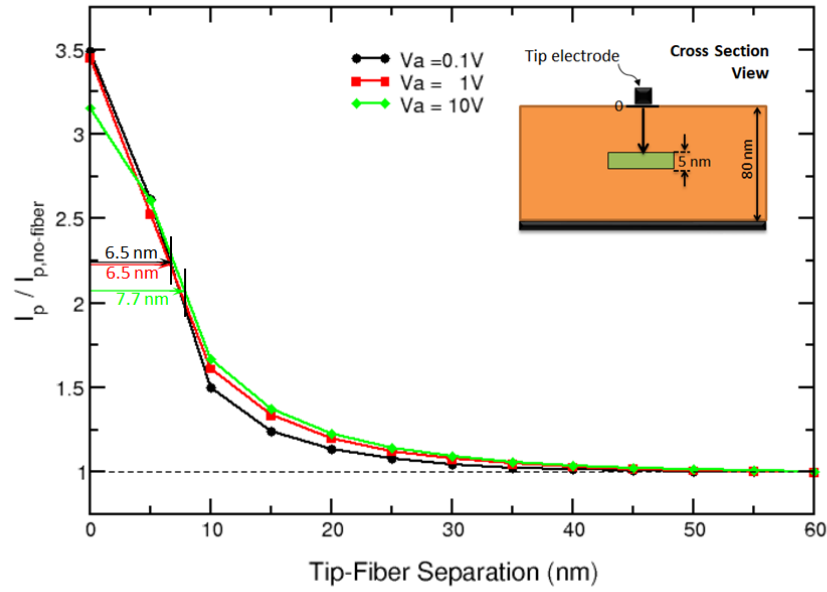


Figure 4.18: Simulating c-AFM measurements, (a) the dependence of the vertical current as a function of tip position on the profile trace crossing the ‘edge-on’ fiber along the polythiophene backbone direction and (b) the dependence of the vertical current as a function of tip-electrode separation, at the applied voltage $V_a = 0.1, 1, 10\text{V}$.

for the varying applied voltages. The vertical current decreases with the increase of the tip-fiber separation. This is expected since the effect of the ‘edge-on’ fiber subsides as the fiber is located further away from the surface, as well as the tip. Similarly, it is useful to parameterize the decay of the vertical current with tip-fiber separation in term of HWHM, as given in the figure 4.18(b). However, in this study, the physical interpretation of HWHM is the vertical separation between tip and fiber that corresponds to reducing the vertical current by half of the maximum current measured when tip is in contact with fiber. The averaged HWHM over three applied voltages is estimated to be $6.9nm$, indicating the vertical sensitivity of c-AFM measurement to a buried ‘edge-on’ fiber.

4.3.2 An ‘Edge-On’ Fiber Network

In this section, we applied the numerical tool of the 3-D DD-SCLC model to study the morphological effect of a nanofibrillar network. In an exemplary way, we carried out the numerical calculations to simulate the charge transport through the network of ‘edge-on’ oriented P3HT fibers in the tip-plane electrode configuration, in analogy to c-AFM measurements. In this study, we consider three types of randomness typically observed in semi-crystalline fiber structure in P3HT films [1, 31, 36, 37, 38], including random fiber spacing, random fiber orientation, and random fiber length. Each model morphology is generated to meet four conditions:

- i) no in-plane fiber crossing,
- ii) no out-of-plane fiber crossing,
- iii) no violation of the periodic boundary condition,
- iv) constant fiber fraction in each cross-sectional area.

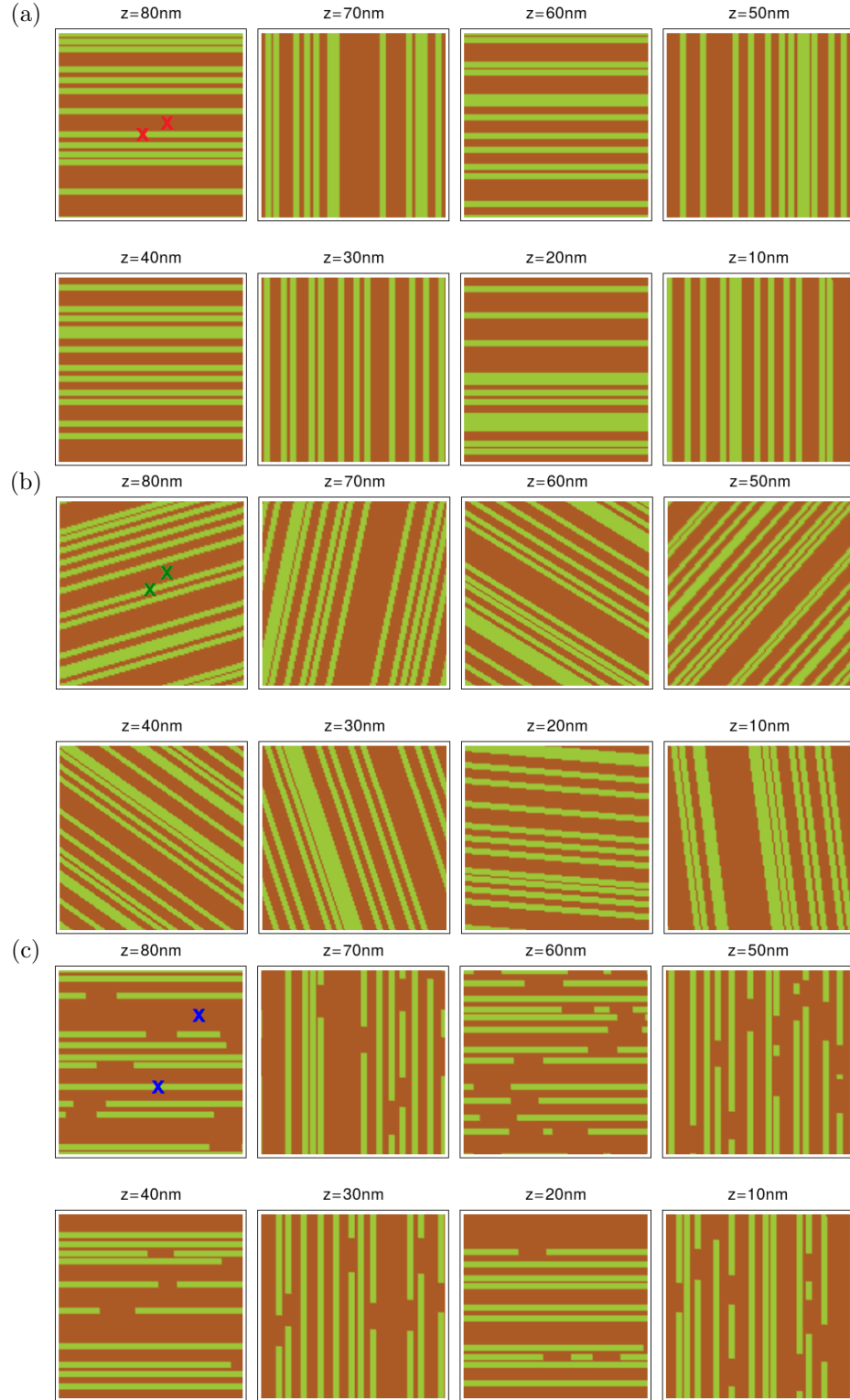


Figure 4.19: The $600nm \times 600nm$ cross-sections of three model morphologies consisting of ‘edge-on’ fibers aligned in-plane with (a) random spacing (fiber fraction = 0.40), (b) random spacing and random orientation (fiber fraction = 0.40) and (c) random spacing and random length (fiber fraction = 0.32).

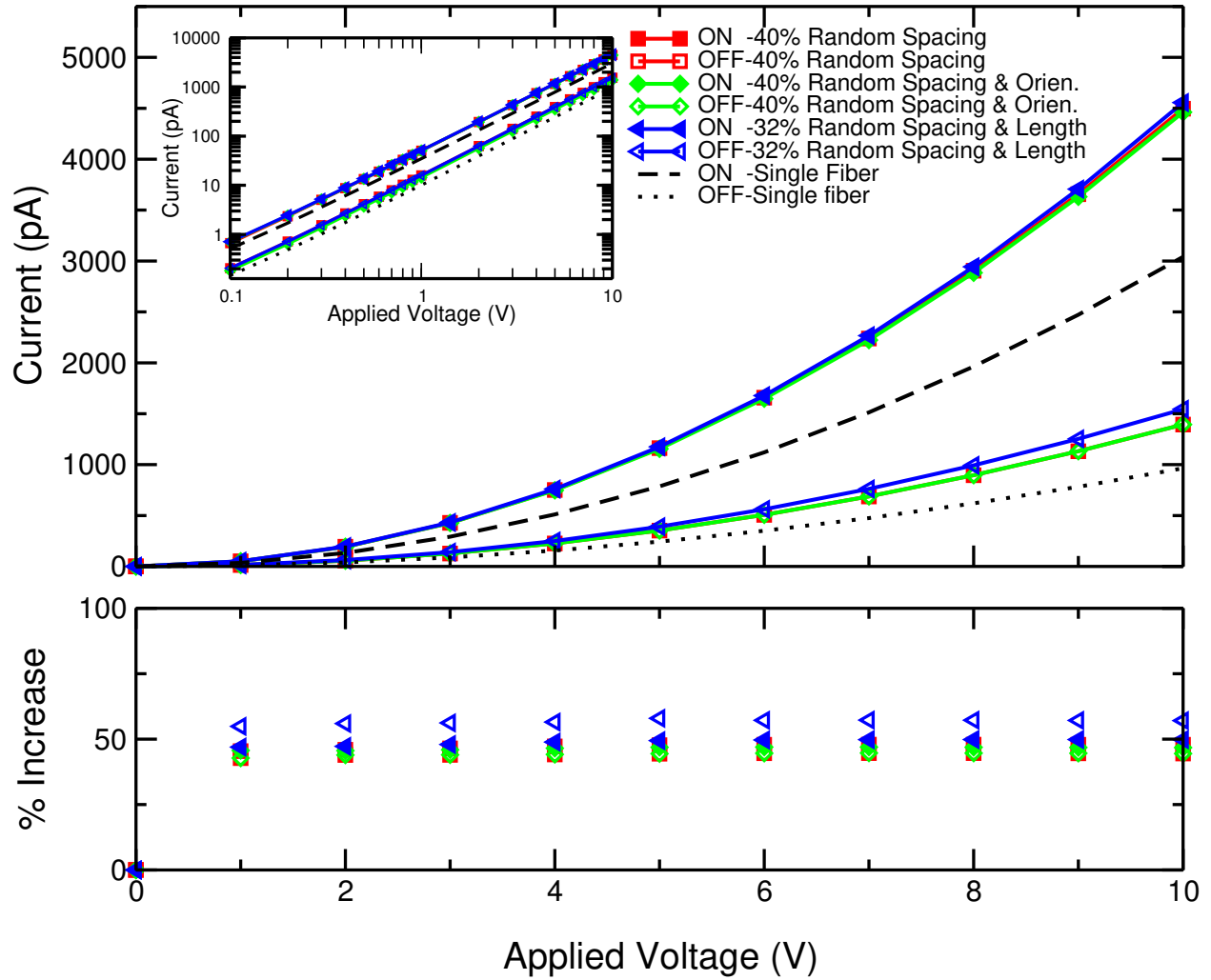


Figure 4.20: Theoretical current-voltage characteristics of hole-only devices in the tip-plane geometry with three model morphologies (see figure 4.19) simulated when the conducting tip is in contact with the fiber and when it is not, as labeled by ‘ON’ and ‘OFF’, respectively. The inset shows the same data plotted in the double logarithmic scale. Despite the differences in model morphologies, the total currents simulated from the devices with an ‘edge-on’ fiber network increase by approximately 50% compared to those simulated from the devices with a single. With the presence of an ‘edge-on’ fiber network, the total currents, despite the differences in model morphologies and tip locations, increases by approximately 50% compared to those simulated from the devices with a single ‘edge-on’ fiber.

Figure 4.19 illustrates the $600nm \times 600nm$ cross-sections of the $x - y$ plane for three model morphologies, consisting of the ‘edge-on’ fibers (depicted by green wires) that are aligned in plane with (a) random spacing, (b) random spacing and random orientation, (c) random spacing and random length. These fibers are embedded in an amorphous domain, colored in brown. Initially, the fraction of fiber in each cross-sectional area is chosen to be 0.40. However, when we assigned the random fiber length to the morphology(c), the fiber fraction in each cross-sectional area is reduced to 0.32 instead. These values of fiber fraction are roughly consistent with the value evaluated from c-AFM current maps in the experiment [1].

In analogy to c-AFM measurements, the local variation in hole transport of the model morphologies is achieved by locating the tip at the spot of interest and generating a theoretical current-voltage characteristic. Figure 4.20 shows the comparison of theoretical current-voltage characteristics simulated from two distinct locations on the top surface ($z = 80nm$) of the device, *i.e.*, ON- and OFF- fiber, as marked on the surface morphologies in figure 4.19. The term ‘ON’ and ‘OFF’ are simply referred to the measurement conditions when the c-AFM tip is in contact and not in contact with fiber, respectively. The theoretical current-voltage characteristics of ON- and OFF- an isolated ‘edge-on’ fiber, as studied in section 4.3.1, are plotted as the baselines. Note that the data for OFF-an isolated fiber is equivalent to the data generated from an amorphous device. The inset shows the same data plot in double logarithmic scale, described by the power law $I \propto V^{1.89}$, which is close to the characteristic of a trap-free no-fiber device. By plotting the current-voltage characteristic this way, we can make two qualitative observations: (i) the current flow is significantly enhanced by the network of high-mobility fibers; (ii) the difference in the theoretical current-voltage characteristics simulated from the three model morphologies is insignificant.

To quantitatively evaluate the morphological effect of a nanofibrillar network shown in figure 4.20, we also plotted the percent increase of current generated from three model morphologies compared to the baseline (an isotropic fiber) as a function of applied voltage. Despite the differences in model morphology, fiber fraction, as well as the measuring condition, we observed approximately 50% increase of current in all devices consisting of a nanofibrillar network when compared with devices consisting of an isolated nanofiber.

4.4 Conclusions

In this chapter, we addressed the theoretical studies of DD-SCLC model for the description of hole transport in hole-only devices. Applying the numerical tools developed in chapter 3, we demonstrated how the hole transport in the devices is affected by charge diffusion, energetically distributed traps and nanoscale morphologies.

First, we investigated the effect of charge diffusion on the SCLC in the conventional planar geometry, which is similar to the electrode configuration of the simplified SCLC theory, by using the 1-D DD-SCLC model. In contrast to those of the simplified SCLC model, the theoretical profiles of electric potential and hole carrier density simulated from the DD-SCLC model shows the strong dependence on the externally applied voltage, exhibiting three transport regimes: (i) diffusion-dominant transport regime, (i) drift-diffusion assisted transport regime, and (iii) drift-dominant transport regime, along the device thickness from the injecting electrode (an *actual* anode) to the extracting electrode (an *actual* cathode). The three transport regimes are separated by two major transitions of the local charge transport occurring at the position of the potential maximum, where the local electric field and drift current vanish, and the position of the hole density minimum, where the diffusion current

becomes zero. These conditions at the turning points are consistent with the boundary conditions at the electrodes of the simplified SCLC theory, marking the location of the *virtual* anode and a *virtual* cathode, respectively. We also found that the positions of the virtual electrodes move toward those of the actual electrodes with increasing applied voltage. The dynamics of the virtual electrodes and the corresponding transport regimes demonstrate the crucial effect of charge diffusion and clarify the transport mechanism near the electrodes.

Furthermore, we carried out the numerical calculation of the devices in tip-plane geometry by using the 2-D DD-SCLC model. Similar to the planar geometry, the vertical transport along the vertical path at the center of the conducting tip exhibits three transport regimes and two virtual electrodes. However, due to the different size of injecting and extracting contacts, *i.e.*, the actual anode and actual cathode, an asymmetric behavior of the virtual electrodes is observed particularly at the low voltage regime.

Next, we examined the effect of traps on the SCLC. In both simplified SCLC model and DD-SCLC model, trap states are assumed to be an exponential distribution of the form (3.4), characterizing by two parameters: (i) trap density (N_t) and (ii) trap temperature (T_t). By assuming the power relation $J(\text{or } I) \propto V^m$, the theoretical current-voltage characteristic simulated from the DD-SCLC model exhibits three distinct regimes corresponding to Ohm's law ($m = 1$), trap-limited SCLC ($m > 2$) and trap-filled SCLC ($m = 2$), ordered from low to high applied voltage. Trap analysis is focused in the trap-limited SCLC regime where trap states are partly filled, which is typically in the range of applied voltage 1 – 10 V. We have found that the fitting exponent m depends on both trap density and trap temperature. However, in the strong trapping limit where the trap temperature is high and the number of traps is large, the fitting exponent depends only on the trap temperature, as previously described by the simplified SCLC theory in equation (2.27). Over the range of the scaled

trap parameters $f_t(N_t) = 00.05$ and $r_t(T_t) = 0.200.40$, the planar geometry yields the fitting exponent in range $m = 1.89 - 5.00$; and the tip-plane geometry yields the fitting exponent in range $m = 2.00 - 5.73$. Particularly in the tip-plane geometry, the mobility anisotropy does not affect the exponent m . This makes the exponent m a suitable fitting parameter for trap characterization in the SCLC regime.

Lastly, we looked into the effect of the nanoscale morphologies on SCLC in the c-AFM geometry. In this study, the semi-crystalline P3HT thin films, including two common fiber orientations: (i) ‘face-on’ and (ii) ‘edge-on’ fibers, are used as the representative systems to demonstrate the effect. The 3-D DD-SCLC model successfully models the nanofibrillar morphologies of semi-crystalline materials, which are composed of isolated nanofibers embedded in an amorphous domain, demonstrating a strongly filamentary structure of the current flow along the percolation path of the high mobility fibers, leading to a significant current enhancement when the conducting tip is in contact with a fiber. The device simulations take the mobility anisotropy of the fibers into account, showing the strong dependence of the hole transport enhancement on the fiber orientation, such that the current simulated when the tip is located on top of the ‘face-on’ fiber is approximately two times larger than that of the ‘edge-on’ fiber. This quantitatively confirms the current enhancement observed in the c-AFM measurements.

Moreover, we found that the lateral and vertical electrical responses of an isolated fiber are very local and over a distance comparable to the tip size, confirming the high resolution of c-AFM measurements. A clear example of this is shown in the study of the more complex morphologies of the ‘edge-on’ fiber network embedded in an amorphous domain. We presented three model morphologies with variations in the fiber spacing, fiber orientation and fiber length. Despite the differences in their nanoscale morphologies, the theoretical current-

voltage characteristics simulated from all three morphologies are consistent with each other, demonstrating the local dependence on tip location rather than the overall morphologies. Additionally, we found that the total current simulated from the case of a fiber network increases by approximately 50% compared to the case of an isolated fiber, owing to the increasing percolation path along the fiber network.

Chapter 5

The Drift-Diffusion SCLC Transport Models - Application to an Experimental System

The hole-only device we model in this chapter is based on the experiments conducted by Jiebing Sun of Dr. Pengpeng Zhang's group at Michigan State University [1]. In the experiment, the effect of a thermal annealing process on P3HT thin film morphology was investigated using c-AFM measurement. It was reported that the crystallinity of P3HT was significantly improved by thermal annealing, based on the comparison of c-AFM images of topography and current maps collected from annealed and non-annealed samples. This is accompanied by the current enhancement observed from the local current-voltage measurement when c-AFM tip is located precisely on top of a crystallized P3HT fiber. Furthermore, thermal annealing also improved the conductivity of P3HT thin films by reducing traps. This is confirmed by the analysis of the current-voltage characteristics of annealed and non-annealed samples.

In order to explain the experimental results, we apply our theoretical models, as described in chapter 3, as well as the trap and morphology analyses presented in chapter 4. First, following the systematic investigation of trap effects on hole-only devices presented in section

4.2, we analyze the c-AFM current-voltage data of annealed and non-annealed samples and also determine the effective hole mobility in the vertical direction. Secondly, the fully 3-D DD-SCLC model was employed to study the transport mechanism leading to c-AFM contrast of annealed samples. The morphology of the film is approximated by the three-dimensional model morphology, as outlined in section 4.3.

5.1 Experiments and Results

According to the publication by Jiebing, *et al.* [1], the hole-only devices were fabricated by the spin-coating process. Transparent indium-tin-oxide (ITO) was used as the bottom electrode of the device. The solution of poly(3,4-ethylenedioxythiophene)/poly (styrenesulfonate) (PEDOT:PSS) was first spin-coated on top of the ITO substrate, followed by the spin-coating of the P3HT solution on top of the PEDOT:PSS film. The annealed samples were later completed by heating at 160° C for 20 min. A platinum (Pt) coated c-AFM tip was selected as the top electrode. The tip contact diameter was estimated to be 12nm. In the current-voltage measurement, the Pt tip was grounded and the biasing voltage was applied to the ITO electrode.

The authors reported a very intriguing feature in P3HT thin films after the thermal annealing process. Unlike those collected from the non-annealed sample, the c-AFM images of topography and current map collected from the annealed sample clearly show the dense fibers of crystallized P3HT, suggesting that these fibers were developed through the annealing process. It was found that these fibers have width of 20 nm and length of several micrometers. The combined techniques of X-ray diffraction (XRD) and ultraviolet-visible (UV-Vis) spectroscopy were used to verify that P3HT formed a crystalline nanofibrillar structure with

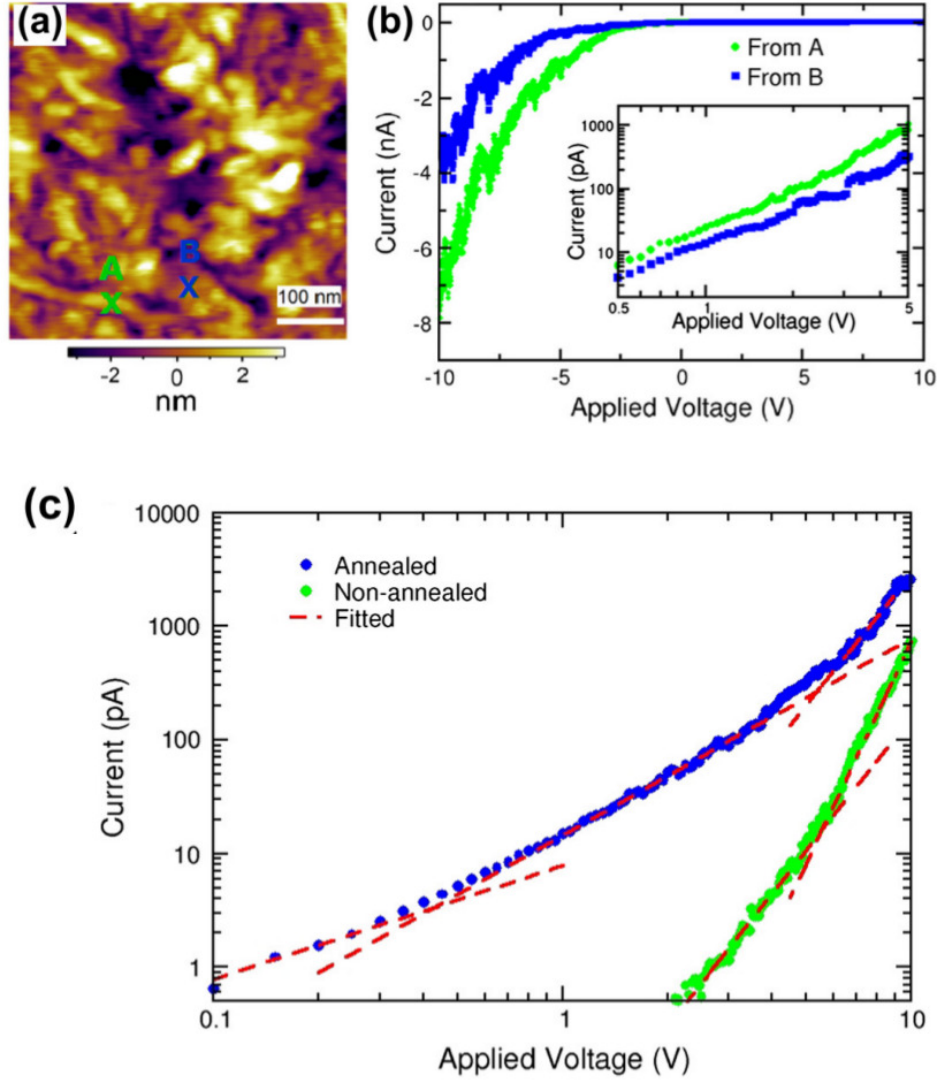


Figure 5.1: Reported in ref. [1], (a) an image of the topography of the annealed sample for fixed-spot current-voltage ($I-V$) measurement; (b) $I-V$ spectra with the tip located on/off the fibers at locations labeled in (a). The inset of (b) shows log-log plots of the $I-V$ spectra ($\text{Log}|I|$ vs. $\text{Log}|V|$) from the negative bias regime. (c) Typical $I-V$ curves in the negative sample bias for annealed samples (blue) and non-annealed samples (green), and the fitting to power laws $I \propto V^m$ (red). For annealed samples, the $I-V$ spectra have three distinct segments: Ohms law ($m = 1$), space-charge limited transport with shallow traps ($m = 2 - 2.25$), and a higher slope regime ($m > 5$) with increase of the applied bias. In non-annealed samples, trap effects are pronounced in the SCLC regime as the exponent is significantly higher ($m = 4 - 5$).

‘edge-on’ orientation as the primary mode.

With the presence of the ‘edge-on’ fiber network, the local variation of electrical conductivity has been determined by c-AFM measurement. Figure 5.1(a) shows the topographic image of the annealed sample marking position A as on a crystallized fiber and position B as on an amorphous region (off fiber). In figure 5.1(b), the corresponding current-voltage responses measured at position A and B exhibit a distinct behavior under positive and negative bias. Under the negative device bias, holes are injected into the device, transport through the P3HT layer, and result in the negative current. The current diminishes as the negatively applied voltage is reduced, and then vanishes when device undergoes the positive bias, where charge transport is prohibited. Since the positively-biased voltage regime has no physical importance, we will focus on the negative device bias case only. The inset of figure 5.1(b) presents the *Log-Log* representation of the absolute values of current-voltage responses in the negatively-biased SCLC regime, showing that c-AFM current is much larger when the measuring tip is located on fiber, even though the fiber is of ‘edge-on’ orientation which exhibits high in-plane mobility. This observation is well-explained by the theoretical study discussed in section 4.3.

More information about the electrical transition of P3HT thin film through the thermal annealing process was also investigated by comparing the charge transport of annealed samples with that of non-annealed samples. To characterize the statistical variation in transport properties across the surface of annealed and non-annealed samples, a number of local current-voltage measurements at different locations on each sample were performed. Figure 5.1(c) shows the typical current-voltage responses of annealed and non-annealed samples, respectively. Quantitatively, at the same applied voltage, the current of annealed samples is much greater than that of non-annealed samples. Assuming the current-voltage relation

as $I \propto V^m$, the current-voltage characteristics of hole-only devices exhibit three different regimes based on the fitting exponent m : (a) Ohm's law regime, (b) trap limited SCLC regime, and (c) anomalous high slope regime, ordered from low to high applied voltage. Particularly in the intermediate voltage regime where traps affect hole transport, the fitting of annealed samples yields the exponent m close to 2 ($m = 2 - 2.25$). Compared to annealed samples, non-annealed samples result in a much larger value of the exponent m typically in the range $m = 4 - 5$. It is clear from the discussion of the trap effects on current-voltage characteristic in section 4.2 that the much steeper dependence of current on voltage is evidence of the higher density of deep traps. The comparison of the c-AFM current-voltage responses measured from annealed and non-annealed samples suggests that thermal annealing also enhances hole transport in the P3HT film by reducing traps.

5.2 Theoretical Simulations and Analyses

Based on the fabrication method reported in the publication, the simple schematic representation of the device structure and the corresponding energy level alignment is illustrated in Figure 5.2. The energy alignment diagram of the interface Pt/P3HT/PEDOT:PSS/ITO, as shown in figure 5.2(b), is based on the values of work functions and HOMO/LUMO level of P3HT given in the literature [92, 93]. It is also important to note that the actual HOMO levels of P3HT and PEDOT:PSS do not exactly match, and a hole injection barrier at this interface was reported [92]. By using ultraviolet photoelectron spectroscopy (UPS), the hole injection barrier was measured to be 0.2 eV, and a much larger interface dipole of -1.0 eV was observed [92]. These two values suggest that fermi-level pinning occurs at this interface, and the potential barrier is negligible.

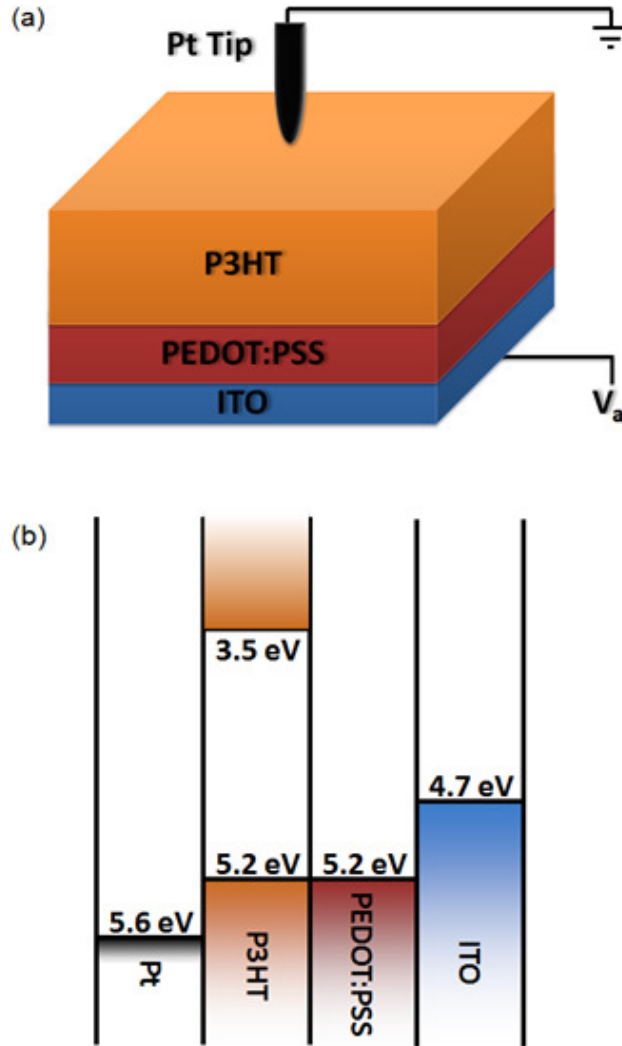


Figure 5.2: The schematic representation of the device structure (a) and the corresponding energy alignment (b) of the hole-only device. This device behaves similarly to a semiconductor diode. When the device is positive biased, no charge carrier transport presents. Conversely, under the negative bias, holes are injected from Pt probe into the system, traveling through the layer of P3HT and PEDOT:PSS, and collected at the ITO contact; while electrons injected from ITO cannot transport into the system due to the layer of PEDOT:PSS. Therefore, this is the hole only injection system.

The device design brings an essential difference between positive- and negative- bias. When the device is positively biased, both electron and hole transports are prohibited. In contrast, under the negative bias, current can be observed. Holes are injected from Pt tip into the device, traveling through the layer of P3HT, and later collected at the ITO electrode. Electrons, on the other hand, are injected from ITO electrode, but cannot transport into the P3HT layer due to the PEDOT:PSS electron blocking layer. Therefore, this device allows us to investigate the single carrier transport of holes in P3HT when applying the negative bias. These behaviors of the device under the positive and negative biases were confirmed by the current-voltage data taken by c-AFM measurement, as previously shown in figure 5.1(b), which is the characteristic of hole-only devices.

The numerical calculations of the DD-SCLC model, as previously explained in chapter 3, were performed to study hole transport in the device. However, one minor adaptation has been made on the electrode boundary conditions to particularly match the behavior of the fabricated P3HT devices under the bias from c-AFM tip, assuming the perfect hole extraction at the bottom electrode. The modified boundary conditions are written as

$$\psi = 0 \quad \text{and} \quad p_f = N_v \quad \text{at the c-AFM tip} \quad (5.1a)$$

$$\psi = -V \quad \text{and} \quad p_f = 0 \quad \text{at the bottom (planar) electrode} \quad (5.1b)$$

This is similar to the boundary conditions used in the simulation of hole-only device by Reid *et al.* [32]. Unless stated otherwise, the parameters used in the device simulations presented in this chapter are summarized in table 5.1.

Table 5.1: Summary of parameters used in the device simulations to analyze c-AFM data

Parameter	Symbol	Numerical value
Dielectric constant	ε_r	3.0
The effective density of states in the HOMO	N_v	10^{21} cm^{-3}
Tip contact diameter	D	12 nm
Temperature	T	300 K
Device thickness	L	80 nm

5.2.1 Trap and Mobility Anisotropic Effects

Evidently, the current-voltage characteristics of hole-only devices obey power laws. In the low and intermediate applied voltage regimes, the c-AFM current-voltage data are in good agreement with the theoretical current-voltage relations simulated using the 2-D DD-SCLC model with tip-plane geometry, and hole transport behaviors can be described by Ohm's law and the theory of SCLC in the presence of traps, respectively (See section 4.2.2 for detailed discussion). However, in the high applied voltage regime, one can observe a much steeper increase of current with applied voltage than predicted by the model. This discrepancy is possibly attributed to the mobility enhancement due to the electric field, so called 'Poole-Frenkel' mobility [32], which is not integrated in the model.

In this section, the systematic method to study trap effects in hole-only devices presented in section 4.2 is used to analyze the c-AFM current-voltage responses in the intermediate applied voltage regime, which is typically between 0.5V and 5V, and also to determine the effective hole mobility in the vertical direction of P3HT samples. First, extensive device simulations over the wide range of traps and a considerable range of hole mobility anisotropy were performed using the parameters summarized in table 5.1. To accommodate the spreading effect, we consider the calculation domain as a circular cylinder of 750nm radius and

80nm thickness. The c-AFM tip is approximated by a circular contact of 6nm radius. In the model, traps are described by the energy states distributed exponentially within the band gap, which are characterized by parameters $f_t = N_t/N_v$ and $r_t = T/T_t$ where N_t is trap density and T_t is trap temperature. The mobility anisotropy is reflected by the ratio of the in-plane (lateral) mobility to the out-of-plane (vertical) mobility (μ_ρ/μ_z). The mobility anisotropic ratio ranges from 1 (isotropic case) to 25, which is the strongest mobility anisotropy observed in P3HT thin films composed of semi-crystalline whiskers [67].

Examples of theoretical current-voltage characteristics of hole-only devices in tip-plane electrode configuration are illustrated in figure 5.3. Figure 5.3(a) shows the dependence of theoretical current-voltage relations on mobility anisotropy in the low deep trap regime ($f_t = 0.001$, $r_t = 0.30$); figure 5.3(b-c) show the current-voltage relations simulated with an isotropic mobility when (b) $f_t = 0.005$ with varying r_t and (c) $r_t = 0.35$ with varying f_t . These data are plotted in the intermediate applied voltage regime involving the trap filling process in space-charge limited transport, which can be described by the semi-empirical expression (4.4). Afterwards, the fitting of all simulated current-voltage relations yield the fitting parameter k_I and the fitting exponent m , summarized in table A.3 of appendix A. Figure 5.4 shows the contour plot of the exponent m as a function of trap parameters f_t and r_t . The exponent m varies from 1.96 to 5.52 corresponding to trap parameter variations of $f_t = 0 - 0.05$ and $r_t = 0.20 - 0.40$. Next, we will present how to determine the effective hole mobility in the vertical direction through the analysis of the experimental data.

To determine the effective hole mobility in the vertical direction represented by μ_o in the semi-empirical expression (4.4), we started by fitting the experimental current-voltage relations in the intermediate applied voltage regime with a power law, then obtained the values of the coefficient $\mu_o \cdot k_I$ and exponent m . Since the exponent m is fixed for each

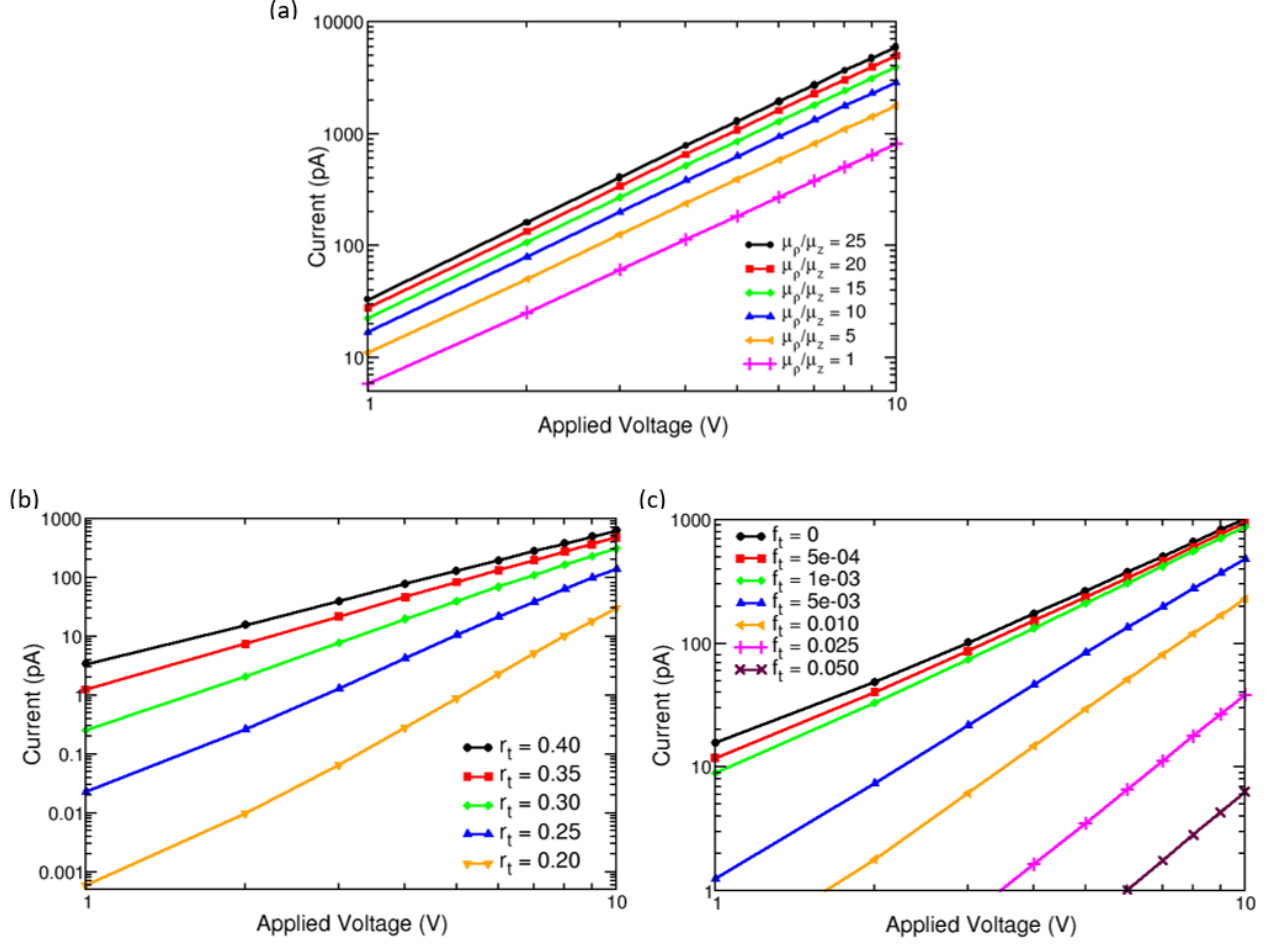


Figure 5.3: Based on the setup of c-AFM measurements [1], the theoretical current-voltage characteristics in the SCLC regime are well-described by the semi-empirical expression (4.4) when (a) trap parameters is fixed ($f_t = 0.001$ $r_t = 0.30$) with varying mobility anisotropic ratios μ_ρ/μ_z ; (b) mobility is isotropic and $f_t = 0.005$ with the varying r_t yielding the exponent in range $m = 2.31 - 5.19$; and (c) mobility is isotropic and $r_t = 0.35$ with varying f_t yielding the exponent in range $m = 1.96 - 3.61$.

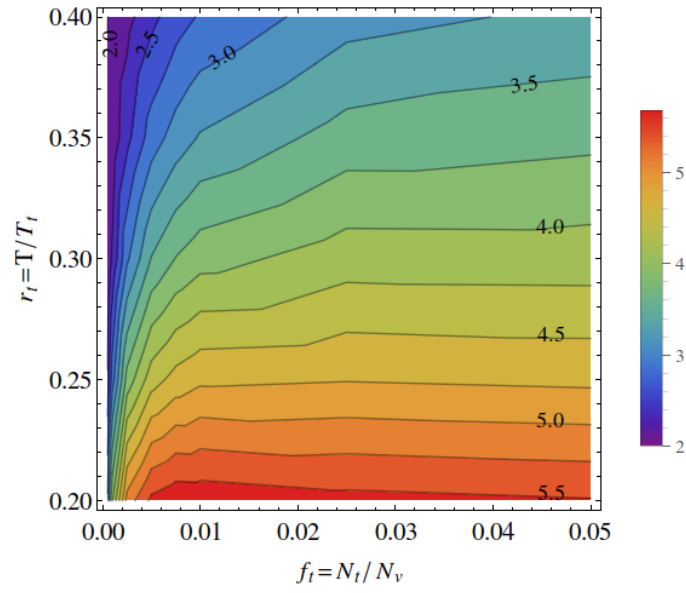


Figure 5.4: Dependence of the exponent m on the parameters f_t and r_t for hole-only devices in the SCLC regime, resulting from extensive calculations of theoretical current-voltage characteristics demonstrated in figure 5.3 [1].

current-voltage curve, the values of f_t and r_t can only be taken along a contour line of the plot in figure 5.4 that has the same value of m . We then compiled a table of k_I values with respect to f_t , r_t and μ_ρ/μ_z , and deduced the mobility μ_o from the fitting coefficient.

Let us begin with the analysis on c-AFM current-voltage data of the annealed samples. In the experiment, the exponent m found from current-voltage responses at different locations in the films exhibits a significantly larger variation as compared to the local variation of current-voltage responses when the c-AFM tip is located on and off a fiber. This is a clear evidence that the transport still is dominated by local traps in the amorphous regimes. Using an average mobility anisotropy is then a reasonable approximation of fibrous morphology in characterizing transport of the semi-crystalline P3HT film. Figure 5.5 illustrates how the theoretical current-voltage characteristics apply to the experimental results of annealed samples. Figure 5.5(a-b) show a representative example of c-AFM current-voltage response measured from annealed P3HT films, *i.e.*, both data (black dots) are identical. The dashed red lines are fits using theoretical current-voltage characteristics simulated from two distinct pairs of trap parameters that result in the same value of m : (a) $f_t = 0.0005$ and $r_t = 0.35$, (b) $f_t = 0.001$ and $r_t = 0.40$. Clearly, agreement with the experimental data is excellent. Additionally, table 5.2 lists four representative pairs of trap parameters f_t and r_t that provide a good fit to the current-voltage response. As the result, the effective mobility demonstrates a weak dependence on trap parameters f_t and r_t , while it is strongly dependent on the mobility anisotropy, exhibiting approximately an order of magnitude difference from the lowest to the highest values of anisotropic ratio. Therefore, the vertical mobility of each current-voltage curve is approximated by averaging the values fitted over the range of valid trap parameters.

By carrying out the extensive analysis of a total of 48 c-AFM current-voltage responses

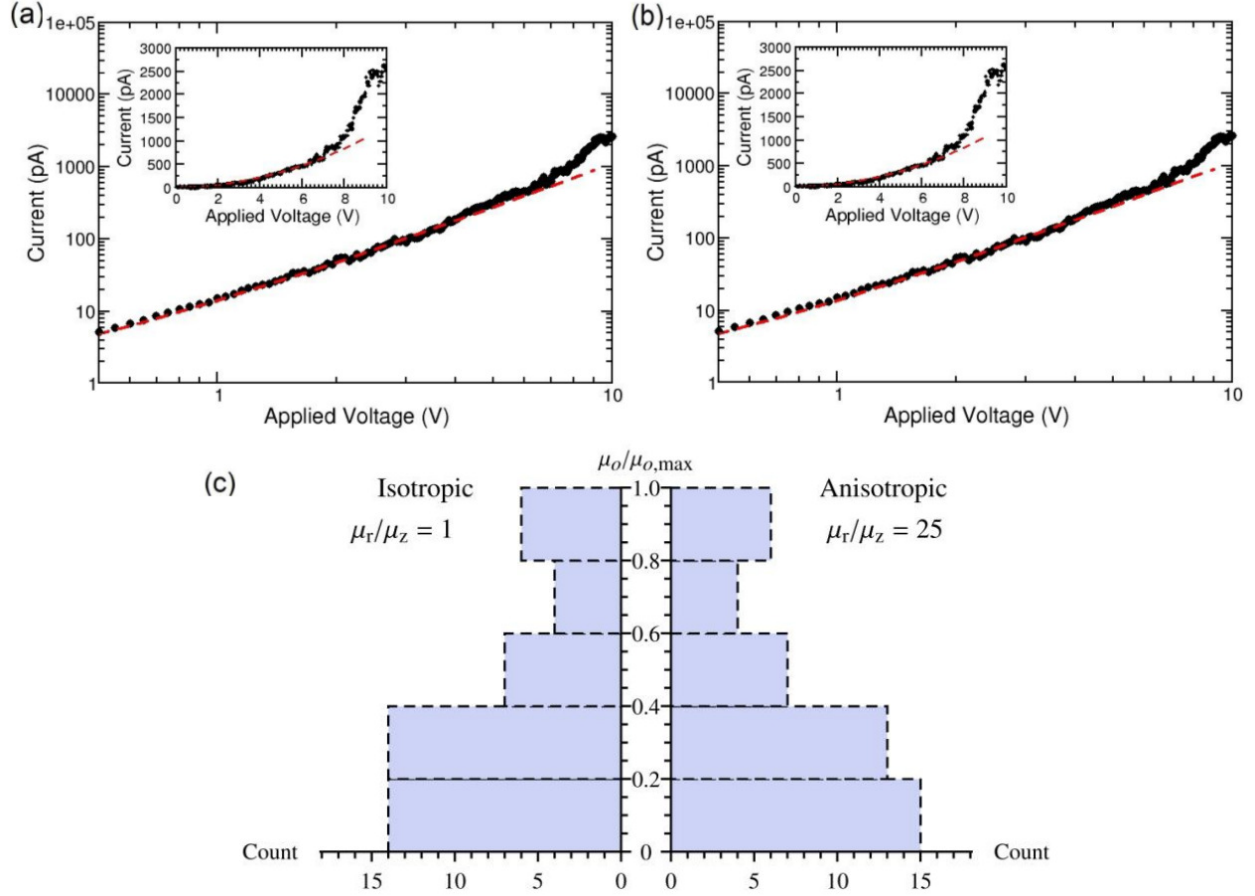


Figure 5.5: The representative current-voltage ($I-V$) response from the annealed sample (solid circle) is fitted to the theoretical $I-V$ relation (solid red line) in the low trap regime with two pairs of trap parameters that result in the same slope: (a) $f_t = 0.0005$ and $r_t = 0.35$, (b) $f_t = 0.001$ and $r_t = 0.40$. Shown in the inset are the same plot in linear scale. (c) A histogram of the normalized vertical hole mobility extracted from 48 $I-V$ datasets on the annealed P3HT film, with the comparison of an isotropic model and an anisotropic model with $\mu_r/\mu_z = 25$. The mobility is normalized to the maximum value of each case.

of annealed samples, we found that the exponent m is fitted in the narrow range of $2 - 2.25$, suggesting that annealed samples exhibit the low deep trap regime with trap parameters $f_t = 0 - 0.001$ and $r_t = 0.30 - 0.40$. Figure 5.5(c) shows the histogram of the vertical mobilities found from the 48 locations on annealed films when assuming isotropic mobility and anisotropic mobility of $\mu_\rho/\mu_z = 25$. Regardless of the mobility model, the effective mobilities, which are normalized to the maximum, demonstrates the same distribution. This scalable property of mobility anisotropy is a signature of low deep trap regime, resulting from the linear dependence of the fitting parameter k_I on the mobility anisotropic ratio. Unfortunately, we cannot simplify the semi-empirical expression (4.4) further since this linear relation between k_I and μ_ρ/μ_z still depends on trap parameters. Varying the mobility anisotropic ratio yields the effective mobility in the vertical direction, as summarized in table 5.3. Assuming isotropic mobility, we found the effective mobility of $2.01 \pm 1.46 \times 10^{-4} \text{ cm}^2 \text{ V}^{-1} \text{ s}^{-1}$. This is consistent with the values of hole mobility measured experimentally [32, 35, 94], validating the methodology used in this study. However, it is inevitable to raise the question on the magnitude of mobility anisotropy. The effective mobility extracted from the anisotropic model, especially when $\mu_\rho/\mu_z \geq 10$, is significantly lower than what has been reported. We speculate that semi-crystalline P3HT films produced by thermal annealing may not exhibit anisotropic conductivity as strong as that composed of whisker-type nanofibers. To prove this statement, further measurements of hole mobility in the device geometry are needed.

Compared to annealed samples, the extensive c-AFM current-voltage measurements at different locations on non-annealed samples yield a significantly steeper exponent m in the range of $4 - 5$, indicating a higher density of deep traps. From the contour plot of the exponent m shown in figure 5.4, one can find the corresponding trap parameters in the range of $f_t = 0.0025 - 0.05$ and $r_t = 0.20 - 0.25$. In addition, the authors reported no clear visualization

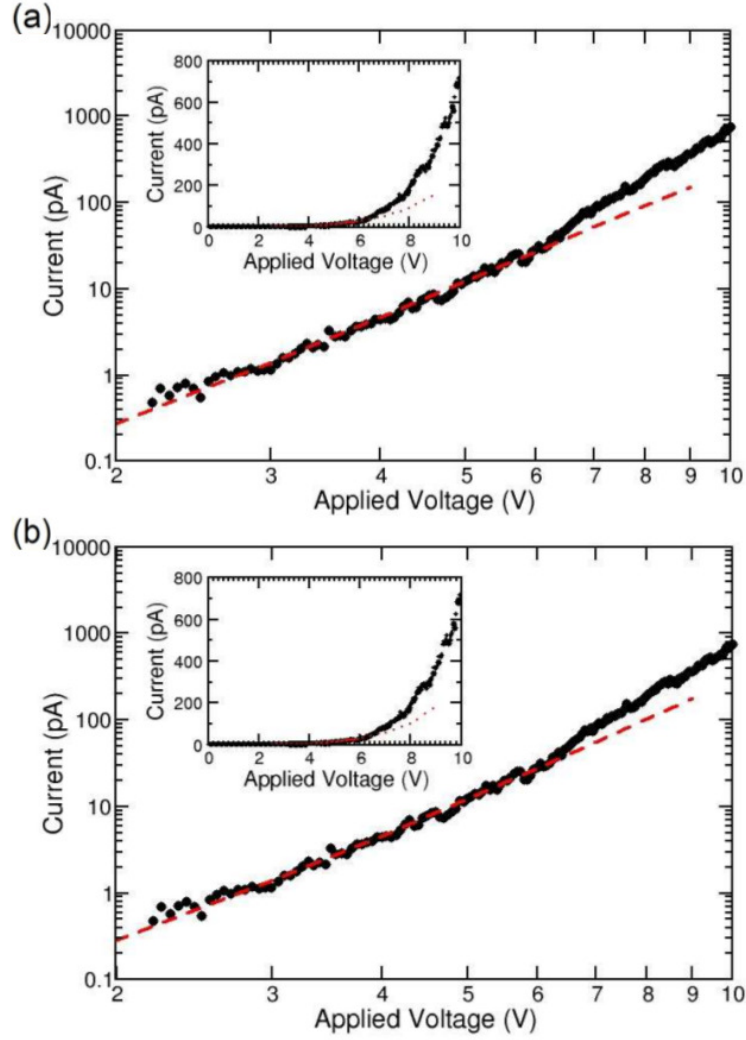


Figure 5.6: The representative current-voltage response from the non-annealed sample (solid circle) is fitted to the theoretical current-voltage relation (solid red line) in the low trap regime with two pairs of trap parameters that result in the same slope: (a) $f_t = 0.0075$ and $r_t = 0.25$, (b) $f_t = 0.01$ and $r_t = 0.25$. Shown in the inset are the same plot in linear scale.

Table 5.2: The effective mobilities in the vertical direction found from fitting a representative examples of c-AFM current-voltage responses measured from an annealed P3HT sample for a range of anisotropic ratios.

$f_t = N_t/N_v$	$r_t = T/T_t$	Effective mobility ($\times 10^{-5} cm^2 V^{-1} s^{-1}$)					
		$\mu_p/\mu_z = 1$	$\mu_p/\mu_z = 5$	$\mu_p/\mu_z = 10$	$\mu_p/\mu_z = 15$	$\mu_p/\mu_z = 20$	$\mu_p/\mu_z = 25$
7.50E-04	0.40	11.67	5.19	3.21	2.36	1.87	1.56
5.00E-04	0.40	11.16	4.93	3.04	2.23	1.78	1.48
5.00E-04	0.35	11.77	5.26	3.25	2.39	1.90	1.59
1.00E-03	0.40	12.21	5.47	3.39	2.49	1.98	1.65
Average		11.70	5.21	3.22	2.36	1.88	1.57

Table 5.3: An analysis of point-to-point variation in transport properties across the film is presented for c-AFM data taken at 48 locations on the surface of an annealed sample. The average, standard deviation, minimum and maximum of the effective mobility in the vertical direction found from fitting the experimental data for a range of anisotropic ratio.

μ_p/μ_z	Effective mobility ($\times 10^{-5} cm^2 V^{-1} s^{-1}$)			
	Mean	SD	Min	Max
1	20.14	14.55	2.89	49.63
5	9.14	6.84	1.25	23.39
10	5.69	4.27	0.77	14.68
15	4.19	3.14	0.57	10.82
20	3.33	2.50	0.45	8.61
25	2.78	2.08	0.38	7.17

Table 5.4: The effective mobilities in the vertical direction found from fitting a representative example of c-AFM current-voltage responses measured from a non-annealed P3HT sample

$f_t = N_t/N_v$	$r_t = T/T_t$	Effective mobility ($\times 10^{-5} cm^2 V^{-1} s^{-1}$)
2.50E-03	0.20	7.97
6.00E-03	0.25	20.10
7.50E-03	0.25	45.29
1.00E-02	0.25	128.16

of crystallized P3HT nanofiber observed in the c-AFM images of non-annealed samples. Without the morphological origin of anisotropic hole transport, we assume hole mobility in non-annealed films to be isotropic. In figure 5.6, a representative example of current-voltage response was fitted with two theoretical current-voltage characteristic (dashed red lines) individually simulated from two pairs of trap parameters that result in the same value of m : (a) $f_t = 0.0075$ and $r_t = 0.25$, (b) $f_t = 0.01$ and $r_t = 0.25$. Clearly, agreement with the experimental data is excellent. Consequently, table 5.4 lists three representative pairs of trap parameters f_t and r_t that achieve a good fit to the current-voltage response. Unlike the annealed sample, the vertical mobility is strongly dependent on trap parameters f_t and r_t . It was in fact revealed that to base the estimate of vertical mobility on the fitting of experimental current-voltage relations led to unrealistic results. Characterization of trap parameters using thermally stimulated current [95, 96], transient spectroscopy [97, 98, 99, 100, 101], or impedance spectroscopy techniques [44, 102, 103, 104, 105] will be required. If we assume that the hole mobility of non-annealed samples is similar to that of annealed samples, the representative example of c-AFM current-voltage response measured from non-annealed samples can be described using trap parameters $f_t = 0.006$ and $r_t = 0.25$, corresponding to significantly more concentration of traps from the deeper states of the DOS distribution when compared to an annealed sample. Evidently, the thermal annealing process enhances the current flow in the film by reducing traps.

5.2.2 Traps and Morphological Effects

The assumption of the cylindrical symmetry used in the analysis of c-AFM data is helpful to elucidate the anisotropic aspect of the carrier transport without introducing the complexity of fully three-dimensional calculations. However, to examine the ability of c-AFM to resolve

the semi-crystalline fiber structures observed in annealed P3HT sample, it is necessary to consider the fully 3-D DD-SCLC model presented in section 3.5. To illustrate the effect, we carried out device simulations, incorporating the nanoscale morphology of a high mobility fiber network embedded in a low mobility background.

In the numerical calculations, we adopted a three-dimensional device domain of $600nm \times 600nm$ in cross-section and $80nm$ in thickness, and modeled the c-AFM tip as a square contact of the size $10nm \times 10nm$. To illustrate the morphological effect observed in c-AFM measurements, we considered the case of a high mobility fiber network embedded in a low mobility background. In the study of ‘edge-on’ P3HT fiber network presented in section 4.3, we observed a consistent theoretical current-voltage characteristic across three model morphologies with a variety of random fiber spacing, random fiber orientation and random fiber length. In this study, we thus choose the simplest morphology with a single randomness of the in-plane spacing between fibers. Similar to assumptions made in the preliminary study, both in-plane and out-of-plane fiber crossing are forbidden while periodic boundary conditions are maintained on the four sides of the device that are not connected to the electrodes. Figure 5.7 shows the $600nm \times 600nm$ cross-section of the representative morphology at the vertical position z . As depicted by green wires, each crystallized P3HT fiber has the size of $20nm$ width and $5nm$ thickness based on the literature [1,31,36,37,38,87]. The background region in brown is then classified as amorphous P3HT. The fraction of fiber in the cross-section area is chosen to be 0.33, which is roughly consistent with the fiber density evaluated from c-AFM images of the annealed samples. One of the key aspects observed in ‘edge-on’ fibers is the mobility anisotropy. In the device simulations, the lateral mobility along the $\pi - \pi$ stacking direction ($[0\ 1\ 0]$) and in the polythiophene backbone direction ($[0\ 0\ 1]$) are taken to be 100 times larger than the vertical mobility along the alkyl

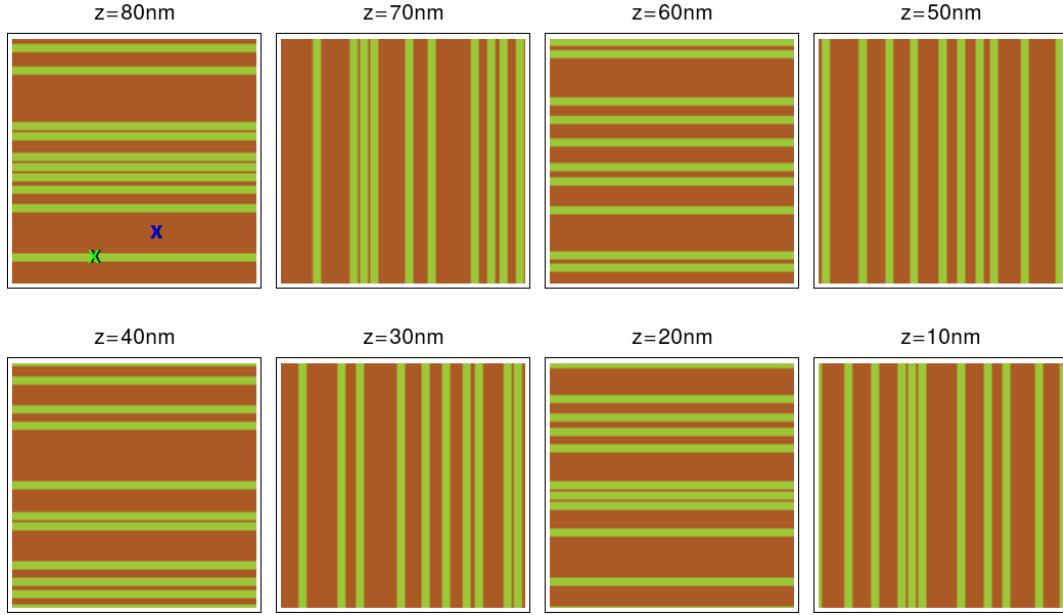


Figure 5.7: The $600nm \times 600nm$ cross-sections of the representative morphology at the vertical position z in the device thickness direction demonstrating the crystallized P3HT fibers of $20nm$ width (green wires) aligned with random spacing in the amorphous region (brown area). The fiber fraction of cross-section surface area is 0.33. The bottom electrode is placed at $z = 0nm$, and the locations of tip contact are marked on the $z = 80nm$ cross-section for the on-fiber and off-fiber c-AFM simulations.

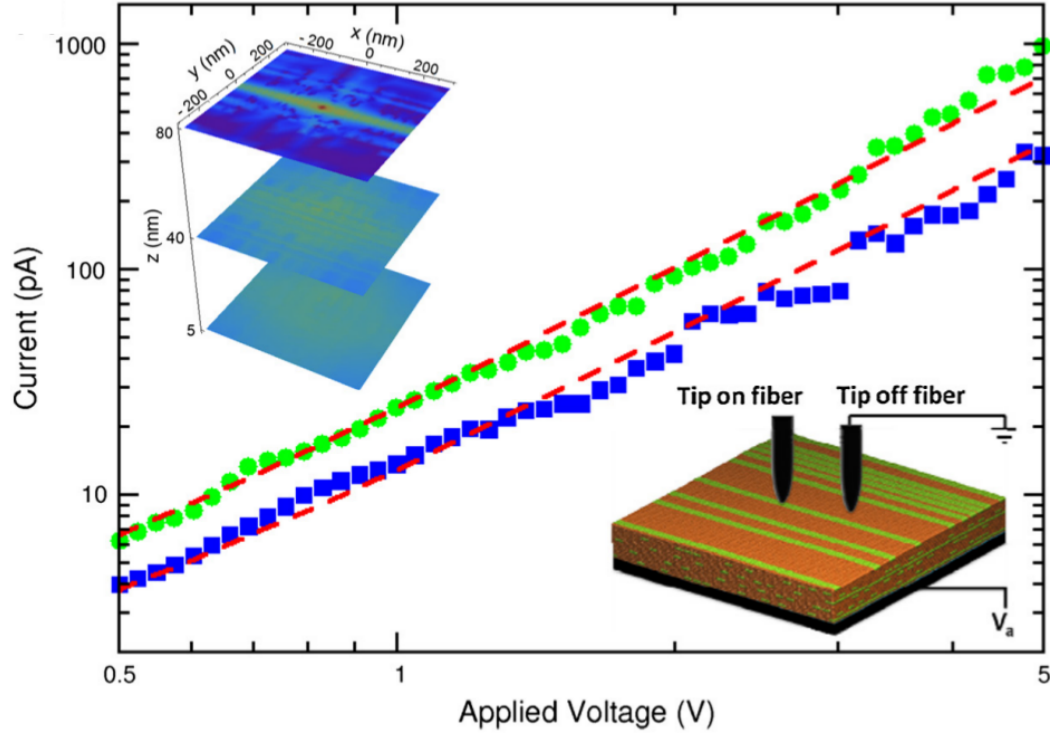


Figure 5.8: Adapted from [1], the on-fiber and off-fiber current-voltage responses of the annealed P3HT sample are well described by the theoretical current-voltage characteristics simulated from the representative 3-D morphology of an ‘edge-on’ fiber network shown in the inset on the bottom-right corner. (see figure 5.7 for cross-section morphology) To describe the anisotropic transport in fibers (green), the in-plane mobility is 100 times larger than the vertical mobility and the background mobility of amorphous region (brown). The background mobility is fitted to be $7.78 \times 10^{-5} \text{cm}^2 \text{V}^{-1} \text{s}^{-1}$ with trap parameters $f_t = 1.00 \times 10^{-3}$ and $r_t = 0.30$. In the inset on the top-left corner, the vertical current flow when the c-AFM tip is located on the fiber is visualized.

side chain direction $([1\ 0\ 0])$ [65, 67, 90, 91]. On the other hand, the hole transport in the amorphous region is assumed to be isotropic with the mobility that is the same value as that of alkyl side chains [34, 67].

To simulate the c-AFM measurements, we performed the device calculations when the tip is located on the fiber and on the amorphous region (off the fiber). The tip locations are indicated on the cross-section image at $z = 80nm$, as shown in figure 5.7. Figure 5.8 illustrates how the theoretical current-voltage characteristics apply to the experimental on-fiber and off-fiber current-voltage responses. The dashed red lines are fits using on-fiber and off-fiber current-voltage characteristics simulated using the trap parameters $f_t = 0.001$ and $r_t = 0.30$, yielding the isotropic mobility of amorphous phase $7.78 \times 10^{-5} cm^2 V^{-1} s^{-1}$. Clearly, agreement with the experimental data is excellent. Evidently, a strong enhancement of current flow can be observed when tip is located on fiber, elucidating the contrast visualized in the c-AFM current map, as discussed in chapter 4.

5.3 Conclusions

In this chapter, we utilized the 2-D and 3-D DD-SCLC models to analyze the current-voltage responses of c-AFM measurements on hole-only devices fabricated from semiconducting P3HT. Experimentally, the comparison of typical current-voltage responses measured from annealed and non-annealed films has shown the correlation between the enhancement of c-AFM current and the thermal annealing process. By assuming the power relation $I \propto V^m$, the annealed samples yield an exponent m close to 2 ($m = 2 - 2.25$) while the non-annealed samples exhibit a much steeper exponent in the range of $m = 4 - 5$. The application of the numerical tool based on the 2-D DD-SCLC model confirms that the thermal anneal-

ing process has significantly enhanced the hole transport in P3HT film by alleviating the effect of traps. Furthermore, statistical analysis of 48 annealed samples suggest that the device corresponds to the low trap regime with trap parameter $f_t = 1.08 \pm 0.28 \times 10^{-3}$ and $r_t = 0.35 \pm 0.04$. By assuming that hole mobility in such devices is isotropic, the effective mobility in the vertical direction is estimated to be $2.01 \pm 1.46 \times 10^{-4} \text{ cm}^2 \text{ V}^{-1} \text{ s}^{-1}$. This is consistent with experiments [32, 35, 94], confirming the validity of the numerical model and methodology used in the analysis. However, if the device mobility is anisotropic, the effective mobility in the vertical direction can be much lower. The comparison of current-voltage data from c-AFM and device measurements is needed to determine the degree of mobility anisotropy as well as the vertical mobility of holes in the annealed samples.

Additionally, the thermal annealing process improve the crystallinity of P3HT films. The c-AFM image of annealed films shows a large spatial variation of the vertical current, indicating a nanoscale morphology comprised of nanofibers and the lower conductivity background. Further characterization using X-ray diffraction and UV-Vis spectroscopy indicates the development of self-organized P3HT nanofibers with the ‘edge-on’ orientation as the primary mode. By incorporating the three-dimensional model morphology of a nanofibrillar network, the simulation based on the 3-D DD-SCLC model in tip-plane geometry has demonstrated the current enhancement when the conducting tip is in contact with the fiber, which visualizes the c-AFM contrast of fibrous films.

Chapter 6

Conclusions

The simplified SCLC theory is a well-established model to explain the unipolar transport in disordered organic semiconductors. However, a shortcoming lies within the assumption that charge diffusion can be neglected. This can lead to the misinterpretation of experimental data when the effect of charge diffusion in the devices is no longer negligible. In this thesis, we developed numerical approaches that efficiently simulate the hole-only SCLC model with the full description of hole drift and diffusion transport mechanisms, *i.e.*, the DD-SCLC model. In the case of fully 3-D calculations, the numerical model is able to treat inhomogeneous systems including spatially varying trap distributions, nanoscale morphologies, and the tip-plane (c-AFM) geometry. The application of the model to the analysis of c-AFM experimental data is presented.

Starting in chapter 2, we provided an overview to the fundamental concepts of injection and transport mechanisms of charge carriers in disordered organic semiconductor devices, and further delved into the simplified SCLC theory which describes the drift-dominated unipolar SCLC. While the earlier work by M.A. Lampert and P. Mark [43] was focused on electron-only SCLC, we demonstrated the analytical derivation of the simplified SCLC theory for holes. As the result, the analytical expressions to describe the relation of hole current to externally applied voltage for the trap-free devices, *a.k.a.* the *Mott-Gurney* equation, and for the devices with the exponentially distributed trap density are summarized in Table 2.1. For

the application to c-AFM measurements, we provided a brief review of the semi-empirical formula by O.G. Reid *et al.* [32] which modified the Mott-Gurney equation to include the effect of tip geometry. While organic semiconductors are typically energetically disordered, to the best of our knowledge, the theoretical model to describe trap-limited SCLC in the c-AFM or tip-plane geometry has never been introduced.

In chapter 3, we introduced the *drift-diffusion* (DD) SCLC model, as in its name, describing hole-only SCL transport by both drift and diffusion mechanisms. The inhomogeneous systems, including spatially varying trap distributions, nanoscale morphologies, as well as tip-plane (c-AFM) geometry are also incorporated. As a matter of fact, traps are commonly found in disordered organic semiconductors, and thus we modelled the trap DOSs for holes as the tail states of HOMO DOS toward the energy gap, which is well approximated by the exponential distribution [43, 44]. The DD- SCLC model is governed by three equations, including Poisson’s equation, the drift-diffusion equation for holes, and the continuity equation at steady state. To stabilize the numerical calculations, we apply the Scharfetter-Gummel discretization [54] to the drift-diffusion equation, then numerically solve the three governing equation simultaneously, similar to the numerical scheme used by L.J.A. Koster *et al.* [52].

We successfully developed the numerical tools for the DD-SCLC model in one-, two-, and three- dimensional systems. Among the three models, the 1-D DD-SCLC model is the simplest one and improves on the simplified SCLC model by including the mechanism of charge diffusion. While the 1-D DD-SCLC model is numerically much more efficient than the fully 3-D SCLC model, the trade-off is the possibility to include the spatially distributed traps, the nanoscale morphologies, and the c-AFM geometry. Unlike the 1-D and 3-D DD-SCLC model that are discretized in Cartesian coordinate system, the 2-D DD-SCLC model is set up in a system with cylindrical symmetry. Thus, the 2-D DD-SCLC model is very

efficient to simulate the SCLC in the c-AFM geometry with mobility anisotropy in the lateral and vertical transport. All 1-D, 2-D, and 3-D DD-SCLC models are verified to be consistent with each other, and validated to be consistent with the simplified SCLC theory in the drift-dominated regime.

The simplified SCLC theory is only the first step to understand the SCL transport in hole-only device, yet far from complete. We saw in chapter 4 that, while the theory has made a major assumption that charge diffusion is negligible in the devices, the theoretical hole carrier density is not uniformly distributed, leading to the extremely large amount of diffusion current near the injecting electrode. This discrepancy becomes more severe with decreasing applied voltage, demonstrating the importance of treating charge diffusion in device modeling. What is its effect on the SCLC? To answer these question, we have achieved the prerequisite task by successfully developing the numerical tools for the DD-SCLC model, and the device simulations, as addressed in chapter 4, have revealed a number of important factors that affect the SCLC, including charge diffusion, traps, as well as nanoscale morphologies.

First, we investigated the effect of charge diffusion on the trap-free SCLC. Unlike those predicted by the simplified SCLC theory for the hole-only device in planar geometry, the theoretical profiles of electric potential and hole density simulated by using the 1-D DD-SCLC model have a non-monotonic distribution along the device thickness, exhibiting three distinct transport regimes: (i) diffusion-dominant transport regime, (ii) drift-diffusion assisted transport regime, and (iii) drift-dominant transport regime, parting from the injecting electrode to the extracting electrode. Two separations of the three transport regimes are determined by (I) the position of the potential maximum, where the local electric field and the correspondent drift current vanish; and (II) the position of the hole density minimum, where the

diffusion current become zero. These separations are consistent with the boundary conditions at the electrode of the simplified SCLC theory, and thus we reintroduced these turning points as the *virtual* electrodes since they are no longer the *actual* ones in the DD-SCLC model. The extensive device simulations over the range of applied voltage have shown that the positions of the *virtual* electrodes move toward the *actual* electrodes with increasing applied voltage. Moreover, we have found that the diffusion current plays an important role near the *actual* injecting electrode, as in transport regime (i), by overcoming the reverse drift current and driving holes away from the contact. Furthermore, the device simulations in tip-plane geometry have demonstrated similar transport regimes, but with an asymmetric behavior of the *virtual* electrodes due to the different size of the *actual* injecting and extracting electrodes. The dynamics of the *virtual* electrodes and the concurrent transport regimes demonstrate the crucial effect of charge diffusion on the SCLC, and also clarify the transport mechanisms near the electrodes that can never be explained by the simplified SCLC theory.

Traps affect the SCLC significantly. We found that the theoretical current-voltage characteristics obey the power relation $J(\text{or } I) \propto V^m$, exhibiting three distinct regimes, corresponding to Ohm's law ($m = 1$), trap-limited SCLC ($m > 2$), and trap-filled SCLC ($m = 2$), ordering from low to high applied voltage. To analyze the effect of traps, we focused on the trap-limited SCLC regime where trap states are partly filled, typically found in the range of applied voltage 1 – 10V. Extensive device simulations have shown that the fitting exponent m depends on two parameters of the field-independent exponential distribution of trap DOSs, including total trap density and trap energy level. However, in the strong trapping limit where the trap temperature is high and the number of traps is large, the fitting exponent depends only on the trap temperature. This strong trap case is previously predicted by the simplified SCLC theory, as described in equation (2.27). Particularly in the tip-plane

geometry, the mobility anisotropy does not affect the exponent m . This makes the exponent m a suitable fitting parameter to characterize traps in the SCLC regime.

Lastly, we examined the effect of the nanoscale morphologies on the SCLC in the tip-plane geometry, in analogy to the c-AFM measurements. The semi-crystalline P3HT thin films, which consist of a mixture of crystalized nanofiber and amorphous domain, is chosen as the reference system to demonstrate the effect. We found that the percolation nature of hole transport in the disordered organic semiconductor yields a strongly filamentary structure of the current along the percolation paths of the high mobility fibers, leading to a significant current enhancement when the conducting tip is in contact with the fibers. Moreover, it has been shown that the lateral and vertical electrical responses of the nanofiber are very local and in a probed distance comparable to the tip size. These observations quantitatively confirm the high resolution of c-AFM measurements, supporting c-AFM as a very useful tool to study the local electrical properties and local morphologies simultaneously.

On the aspect of the application to the experiments, in chapter 5, we utilized the DD-SCLC model to elucidate the c-AFM measurements on the P3HT based hole-only devices. The experiments addressed in this chapter were carried out by Professor Zhang's group at Michigan State University [1], aiming to investigate the effect of thermal annealing process on the electrical properties and nanoscale morphologies of the P3HT thin films. With the device simulations of the 2-D DD-SCLC model, we have shown that the thermal annealing process has significantly improved hole transport in P3HT thin films by alleviating the effect of traps, yielding the effective mobility of an annealed device that is consistent with previously published experiments. Furthermore, the 3-D DD-SCLC model enables the simulation of hole transport in the semi-crystalline P3HT thin film, consisting of a mixture of crystalized P3HT nanofibers and amorphous P3HT domains. By incorporating the 3-D model morphology of

the nanofibrillar network, the device simulation in the tip-plane geometry has evidently shown the current enhancement when the conducting tip is in contact with the fiber, which demonstrates the c-AFM contrast of fibrous films.

While the current state of DD-SCLC model is limited to the numerical solutions, the model polishes our understanding of hole transport with the full description of drift and diffusion, and elucidates mechanisms missing from the simplified SCLC theory. The DD-SCLC model can be significantly improved by considering the field-dependent hole carrier density as a boundary condition at the electrodes, based on the expression by J.C. Scott and G.G. Malliaras [106]. Furthermore, the accuracy of the DD-SCLC model in the high voltage regime can be enhanced by including the field- and carrier-density- dependent mobilities, the so-called ‘Poole-Frankel’ model [39, 107] and ‘Pasveer’ model [39, 108], respectively, as well as using the general form of Einstein relation to describe the charge diffusion coefficient. We anticipate that these improvements will lead to more realistic models, shedding light on the investigation of charge transport in disordered organic semiconductors. To have a clearer understanding on the subject would be very beneficial, not only for developing future organic photovoltaics (OPVs), but also other organic semiconductor devices such as organic light emitting diodes (OLEDs) and organic field-effect transistors (OFETs).

APPENDIX

Appendix A

Fitting Parameters of Theoretical Current-Voltage Characteristics

Table A.1: Summary of parameters m and k_J estimated by fitting theoretical current-voltage characteristics of planar devices in the SCLC regime (see section 4.2.1 for details of device simulations) to the semi-empirical expression (4.3) for a range of trap parameters f_t and r_t . Note that R-square of regression is high ($R^2 > 0.9999$).

$f_t = N_t/N_v$	$r_t = T/T_t$	m	k_J	$f_t = N_t/N_v$	$r_t = T/T_t$	m	k_J
0.00E+00	0.00	1.89	9.55E+02	5.00E-03	0.30	3.02	1.97E+01
5.00E-04	0.20	2.38	3.01E+02	5.00E-03	0.35	2.54	9.59E+01
5.00E-04	0.25	2.04	5.60E+02	5.00E-03	0.40	2.23	2.53E+02
5.00E-04	0.30	1.97	6.94E+02	7.50E-03	0.20	4.91	2.89E-03
5.00E-04	0.35	1.94	7.80E+02	7.50E-03	0.25	3.98	2.51E-01
5.00E-04	0.40	1.92	8.40E+02	7.50E-03	0.30	3.27	5.12E+00
7.50E-04	0.20	2.77	1.32E+02	7.50E-03	0.35	2.76	3.68E+01
7.50E-04	0.25	2.21	3.72E+02	7.50E-03	0.40	2.39	1.33E+02
7.50E-04	0.30	2.02	5.88E+02	1.00E-02	0.20	4.94	7.06E-04
7.50E-04	0.35	1.96	7.05E+02	1.00E-02	0.25	4.13	6.73E-02
7.50E-04	0.40	1.93	7.88E+02	1.00E-02	0.30	3.43	1.78E+00
1.00E-03	0.20	3.07	5.92E+01	1.00E-02	0.35	2.90	1.68E+01
1.00E-03	0.25	2.40	2.41E+02	1.00E-02	0.40	2.52	7.56E+01
1.00E-03	0.30	2.08	4.80E+02	2.50E-02	0.20	4.94	8.89E-06
1.00E-03	0.35	1.99	6.36E+02	2.50E-02	0.25	4.22	1.76E-03
1.00E-03	0.40	1.95	7.39E+02	2.50E-02	0.30	3.71	6.58E-02
2.50E-03	0.20	4.08	1.27E+00	2.50E-02	0.35	3.28	9.68E-01
2.50E-03	0.25	3.16	2.33E+01	2.50E-02	0.40	2.90	7.74E+00
2.50E-03	0.30	2.55	1.24E+02	5.00E-02	0.20	4.93	3.18E-07
2.50E-03	0.35	2.20	3.12E+02	5.00E-02	0.25	4.22	1.21E-04
2.50E-03	0.40	2.04	5.02E+02	5.00E-02	0.30	3.72	6.92E-03
5.00E-03	0.20	4.71	2.69E-02	5.00E-02	0.35	3.36	1.30E-01
5.00E-03	0.25	3.70	1.57E+00	5.00E-02	0.40	3.05	1.24E+00

Table A.2: Summary of parameters m and k_J estimated by fitting theoretical current-voltage characteristics in the tip-plane geometry in the SCLC regime (see section 4.2.2 for details of device simulations) to the semi-empirical expression (4.4) for a range of trap parameters f_t and r_t and a range of mobility anisotropy μ_ρ/μ_z . Note that $R^2 > 0.9999$ for all regressions. Table continued on the next page.

$f_t = N_t/N_v$	$r_t = T/T_t$	m	k_J					
			$\mu_\rho/\mu_z = 1$	$\mu_\rho/\mu_z = 5$	$\mu_\rho/\mu_z = 10$	$\mu_\rho/\mu_z = 15$	$\mu_\rho/\mu_z = 20$	$\mu_\rho/\mu_z = 25$
0.00E+00	0.00	2.00	7.43E+00	1.83E+01	3.21E+01	4.30E+01	5.32E+01	6.29E+01
5.00E-04	0.20	4.22	1.67E+00	2.50E+00	3.45E+00	4.41E+00	5.34E+00	6.25E+00
5.00E-04	0.25	3.28	4.51E+00	8.90E+00	1.32E+01	1.67E+01	2.03E+01	2.39E+01
5.00E-04	0.30	2.67	6.00E+00	1.35E+01	2.08E+01	2.74E+01	3.35E+01	3.93E+01
5.00E-04	0.35	2.35	6.70E+00	1.64E+01	2.52E+01	3.34E+01	4.10E+01	9.36E+02
5.00E-04	0.40	2.18	7.00E+00	1.76E+01	2.75E+01	3.66E+01	4.52E+01	5.34E+01
7.50E-04	0.20	4.56	4.82E-01	6.06E-01	8.33E-01	1.07E+00	1.29E+00	1.52E+00
7.50E-04	0.25	3.58	2.36E+00	4.16E+00	5.94E+00	7.71E+00	9.39E+00	1.10E+01
7.50E-04	0.30	2.91	4.68E+00	9.88E+00	1.50E+01	1.95E+01	2.38E+01	2.79E+01
7.50E-04	0.35	2.49	5.99E+00	1.39E+01	2.16E+01	2.85E+01	3.50E+01	4.12E+01
7.50E-04	0.40	2.26	6.62E+00	1.64E+01	2.54E+01	3.38E+01	4.16E+01	4.91E+01
1.00E-03	0.20	4.77	1.68E-01	1.93E-01	2.65E-01	3.34E-01	4.05E-01	4.74E-01
1.00E-03	0.25	3.78	1.28E+00	2.01E+00	2.92E+00	3.74E+00	4.57E+00	5.39E+00
1.00E-03	0.30	3.11	3.54E+00	7.13E+00	1.04E+01	1.36E+01	1.66E+01	1.95E+01
1.00E-03	0.35	2.61	5.15E+00	1.17E+01	1.80E+01	2.37E+01	2.91E+01	3.42E+01
1.00E-03	0.40	2.33	6.21E+00	1.48E+01	2.33E+01	3.10E+01	3.81E+01	4.49E+01
2.50E-03	0.20	5.21	3.19E-03	2.87E-03	3.86E-03	4.98E-03	6.09E-03	7.22E-03
2.50E-03	0.25	4.24	8.43E-02	1.06E-01	1.50E-01	1.94E-01	2.37E-01	2.80E-01
2.50E-03	0.30	3.54	6.21E-01	9.74E-01	1.43E+00	1.88E+00	2.32E+00	2.76E+00
2.50E-03	0.35	3.05	2.05E+00	3.98E+00	5.89E+00	7.76E+00	9.55E+00	1.13E+01
2.50E-03	0.40	2.65	3.85E+00	8.48E+00	1.31E+01	1.72E+01	2.10E+01	2.47E+01
5.00E-03	0.20	5.53	9.65E-05	7.58E-05	1.01E-04	1.30E-04	1.59E-04	1.89E-04
5.00E-03	0.25	4.46	6.77E-03	7.45E-03	1.06E-02	1.43E-02	1.78E-02	2.13E-02
5.00E-03	0.30	3.77	9.53E-02	1.31E-01	1.95E-01	2.60E-01	3.24E-01	3.87E-01
5.00E-03	0.35	3.27	5.43E-01	9.04E-01	1.37E+00	1.81E+00	2.25E+00	2.67E+00
5.00E-03	0.40	2.89	1.68E+00	3.29E+00	4.97E+00	6.61E+00	8.18E+00	9.72E+00
7.50E-03	0.20	5.64	1.17E-05	8.97E-06	1.21E-05	1.56E-05	1.92E-05	2.29E-05
7.50E-03	0.25	4.60	1.34E-03	1.39E-03	1.98E-03	2.61E-03	3.25E-03	3.90E-03
7.50E-03	0.30	3.87	2.79E-02	3.68E-02	5.48E-02	7.32E-02	9.15E-02	1.10E-01
7.50E-03	0.35	3.37	2.12E-01	3.36E-01	5.05E-01	6.69E-01	8.30E-01	9.88E-01
7.50E-03	0.40	2.99	8.39E-01	1.52E+00	2.34E+00	3.13E+00	3.90E+00	4.66E+00
1.00E-02	0.20	5.70	2.63E-06	1.93E-06	2.57E-06	3.30E-06	4.07E-06	4.84E-06
1.00E-02	0.25	4.67	4.15E-04	4.17E-04	5.97E-04	7.89E-04	9.84E-04	1.18E-03
1.00E-02	0.30	3.95	1.12E-02	1.42E-02	2.11E-02	2.83E-02	3.55E-02	4.27E-02
1.00E-02	0.35	3.43	1.03E-01	1.56E-01	2.40E-01	3.25E-01	4.00E-01	4.80E-01
1.00E-02	0.40	3.05	4.81E-01	8.47E-01	1.30E+00	1.74E+00	2.17E+00	2.60E+00

Table A.2: (cont'd)

$f_t = N_t/N_v$	$r_t = T/T_t$	m	k_I					
			$\mu_\rho/\mu_z = 1$	$\mu_\rho/\mu_z = 5$	$\mu_\rho/\mu_z = 10$	$\mu_\rho/\mu_z = 15$	$\mu_\rho/\mu_z = 20$	$\mu_\rho/\mu_z = 25$
2.50E-02	0.20	5.75	9.20E-10	6.55E-10	8.59E-10	1.10E-09	1.35E-09	1.60E-09
2.50E-02	0.25	4.81	5.98E-07	5.63E-07	7.93E-07	1.04E-06	1.30E-06	1.55E-06
2.50E-02	0.30	4.13	5.00E-04	5.94E-04	8.83E-04	1.19E-03	1.49E-03	1.80E-03
2.50E-02	0.35	3.62	8.28E-03	1.16E-02	1.78E-02	2.41E-02	3.04E-02	3.67E-02
2.50E-02	0.40	3.22	6.37E-02	1.03E-01	1.61E-01	2.19E-01	2.76E-01	3.34E-01
5.00E-02	0.20	5.73	6.56E-10	8.62E-10	9.19E-10	1.10E-09	1.35E-09	1.60E-09
5.00E-02	0.25	4.82	5.64E-07	5.97E-07	7.93E-07	1.04E-06	1.30E-06	1.55E-06
5.00E-02	0.30	4.19	4.64E-05	5.37E-05	7.92E-05	1.06E-04	1.33E-04	1.61E-04
5.00E-02	0.35	3.71	1.09E-03	1.48E-03	2.26E-03	3.07E-03	3.88E-03	4.70E-03
5.00E-02	0.40	3.33	1.14E-02	1.77E-02	2.77E-02	3.79E-02	4.78E-02	5.78E-02

Table A.3: Summary of parameters m and k_I estimated by fitting theoretical current-voltage characteristics in the tip-plane geometry in the SCLC regime (see section 5.2.1 for details of device simulations) to the semi-empirical expression (4.4) for a range of trap parameters f_t and r_t and a range of mobility anisotropy μ_p/μ_z . Note that $R^2 > 0.9999$ for all regressions. Table continued on the next page.

$f_t = N_t/N_v$	$r_t = T/T_t$	m	k_I					
			$\mu_p/\mu_z = 1$	$\mu_p/\mu_z = 5$	$\mu_p/\mu_z = 10$	$\mu_p/\mu_z = 15$	$\mu_p/\mu_z = 20$	$\mu_p/\mu_z = 25$
0.00E+00	0.00	1.96	1.12E+01	2.58E+01	4.19E+01	5.72E+01	7.19E+01	8.61E+01
5.00E-04	0.20	2.59	3.12E+00	4.58E+00	6.49E+00	8.33E+00	1.01E+01	1.19E+01
5.00E-04	0.25	2.13	6.47E+00	1.36E+01	2.07E+01	2.79E+01	3.49E+01	4.18E+01
5.00E-04	0.30	2.04	8.27E+00	1.85E+01	2.99E+01	4.07E+01	5.11E+01	6.14E+01
5.00E-04	0.35	2.01	9.28E+00	2.10E+01	3.41E+01	4.66E+01	5.86E+01	7.03E+01
5.00E-04	0.40	1.99	9.96E+00	2.27E+01	3.69E+01	5.03E+01	6.33E+01	7.59E+01
7.50E-04	0.20	3.10	1.23E+00	1.49E+00	2.00E+00	2.50E+00	3.01E+00	3.50E+00
7.50E-04	0.25	2.31	4.23E+00	7.14E+00	1.06E+01	1.39E+01	1.71E+01	2.02E+01
7.50E-04	0.30	2.09	6.95E+00	1.50E+01	2.41E+01	3.22E+01	4.04E+01	4.84E+01
7.50E-04	0.35	2.03	8.43E+00	1.89E+01	3.08E+01	4.20E+01	5.27E+01	6.33E+01
7.50E-04	0.40	2.00	9.38E+00	2.13E+01	3.46E+01	4.72E+01	5.94E+01	7.12E+01
1.00E-03	0.20	3.50	5.00E-01	5.23E-01	6.76E-01	1.14E+00	1.39E+00	1.64E+00
1.00E-03	0.25	2.54	2.65E+00	4.03E+00	5.82E+00	7.54E+00	9.23E+00	1.09E+01
1.00E-03	0.30	2.16	5.66E+00	1.17E+01	1.86E+01	2.52E+01	3.16E+01	3.60E+01
1.00E-03	0.35	2.06	7.66E+00	1.70E+01	2.74E+01	3.74E+01	4.70E+01	5.61E+01
1.00E-03	0.40	2.02	8.84E+00	1.99E+01	3.24E+01	4.42E+01	5.57E+01	6.68E+01
2.50E-03	0.20	4.62	9.06E-03	8.57E-03	1.12E-02	1.42E-02	1.72E-02	2.02E-02
2.50E-03	0.25	3.41	2.38E-01	3.23E-01	4.63E-01	6.05E-01	7.47E-01	8.88E-01
2.50E-03	0.30	2.68	1.44E+00	2.50E+00	3.47E+00	4.60E+00	5.71E+00	6.81E+00
2.50E-03	0.35	2.28	3.79E+00	7.48E+00	1.18E+01	1.60E+01	2.01E+01	2.41E+01
2.50E-03	0.40	2.12	6.12E+00	1.32E+01	2.13E+01	2.90E+01	3.62E+01	4.34E+01
5.00E-03	0.20	5.19	2.14E-04	1.78E-04	2.36E-04	2.98E-04	3.62E-04	4.26E-04
5.00E-03	0.25	4.05	1.55E-02	1.76E-02	2.46E-02	3.20E-02	3.94E-02	4.68E-02
5.00E-03	0.30	3.23	2.26E-01	3.14E-01	4.58E-01	6.04E-01	7.48E-01	8.92E-01
5.00E-03	0.35	2.65	1.19E+00	2.04E+00	3.14E+00	4.21E+00	5.27E+00	6.32E+00
5.00E-03	0.40	2.31	3.14E+00	6.26E+00	9.68E+00	1.31E+01	1.65E+01	1.98E+01
7.50E-03	0.20	5.41	2.21E-05	1.75E-05	2.21E-05	2.76E-05	3.33E-05	3.90E-05
7.50E-03	0.25	4.31	2.65E-03	2.86E-03	3.96E-03	5.14E-03	6.33E-03	7.53E-03
7.50E-03	0.30	3.51	5.94E-02	8.02E-02	1.18E-01	1.56E-01	1.94E-01	2.32E-01
7.50E-03	0.35	2.90	4.60E-01	7.47E-01	1.14E+00	1.53E+00	1.92E+00	2.30E+00
7.50E-03	0.40	2.48	1.69E+00	3.17E+00	4.81E+00	6.50E+00	8.15E+00	9.78E+00
1.00E-02	0.20	5.52	4.64E-06	3.57E-06	4.46E-06	5.52E-06	6.61E-06	7.73E-06
1.00E-02	0.25	4.45	7.33E-04	7.69E-04	1.06E-03	1.38E-03	1.70E-03	2.02E-03
1.00E-02	0.30	3.67	2.15E-02	2.78E-02	4.04E-02	5.34E-02	6.64E-02	7.94E-02
1.00E-02	0.35	3.07	2.12E-01	3.22E-01	4.85E-01	6.47E-01	8.09E-01	9.69E-01
1.00E-02	0.40	2.62	9.75E-01	1.74E+00	2.71E+00	3.67E+00	4.62E+00	5.55E+00

Table A.3: (cont'd)

$f_t = N_t/N_v$	$r_t = T/T_t$	m	k_I					
			$\mu_\rho/\mu_z = 1$	$\mu_\rho/\mu_z = 5$	$\mu_\rho/\mu_z = 10$	$\mu_\rho/\mu_z = 15$	$\mu_\rho/\mu_z = 20$	$\mu_\rho/\mu_z = 25$
2.50E-02	0.20	5.51	5.60E-08	4.24E-08	5.21E-08	6.37E-08	7.58E-08	8.81E-08
2.50E-02	0.25	4.64	1.53E-05	1.49E-05	2.00E-05	2.56E-05	3.12E-05	3.69E-05
2.50E-02	0.30	4.01	7.34E-04	8.72E-04	1.24E-03	1.63E-03	2.02E-03	2.42E-03
2.50E-02	0.35	3.47	1.31E-02	1.86E-02	2.78E-02	3.71E-02	4.65E-02	5.59E-02
2.50E-02	0.40	3.03	1.09E-01	1.76E-01	2.71E-01	3.59E-01	4.51E-01	5.42E-01
5.00E-02	0.20	5.44	2.12E-09	1.61E-09	1.96E-09	2.39E-09	2.83E-09	3.28E-09
5.00E-02	0.25	4.62	1.07E-06	1.04E-06	1.38E-06	1.76E-06	2.14E-06	2.52E-06
5.00E-02	0.30	4.05	7.24E-05	8.42E-05	1.19E-04	1.55E-04	1.92E-04	2.28E-04
5.00E-02	0.35	3.61	1.56E-03	2.10E-03	3.09E-03	4.11E-03	5.13E-03	6.14E-03
5.00E-02	0.40	3.23	1.65E-02	2.53E-02	3.85E-02	5.18E-02	6.51E-02	7.83E-02

BIBLIOGRAPHY

BIBLIOGRAPHY

- [1] J. Sun, K. Pimcharoen, S. R. Wagner, P. M. Duxbury, and P. Zhang. Nanoscale imaging of dense fiber morphology and local electrical response in conductive regioregular poly(3-hexylthiophene). *Organic Electronics*, 15(2):441–448, 2014.
- [2] M. A. Green. Third generation photovoltaics: Ultra-high conversion efficiency at low cost. *Progress in Photovoltaics: Research and Applications*, 9(2):123–135, 2001.
- [3] J. Nelson. *The Physics of Solar Cells*. London: Imperial College Press, 2003.
- [4] A. C. Mayer, S. R. Scully, B. E. Hardin, M. W. Rowell, and M. D. McGehee. Polymer-based solar cells. *Materials Today*, 10(11):28–33, 2007.
- [5] M.C. Scharber and N.S. Sariciftci. Efficiency of bulk-heterojunction organic solar cells. *Progress in Polymer Science*, 38(12):1929–1940, 2013.
- [6] A. J. Heeger. 25th anniversary article: Bulk heterojunction solar cells: Understanding the mechanism of operation. *Advanced Materials*, 26(1):10–28, 2014.
- [7] C. Liu, C. Yi, K. Wang, Y. Yang, R. S. Bhatta, M. Tsige, S. Xiao, and X. Gong. Single-junction polymer solar cells with over 10% efficiency by a novel two-dimensional donor-acceptor conjugated copolymer. *ACS Applied Materials & Interfaces*, 7(8):4928–4935, 2015.
- [8] C. J. Traverse, R. Pandey, M. C. Barr, and R. R. Lunt. Emergence of highly transparent photovoltaics for distributed applications. *Nature Energy*, 2(11):849–860, 2017.
- [9] A. Bree, D. J. Carswell, and L. E. Lyons. Photo- and semi-conductance of organic crystals. Part I. Photo-effects in tetracene and anthracene. *Journal of the Chemical Society*, 0:1728–1733, 1955.
- [10] L. E. Lyons. Photo- and semi-conductance in organic crystals. Part V. Ionized states in molecular crystals. *Journal of the Chemical Society*, 0:5001–5007, 1957.
- [11] D. Kearns and M. Calvin. Photovoltaic effect and photoconductivity in laminated organic systems. *The Journal of Chemical Physics*, 29(4):950–951, oct 1958.

- [12] H. Kallmann and M. Pope. Electrolytic contacts for photoconductivity measurements. *Review of Scientific Instruments*, 30(1):44–46, 1959.
- [13] A. K. Ghosh, D. L. Morel, T. Feng, R. F. Shaw, and C. A. Rowe. Photovoltaic and rectification properties of Al/Mg phthalocyanine/Ag Schottkybarrier cells. *Journal of Applied Physics*, 45(1):230–236, 1974.
- [14] B. R. Weinberger, M. Akhtar, and S. C. Gau. Polyacetylene photovoltaic and devices. *Synthetic Metals*, 4:187–197, 1982.
- [15] G. A. Chamberlain. Organic solar-cells - a review. *Solar Cells*, 8(1):47–83, 1983.
- [16] D. Whrle and D. Meissner. Organic solar cells. *Advanced Materials*, 3(3):129–138, 1991.
- [17] C. W. Tang. Twolayer organic photovoltaic cell. *Applied Physics Letters*, 48(2):183–185, 1986.
- [18] G. Yu, J. Gao, J. C. Hummelen, F. Wudl, and A. J. Heeger. Polymer photovoltaic cells: Enhanced efficiencies via a network of internal donor-acceptor heterojunctions. *Science*, 270(5243):1789–1791, 1995.
- [19] G. Zhang, K. Zhang, Q. Yin, X.-F. Jiang, Z. Wang, J. Xin, W. Ma, H. Yan, F. Huang, and Y. Cao. High-performance ternary organic solar cell enabled by a thick active layer containing a liquid crystalline small molecule donor. *Journal of the American Chemical Society*, 139(6):2387–2395, 2017.
- [20] W. Zhao, S. Li, H. Yao, S. Zhang, Y. Zhang, B. Yang, and J. Hou. Molecular optimization enables over 13% efficiency in organic solar cells. *Journal of the American Chemical Society*, 139(21):7148–7151, 2017.
- [21] L. S. C. Pingree, M. C. Hersam, M. M. Kern, B. J. Scott, and T. J. Marks. Spatially-resolved electroluminescence of operating organic light-emitting diodes using conductive atomic force microscopy. *Applied Physics Letters*, 85(2):344–346, 2004.
- [22] B. Geffroy, P. Le Roy, and C. Prat. Organic light-emitting diode (OLED) technology: materials, devices and display technologies. *Polymer International*, 55(6):572–582, 2006.
- [23] M. Kuik, G.-J. A. H. Wetzelaer, H. T. Nicolai, N. I. Craciun, D. M. De Leeuw, and P. W. M. Blom. 25th anniversary article: Charge transport and recombination in polymer light-emitting diodes. *Advanced Materials*, 26(4):512–531, 2014.

- [24] H. Sirringhaus, N. Tessler, and R. H. Friend. Integrated optoelectronic devices based on conjugated polymers. *Science*, 280(5370):1741–1744, 1998.
- [25] H. Sirringhaus. 25th anniversary article: Organic field-effect transistors: The path beyond amorphous silicon. *Advanced Materials*, 26(9):1319–1335, 2014.
- [26] V. Coropceanu, J. Cornil, D. A. da Silva, Y. Olivier, R. Silbey, and J. L. Bredas. Charge transport in organic semiconductors. *Chemical Reviews*, 107(4):926–952, 2007.
- [27] C. Goh, R. J. Kline, M. D. McGehee, E. N. Kadnikova, and J. M. J. Frchet. Molecular-weight-dependent mobilities in regioregular poly(3-hexyl-thiophene) diodes. *Applied Physics Letters*, 86(12):122110, 2005.
- [28] Z. Chiguvare and V. Dyakonov. Trap-limited hole mobility in semiconducting poly(3-hexylthiophene). *Physical Review B*, 70(23):235207, 2004.
- [29] O. Douhret, L. Lutsen, A. Swinnen, M. Bresselge, K. Vandewal, L. Goris, and J. Manca. Nanoscale electrical characterization of organic photovoltaic blends by conductive atomic force microscopy. *Applied Physics Letters*, 89(3):032107, 2006.
- [30] A. Alexeev, J. Loos, and M. M. Koetse. Nanoscale electrical characterization of semiconducting polymer blends by conductive atomic force microscopy (C-AFM). *Ultramicroscopy*, 106(3):191–199, 2006.
- [31] M. Dante, J. Peet, and T. Q. Nguyen. Nanoscale charge transport and internal structure of bulk heterojunction conjugated polymer/fullerene solar cells by scanning probe microscopy. *Journal of Physical Chemistry C*, 112(18):7241–7249, 2008.
- [32] O. G. Reid, K. Munechika, and D. S. Ginger. Space charge limited current measurements on conjugated polymer films using conductive atomic force microscopy. *Nano Letters*, 8(6):1602–1609, 2008.
- [33] G. A. MacDonald, R. A. Veneman, D. Placencia, and N. R. Armstrong. Electrical property heterogeneity at transparent conductive oxide/organic semiconductor interfaces: Mapping contact ohmicity using conducting-tip atomic force microscopy. *ACS Nano*, 6(11):9623–9636, 2012.
- [34] H. Yang, E. Glynnos, B. Huang, and P. F. Green. Out-of-plane carrier transport in conjugated polymer thin films: Role of morphology. *Journal of Physical Chemistry C*, 117(19):9590–9597, 2013.

- [35] C. Tanase, E. J. Meijer, P. W. M. Blom, and D. M. de Leeuw. Unification of the hole transport in polymeric field-effect transistors and light-emitting diodes. *Physical Review Letters*, 91(21):216601, 2003.
- [36] X. N. Yang, J. Loos, S. C. Veenstra, W. J. H. Verhees, M. M. Wienk, J. M. Kroon, M. A. J. Michels, and R. A. J. Janssen. Nanoscale morphology of high-performance polymer solar cells. *Nano Letters*, 5(4):579–583, 2005.
- [37] G. Li, V. Shrotriya, Y. Yao, and Y. Yang. Investigation of annealing effects and film thickness dependence of polymer solar cells based on poly(3-hexylthiophene). *Journal of Applied Physics*, 98(4):043704, 2005.
- [38] W. L. Ma, C. Y. Yang, X. Gong, K. Lee, and A. J. Heeger. Thermally stable, efficient polymer solar cells with nanoscale control of the interpenetrating network morphology. *Advanced Functional Materials*, 15(10):1617–1622, 2005.
- [39] P. W. M. Blom, M. J. M. de Jong, and M. G. van Munster. Electric-field and temperature dependence of the hole mobility in poly(p-phenylene vinylene). *Physical Review B*, 55:R656–R659, 1997.
- [40] H.-N. Lin, H.-L. Lin, S.-S. Wang, L.-S. Yu, G.-Y. Perng, S.-A. Chen, and S.-H. Chen. Nanoscale charge transport in an electroluminescent polymer investigated by conducting atomic force microscopy. *Applied Physics Letters*, 81(14):2572–2574, 2002.
- [41] C. Ionescu-Zanetti, A. Mechler, S.A. Carter, and R. Lal. Semiconductive polymer blends: Correlating structure with transport properties at the nanoscale. *Advanced Materials*, 16(5):385–389, 2004.
- [42] R. Yang, A. Garcia, D. Korystov, A. Mikhailovsky, G. C. Bazan, and T. Q. Nguyen. Control of interchain contacts, solid-state fluorescence quantum yield, and charge transport of cationic conjugated polyelectrolytes by choice of anion. *Journal of the American Chemical Society*, 128(51):16532–16539, 2006.
- [43] M. A. Lampert and P. Mark. *Current injection in solids*. Academic Press, New York, 1970.
- [44] A. J. Campbell, D. D. C. Bradley, and D. G. Lidzey. Space-charge limited conduction with traps in poly(phenylene vinylene) light emitting diodes. *Journal of Applied Physics*, 82(12):6326–6342, 1997.
- [45] J. Dacuna and A. Salleo. Modeling space-charge-limited currents in organic semiconductors: Extracting trap density and mobility. *Physical Review B*, 84(19):9, 2011.

- [46] O. Douhret, A. Swinnen, S. Bertho, I. Haeldermans, J. D’Haen, M. D’Olieslaeger, D. Vanderzande, and J. V. Manca. Highresolution morphological and electrical characterisation of organic bulk heterojunction solar cells by scanning probe microscopy. *Progress in Photovoltaics: Research and Applications*, 15(8):713–726, 2007.
- [47] M. Pope and C. E. Swenberg. *Electronic processes in organic crystals and polymers*. Oxford University Press, New York, 1999.
- [48] A. J. Mozer and N. S. Sariciftci. Negative electric field dependence of charge carrier drift mobility in conjugated, semiconducting polymers. *Chemical Physics Letters*, 389(46):438–442, 2004.
- [49] D. Wood, I. Hancox, T. S. Jones, and N. R. Wilson. Quantitative nanoscale mapping with temperature dependence of the mechanical and electrical properties of poly(3-hexythiophene) by conductive atomic force microscopy. *The Journal of Physical Chemistry C*, 119(21):11459–11467, 2015.
- [50] Y. Roichman and N. Tessler. Generalized Einstein relation for disordered semiconductors - Implications for device performance. *Applied Physics Letters*, 80(11):1948–1950, 2002.
- [51] G. A. H. Wetzelaer, L. J. A. Koster, and P. W. M. Blom. Validity of the Einstein relation in disordered organic semiconductors. *Physical Review Letters*, 107(6):4, 2011.
- [52] L. J. A. Koster, E. C. P. Smits, V. D. Mihailetschi, and P. W. M. Blom. Device model for the operation of polymer/fullerene bulk heterojunction solar cells. *Physical Review B*, 72(8):085205, 2005.
- [53] N. Kopteva, E. O’Riordan, and L. Vulkov. Computational methods for boundary and interior layers. *International Journal of Numerical Analysis and Modeling*, 7(3):I–II, 2010.
- [54] D. L. Scharfetter and H. K. Gummel. Large-signal analysis of a silicon Read diode oscillator. *IEEE Transactions on Electron Devices*, 16(1):64–77, 1969.
- [55] S. Selberherr. *Analysis and Simulation of Semiconductor Devices*. Springer Vienna, 1984.
- [56] F. Brezzi, L. D. Marini, S. Micheletti, P. Pietra, R. Sacco, and S. Wang. Discretization of semiconductor device problems (i). *Special Volume: Numerical Methods in Electromagnetics, Vol 13*, 13:317–441, 2005.

- [57] E. A. B. Cole. *Mathematical and Numerical Modelling of Heterostructure Semiconductor Devices: From Theory to Programming*. Springer-Verlag London, 2009.
- [58] J. van Dijk, G. M. W. Kroesen, and A. Bogaerts. Plasma modelling and numerical simulation. *Journal of Physics D: Applied Physics*, 42(19):190301, 2009.
- [59] C. Jacoboni. *Theory of Electron Transport in Semiconductors: Pathway from Elementary Physics to Nonequilibrium Green Functions*, volume 165. Springer-Verlag Berlin Heidelberg, 2010.
- [60] T. Kirchartz and J. Nelson. Device modelling of organic bulk heterojunction solar cells. *Multiscale Modelling of Organic and Hybrid Photovoltaics*, 352:279–324, 2014.
- [61] . Bjrcck. *Numerical Methods in Matrix Computations*. Springer, Cham, 2015.
- [62] P. J. Olver and C. Shakiban. *Applied Linear Algebra*. Springer, Cham, 2018.
- [63] R. A. Usmani. Inversion of Jacobi’s tridiagonal matrix. *Computers & Mathematics with Applications*, 27(8):59–66, 1994.
- [64] T. Yamamoto. Inversion formulas for tridiagonal matrices with applications to boundary value problems. *Numerical Functional Analysis and Optimization*, 22(3-4):357–385, 2001.
- [65] H. Sirringhaus, P. J. Brown, R. H. Friend, M. M. Nielsen, K. Bechgaard, B. M. W. Langeveld-Voss, A. J. H. Spiering, R. A. J. Janssen, E. W. Meijer, P. Herwig, and D. M. de Leeuw. Two-dimensional charge transport in self-organized, high-mobility conjugated polymers. *Nature*, 401(6754):685–688, 1999.
- [66] J. A. Merlo and C. D. Frisbie. Field effect transport and trapping in regioregular polythiophene nanofibers. *Journal of Physical Chemistry B*, 108(50):19169–19179, 2004.
- [67] W. D. Oosterbaan, J. C. Bolsee, A. Gadisa, V. Vrindts, S. Bertho, J. D’Haen, T. J. Cleij, L. Lutsen, C. R. McNeill, L. Thomsen, J. V. Manca, and D. Vanderzande. Alkyl-chain-length-independent hole mobility via morphological control with poly(3-alkylthiophene) nanofibers. *Advanced Functional Materials*, 20(5):792–802, 2010.
- [68] H. A. van der Vorst. Bi-CGSTAB: A fast and smoothly converging variant of Bi-CG for the solution of nonsymmetric linear systems. *SIAM Journal on Scientific and Statistical Computing*, 13(2):631–644, 1992.

- [69] A. A. Grinberg and S. Luryi. Space-charge-limited current and capacitance in double-junction diodes. *Journal of Applied Physics*, 61(3):1181–1189, 1987.
- [70] H. T. Nicolai, M. M. Mandoc, and P. W. M. Blom. Electron traps in semiconducting polymers: Exponential versus gaussian trap distribution. *Physical Review B*, 83(19):5, 2011.
- [71] H. T. Nicolai, M. Kuik, G. A. H. Wetzelaer, B. de Boer, C. Campbell, C. Risko, J. L. Bredas, and P. W. M. Blom. Unification of trap-limited electron transport in semiconducting polymers. *Nature Materials*, 11(10):882–887, 2012.
- [72] A. Salleo, R. J. Kline, D. M. DeLongchamp, and M. L. Chabinyc. Microstructural characterization and charge transport in thin films of conjugated polymers. *Advanced Materials*, 22(34):3812–3838, 2010.
- [73] F. Liu, Y. Gu, X. B. Shen, S. Ferdous, H. W. Wang, and T. P. Russell. Characterization of the morphology of solution-processed bulk heterojunction organic photovoltaics. *Progress in Polymer Science*, 38(12):1990–2052, 2013.
- [74] D. A. Chen, A. Nakahara, D. G. Wei, D. Nordlund, and T. P. Russell. P3HT/PCBM bulk heterojunction organic photovoltaics: Correlating efficiency and morphology. *Nano Letters*, 11(2):561–567, 2011.
- [75] B. A. Collins, J. R. Tumbleston, and H. Ade. Miscibility, crystallinity, and phase development in P3HT/PCBM solar cells: Toward an enlightened understanding of device morphology and stability. *Journal of Physical Chemistry Letters*, 2(24):3135–3145, 2011.
- [76] C. R. McNeill. Morphology of all-polymer solar cells. *Energy & Environmental Science*, 5(2):5653–5667, 2012.
- [77] D. M. DeLongchamp, R. J. Kline, and A. Herzing. Nanoscale structure measurements for polymer-fullerene photovoltaics. *Energy & Environmental Science*, 5(3):5980–5993, 2012.
- [78] Y. Kim, S. Cook, S. M. Tuladhar, S. A. Choulis, J. Nelson, J. R. Durrant, D. D. C. Bradley, M. Giles, I. McCulloch, C. S. Ha, and M. Ree. A strong regioregularity effect in self-organizing conjugated polymer films and high-efficiency polythiophene: fullerene solar cells. *Nature Materials*, 5(3):197–203, 2006.

- [79] K. Sivula, C. K. Luscombe, B. C. Thompson, and J. M. J. Frchet. Enhancing the thermal stability of polythiophene:fullerene solar cells by decreasing effective polymer regioregularity. *Journal of the American Chemical Society*, 128(43):13988–13989, 2006.
- [80] Z. Y. Wu, A. Petzold, T. Henze, T. Thurn-Albrecht, R. H. Lohwasser, M. Sommer, and M. Thelakkat. Temperature and molecular weight dependent hierarchical equilibrium structures in semiconducting poly(3-hexylthiophene). *Macromolecules*, 43(10):4646–4653, 2010.
- [81] S. Joshi, S. Grigorian, and U. Pietsch. X-ray structural and crystallinity studies of low and high molecular weight poly(3-hexylthiophene). *Physica Status Solidi (a) - Applications and Materials Science*, 205(3):488–496, 2008.
- [82] A. M. Ballantyne, L. Chen, J. Dane, T. Hammant, F. M. Braun, M. Heeney, W. Duffy, I. McCulloch, D. D. C. Bradley, and J. Nelson. The effect of poly(3-hexylthiophene) molecular weight on charge transport and the performance of polymer:fullerene solar cells. *Advanced Functional Materials*, 18(16):2373–2380, 2008.
- [83] A. Zen, M. Saphiannikova, D. Neher, J. Grenzer, S. Grigorian, U. Pietsch, U. Asawapirom, S. Janietz, U. Scherf, I. Lieberwirth, and G. Wegner. Effect of molecular weight on the structure and crystallinity of poly(3-hexylthiophene). *Macromolecules*, 39(6):2162–2171, 2006.
- [84] J. A. Lim, F. Liu, S. Ferdous, M. Muthukumar, and A. L. Briseno. Polymer semiconductor crystals. *Materials Today*, 13(5):14–24, 2010.
- [85] H. H. Yang, S. W. LeFevre, C. Y. Ryu, and Z. N. Bao. Solubility-driven thin film structures of regioregular poly(3-hexylthiophene) using volatile solvents. *Applied Physics Letters*, 90(17):3, 2007.
- [86] D. H. Kim, Y. Jang, Y. D. Park, and K. Cho. Layered molecular ordering of self-organized poly(3-hexylthiophene) thin films on hydrophobized surfaces. *Macromolecules*, 39(17):5843–5847, 2006.
- [87] J. Liu, M. Arif, J. Zou, S. I. Khondaker, and L. Zhai. Controlling poly(3-hexylthiophene) crystal dimension: nanowhiskers and nanoribbons. *Macromolecules*, 42(24):9390–9393, 2009.
- [88] J. Ma, K. Hashimoto, T. Koganezawa, and K. Tajima. End-on orientation of semiconducting polymers in thin films induced by surface segregation of fluoroalkyl chains. *Journal of the American Chemical Society*, 135(26):9644–9647, 2013.

- [89] I. Osaka and K. Takimiya. Backbone orientation in semiconducting polymers. *Polymer*, 59:A1–A15, 2015.
- [90] Y. K. Lan and C. I. Huang. Charge mobility and transport behavior in the ordered and disordered states of the regioregular poly(3-hexylthiophene). *Journal of Physical Chemistry B*, 113(44):14555–14564, 2009.
- [91] J. C. Bolsee, W. D. Oosterbaan, L. Lutsen, D. Vanderzande, and J. Manca. C-AFM on conjugated polymer nanofibers: Capable of assessing one fiber mobility. *Organic Electronics*, 12(12):2084–2089, 2011.
- [92] F. Zhang, A. Vollmer, J. Zhang, Z. Xu, J. P. Rabe, and N. Koch. Energy level alignment and morphology of interfaces between molecular and polymeric organic semiconductors. *Organic Electronics*, 8(5):606–614, 2007.
- [93] Z. Xu, L.-M. Chen, M.-H. Chen, G. Li, and Y. Yang. Energy level alignment of poly(3-hexylthiophene): [6,6]-phenyl C61 butyric acid methyl ester bulk heterojunction. *Applied Physics Letters*, 95(1):013301, 2009.
- [94] B. Huang, E. Glynos, B. Frieberg, H. Yang, and P. F. Green. Effect of thickness-dependent microstructure on the out-of-plane hole mobility in poly(3-hexylthiophene) films. *ACS Applied Materials & Interfaces*, 4(10):5204–5210, 2012.
- [95] K. Kawano and C. Adachi. Evaluating carrier accumulation in degraded bulk heterojunction organic solar cells by a thermally stimulated current technique. *Advanced Functional Materials*, 19(24):3934–3940, 2009.
- [96] W. Weise, T. Keith, N. von Malm, and H. von Seggern. Trap concentration dependence of thermally stimulated currents in small molecule organic materials. *Physical Review B*, 72(4):235207, 2005.
- [97] R. A. Street. Localized state distribution and its effect on recombination in organic solar cells. *Physical Review B*, 84(7):075208, 2011.
- [98] J. H. Youn, Y. I. Lee, H. T. Moon, M. S. Ryu, J. Kim, and J. Jang. Trap energy level of P3HT: PCBM-71 bulk heterojunction solar cells with PICTS (photo-induced current transient spectroscopy). *Current Applied Physics*, 10(3):S525–S527, 2010.
- [99] A. J. Campbell, D. D. C. Bradley, E. Werner, and W. Brtting. Transient capacitance measurements of the transport and trap states distributions in a conjugated polymer. *Organic Electronics*, 1(1):21–26, 2000.

- [100] T. P. Nguyen. Defects in organic electronic devices. *Physica Status Solidi (a) - Applications and Materials Science*, 205(1):162–166, 2008.
- [101] C. Renaud and T.-P. Nguyen. Identification of the nature of trapping centers in polyspirobifluorene based diodes by using electrical characterization. *Journal of Applied Physics*, 107(12):124505, 2010.
- [102] K. Fukuda, T. Sekitani, and T. Someya. Effects of annealing on electronic and structural characteristics of pentacene thin-film transistors on polyimide gate dielectrics. *Applied Physics Letters*, 95(2):023302, 2009.
- [103] A. Sharma, P. Kumar, B. Singh, S. R. Chaudhuri, and S. Ghosh. Capacitance-voltage characteristics of organic schottky diode with and without deep traps. *Applied Physics Letters*, 99(2):023301, 2011.
- [104] I. H. Campbell, D. L. Smith, and J. P. Ferraris. Electrical-impedance measurements of polymer light-emitting-diodes. *Applied Physics Letters*, 66(22):3030–3032, 1995.
- [105] G. Garcia-Belmonte, P. P. Boix, J. Bisquert, M. Sessolo, and H. J. Bolink. Simultaneous determination of carrier lifetime and electron density-of-states in P3HT:PCBM organic solar cells under illumination by impedance spectroscopy. *Solar Energy Materials and Solar Cells*, 94(2):366–375, 2010.
- [106] J. C. Scott and G. G. Malliaras. Charge injection and recombination at the metal-organic interface. *Chemical Physics Letters*, 299(2):115–119, 1999.
- [107] P. N. Murgatroyd. Theory of space-charge-limited current enhanced by frenkel effect. *Journal of Physics D: Applied Physics*, 3(2):151, 1970.
- [108] W. F. Pasveer, J. Cottaar, C. Tanase, R. Coehoorn, P. A. Bobbert, P. W. M. Blom, D. M. de Leeuw, and M. A. J. Michels. Unified description of charge-carrier mobilities in disordered semiconducting polymers. *Physical Review Letters*, 94:206601, 2005.